TAMPEREEN TEKNILLINEN YLIOPISTO
TAMPERE UNIVERSITY OF TECHNOLOGY

Elena Heikkilä

Computational Modeling of Functional Gold Nanoparticles in Biological Environment

Julkaisu 1234 • Publication 1234

Tampere 2014

Tampereen teknillinen yliopisto. Julkaisu 1234
Tampere University of Technology. Publication 1234

Elena Heikkilä

Computational Modeling of Functional Gold Nanoparticles in Biological Environment

Thesis for the degree of Doctor of Science in Technology to be presented with due permission for public examination and criticism in Sähkötalo Building, Auditorium S3, at Tampere University of Technology, on the 8th of September 2014, at 12 noon.

Tampereen teknillinen yliopisto - Tampere University of Technology
Tampere 2014

Doctoral candidate

Elena Heikkilä, MSc
Materials and Molecular Modeling Group
Department of Physics
Tampere University of Technology
Tampere, Finland

Supervisor

Jaakko Akola, PhD
Materials and Molecular Modeling Group
Department of Physics
Tampere University of Technology
Tampere, Finland

Pre-examiners

Kai Nordlund, Prof.
Division of Materials Physics
Department of Physics
Helsinki Institute of Physics
University of Helsinki
Helsinki, Finland

Juha Vaara, Prof.
NMR Research Group
Department of Physics
University of Oulu
Oulu, Finland

Opponent

Henrik Grönbeck, Prof.
Competence Centre for Catalysis
Department of Applied Physics
Chalmers University of Technology
Gothenburg, Sweden

ISBN 978-952-15-3337-2 (printed)
ISBN 978-952-15-3346-4 (PDF)
ISSN 1459-2045

ABSTRACT

TAMPERE UNIVERSITY OF TECHNOLOGY
ELENA HEIKKILÄ : Computational modeling of functional gold nanoparticles in biological environment

This work focuses on exploring the properties and functions of charged monolayer-protected gold nanoparticles (AuNPs) in biologically relevant environments by use of atomic-scale molecular dynamics (MD) simulations.

The use of nanoparticles (NPs) in modern technology has been increasing rapidly during the last few years. NPs of different kinds have already been employed, *e.g.,* in nanomedicine as cancer treatments, cleaning agents, cosmetics and new materials for industrial purposes. AuNPs are one type of nanoagents that are being employed for such purposes, and according to recent experimental findings they may have cytotoxic properties. In particular, AuNPs of 2-nm diameter or less are known to permeate through plasma membranes and induce cell death. Hence, studying potential harmful effects of AuNPs is of importance. Understanding the interaction between NPs and cell membranes is relevant also because all trafficking between the cell interior and extracellular space takes place through the cell membrane.

The first study concentrated on the properties of AuNPs in aqueous solution at physiological temperature (310 K). The results showed that electrostatic properties modulate the formation of a complex comprised of the AuNP together with surrounding ions and water, and suggested that electrostatics is one of the central factors in the complexation of AuNPs with other nanomaterials and biological systems. The results highlighted the importance of long-range electrostatic interactions in determining NP properties in aqueous solutions. This observation was concluded to indicate an important a role in the interplay between NPs and lipid membranes, which surround cells.

The second part of the research comprises of studying AuNPs in the presence of model cell membranes. The binding of AuNP and membrane reorganization processes were discovered to be governed by co-operative effects where AuNP, counter ions, water and membrane all contribute. The results suggest that a permeation of a cationic AuNP takes place through pore-formation with partial NP neutralization, leading to membrane disruption at higher NP concentrations. The results also suggested a potential mechanism for cytotoxity as cationic AuNP binding to the extracellular leaflet may trigger apoptosis through translocation of phophatidylserine.

Summa summarum, the work presented here provides novel aspects on the interactions of functional AuNPs on cellular level by means of atomistic MD simulation.

TIIVISTELMÄ

TAMPEREEN TEKNILLINEN YLIOPISTO
ELENA HEIKKILÄ: Kultananohiukkasten laskennallinen mallintaminen biologisissa olosuhteissa

Tutkimuksessa mallinnettiin kultananohiukkasia laskennallisen molekyylidynamiikan keinoin biologisesti relevantissa ympäristössä. Kultananohiukkasia ja solukalvoja kuvaamaan luotiin teoreettiset mallit, joille suoritettiin atomitason simulaatioita. Tutkimuksella saavutettiin uutta informaatiota kultananohiukkasten vuorovaikutuksista solutasolla.

Nanohiukkasia käytetään nykypäivänä teknologiassa yhä enenevissä määrin ja mitä moninaisimpiin tarkoituksiin. Käyttökohteita ovat muun muassa nanolääketieteen syöpähoidot, puhdistusaineet, kosmetiikka sekä uudet teollisuusmateriaalit. Kultananohiukkaset muodostavat yhden lukuisista nanohiukkastyypeistä. Viimeaikaiset tutkimuslöydökset ovat antaneet viitteitä siitä, että nanohiukkasilla olisi sytotoksisia ominaisuuksia. Erityisesti pienten, 2-nm kokoisten ja sitä pienempien, nanohiukkasten on todettu kulkeutuvan solukalvojen läpi ja aiheuttavan solukuolemia. Mahdollisten terveyshaittojen vuoksi kultananohiukkasten solutason vaikutusten kartoittaminen on tärkeää. Lisäksi nanohiukkasten ja solukalvojen vuorovaikutusprosessien ymmärtäminen on merkityksellistä, sillä kaikki liikenne solujen sisä- ja ulkopuolen välillä on solukalvovälitteistä.

Tutkimuksen ensimmäisessä osassa tarkasteltiin kultananohiukkasten ominaisuuksia nestemäisessä vesiliuoksessa fysiologisessa lämpötilassa (310 K). Tulokset osoittivat, että sähköstaattiset vuorovaikutukset karakterisoivat kultananohiukkasten käyttäytymistä vesiliuoksessa. Tutkimuksessa selvisi, että kultananohiukkaset muodostavat yhdessä ionien ja veden kanssa komplekseja eikä niitä tule näin ollen käsitellä irrallisina kappaleina. Kompleksoitumisen keskeiseksi aiheuttajaksi osoittautui sähköstatiikka. Tuloksista tehtiin johtopäätös, että pitkän kantaman sähköiset vuorovaikutukset ovat tärkeässä osassa myös kultananohiukkasten ja solukalvojen välisessä dynamiikassa.

Tutkittaessa kultananohiukkasen sitoutumista solukalvon pinnalle sekä solukalvon uudelleenjärjestäytymistä, havaittiin, että ilmöiden taustalla on yhteisvaikutteinen prosessi, johon osallistuvat kultananohiukkaset, vastaionit, vesi ja solukalvo. Tulokset puhuvat sen puolesta, että kultananohiukkasen kulkeutuminen solukalvoon voisi tapahtua kalvorakkulan muodostumisen kautta, johtaen solukalvon toiminnan häiriintymiseen. Yksi mahdollinen mekanismi sytotoksisuudelle olisi tulosten perusteella positiivisesti varatun nanopartikkelin solukalvon ulkopintaan sitoutumisesta aiheutuva fosfadityyliseriinin translokaatio, joka käynnistää apoptoosin.

LIST OF PUBLICATIONS

This thesis consists of the following articles:

I E. Heikkilä, A. Gurtovenko, H. Martinez-Seara, H. Häkkinen, I. Vattulainen and J. Akola. Atomistic Simulations of Functional $Au_{144}(SR)_{60}$ Gold Nanoparticles in Aqueous Environment, J. Phys. Chem. C, **116** (17), 9805–9815, (2012). DOI: 10.1021/jp301094m

II E. Heikkilä, H. Martinez-Seara, A. Gurtovenko, M. Javanainen, H. Häkkinen, I. Vattulainen, J. Akola. Cationic Au Nanoparticle Binding with Plasma Membrane-Like Lipid Bilayers: Potential Mechanism for Spontaneous Permeation to Cells Revealed by Atomistic Simulations, J. Phys. Chem. C, **118** (20), 11131–11141, (2014). DOI: 10.1021/jp5024026

III E. Heikkilä, H. Martinez-Seara, A. Gurtovenko, I. Vattulainen and J. Akola. Atomistic Simulations of Anionic $Au_{144}(SR)_{60}$ Nanoparticles Interacting with Asymmetric Model Lipid Membranes, BBA Biomembranes, **1838** (11), 2852–2860, (2014). DOI: 10.1016/j.bbamem.2014.07.027

Major part of the simulations and the analysis were carried out by the author. The models in articles **I**–**III** were originally constructed by Andrey Gurtovenko and complemented by the author. The ESP analysis in article **I** and the constraint-released simulation in article **II** were carried out by Hector Martinez-Seara. The free-energy calculation in article **II** was performed by Matti Javanainen. The original article manuscripts were written by the author. Jaakko Akola and Ilpo Vattulainen contributed to the article writing in articles **I**–**III**. Hector Martinez-Seara contributed in article writing in article **II**.

CONTENTS

LIST OF FIGURES AND TABLES

LIST OF ABBREVIATIONS AND SYMBOLS

AuNP	Gold nanoparticle $Au_{144}(SR)_{60}$
$AuNP^+$	Cationic (positively charged) gold nanoparticle
$AuNP^-$	Anionic (negatively charged) gold nanoparticle
NP	Nanoparticle
MPC	Monolayer protected cluster
MD	Molecular dynamics
MM	Molecular mechanics
QM	Quantum mechanics
DFT	Density functional theory
CG	Coarse-grained
POPC	Phosphatidylcholine lipid (1-palmitoyl-2-oleoyl-*sn*-glycero-3-phosphocholine)
POPS	Phosphatidylserine lipid (1-palmitoyl-2-oleoyl-*sn*-glycero-3-phosphoserine)
DSPC	Phosphatidylcholine lipid (1,2-distearoyl-*sn*-glycero- 3-phosphocholine)
EC	Extracellular
IC	Intracellular, cytosolic
H-bond	Hydrogen bond
NVE	Constant number of particles, volume and energy
NPT	Constant number of particles, pressure and temperature
NVT	Constant number of particles, volume and temperature
PBC	Periodic boundary conditions
SPC	Single point charge water model
TIP3P	Transferable intermolecular potential with 3 points
OPLS	Optimized potentials for liquid simulations
PME	Particle mesh Ewald method
ESP	Electrostatic potential
COM	Center of mass
LJ	Lennard-Jones
MSD	Mean Square Displacement
RDF	Radial distribution function
MOI	Moment of inertia
ACF	Auto-correlation function
RCF	Rotational correlation function

Δt	Timestep
e	Elementary charge
$\mathbf{F}_i$	Force acting on particle i
$\mathbf{v}_i$	Velocity of particle i
m_i	Mass of particle i
t	Time coordinate
N	Number of particles
P	Pressure
q_i	Charge of particle i
r	Distance
$\mathbf{r}_i$	Position vector of particle i
r_{ij}	Distance between particles i and j
k_B	Boltzmann constant
k^b_{ij}	Force constant for bond stretching
$\mathbf{r}_{ij}$	Vector from particle i to j
$\sigma_{ij}, \epsilon_{ij}$	Lennard-Jones parameters for particles i and j
τ	Berendsen temperature coupling time constant
T	Temperature
T_0	Reference temperature
ϕ_{ijkl}	Dihedral angle describing the rotation of bond $i-j$ around $j-k$ with respect to $k-l$, *i.e.,* it is the angle between planes ijk and jkl, defined by the particles i, j, k and l.
ϕ_s	Equilibrium angle for a dihedral angle
V	Potential energy
V_b	Bond stretching contributions to the potential energy
V_a	Bond angle contributions to the potential energy
V_d	Dihedral angle contributions to the potential energy
V_C	Coulombic potential
V_LJ	Lennard-Jones potential
x, y, z	Cartesian coordinates
S_CD	Deuterium order parameter tensor
ϕ	Electrostatic potential
$\mathbf{E}$	Electric field
Q_r	Charge enclosed by a sphere of radius r
ε_0	Permittivity of vacuum
k	Wave vector
$n(\mathbf{r})$	Charge density
ρ	Particle density
ρ_A	Density of particles A

$\langle \rho_A \rangle$	Average density of particles A
$C_f(t)$	Correlation function of species f
τ_f	Correlation time of species f
P_n	n^{th} order Legendre polynomial
λ_D	Debye length
l_B	Bjerrum length
τ_{HB}	Hydrogen bond lifetime
g_{AB}	Pair correlation function of particles of type A and B
R_g	Radius of gyration
D_{A}	Diffusion coefficient of particle A

1. OVERVIEW

The use of nanoparticles in modern technology has been increasing rapidly during the last few years. Nanoparticles of different kinds have already been employed, *e.g.,* in nanomedicine as cancer treatments, cleaning agents, cosmetics and new materials for industrial purposes — only imagination seems to set limits for the number of potential future applications of nanoparticles. On the other hand, the novelty of using nanoparticles in applications is not just an advantage, since it brings in unknown properties of nanoparticles: possible toxicity to human and other living organisms or other yet unknown environmental effects. Signs of nanoparticle cytotoxicity have been observed in the experiments. As long as we do not know better, nanoparticles can reasonably be considered as a potential hazard to the health and environment. Hence, it is essential to investigate the effects of nanoparticles at the cellular level.

Gold nanoparticles (AuNPs) are one type of nanoagents used in nanomedicine, since they have optical properties that are useful for marker substances and in photoimaging. Medical applications of AuNPs cover in practice all fields, including diagnostics, therapy and hygiene. AuNPs can be used as intrinsic drug agents or drug delivery vehicles, and they can be applied as stabilizing agents for other drug delivery vehicles such as vesicles. Understanding the interaction between NPs and cell membranes is relevant also because all trafficking between the cell interior and the extracellular space takes place through the cell membrane.

Not only the novelty of the topic, but also the importance of revealing the details of interactions at the cellular level makes studies of monolayer-protected AuNPs interesting. This research project was inspired by an experimental study at which gold nanoparticles had been found to cause cell death. The purpose was to create a theoretical model to study the problem by performing computer simulations, to reveal the mechanism that could not be seen in detail in the experiments. What happens at the cellular level? Why nano kills? The aim was to check the self-

penetration theory and the source of the toxicity of AuNPs through computational simulations.

The present work consists of three articles. *Paper I* concentrates on the properties of gold nanoparticles, $Au_{144}(SR)_{60}$, in aqueous solution at physiological temperature. It also describes the gold nanoparticle model. This was the first step towards the final goal, presented in *Papers II–III,* — revealing details of interactions between gold nanoparticles and realistic cell membranes. In *Paper II* a positively charged gold nanoparticle, $Au_{144}(SRNH_3^+)_{60}$, is being studied in the presence of model membranes. *Paper III* presents negatively charged gold nanoparticle, $Au_{144}(SRCOO^-)_{60}$, with the model membranes.

In addition to the bundle of articles, the thesis contains a brief introductory part to discuss the background, methods and outcome of present work more in detail. The research topic is being put into context in Chapter 2. The background of the field and the methods are described in Chapter 3. The models used in the study are described in Chapter 4. Chapter 5 focuses on the results. The outcome of the study is being discussed in Chapter 6. Chapter 7 summarizes the work.

This study succeeded in shedding light on the interactions of gold nanoparticles at the cellular level. Among all the relevant outcomes of the study, the results suggest potential mechanisms for what is seen in the experiments and provide novel views on gold nanoparticles in biological environment.

2. INTRODUCTION

2.1 Interesting Gold Nanoparticles

The rapid development of nanotechnology during the last decade has led to dramatic expansion of using nanomaterials for the purposes of industry, in medical applications, and in commercially available products. The variety in origins and properties of nanomaterials is overwhelming. There are currently over 1 600 consumer products containing nanomaterials on the market [1], and the world nanotechnology market is expected to exceed 30 billion USD by the year 2015 [2].

Some of the most commonly used nanomaterials are carbon nanoparticles, (*e.g.,* carbon dots, carbon nanotubes, fullerenes, nanodiamonds, nanofibers, nanofoam, nanohorns, nano-onions), metal nanoparticles (*e.g.,* Fe, Ag, Au, Ti), semiconductor nanoparticles (the so-called quantum dots, *e.g.,* CdSe, CdTe, CdS, ZnS, ZnSe, PbSe, GaAs, GaN, InP, InAs), dendrimers, peptides, silica nanoparticles, polymers, proteins, micelles, liposomes and viral nanoparticles. Nanoparticles are manufactured in a wide variety of shapes to alter their functionality, *e.g.,* spheres, rods, wires, ellipsoids, discs, shells and hollow structures (see Figure 2.1). There is such a large body of literature published on experimental, theoretical and computational research of nanomaterials that it is impossible to give a broad overview of the topic, and hence, the references considered here are limited to the studies that are closest to the scope of the work presented here.

Nanoparticles (NPs, size range 1–100 nm) have many interesting properties, and they provide new functionalities of matter at the nanoscale. The variety of products containing NPs include drugs, industrial applications, and consumer products such as paints, plastics, inks, lotions and cosmetics [3–7]. The properties of NPs can be tuned via chemical composition, size, binding strength between the core and ligand shell, charge and stability in a given medium [8].

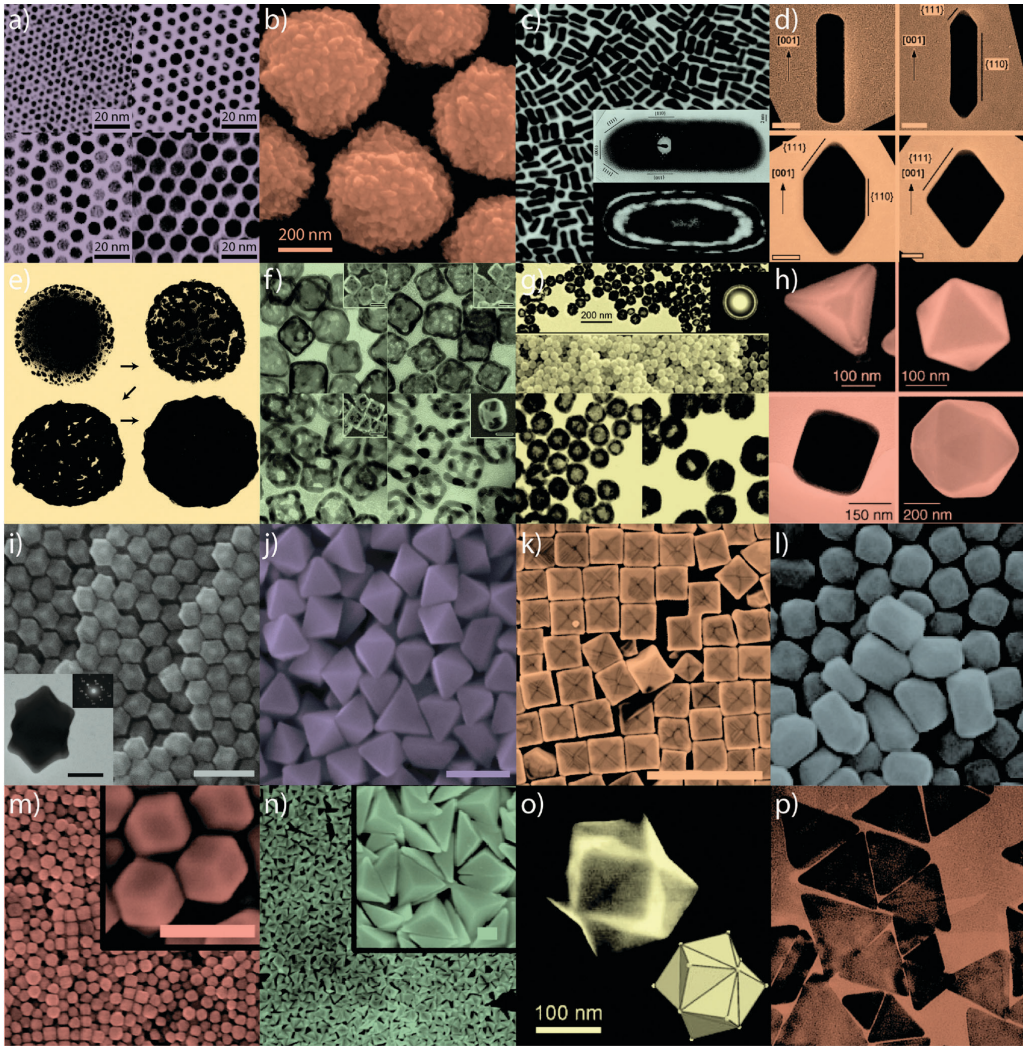

Figure 2.1: Gold nanoparticles of various size and shape. (a) small nanospheres, (b) large nanospheres, (c) nanorods, (d) sharpened nanorods, (e) nanoshells, (f) nanocages/frames, (g) hollow nanospheres, (h) tetrahedra/octahedra/cubes/icosahedra, (i) rhombic dodecahedra, (j) octahedra, (k) concave nanocubes, (l) tetrahexahedra, (m) rhombic dodecahedra, (n) obtuse triangular bipyramids, (o) trisoctahedra, and (p) nanoprisms. Figure taken with permission from Ref. [9]. Copyright © 2011, Royal Society of Chemistry. Link to Full Article
(Copyright © (a) 2003 American Chemical Society, (b) 2008 Wiley-VCH Verlag GmbH & Co., (c) 2004 American Chemical Society and 1999 Elsevier Science B.V., (d) 2007 Wiley-VCH Verlag GmbH & Co., (e) 1998 Elsevier Science B.V., (f) 2007 American Chemical Society, (g) 2005 American Chemical Society, (h) 2004 Wiley-VCH Verlag GmbH & Co., (i-j) 2009 American Chemical Society, (k) 2010 American Chemical Society, (l) 2009 American Chemical Society, (m-n) 2011 American Chemical Society, (o) 2008 VCH Verlag GmbH & Co., and (p) 2005 American Chemical Society.)

NPs bridge the gap between bulk materials and atomic or molecular structures [10, 11]. Typically, the physical properties of bulk materials do not depend on the size of the sample, while at the nanoscale size-dependent properties are frequently encountered. Two contributing factors for the size-dependence are the number of surface atoms and quantum confinement effects. The percentage of the surface volume

ratio reduces as the NP size increases towards the bulk limit. Quantum confinement effects arise at the smallest length scales (< 10 nm) down to few nanometers, where the electronic structure plays a significant role in determining the composition, stability, structure, and function of NPs, such as catalytic reactivity and optical properties [12–15].

Metal NPs often display fascinating optical properties because of quantum effects, and gold nanoparticles (AuNPs) can appear from yellow to deep red and black in solution depending on their size [14]. In photovoltaic cells, absorption of solar radiation is much higher for semiconductor materials comprised of NPs than for continuous sheets of thin films (*e.g.,* CdTe, ZnO) [16]. For phase-change materials used in optical data storage and non-volatile computer memory, chalcogenide (*e.g.,* GeTe) NPs offer an intriguing route of manufacturing composite materials with tuned (size-dependent) melting point and re-crystallization temperature [17]. Other size-dependent properties include surface plasmon resonance in metal NPs [18], quantum confinement effects in semiconductor NPs (quantum dots) [19], and superparamagnetism in magnetic materials [20]. The changes in physical properties are not always desirable, for example, the magnetization direction of small ferromagnetic NPs can switch at low temperature making them unsuitable for applications [21].

Several NPs are used in nanomedicine and biochemistry for drug delivery, diagnostics, therapeutics, and bio-imaging [22–27]. AuNPs are one type of nanoagents that are being employed for such purposes [28–32]. In fact, AuNPs are one of the most studied species of nanoparticles, since they have numerous possible uses both in scientific and commercial applications such as molecular electronics, molecular recognition, catalysis, biolabeling and biosensing [8, 10, 33, 34].

Medical applications of AuNPs cover practically all fields, including diagnostics, therapy, prophylaxis and hygiene [35]. AuNPs can be used as intrinsic drug agents or drug delivery vehicles, and they can be applied as stabilizing agents for other drug delivery vehicles such as vesicles. AuNPs have demonstrated applicability in photo-thermal therapy due to their optical properties, which enable local heating at the cellular level. As composite materials, AuNPs may function as triggers for drug

release. For example, they enable an efficient treatment of diseased sites (tumors) with small side effects in the body as the local AuNP concentration is high only at the targeted site [9]. This approach is based on size-selective accumulation of AuNPs due to the disordered vascular characteristics of tumors, and the targeting effects can be further enhanced by covering nanoparticles by additional recognition units, which are selective for specific tumor sites [9].

The interaction between NPs and cell membranes is very relevant also, because all trafficking between cell interior and the extracellular space takes place through the cell membrane [28, 36–43]. The permeation rates of particles translocating through a membrane are therefore affected by the membrane potential, which in mammalian cells is known to be rather complicated and arise from asymmetric lipid [44–46] and ion distributions [45–49] on the extracellular and cytosolic sides of a cell.

2.2 Experiments: Cytotoxicity

Nanotoxicology is a special field of toxicology, which considers potential harmful effects of NPs in living organisms [50]. These effects differ from those of larger particles as NPs are able to translocate inside the body from the site of deposition (*e.g.,* lungs) to different organs and tissues (such as the blood-brain barrier) more effectively. The important factors for NP toxicity are particle size, composition, shape, surface modification, concentration, agglomeration, and solubility [50]. For example, the large surface-to-volume ratio of NPs is related to increasing chemical reactivities, leading to enhanced formation of reactive oxygen species, which may cause damage to proteins, DNA, and cell membranes via oxidative stress [50]. Recently AuNPs have also been found to enhance the formation of amyloid fibrils that is known as a fundamental step in Alzheimer's and Parkinson's diseases [51, 52].

According to recent experimental findings, AuNPs (among other particle types) have cytotoxic properties [53, 54]. Small cationic AuNPs of diameters less than 2 nm are able to penetrate cell membranes, and they can be extremely toxic [3, 15, 33, 55, 56]. This has been demonstrated, *e.g.,* for 1.4 nm AuNPs, which were observed to cause necrosis and mitochodrial damage to various cell lines [57]. Experimental results indicate that the nanoparticle translocation occurs via self-

penetration, where the charge and specific structure/composition of the ligand shell affects the process: Cationic AuNPs with an alternating pattern of aliphatic (hydrophobic[1]) and functionalized side groups (striped AuNPs) show increased penetration activity in comparison to randomly distributed side groups [53]. Illustration of nanoparticle surface morphologies is presented in Figure 2.2. Cationic nanoparticles have been reported to generate holes both in model and living cell membranes, where the phase of the lipid bilayer plays a role for the level of disruption [54, 55, 58, 59].

Interactions of charged or polar NPs with the cell membrane are expected to be strong and long-ranged. This view is quite relevant, since NPs are often layered for medical applications, and grafting polar surface groups onto AuNPs indeed affects their water solubility and ability to penetrate cell membranes [53]. Extracellular positively charged NPs (such as SiO_2, TiO_2, AuNPs) have also been reported to intrude through cell membranes, and, in some cases, to cause a large-scale cell death in comparison with the negatively charged particles, which remain on the extracellular side [22, 23, 29, 30, 53, 54]. It has been concluded that, among other factors (such as NP size/shape and hydrophobicity of grafted side chains), the toxicity of nanoparticles depends on the sign of charge [54, 60].

Another feature that is also of concern is the fact that some NPs spontaneously form complexes with biological molecules. In a recent study this was shown to take place for fullerenes with gallic acid (GA) [61], the latter being a typical phenolic compound found in tea and berries, among other substances. Through a mechanism that is currently unclear, cells that were exposed to the fullerene-GA mixtures died in 15 minutes [61]. While this example highlights the possible gain of NP complexation in terms of biomedical applications for the treatment of, *e.g.,* cancer tissues, it also pictures possible threats, and yet it is still a single case. Considering that the number of different combinations of NPs and native biological molecules is universally large, the idea of studying all possible situations is not feasible. More realistic is to aim for gaining understanding of the NPs properties in biological envi-

[1]Hydrophilic (comes from Greek words meaning "water loving") molecules or compounds dissolve in water and are often polar or charged. Hydrophobic ("water fearing") molecules or compounds repel water, and are often nonpolar or have neutral charge (*e.g.,* oils, fat and alkanes). Usually, hydrophobic molecules can be considered as lipophilic ("fat loving"), as well, with some exceptions; *i.e.,* silicones are hydrophobic but not lipophilic.

ronments, and to do that in a systematic manner under controlled conditions where the underlying physical and chemical processes associated with nanomaterials in biological environments can be unlocked.

Figure 2.2: Illustration of nanoparticle surface morphologies. Figure adapted with permission from Ref. [62]. Copyright © 2013, American Chemical Society. Link to Full Article

Recent experiments by Tatur *et al.* [63] for model membrane systems provide a valuable reference for simulations, as they considered 2-nm diameter AuNPs floating between single-component bilayers comprised of zwitterionic DSPC lipids (1,2-distearoyl-*sn*-glycero- 3-phosphocholine). Based on neutron reflectometry measurements, they concluded that AuNPs with cationic head groups penetrate inside the hydrophobic interior of the lipid bilayers and disrupt the membranes at increased concentrations, while anionic AuNPs stay outside. The penetration of cationic AuNPs occurs after elevating the temperature up to 53°C, which suggests that the process requires the crossing of a free energy barrier at physiological temperatures. These findings can be compared straightforwardly with simulations, as there are no complications arising from other components that exist in real membranes, such as membrane proteins and the protruding glycocalyx network.

2.3 Computational State-of-Art

Computer simulations are a suitable method to study the properties of commonly used nanomaterials. During recent years, the computational research of nanomaterials and their effects on biological systems has been increasing rapidly. Nowadays computational modeling is a powerful tool in the field of natural sciences, and it can be considered as important as performing traditional experiments. Several different kind of simulation techniques are being used — the choice of the most suitable approach depends on the problem to be solved.

Quantum-mechanical (QM) simulations are a proper approach in the cases where

the electronic structure, chemical properties or reactions are investigated. However, the scope of the QM approach is restricted; time scales reached employing QM simulations are usually measured in picoseconds, and the system sizes are limited to 100–1000 atoms.

Classical atomistic molecular dynamics (MD) simulations are an efficient tool for revealing atomistic details of relatively large system sizes (100 000–1 000 000 atoms). Time scales accessible for atomistic approaches are from hundreds of nanoseconds up to tens of microseconds. The strength of the atomistic classical MD lays in the computational efficiency and the atomistic resolution, but its weakness is that chemical reactions can not usually be simulated. However, there exist a few force-fields for special purposes, which make it possible to model also chemical reaction using classical MD [64].

Coarse-grained (CG) methods are relevant for predicting thermodynamical properties and describing the dynamics over long time scales up to milliseconds. The basic concept of the CG approach is that the degrees of freedom are reduced in the studied system. In practice, this is accomplished by describing a set of atoms or molecules as a single bead. This speeds up the computations, since fewer objects are to be taken into account, but the other side of the coin is that resolution decreases and some of the details will be lost.

Also hybrid methods have been developed. One of the most famous ones is the QM/MM approach, which combines the accuracy of the QM methods and the efficiency of the classical MD. The basic idea is that part of the system is treated classically, and a small part of the system of particular interest (in which, *e.g.,* a specific chemical reaction occurs) is treated quantum-mechanically. The QM/MM method was first introduced by Wahrshel and Levitt in 1976 [65], and the authors (together with Karplus) were awarded the 2013 Nobel prize in Chemistry [66] for development of multiscale modeling techniques.

The simulations presented in this work are classical MD simulations, and hence, the focus of the computational research overview is on this approach.

In general, modeling the complexity of nanoparticles or biological systems is quite challenging. Computational approaches can have atomic-level resolution, but are in

any case simplified models that can capture only limited features of biological systems. However, simulations can provide useful molecular-level insight and complement the experiments, in particular, if experiments can be performed for simplified model systems (as mentioned above in the case of Ref. [63]).

2.3.1 AuNP Simulations in Water

Recently, a few molecular dynamics (MD) simulations have been performed for AuNPs in water. The properties of monolayer-protected (MPC) AuNPs in water have been studied by 1-ns all atom MD simulations [40]. The AuNPs were modeled with methyl, carboxyl, amine and hydroxyl ligand tail groups. The 4-nm bulk gold core comprised 1956 gold atoms. The less well known ENCAD force-field was employed in the study. The conclusions focused on the MPC-induced effects on the surrounding water, and the results were compared with an unprotected bare gold nanocluster.

In Ref. [67], a set of 100-ns all atom simulations of AuNPs in water and 150 mM salt were presented for MPC AuNPs with anionic 11-mercapto-1-undecasulfonate (MUS) and hydrophobic 1-octanethiol (OT) head groups; striped, mixed and random morphologies of the monolayers were studied. The united atom GROMOS force-field was used in the model with SPC (single point charge) water. The 2-nm gold core was modeled as a rigid, hollow spherical shell. The results indicated that the NP size and relative ligand lengths affect the particle properties, but the relative position of the ligands had only minimal effect.

The dynamics of hydrogen bonding of cationic AuNP's with amine head groups has been studied, also combining density functional theory (DFT) and classical MD in a recent study [68]. The AuNP was modeled as a truncated octahedral motif consisting of 140 Au atoms with 62 hydrocarbon tails. The water model was TIP3P (transferable intermolecular potential with 3 points) and OPLS (optimized potentials for liquid simulations) force-field was employed for the ligands. The length of the MD simulations was 4 ns. The binding energies calculated using DFT gave a new insight to the dynamics of AuNP-solvent interactions.

2.3.2 NP-Permeation

Computational studies of AuNPs have become more and more relevant because of the increase of their use in nanotechnology. The interface between AuNP and polymers has been simulated in order to achieve all-atom models for AuNP-polymer nanocomposites (polymeric memory devices) [69]. Simulating AuNP interactions with biological systems can provide important information for evaluating cytotoxicity, and it can be useful for developing biomedical applications. AuNP penetration in lipid bilayers has been simulated with coarse-grained MD by enforcing AuNP intrusion via external potentials [39, 42, 70], and considerable disruptions of cell membranes have been reported, including a large hole of about 5.5 nm diameter with a positively charged AuNP [39, 42]. It has been shown that striped anionic AuNPs (with amphiphilic surface) can pass non-disruptively through model membranes, and this activity depends closely on the AuNP diameter [62]. Most recently, a CG simulation study was published, focusing on several properties of AuNP monolayers influencing the membrane insertion, such as the size, ligand structure and morphology of the MPC [71]. The results of this report highlighted the importance of hydrophobicity strength on the change in free-energy in AuNP insertion into membranes.

The number of simulations studies of AuNP-membrane interactions is still rather limited, and simulation studies of other nanomaterials with membranes, such as carbon NPs [72], dendrimers [48, 73, 74] or cell-penetrating peptides [75], provide useful insights for understanding the NP-membrane interactions, as well. NPs with similar properties may, *e.g.,* share the same translocation mechanism.

The interactions between NPs and cell membranes are dependent on size, surface structure and ligand chemistry of the nanoparticle. It has been shown that increasing particle size inhibits the NP insertion [71]. However, NPs of similar size do not necessarily interact in a similar manner with membranes [70, 71, 76]; the shape of the NP can have a significant meaning, as well, as demonstrated in the case of cationic dendrimers; larger spheroidal dendrimers have been found to cause membrane disruption, but in contrast, this size-dependence was not observed for linear ones [48]. The permeation of nonpolar carbon NPs (including fullerene in different conforma-

tions) through a lipid membrane has also been reported to be morphology dependent [76]. It has been shown that for anisotropic particles, the particle penetration into membrane may be somewhat independent of particle volume, while translocation of isotropic spherical particles is more difficult with increasing size [77]. On the other hand, flexibility vs. rigidity of the NP may play a role in NP-membrane interaction; it has been suggested that for charged flexible NPs, such as dendrimers, the hole-formation ability is better than for rigid NPs [73]. The MPC ligand length has been demonstrated to have an effect on the NP-membrane interaction, as well; the force required for membrane penetration has been found to increase with increasing alkyl chain lengths for nanoparticles with hydrophobic ligands [78]. However, increasing ligand lengths of AuNPs with mixed hydrophobic/hydrophilic monolayer structure have been shown to encourage the insertion, and this relation was found to be independent of the difference of lengths between two different type of ligands on the MPC [71]. The flexibility of the ligands may be one factor in the process of cell internalization, since flexibility allows the ligands to bend the charged head group out of the hydrophobic membrane core area [62, 71].

In Ref. [79], it was concluded that the free-energy barrier for NP-insertion inside the membrane can be lowered by making the striped NP (mixture of hydrophobic and charged ligand head groups) surface structure more hydrophobic. Increasing the number of hydrophobic ligands on gold MPCs resulted in an increase of membrane penetration also in Ref. [71]. The manner in which the ligands are distributed on the NP surface (often called as morphology) might be meaningful, as well (see Figure 2.2). The results presented in Ref. [80] indicate that the so-called striated NPs with alternating hydrophilic and hydrophobic ligands encounter the lowest energy barrier during the translocation process in comparison to randomly mixed or homogeneous surface morphologies. In contrast, according to a recent computational study, modifying morphology does not make a significant difference when it comes to membrane insertion; a visible difference was observed only for a Janus type particle with macroscopic phase separation [71]. It has been shown that semihydrophilic NPs tend to adsorpt to the surface of the membrane, whereas hydrophobic NPs favor inclusion into the core area of the membrane [81] Increasing the hydrophobicity de-

creases the barrier for translocation, since it is favorable for the NP to interact with the hydrophobic lipid tail region of the membrane [77, 82]. These results suggest that the translocation takes place through an energy-dependent mechanism.

Membrane tension has been shown to play a role in the process of translocation [41, 82]. The results of an NP-membrane simulation study in Ref. [83] indicate that the membrane curvature facilitates the translocation of NPs into cells. The penetration efficiency of NPs was found to be higher for asymmetric curved membranes than for planar ones. NP-induced membrane curvature effects have been suggested to be important to the translocation process, suggesting a hole-formation mechanism for insertion of NPs [84]. The free-energy barrier for internalization of charged NP to membranes has been suggested to arise partly from the bending energy of the membrane and partly from the electrostatic repulsive forces between similar charges of the NP ligands and membrane lipid head groups [85].

NP-membrane interaction has been studied also by exposing the membrane to mechanical stress, and the results demonstrated that NPs can adjust the structural and dynamical properties of the membrane, and are able to regulate the hole or pore formation in membranes [42, 86]. The cellular uptake of ligand-coated NPs is shown to be size-dependent, and it has been suggested that the optimal size for endocytosis is in the range of 25–30 nm, while particles smaller than 20 nm or larger than 60 nm, would undergo other energetically more favorable endocytic-like pathways during translocation because of the energy barrier arising from the membrane bending/wrapping required for endocytosis [41]. The charge-dependent behavior of NPs observed in the experiments has been seen also in the simulations. Cationic dendrimers have been shown to induce pore-formation and membrane disruption [48, 74], and the effect was increased with increasing NP charge [48]. The work presented in Ref. [75] suggests that the translocation of a cationic peptide is likely to occur through water-pore formation. Cationic NPs have been shown to induce disorder lipid bilayers [42, 85], whereas the presence of similar anionic NPs has caused highly ordered regions in membranes [85]. However, according to some studies, the membranes are able to recover from NP penetration [70, 78].

2.4 Present Work

The primary objective of the present work was to study the atomistic details of interaction between AuNPs and mammalian-like cell membranes — to find out how AuNPs can permeate spontaneously through plasma membranes, in what way they alter the cell function and the possible source of cytotoxicity. For this purpose, a series of MD simulations were performed for monolayer-protected AuNPs with functionalized (charged) alkanethiol side groups ($Au_{144}(SR)_{60}$ where R=$C_{11}H_{22}$ + amine/carboxylate terminal group) first in aqueous solution and then in the presence of model cell membranes to study their structural and dynamical properties, and the interaction with solvent (water, counter-ions) and plasma membranes.

The composition of the AuNPs modeled in the study corresponds to one of the most ubiquitous synthesized AuNP sizes (29 kDa, core diameter ~ 2 nm) matching also the mass-spectrometrical analysis for $Au_{144}(SR)_{60}$ [87–90]. The AuNP structure matches the common structural details reported for several cluster sizes in this size regime ($d \leq 2$ nm) [12, 91–94]. The structural model of $Au_{144}(SR)_{60}$ is based on the recent theoretical model by Lopez-Acevedo *et al.* [95], which was shown to be in very good agreement with the experimental x-ray powder diffraction measurements [96], and the AuNP electronic structure is consistent with the chemical voltammetry measurements and optical properties [87, 97, 98]. Recently, it was also demonstrated theoretically that this cluster size, unlike several smaller ones, is not catalytically active for CO oxidation, and that the borderline for binding and activating O_2 is located below 100 Au atoms [13].

The article of AuNPs in aqueous environment, *Paper I,* was the first study of an extensive period of time (200 ns) with sufficient sampling, presenting two different AuNPs on equal footing and theoretically correct structure. The simulations of AuNPs in the presence of model plasma membrane, *Papers II–III*, were the first attempt to approach the complex problem at atomistic scale. Therefore, this work provides novel insight to the topic and a great deal of added value to previous theoretical work on AuNPs interacting with lipid bilayers, as previous studies [39, 70, 71, 80, 81, 85] have been based on coarse-grained (CG) models, that lack the atomistic details for AuNP as well as the hydrodynamic details, or have explored

only the role of solvent [67, 68].

In the analysis, several aspects of electrostatics for systems comprised of charged AuNPs and ions in aqueous environment and in the presence of model cell membranes are taken into consideration. Particular attention is paid to the role of counter-ions, water, and specific lipid molecules to gain a full understanding of electrostatics that is expected to be important in the binding and permeation events. The ordering and dynamics of ions and water around AuNPs and the range of water-mediated interactions between AuNPs and other objects are considered. Ion distributions based on the Debye-Hückel description and the use of this treatment for nanoparticle coagulation in terms of the zeta potential is being discussed. The results emphasize the importance of electrostatics and the interface between AuNP and solvent as the decisive factors in determining the properties of nanoparticle complexes in aqueous environments. Finally, atomistic details of the complexation between AuNPs and plasma membrane-like lipid membranes will be discussed, suggesting mechanisms how the complexation can possibly alter the cell function.

3. METHODS

3.1 Classical Molecular Dynamics Simulations

In this study, gold nanoparticles were studied by atomistic classical molecular dynamics simulations. Molecular modeling means creating theoretical models of molecules and atomistic systems. Computer simulations are being used to calculate structure and dynamics of modeled molecules or sets of atoms by using theoretical models of atoms and molecular interactions. Classical molecular dynamics (MD) is about solving Newtonian equations of motion for atoms or molecules [99].

3.1.1 Equations of Motion

In a classical MD simulation, time evolution of a particle's coordinates and velocities (also known as the trajectory of the particle) are computed using Newton's equations of motion. The classical Newtonian equation of motion is

$$\mathbf{F}_i = m_i \frac{\partial^2 \mathbf{r}_i}{\partial t^2} \tag{3.1}$$

where $\mathbf{F}_i$ is the force acting on particle i of mass m and $\mathbf{r}_i$ is the position vector of the particle [100, 101]. The force acting on a particle can also be calculated from the potential energy

$$\mathbf{F}_i = -\frac{\partial V}{\partial \mathbf{r}_i}, \tag{3.2}$$

where V is the potential energy, also known as the force-field [99, 101]. The force-field is a function of all spatial degrees of freedom of the system.

The differential equations are solved using a finite difference approach. In the beginning of a simulation there is an initial structure, starting coordinates and velocities for the atoms of the system. After calculating the force acting on the

atoms, the new dynamic properties for the atoms can be calculated after a discrete interval of time, a time step, Δt. When this calculation is repeated for the total time consisting of time steps, it gives the trajectory of the system. These evolution procedures are commonly called as integrators. One of the most famous one is the Verlet algorithm [102], in which the positions and atoms of velocities are calculated at half-steps for a time interval Δt between time steps:

$$\mathbf{v}_i(t + \frac{1}{2}\Delta t) = \mathbf{v}_i(t - \frac{1}{2}\Delta t) + \frac{\mathbf{F}_i(t)}{m_i}\Delta t, \tag{3.3}$$

$$\mathbf{r}_i(t + \Delta t) = \mathbf{r}_i(t) + \mathbf{v}_i(t + \frac{1}{2}\Delta t)\Delta t. \tag{3.4}$$

Verlet is an efficient algorithm, and its benefits are stability, time-reversibility and energy conservation. The Verlet algorithm was used in the simulations of this work.

The time step, Δt, should be chosen in such manner that the simulation system is stable and energy is conserved, that is to say that the provided Δt should be short enough. Usually, in classical MD simulations time steps of order 1–2 fs are being used (especially when using constraints), but in some cases time steps can be even 4–5 fs (when using virtual site algorithms) [101]. The length of the time step is dominated by the fastest degrees of motion in the system, and usually theses are bond vibrations. Most often constraints are used in simulations to reduce the degrees of freedom, removing high-frequency vibrations by restricting the movement of covalent bonds. This is implemented by fixing the covalent bonds to constant angles and lengths. In addition to constraints, also restraints can be used to fix atomic positions, bond lengths, bond angles and dihedrals. In this work, time steps of 1 and 2 fs were used. In all simulations, restraints were used to maintain the correct AuNP core geometry, and in AuNP-membrane simulations the constraint algorithm SHAKE [103] was being used.

3.1.2 Force-Field

The potential energy function, also known as the force-field, defines interactions within and between molecules. The total potential energy can be presented as a sum of bonded and non-bonded interactions

$$V_{total} = V_{bonded} + V_{non-bonded}. \tag{3.5}$$

Bonded interactions include bond-stretching V_b, bond angle-bending, V_a, and dihedral angle, V_d, potentials as

$$V_b(\mathbf{r}_i, \mathbf{r}_j) = \frac{1}{2} k_b (r_{ij} - b)^2, \tag{3.6}$$

$$V_a(\mathbf{r}_i, \mathbf{r}_j, \mathbf{r}_k) = \frac{1}{2} k_\theta (\theta - \theta_0)^2, \tag{3.7}$$

$$V_d(\phi) = k_\phi (1 + \cos(n\phi - \phi_0)), \tag{3.8}$$

where r_{ij} is the distance between atoms i and j, θ is the bond angle between atoms i, j and k, k_b is a force constant, k_θ is the angle force constant, k_ϕ is the dihedral force constant and b and θ_0 are reference values in equilibrium [101].

Non-bonded interactions include Pauli repulsion, van der Waals and electrostatic interactions. The electrostatic interactions arising from atomic charges are described by the Coulombic potential

$$V_C(r_{ij}) = \frac{q_i q_j}{4\pi\epsilon_0 r_{ij}}, \tag{3.9}$$

where q_i and q_j are the charges of atoms i and j, ϵ_0 is permittivity of vacuum, and r_{ij} is the distance between atoms i and j. Pauli repulsion and van der Waals potential are included in the Lennard-Jones potential

$$V_{LJ}(r_{ij}) = \frac{C_{ij}^{12}}{r_{ij}^{12}} - \frac{C_{ij}^{6}}{r_{ij}^{6}}, \tag{3.10}$$

where C_{ij}^{12} and C_{ij}^{6} are atom-pair specific parameters [101].

Usually a cut-off distance is used in the calculation of Lennard-Jones interactions, since they are relatively short-ranged. However, electrostatic interactions decay slower than Van der Waals interactions, and short-range electrostatics have to be calculated exactly to avoid artefacts. Methods evaluating long-range electrostatic interactions usually involve cut-offs for short- and long-range interactions for speeding up the computation. Particle Mesh Ewald (PME) [104] is one of the most

commonly used and efficient approaches to calculate the long-range electrostatic interactions in a simulation system. It is a lattice-sum based method using reciprocal space to evaluate electrostatics. The long-range part uses reciprocal space mesh to evaluate electrostatics whereas the short range electrostatics are calculated exactly as individual particles; hence, the name particle-mesh.

There are several commonly used forms of force-fields in the field of molecular modeling, such as GROMOS [105], Charmm [106], Amber [107], and OPLS (optimized potentials for liquid Simulations) [108, 109]. For this work, the united atom force-field [110] was used. The united atom force-field definition includes only polar hydrogen atoms (excluding the explicit representation of non polar hydrogens) [101]. The force-field chosen was a mixture of GROMOS [105] (bonded-interaction) and OPLS [109] (non-bonded interaction), since they are known to be suitable for modeling of lipids used in this study (POPC and POPS, see Figure 4.3). Modeling metallic NPs in a biologically relevant environment has been problematic, since metals are not normally included in biomolecular force-fields. Recently, Lennard-Jones parameters for several metals were developed [111], and the parameters are compatible with some widely used empirical force-fields. Therefore, the corresponding OPLS-compatible Lennard-Jones parameters for Au atoms were taken from Ref. [111]. The SPC (single point charge) model [112] was used for water.

3.1.3 Ensembles

Molecular dynamics simulations can be performed in various kinds of ensembles by fixing part of the thermodynamic variables in order to maintain the desired properties constant. The number of particles, N, is constant in all ensembles considered here. The basic ensemble, *NVE,* where volume, V, and the total energy, E, are preserved is given directly by Newtonian equations of motion, since they conserve energy. Other commonly used ensembles are *NPT,* in which pressure, P, and temperature, T, are kept invariant and *NVT,* with constant volume and temperature. Several algorithms have been developed to extend Newtonian equations of motion to NPT and NVT ensembles, *i.e.,* barostats and thermostats [113], for example Berendsen [114], Nose-Hoover [115] and Parrinello-Rahman [116].

The kinetic energy, K, and temperature, T, of a simulation system can be connected by using the equipartition theorem:

$$K = \frac{1}{2}\sum_{i=1}^{N} m_i v_i^2(t) = \frac{1}{2} N_f k_B T, \tag{3.11}$$

where k_B is the Boltzmann constant and N_f is the number of degrees of freedom of the system [117]. Moreover, the temperature can be defined as a function of velocities

$$T = \sum_{i=1}^{N} \frac{m_i v_i^2(t)}{N_f k_B}. \tag{3.12}$$

Consequently, in a simulation, the temperature fluctuates when velocities vary. The situation where the temperature is set constant corresponds to conditions where the kinetic energy is invariant. However, this means the average kinetic energy of the system — the energies of the individual particles of the system may vary.

In the simulations of this work, the NPT and NVT ensembles were used for the production simulations. For AuNPs in aqueous solution, the Berendsen thermostat [114] was applied for the NVT ensemble. For the NPT ensemble the Berendsen algorithm [114] was used for temperature and pressure coupling for both the simulations of AuNPs in aqueous solution and in the presence of model cell membranes.

The Berendsen temperature coupling algorithm connects the system weakly to an external heat bath by scaling the velocities of the particles at every time step by a time-dependent coefficient. The thermostat maintains the system temperature T somewhat at a desired temperature T_0 [101]

$$\frac{\mathrm{d}T}{\mathrm{d}t} = \frac{T_0 - T}{\tau}, \tag{3.13}$$

where time constant τ determines the coupling strength. It is important to choose the value of the coupling strength in an appropriate range. Too small values cause unrealistic low temperature fluctuations, while too large value may end up in a systematic temperature drift [114, 118]. The barostat functions in similar manner as the thermostat, maintaining the system at a certain pressure, P_0, by letting the sim-

ulation box volume and dimensions rescale during the simulation. It can be applied uniformly to in all simulation box dimensions (called as isotropic pressure coupling), independently in the x-y and z directions (semi-isotropic pressure coupling), or independently in all directions (anisotropic pressure coupling) [101].

Thermostats and barostats are efficient in stabilising the thermodynamic conditions of the systems, but they have limitations and do not implement thermodynamic ensembles perfectly. For example, the way the Berendsen method affects the fluctuations of the kinetic energy can be considered physically unrealistic. But while some methods can be considered more sophisticated than the others, the difference in results of biomolecular simulations gained using different algorithms are in many cases negligibly small [118, 119].

3.2 Analysis Methods

3.2.1 Radial Distribution Function

The radial distribution function (RDF) describes the structure of the system. That is to say, how its constituents are distributed in space with respect to each other. RDF, $g_{AB}(r)$, (also known as pair correlation function), is often averaged over time for particles of type A and B, and it is defined as [120]

$$\begin{aligned} g_{AB}(r) &= \frac{\langle \rho_B(r) \rangle}{\langle \rho_B \rangle_{local}} \\ &= \frac{1}{\langle \rho_B \rangle_{local}} \frac{1}{N_A} \sum_{i \in A}^{N_A} \sum_{j \in B}^{N_B} \frac{\delta(r_{ij} - r)}{4\pi r^2}, \end{aligned} \tag{3.14}$$

where $\langle p_B(r) \rangle$ is the particle density of particles of type B at a radial distance r from particles of type A. $\langle p_B \rangle_{local}$ is the particle density averaged over all spheres. The pair correlation function describes how much more likely it is to find the atom pair AB from distance r in comparison to ideal gas.

3.2.2 Radius of Gyration

Radius of gyration, R_g, is a measure of the compactness of a structure. It can be defined as [120]

$$R_g = \left(\frac{\sum_i \|\mathbf{r}_i\|^2 m_i}{\sum_i m_i} \right)^{\frac{1}{2}}, \tag{3.15}$$

where m_i is the mass of atom i and $\mathbf{r}_i$ is its position with respect to the center of mass of the molecule. $\|\mathbf{r}_i\|$ is the norm of the vector.

3.2.3 Moment of Inertia Vector Auto-correlation Function

Correlation is dependence of variables or data sets. The cross-correlation function, $C_{fg}(t)$, of properties $f(t)$ and $g(t)$ is

$$C_{fg}(t) = \langle f(\xi) g(\xi + t) \rangle_\xi. \tag{3.16}$$

If f and g are normalized to zero expectation value and unity variance, the cross correlation function is between -1 and 1; 1 is perfect linear correlation, 0 is no correlation, and -1 is anticorrelation.

Performing autocorrelation analyses for the properties of simulation objects is one way of monitoring the quality of the data. Short correlation time (fast decay of the autocorrelation function) compared to the simulation time indicates sufficient phase space sampling. In addition, autocorrelation functions can also be used to gain information about the physics in the system (*e.g.,* slow processes have more slowly decaying autocorrelation functions). Autocorrelation function (ACF), $C_f(t)$, of a property $f(t)$ is [113, 120]

$$C_f(t) = \langle f(\xi) f(\xi + t) \rangle_\xi, \tag{3.17}$$

The correlation time, τ, of property f is defined as

$$\tau_f = \int_0^\infty C_f(t) dt, \tag{3.18}$$

and can be written in a discretized form for computations, as a sum

$$\tau_f = \sum_t C_f(t)\Delta t. \tag{3.19}$$

The moment of inertia (MOI) vector autocorrelation function (ACF), $C(t)$, was computed for the AuNP's x, y and z axes as a function of time and for explicitly mass weighted atoms.

3.2.4 Rotational Correlation Function

Rotational correlation function (RCF) of the AuNPs was calculated using three Au atoms (i, j, k) as a reference for defining two vectors, $\mathbf{r}_{ij}$ and $\mathbf{r}_{jk}$, at the inner gold core. The vector cross product $\mathbf{r}_\perp = \mathbf{r}_{ij} \times \mathbf{r}_{jk}$ was used for computing the RCF with respect to the vector $\mathbf{r}_\perp$ at time zero. Thus, $\mathbf{r}_\perp$ effectively gives the direction of the particle's north pole as an analogy. Rotational correlation function of property a $\mathbf{r}_\perp(t)$ can be calculated as [101]

$$C^{(n)}_{\mathbf{r}_\perp}(t) = \int_0^\infty P_n \left[\cos \angle(\mathbf{r}_\perp(\xi), \mathbf{r}_\perp(\xi + t))\right] d\xi, \tag{3.20}$$

where $\angle(\mathbf{r}_\perp(\xi), \mathbf{r}_\perp(\xi + t))$ is the angle between $\mathbf{r}_\perp(\xi)$ and $\mathbf{r}_\perp(\xi + t)$, and P_n is the n^{th} order Legendre polynomial. RCF of the AuNPs was calculated using a first order Legendre polynomial, which is just $P_1(x) = x$. In this case, Equation (3.20) simplifies to

$$C^{(1)}_{\mathbf{r}_\perp}(t) = \int_0^\infty \hat{\mathbf{r}}_\perp(\xi) \cdot \hat{\mathbf{r}}_\perp(\xi + t)\ d\xi. \tag{3.21}$$

3.2.5 Diffusion and Mobility

Self-diffusion coefficients D_A of particles A can be calculated by using the Einstein relation [121]. The mean-squared displacement of particles of type A is defined as

$$\mathrm{MSD}_A(t) = \langle |\mathbf{r}_i(t) - \mathbf{r}_i(0)|^2 \rangle_{i \in A}, \tag{3.22}$$

and then the diffusion coefficient is given by

$$D_A = \lim_{t\to\infty} \frac{\mathrm{MSD}_A(t)}{6t}, \tag{3.23}$$

where in practice, the diffusion coefficient is calculated as linear fitting of the mean-square displacement between a time interval of 10-90 % in the simulation time.

The short-time diffusion factor (mobility), M, was used to characterize the diffusive motion of water and ions in the simulation systems. Mobility was determined as an effective slope of the mean-square displacement over a short period of time for water and counter-ions. Mobility, M, is computed largely in a similar manner as the hydrodynamic diffusion coefficient in Equation (3.23), but without the long-time limit. Since M is not defined in the hydrodynamic long-time limit, it is called a diffusion factor instead of a true diffusion coefficient.

3.2.6 Debye Length and Zeta Potential

When a charged object is exposed to a fluid with charge carriers, a layered structure forms on its surface. The complex is often called the (electric) double layer. The first layer (known as the Stern layer) consists of charges of opposite signs than that of the object and are tightly bound at the surface of the object. The charge carriers at the second layer are more loosely bound and, hence, able to move more freely. In the case of this study, the AuNP is being considered as a charged sphere with a electric double layer at its surface — the counter-ions gather at the AuNP head group surroundings forming the layered structure (see Figure 3.1).

The electric potential at the plane between bound and loosely associated ions is called the zeta potential (also known as the electrokinetic potential). The idea of zeta potential was originally introduced by Smoluchowski [123]. The zeta potential can be used as a measure for electrostatic repulsion of charged particles in a solution and their tendency to aggregate. The higher the zeta potential, the stronger the repulsion. The range of zeta potential is from 0 to ± 100 mV, where the region for coagulation or dispersion is at 14–30 mV [124], and 30 mV [124–126] is usually considered as the limit value, under which the particles tend to coagulate (commercial sources, such as enterprises manufacturing nanoparticles and measurement equipment, commonly use 25 mV as the threshold value, *e.g.,* [127–129]). If the double

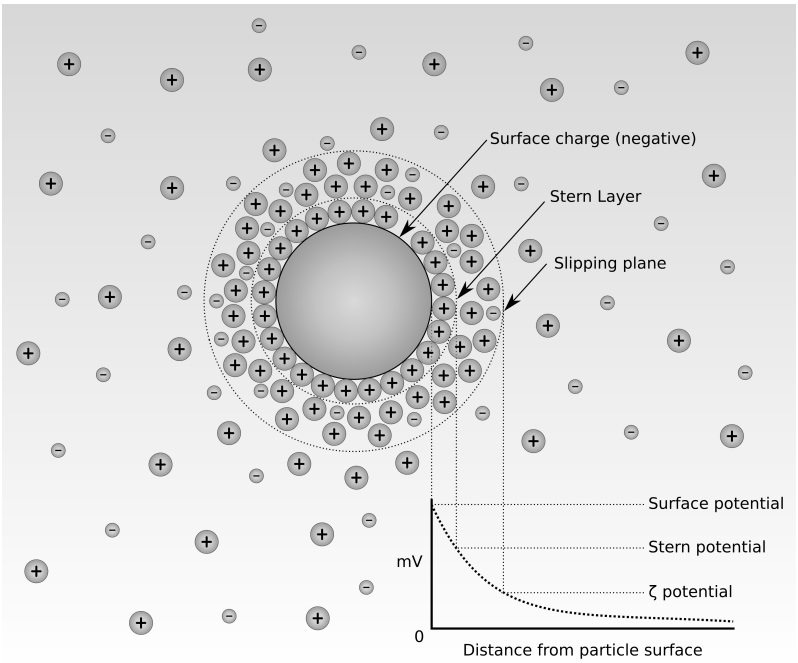

Figure 3.1: Schematic figure of electric double layer. Figure adopted from Ref. [122].

layer is much thinner than the size of the particle, the Smoluchowski theory can be used for defining the zeta potential [123, 130, 131].

The Gouy-Chapman model [131–134] describes the electric double layer model taking into account the thermal diffusive motion causing disordering of the electric double layer. This theory relates the mean electrostatic potential to the ion density profile by combining the formally exact Poisson equation to specify the electrostatic potential of an ion with the Boltzmann equation for charge distribution [131, 135]. The Debye-Hückel theory [135] applies the linearized Poisson-Boltzmann equation for describing the double layer model. This approximation takes into account the activity of ions in a solution, and it holds for low salt concentrations. The Debye-Hückel theory was employed to study the counter-ions around the AuNPs.

The electrostatic field, ϕ, set up by ions in a solution obeys the Poisson equation [134]

$$\nabla^2\phi = -\frac{\rho_e}{\epsilon_w} = -\frac{e(n_+ - n_-)}{\epsilon_w}, \tag{3.24}$$

where $n_\pm$ and $\pm e$ are the number density and the charge of ions, respectively, and ϵ_w is the permittivity of the solution. The statistical distribution of ions in equilibrium

follows the Boltzmann distribution [134]

$$n_{\pm} = n_0 \mathrm{e}^{\mp \frac{e\Psi}{k_B T}}, \tag{3.25}$$

where n_0 is the bulk concentration of ions, k_B is the Boltzmann constant, T is temperature, and Ψ is the potential arising from the response of the mobile ions to the local electric field. Applying the mean-field assumption, the electrostatic potential set by the ions, ϕ, can be considered to be the same as potential of the field the ions respond to, Ψ. Combining Equations (3.24) and (3.25) gives the nonlinear Poisson-Boltzmann equation

$$\nabla^2 \left(\frac{e\phi}{k_B T} \right) = k^2 \sinh \left(\frac{e\phi}{k_B T} \right). \tag{3.26}$$

Equation (3.26) can be linearized for small potentials using the first order Taylor series approximation $\mathrm{e}^x = 1 + x$ for $0 < x \ll 1$ ($\phi \ll k_B T/e \sim 26$ mV) as

$$\nabla^2 \phi = \kappa^2 \phi, \tag{3.27}$$

where $\kappa = (8\pi e^2 \rho_e)/(\epsilon_w k_B T)$, since

$$\sinh(x) = \frac{\mathrm{e}^x - \mathrm{e}^{-x}}{2} \approx \frac{(1+x) - (1+x)}{2} = x. \tag{3.28}$$

Equation (3.27) is known as the Helmholtz equation. Expecting radial symmetry, it can expressed in spherical coordinates as

$$\frac{1}{r^2} \frac{\partial}{\partial r} \left(r^2 \frac{\partial \phi(r)}{\partial r} \right) = \kappa^2 \phi(r). \tag{3.29}$$

Equation (3.29) can be solved through separation of variables, and the general solution is

$$\phi(r) = \sum_{l=0}^{\infty} a_l j_l(\kappa r) \tag{3.30}$$

where j_l is the spherical Bessel function and a_l is a coefficient. The electric potential goes to zero when distance goes to infinity, and using the boundary condition $\phi \to 0$

when $r \to \infty$ gives

$$\phi(r) = A\frac{e^{-\kappa r}}{r}, \tag{3.31}$$

where A is a constant.

The electric potential decays exponentially when moving away from the charged surface. The Debye screening length, $\lambda_D = \kappa^{-1}$, describes the charge carrier's net electrostatic effect and its range in solution, giving an estimate for the thickness of the double layer. The Debye length is defined as [131, 134, 136]

$$\lambda_D = \left(\frac{\epsilon_w k_B T}{2n_0 e^2}\right)^{\frac{1}{2}} = (8\pi l_B c)^{-\frac{1}{2}}, \tag{3.32}$$

where c is concentration of salt and $l_B = e^2/(4\pi\epsilon k_B T)$ is the Bjerrum length [131, 134, 136]. The Bjerrum length describes how closely two similarly charged ions can be brought together — in other words, the distance that has to be maintained to prevent aggregation of oppositely charged ions. For example, the Bjerrum length for water at room temperature is 0.71 nm, and for 0.1 M table salt solution (NaCl), the screening length is approximately 1 nm [136].

3.2.7 Electrostatic Potential

Since work done by a unit charge when moving in an electric field is given by $e\mathbf{E} \cdot d\mathbf{r} = dW$, the radial electrostatic potential (ESP), ϕ, can be defined as

$$\phi(r) = e\int_0^r E_r(r')dr', \tag{3.33}$$

where $E_r(r')$ stands for radial component of electric field, which can be written as follows using the Gauss theorem:

$$E_r(r) = \frac{Q_r}{4\pi\varepsilon_0 r^2}, \tag{3.34}$$

where Q_r is the total charge enclosed by a sphere of radius r. [104]

Another method for determining ESP in a periodic simulation cell, consists of the direct solution of the Poisson equation by using discrete Fourier transforms. Any periodic charge density

$$n(\mathbf{r}) = n(\mathbf{r} + \mathbf{R}), \tag{3.35}$$

where $\mathbf{R} = L_x a + L_y b + L_z c$ is any point in the lattice composed from periodic images of the simulation cell, can be represented as

$$n(\mathbf{r}) = \sum_{\mathbf{G}} n(\mathbf{G}) e^{i\mathbf{G}\cdot\mathbf{r}}. \tag{3.36}$$

Here, $n(\mathbf{G})$ are given by Fourier transform

$$n(\mathbf{G}) = \frac{1}{V} \int_{\text{cell}} d\mathbf{r} n(\mathbf{r}) e^{-i\mathbf{r}\cdot\mathbf{G}}, \tag{3.37}$$

where V is the volume of simulation cell. The periodicity described in Eq. (3.35) sets restrictions for the values of $\mathbf{G}$ according to

$$e^{i\mathbf{G}\cdot\mathbf{R}} = 1, \tag{3.38}$$

which is also the definition of reciprocal lattices, in case of orthorhombic simulation cell given by

$$\mathbf{G} = \left(\frac{2\pi}{L_x} i, \frac{2\pi}{L_y} j, \frac{2\pi}{L_z} k \right) \tag{3.39}$$

where i, j and k are integers. After substituting the reciprocal expansions of potential and density to the Poisson equation,

$$\nabla^2 \sum_{\mathbf{G}} V(\mathbf{G}) e^{i\mathbf{G}\cdot\mathbf{r}} = \sum_{\mathbf{G}} V(\mathbf{G}) \nabla \cdot \nabla e^{i\mathbf{G}\cdot\mathbf{r}} = -\frac{1}{\varepsilon} \sum_{\mathbf{G}} n(\mathbf{G}) e^{i\mathbf{G}\cdot\mathbf{r}} \tag{3.40}$$

$$\sum_{\mathbf{G}} (i\mathbf{G}) \cdot (i\mathbf{G}) V(\mathbf{G}) e^{i\mathbf{G}\cdot\mathbf{r}} = -\frac{1}{\varepsilon} \sum_{\mathbf{G}} n(\mathbf{G}) e^{i\mathbf{G}\cdot\mathbf{r}} \tag{3.41}$$

$$\Rightarrow V(\mathbf{G}) = \frac{1}{\varepsilon \mathbf{G}^2} n(\mathbf{G}), \tag{3.42}$$

this equation diagonalizes the Poisson equation in the reciprocal space thus making it straightforward to calculate. Furthermore, periodic boundary conditions are naturally taken into account. Atomic charges are placed by linear interpolation in a 3D grid, which is then Fourier transformed, divided by $\mathbf{G}^2$ and inverse Fourier trans-

formed. Note that all simulations need to be and are charge neutral, as otherwise the periodic potential diverges as $|\mathbf{G}| \to 0$, since $n(\mathbf{G} = \mathbf{0})$ is given by $\frac{1}{V}\int_{\text{cell}} d\mathbf{r} n(\mathbf{r})$ (*e.g.,* the average charge density of the system).

3.2.8 AuNP-Solvent Contacts

To determine the lifetimes of hydrogen bonds, an approach suggested by van der Spoel *et al.* [137] was used. In essence, the lifetime of a hydrogen bond τ_{HB} was given by the inverse forward rate constant k through

$$\tau_{\text{HB}} = \frac{1}{k}. \tag{3.43}$$

The parameter k was determined as follows. The hydrogen bonds during the simulations are allowed to break and reform, allowing analysis of lifetimes by using a binary function $h(t)$, which is unity when a hydrogen bond is present and zero otherwise. Then, the forward rate constant k for hydrogen bond breakage and the backward rate constant $k^{'}$ for hydrogen bond formation can be determined from the reactive flux correlation

$$K(t) = k\, c(t) - k^{'}\, n(t), \tag{3.44}$$

where $c(t)$ is the autocorrelation function of $h(t)$, and $n(t)$ is the probability that a hydrogen bond that existed at $t = 0$ is broken, but the groups forming the hydrogen bond are still within the hydrogen bonding distance. For more details of the lifetime determination, see Ref. [137].

3.2.9 Order Parameter

The order parameter of the lipid carbon tails of the membranes was calculated using:

$$\text{S}_{CD} = \frac{3}{2}\langle \cos^2 \theta \rangle - \frac{1}{2}, \tag{3.45}$$

where θ is the angle between the bilayer surface normal and a vector defined by two carbon tail atoms C_{n-1} and C_{n+1} [120, 138].

4. DESCRIPTIONS OF MODEL SYSTEMS

4.1 AuNP Model

In this work, monolayer-protected gold nanoparticles (AuNPs) of 144 Au atoms were modeled with functionalized alkanethiol side groups (undecanyl chain, R=$(CH_2)_{11}$, and a terminal group), shown in Figure 4.1. The alkanethiol chains were modeled based on the united atom concept that describes a CH_2 group as a single "united" bead. The rigid 114-atom gold core possesses a nearly-spherical polyhedral geometry (rhombicosidodecahedron, one of the 13 Archimedean solids) based on the previous theoretical suggestion [95]. The monolayer covering the Au core consists of 30 "oxidized" surface gold atoms and 60 alkylthiol ligands (SR− with R = $C_{11}H_{22}$) with polar terminal groups, and two ligands attached to each surface gold atom (see Figure 4.2). This feature of the Au-S interface, which exists also for self-assembled monolayers on bulk Au surfaces, has not been incorporated previously for AuNP simulations with classical force-fields [39, 40, 42, 69]. Two types of Au nanoparticles were prepared: one with a terminal amine group (-NH_3^+) and the other with a carboxylic group (-COO^-) attached to each hydrocarbon chain (Figure 4.1). The molecular formulas of the corresponding particles can be represented as $Au_{144}(SRNH_3^+)_{60}$ and $Au_{144}(SRCOO^-)_{60}$ for $AuNP^+$ and $AuNP^-$, respectively. The charge of ± 60 e is unnaturally high, but it was considered reasonable for the visibility of the electrostatic interactions and the dynamics of counter-ions in the simulations.

From the beginning, the goal was to model interactions of functionalized AuNPs with cell membranes, and the AuNP force-field had to be consistent with the force-field for lipid membranes. Hence, the united-atom force-field by Berger *et al.* [110] was used for the alkythiol side groups. Partial charges for the ionized head groups of $AuNP^+$ and $AuNP^-$ were modeled by homology to POPE acyl chains as in

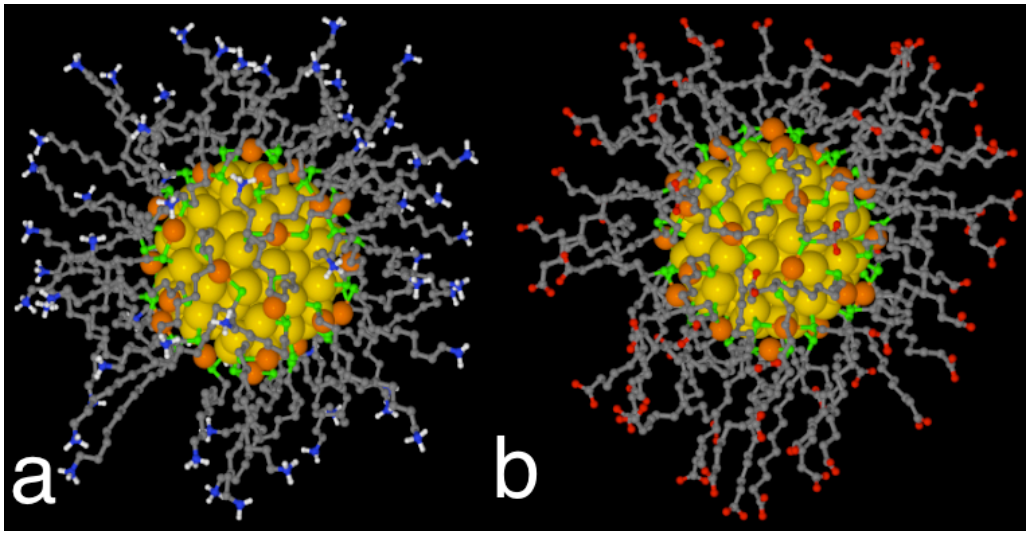

Figure 4.1: Visualization of Au Nanoparticles. (a) The cationic $Au_{144}(SRNH_3^+)_{60}$ and (b) the anionic $Au_{144}(SRCOO^-)_{60}$, where R = $C_{11}H_{22}$. Color code: Au (core), gold; Au (interface), orange; S, green; C (united atom), grey; N, blue; O, red; and H, white.

Ref. [110, 139] and as POPS in Ref. [140]. Na^+ and Cl^- ions use their original GROMOS87 parameters [105]. Lennard-Jones parameters for Au atoms were taken from Ref. [111]. Partial charges of the AuNP core (144 Au and 60 S atoms) were evaluated from the density functional calculations of Ref. [95] by using electron density and the method of Bader charges [141].

The gold core was maintained rigid by using a number of virtual constant bonds and constraint potentials between Au atoms of the core. Additional bonds and constraint potentials were set for the Au-S interface structure in order maintain the correct geometry of the NP interior. The potential parameters, $k_\theta \sim 460.24 - 1460.24$ kJ mol^{-1} rad^{-2}, were not fitted to vibrational properties — the values were chosen to be approximately from one to three times larger than regular angle parameter values, because the purpose was to keep the surface structure somewhat rigid and unchanged during the simulation. (Exact values/angles: $k_{125^\circ}(Au_{core} - Au_{core} - S) = 460.24\,\mathrm{kJ\,mol^{-1}\,rad,^{-2}}$ $k_{180^\circ}(S - Au_{surf} - S) = 1460.24\,\mathrm{kJ\,mol^{-1}\,rad,^{-2}}$ $k_{88^\circ}(Au_{core} - S - Au_{surf}) = 460.24$ kJ mol^{-1} rad^{-2}, and for example, the value for carbon chains k_θ: $k_{111^\circ}(\mathrm{CH_2} - \mathrm{CH_2} - \mathrm{CH_2}) = 460.24$ kJ mol^{-1} rad^{-2}.) Missing force-field parameters of Au and other elements (C, O, S, N and H) were added for the non-bonded interactions in the simulation setup. These values were computed according to the standard combination rule, $C_{ij}^{(k)} = \left(C_i^{(k)} C_j^{(k)}\right)^{\frac{1}{2}}$, where $k = 6, 12$

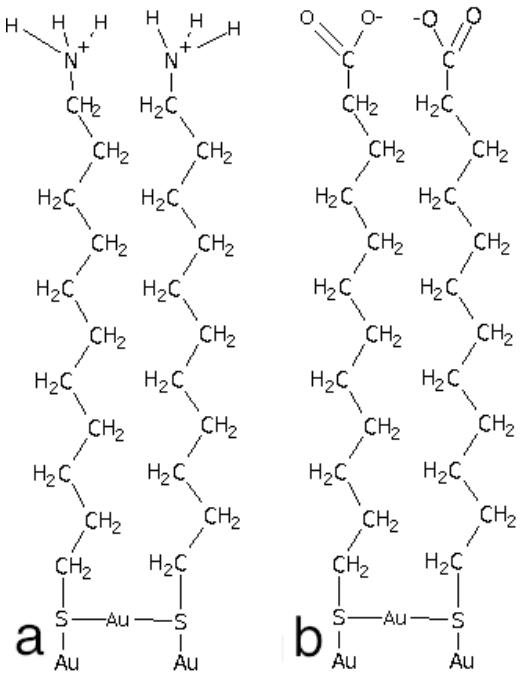

Figure 4.2: Schematic description of the atom nomenclature of alkanethiol groups. (a) $AuNP^+$ with amine and (b) $AuNP^-$ with carboxylic terminal group (charged). Pairs of hydrocarbon chains are connected via one Au (surface) in each case, and the RS-Au-SR oligomers (R standing for the hydrocarbon chain) make additional Au-S bonds with the Au core. CH_2 groups are treated using the united-atom description.

[120] and C_i values where taken from the GROMOS87 force-field [105].

4.2 AuNPs in Aqueous Environment

In *Paper I,* the AuNPs were placed into aqueous solution consisting of water and biologically relevant counter-ions Na^+ and Cl^-. The simulation box dimensions were set to $7.06 \times 7.06 \times 7.06$ nm^3. After placing the AuNP inside the box, the box was filled with water, and 60 counter-ions were added for each AuNP: Cl^- ions for $AuNP^+$ and Na^+ ions for $AuNP^-$. The chosen system size was confirmed to be consistent with the water density at the given temperature. The overall number of atoms in the simulated systems was around 33 000.

Water molecules were represented using the SPC model [112]. The PME method [104] was used for the electrostatic interactions with a real space cut-off of 10.0 Å and a reciprocal grid of $60 \times 60 \times 60$ cells with a 4^{th} order B-spline interpolation. For van der Waals interactions, a cut-off distance of 10.0 Å was used. All MD simulations were performed by using GROMACS (version 4.0.5) [142].

The systems were energy minimized and equilibrated by short 20-ns MD runs. The production simulations were performed over a period of 200 ns for each AuNP. The time step was set to 1 fs and the neighbor list (cut-off 10.0 Å) was updated for every frame. The simulations were performed both in the *NVT* and *NPT* ensembles for 200 ns, respectively. For the *NVT* ensemble, the temperature was set to 310 K using the Berendsen thermostat [114] with a time constant of 0.1 ps. In addition, for the *NPT* ensemble, the Berendsen algorithm [114] with a compressibility of 4.5×10^{-5} bar^{-1}, time constant of 5 ps, and reference pressure of 1 bar was used for isotropic pressure coupling. The variable cell size in *NPT* resulted in 0.2-0.3 Å changes in the simulation box dimensions (70.6 Å). However, most of the analysis was performed using the *NVT* simulation data (constant simulation box size) for practical reasons, mainly due to determination of the electrostatic potential where a constant system size is most appropriate. Several tests showed that the difference between the *NVT* and *NPT* simulation data was negligibly small (as an example, see *Paper I* Table 2 and *Paper I* Supplementary Table 1).

4.3 AuNPs in Presence of Cell Membranes

After studying the AuNPs in aqueous environment, AuNPs were placed into solution in the presence of model cell membranes, *Papers II-III,* to explore their interaction on the cellular level (see Figure 4.4). Native membranes are so complex that there was no chance to consider the membranes in full through MD simulation models. Hence, a model that disregards the role of membrane proteins and other integral membrane structures was used, and the focus was set on lipids in the NP-membrane interaction. When it comes to lipid composition, the purpose was to employ a membrane model as simple as possible. On the other hand, since AuNPs are charged, taking the electrostatics of the membrane into account as accurately as possible was of importance, and hence, single-component lipid bilayer models (which have been considered in many experimental and theoretical studies) were not a suitable choice. The actual plasma membranes contain a certain amount of charged anionic lipids, which could be essential for NP-membrane interactions, and anionic lipids such as phosphatidylserine are localized mostly within the inner leaflets of plasma

membranes. Consequently, anionic lipids were inserted in one of the leaflets of an initially symmetric lipid bilayer.

The model membranes were implemented using POPC (phosphatidylcholine, 1-palmitoyl-2-oleoyl-*sn*-glycero-3-phosphocholine) and POPS (phosphatidylserine,1-palmitoyl-2-oleoyl-*sn*-glycero-3-phosphoserine) lipids (see Figure 4.3). Cholesterol is one of the essential constituents in plasma membranes of eukaryotic cells, but it was not included in the model membrane for computational efficiency, since it would have slowed down the dynamics of the systems. The outer extracellular (EC) leaflet consisted of zwitterionic POPC lipids, and the lipid composition of the inner cytosolic (IC) leaflet was a mixture of POPC (81.25%) and negatively charged POPS (18.75%). The POPS fraction in membrane leaflets of mammalian cells varies rather widely depending on the cell type, but normally does not exceed 30%, most commonly being in the range of 10 – 20% [45, 143, 144]. Therefore, a fraction of approximately 20% was chosen as one of the most appropriate ones. This choice made it possible to explicitly take into account the asymmetric transmembrane distribution of anionic lipids inherent for plasma membranes of eukaryotic cells, keeping the membrane model relatively simple.

The POPC lipid force-field was originally developed by Berger *et al.* [139, 145] with adjustments for the double bond extracted from Barchar *et al.* [146]. The POPS lipid force-field models were implemented by Mukhopadhyay *et al.* [140]. The corresponding Lennard-Jones parameters were obtained from Ref. [111]. Every simulation setup comprised two model membranes, each having 252 lipids in two asymmetric layers. Based on tests, this choice of lipid numbers was confirmed to result in flat lipid bilayers (with no spontaneous curvature). Cytosolic layer consisted of a mixture of 104 POPC and 24 POPS lipids and extracellular layer consisted of 124 POPC lipids. The membranes were (3.8 ± 0.1) nm thick for the POPC head group (phosphorus) distances between the upper and lower leaflet, and the bilayer centre of masses (COMs) were separated by a distance of (15.1 ± 0.2) nm in AuNP hosting systems. Water molecules were represented using the SPC model [112] as in the case of AuNPs in the absence of membranes.

Periodic boundary conditions (PBCs) were used in all directions to achieve com-

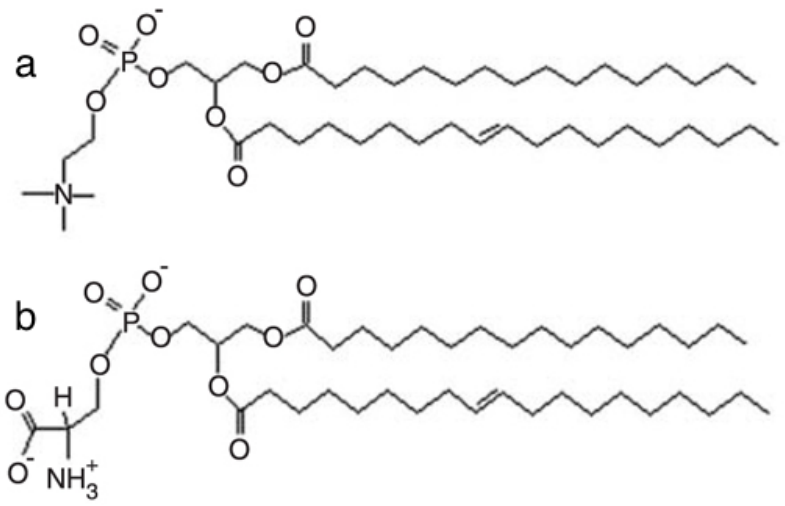

Figure 4.3: Schematic structures of POPC and POPS lipids: (a) POPC (1-palmitoyl-2-oleoyl-*sn*-glycero-3-phosphocholine) and (b) POPS (1-palmitoyl-2-oleoyl-*sn*-glycero-3-phosphoserine). Figure is adapted with permission from Ref. [147].

partmentalisation in simulations. This double membrane setup effectively forms two independent compartments in each system and makes it possible to maintain different compositions for solvents in each compartment. The technique was chosen to keep the size of the systems reasonable for extended simulation times, and also to avoid artefacts, such as finite size effects arising from artificial walls. The extracellular (EC) and intracellular/cytosolic (IC) environments were modeled using inverted asymmetric bilayers with lipid compositions resembling eukaryotic plasma membranes with different ion compositions in each compartment.

The simulation box dimensions were adjusted to $9 \times 9 \times 22$ nm^3 for the AuNP membrane runs. After placing the AuNP and the two POPC/POPS model membranes inside the box, the box the was filled with water, and 60 counter-ions were added for each AuNP surroundings: Cl^- ions for $AuNP^+$ and Na^+ ions for $AuNP^-$, and 24 K^+ ions were added for each POPS containing leaflet. The chosen system sizes were confirmed to be consistent with the water density at the given temperature. The overall number of atoms in the simulated AuNP systems were around 143 000, including 38 800 water molecules .

Both AuNPs with counter-ions were placed in the EC and IC side of the membranes for 200-ns simulations each (see Table 4.1). Two water paths, the EC and IC fluids, were separated by model membranes. The AuNP-counter-ion simulations were all repeated 4 times for 100-ns simulations to ensure that the results were

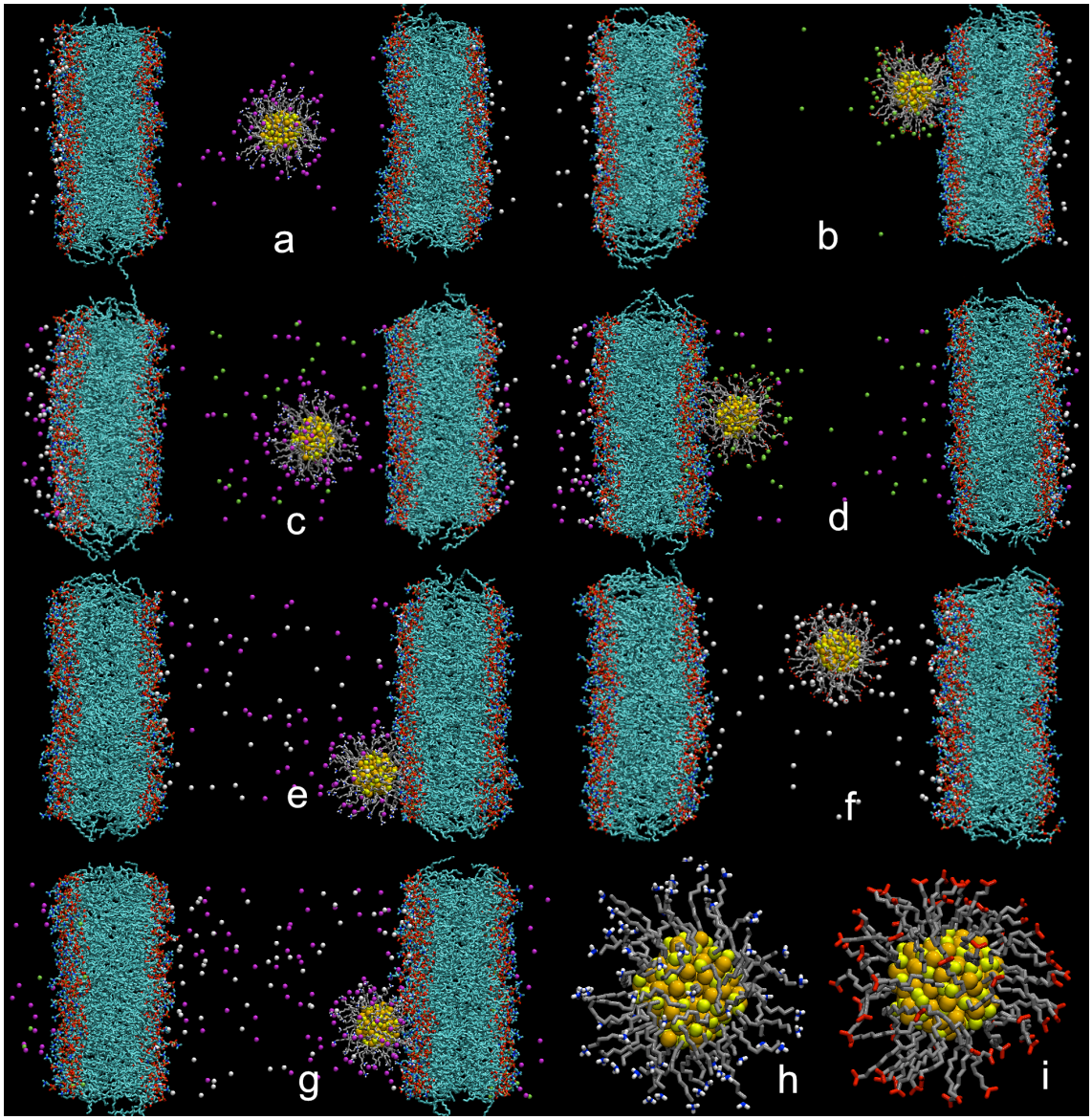

Figure 4.4: Visualization of AuNP-membrane simulation systems. AuNPs in extracellular (EC) and intracellular (IC) compartments (a) $AuNP^+$ in EC, (b) $AuNP^-$ in EC, (c) $AuNP^+$ in EC with salt (d) $AuNP^-$ in EC with salt (e) $AuNP^+$ in IC (f) $AuNP^-$ in IC (g) $AuNP^+$ in IC with salt Close up of AuNPs in (h) AuNP+ and (i) IC AuNP− . Color code: NPs: Au, gold; S, yellow; C (united atom), grey CPK; Na^+, lime; Cl^-, magenta; O, red; N, blue; and K^+ and H, white; lipid bilayers cyan.

reproducible and to eliminate the possibility of randomness. In addition to AuNP/counter-ion simulations, 150 mM of salt was added to both water baths performing 200-ns salt runs for $AuNP^+$ in EC and IC and for $AuNP^-$ in EC (NaCl and KCl in the EC and IC compartment, respectively). To study the behavior of water and ions in the systems, additional 1-ns simulations with a data storage rate of 1/(0.5) ps were performed for all systems using snapshots taken from the middle

Table 4.1: Simulations of the AuNP-membrane systems. Systems with AuNPs contain AuNP with counter-ions in water. Reference system contains no AuNP. All systems contain counter-ions for POPSs. Both extracellular (EC) and intracellular (IC) compartment simulations (without added salt) have been repeated 4 times with same parameters and initial coordinates but with arbitrary starting velocities. In simulations with 150 mM salt was added both into EC and IC. "C.R." refers to constraint-released simulations. Systems are visualized in Figure 4.4.

System	EC Compartment	IC Compartment	Simulations
$AuNP^+$ EC	$AuNP^+ + Cl^-$	K^+	1×200 ns, 4×100 ns, 10×1 ns
$AuNP^+$ salt EC	$AuNP^+ + Cl^- + NaCl$	$K^+ + KCl$	1×200 ns, 10×1 ns
$AuNP^+$ IC	–	$AuNP^+ + Cl^- + K^+$	1×200 ns, 4×100 ns, 10×1 ns
$AuNP^+$ salt IC	NaCl	$AuNP^+ + Cl^- + KCl$	1×200 ns, 4×100 ns, 10×1 ns
$AuNP^+$ EC C.R.	$AuNP^+ + Cl^-$	K^+	1×300 ns
$AuNP^-$ EC	$AuNP^- + Na^+$	K^+	1×200 ns, 4×100 ns, 10×1 ns
$AuNP^-$ salt EC	$AuNP^- + Na^+ + NaCl$	$K^+ + KCl$	1×200 ns, 10×1 ns
$AuNP^-$ IC	–	$AuNP^- + K^+ + Cl^-$	1×200 ns, 4×100 ns, 10×1 ns
Reference EC	–	K^+	1×200 ns, 10×1 ns

of the long trajectory as starting structures.

In order to evaluate the effects of the presence of AuNPs, a reference system without AuNP was constructed and simulated for 200 ns. For the reference systems without AuNP, the simulation box dimensions were adjusted to $9 \times 9 \times 13$ nm^3. The reference system comprised around 75 000 atoms, including 16 000 water molecules. After placing the membranes inside the box, the box the was filled with water. In all simulations, 24 K^+ ions were added for each POPS containing membrane surface. The membrane center of masses (COMs) were separated by a distance of 6.8 nm.

To study activated binding on the EC side, $AuNP^+$ was gradually pulled closer to the membrane using a harmonic potential. Once in contact, 0.9 nm from $AuNP^+$ COM to the membrane surface, the constraint was released and the system was simulated for 300 ns. This system is referred to as "EC constrained-released".

Prior to the actual production runs, all prepared systems were energy minimized. The time step was set to 2 fs and the neighbor list (cut-off 1.0 nm) was updated for every 10^{th} step (20 fs). The SHAKE algorithm was employed in the simulations. The simulations were performed in the canonical *NPT* ensemble by setting the temperature equal to 310 K using the Berendsen thermostat [114] with a time constant of 0.1 ps and with a semi-isotropic pressure coupling using the Berendsen algorithm [114] with a compressibility of 4.5×10^{-5} bar^{-1}, time constant of 5 ps and reference pressure of 1 bar. Long-range electrostatic interactions where calculated using the particle-mesh Ewald summation (PME) method [104]. A real space cut-off of 1.00 nm and a reciprocal grids of $77 \times 78 \times 189$ cells with a 4^{th} order *B*-spline interpolation was used. For van der Waals interactions, a cut-off distance of 10 Å was set. All MD simulations were performed with the use of the GROMACS package(versions 4.0.5, 4.0.7 and 4.5.2) [142].

4.4 Details of Analysis

Data for analysis was stored every 10 ps (RDF, ESP, diffusion coefficients, water orientation). In order to study particularly rapid processes related to hydrogen bonds (water) and other contacts (counter-ions and membrane) between the AuNPs and the surrounding solution, a set of 10 × 1-ns MD simulations starting at 80 ns

were performed, storing data every 0.5 ps. The GROMACS [137, 142] suite of programs was used for the data analysis, complemented by self-made analysis codes.

The AuNP size was calculated as a time average of the average distance per time step between the COM of the Au core and the terminal groups. The terminal group reference atoms for the cationic and anionic NP are the amine hydrogens and the carboxylic oxygens, respectively. The Au core size was calculated in a similar manner as an average distance between the COM of the core and the surface Au atoms.

Radial distribution functions (RDFs) were calculated as a function of the radial distance from the Au core COM, r, for a time window from 100 to 200 ns as in Equation (3.14). Partial densities for groups of atoms of the systems were calculated also for a time window between 50–200 ns, taking into account the masses of atoms, but in contrast to RDFs, against the box axis along the membrane surface normal.

The radius of gyration, R_g, MOI-vector ACF and RCF were computed for the AuNP's x, y and z axes as a function of time, and for explicitly mass weighted atoms (as presented in Equations (3.15), (3.17) and (3.20), respectively) for a 150-ns simulation within a time window between 50–200 ns.

The electrostatic potential (ESP) of the AuNPs in aqueous solution was calculated in two ways to ensure the consistency of results. The first method takes advantage of the spherically symmetric topology of the system. In this, case the radial electrostatic potential was calculated as in Equations (3.33) and (3.34). The used grid size was 0.001 nm for the calculation of Q_r. No significant changes were observed when the grid size was decreased further. The second method consists of the direct solution of the Poisson equation by using discrete Fourier transforms. The AuNP was centered in a three-dimensional grid where the atomic charges are placed by linear interpolation. ESP of the system was calculated as in Equation (3.42). An equally spaced grid of 100 nodes in each direction (grid spacing being 0.07 nm) was used in the computation. This method was significantly less sensitive to the grid size than the double integration above, and grids of 50 (0.14 nm) or 200 nodes (0.035 nm) were found to provide essentially the same results. As for the two methodologies for ESP calculation, in both cases averages over all MD frames were performed. Im-

portantly, the two approaches to compute ESP provided consistent results in every case. The data presented here is based on the first (radial integration) technique presented in Equations (3.33) and (3.34).

The analysis of hydrogen bonds (H-bonds) of AuNP terminal groups and water, and membrane-water contacts, ionic contacts of the AuNP terminal groups, and AuNP-membrane contacts was carried out by averaging over five time windows using ten snapshots of the total trajectory as starting structures for 1-ns simulations with a data storage rate of 1/0.5 ps (as described in Chapter 3.2.8). Contacts between the AuNP terminal groups and water molecules and between membrane headgroups and water were considered within a cut-off distance of 0.35 nm for non-hydrogen atoms and an H-bond angle of 30°. The ion contact analysis of the AuNP solutions and the AuNP-membrane contact analysis were performed considering ions or charged lipid headgroup atoms within a cut-off distance of 0.35 nm from the AuNP terminal groups.

Self-diffusion coefficients were calculated as presented in Equations (3.22) and 3.23, as linear fitting of the mean-square displacement between a time interval of 10–90 % of the simulation time. The error estimate is the difference of the diffusion coefficients obtained from fits over two halves of the initial fitting interval.

The mobility, M, of solvent was computed as described in Chapter 3.2.5. For AuNPs in aqueous solution, the mobility was calculated radially inside AuNP-centered spherical shells of thickness $\Delta r = 0.5$ nm. That is, at every time t during the simulation, the water molecules and ions that at this moment t were at a given distance from the center of the AuNP were determined, after which their mean-square displacement was determined over a short period of time. The width of the time window was Δt = 200 ps and Δt = 500 ps for water and counter-ions, respectively. The data for mean-square displacement, MSD(t), in every shell (representing a fixed distance from the AuNP center) was averaged separately for water molecules and ions over the total simulation time of 200 ns. Finally, the short-time diffusion factor, M, was calculated as an effective slope of the mean-square displacement over the short time window. For AuNP-membrane systems the mobility was calculated in similar manner, but in this case, slicing the simulation box along the membrane

surface normal, starting at the leaflet closest to the AuNP and ending at the other one, and using 0.5-nm and 1.0-nm thick slices for water and counter-ions, respectively. Short-time diffusion factors of molecules and counter-ions inside the slice were calculated by fitting their MSDs within time windows of $\Delta t = 20$ ps and averaging over 10×1-ns trajectories.

The orientation of water molecules was calculated for a time window of 50–200 ns for AuNP-centered spherical shells of thickness $\Delta r = 0.2$ nm using the angle α between a vector from the AuNP center to a water oxygen and a vector from the oxygen to a midpoint between two water hydrogens in the same molecule.

The umbrella sampling method [148] was employed to calculate the free-energy profile of $AuNP^+$ in the EC compartment. The reaction coordinate was chosen to be the distance between the core gold atoms and the phosphorus atoms of the target leaflet in the membrane normal direction. A harmonic biasing potential was employed and a total of 23 windows were simulated with the minimum of this biasing potential located between 0.6 and 5.0 nm with a spacing of 0.2 nm. A force constant of 2000 kJ/mol/nm^2 was chosen as this resulted in sufficient sampling of the total reaction coordinate. The windows with the nanoparticle close to the membrane interface (0.6 to 3.6 nm) were simulated for 100 ns, whereas the rest of the windows (3.8 to 5.0 nm) were simulated for 50 ns. The data for the last 40 ns was employed in the analysis for all windows. Other simulation parameters followed those of the presented equilibrium simulations. The profiles and their statistical error estimates were obtained by the GROMACS tool g_wham [149].

5. RESULTS

5.1 AuNPs Form Complexes with Solvent Molecules

Structural details of AuNP with water and counter-ions were studied by analyzing the three-dimensional RDFs shown in Figure 5.1. The RDFs were drawn for relevant groups with respect to the AuNP-COM in the $AuNP^+$ (Figure 5.1(a)) and $AuNP^-$ (Figure 5.1(b)) solutions. The size (diameter) of the metal core is $d = 1.82$ nm, and the average overall diameter is 4.06 and 4.13 nm for $AuNP^+$ and $AuNP^-$, respectively, including the alkanethiol chains and terminal groups.

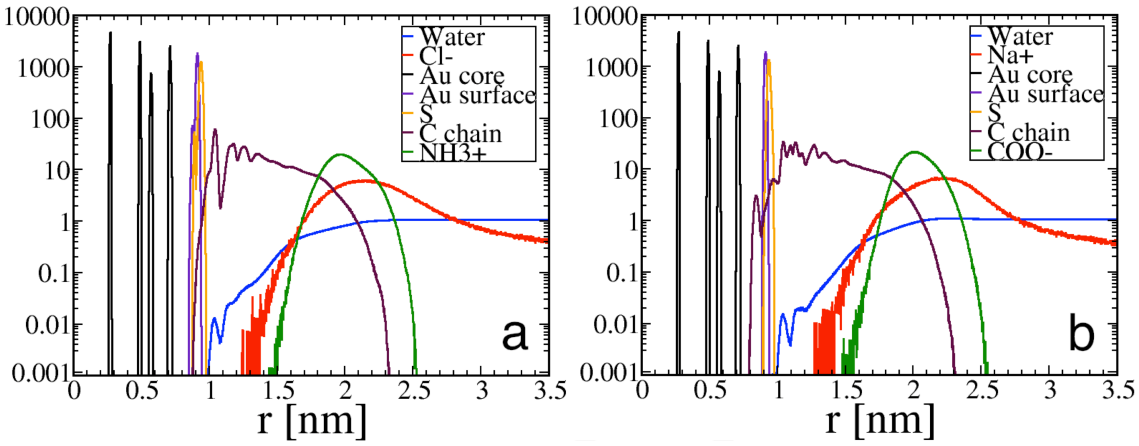

Figure 5.1: RDFs averaged over a time window of 200 ns. (a) $AuNP^+$ and (b) $AuNP^-$ solutions. The distance of $r = 0$ corresponds to the center of the nanoparticle.

The three stacked polyhedral Au layers that constitute the metallic core (114 atoms, rhombicosidodecahedron) are clearly visible in the RDF profiles. The first two shells of the core consist of 12 and 42 atoms, respectively. The first peak corresponds to the first Au layer and those of the second and third peak correspond to the second Au layer (MacKay icosahedron). The fourth peak at 0.7 nm corresponds to the outer layer of the Au core and gives an estimate for the size of the metallic core. Between 0.9 and 1.0 nm, there are S and Au (surface) atoms according to their co-linear positioning in the RS-Au-SR oligomers (Figure 4.2) as suggested

by electronic structure calculations and x-ray diffraction measurements for AuNPs [12]. This important structural feature has been so far neglected in other classical simulations of AuNPs.

The undecanyl chains (R=$C_{11}H_{22}$) are displayed without the terminal groups, and they span a range from 0.8 to 2.4 nm. From the shape of this distribution we can conclude that the tails are very flexible and disordered. This is demonstrated also in Figures 5.2, 5.3 and 5.4. The detailed RDFs of the AuNP terminal groups are shown in Figure 5.2. The terminal group distance distributions (among terminal groups themselves) are shown as histograms in Figure 5.3. The distance histograms display the number distribution as a function of distance, and the distances have been measured between amine nitrogens for $AuNP^+$ and carboxylic carbons for $AuNP^-$.

Snapshots demonstrating tail-end flexibility are presented Figure 5.4. The alkyl chain ends close to the Au core that penetrate between the RS-Au-SR oligomers are visualized in Figure 5.4(a-b). The overall AuNP conformations are given in Figure 5.4(c-d) with a special emphasis on the bent side group configurations. The flexibility of the hydrocarbon chain tail ends at RS-Au can be seen as overlapping peaks of Au surface, S and C chain in the RDF profile (Figure 5.1). The outermost surface of the gold core contains small empty cravices between Au surface atoms, where the C chain tail ends have room to bend themselves into. As can be seen from the RDF figure, water can not access this area, so it is favourable and accessible for flexible hydrocarbon chain tail ends. The differences between the two AuNPs in the C chain RDFs close to core arise from electrostatistics and interactions with the solvent. The RDF profiles (Figure 5.1) of the two AuNPs are rather similar, but the terminal group distribution is slightly narrower in shape for $AuNP^-$ (carboxyls). This implies that the NH_3^+ groups in $AuNP^+$ are more flexible, which is coupled to the interaction with the solvent.

The average hydrocarbon chain length is 1.16 and 1.17 nm for $AuNP^+$ and $AuNP^-$, respectively, measured as the distance between the first carbon (connected to S) and the amine nitrogen or carboxylic carbon, respectively. The segment length of a single unit of the alkyl chain, CH_2, is 0.096 nm for both AuNPs. The radius of

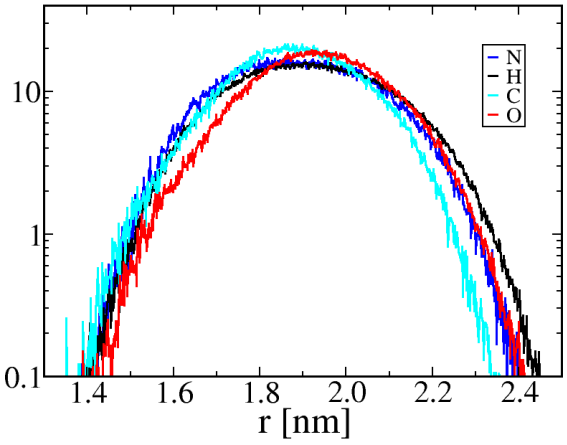

Figure 5.2: The RDF profiles for AuNP side groups in AuNP solutions. The RDFs were calculated over a simulation time scale of 80-180 ns. The sidegroup atoms of $AuNP^+$ are drawn using blue and black colors (NH_3^+), and the sidegroup atoms of $AuNP^-$ using red and cyan (COO^-).

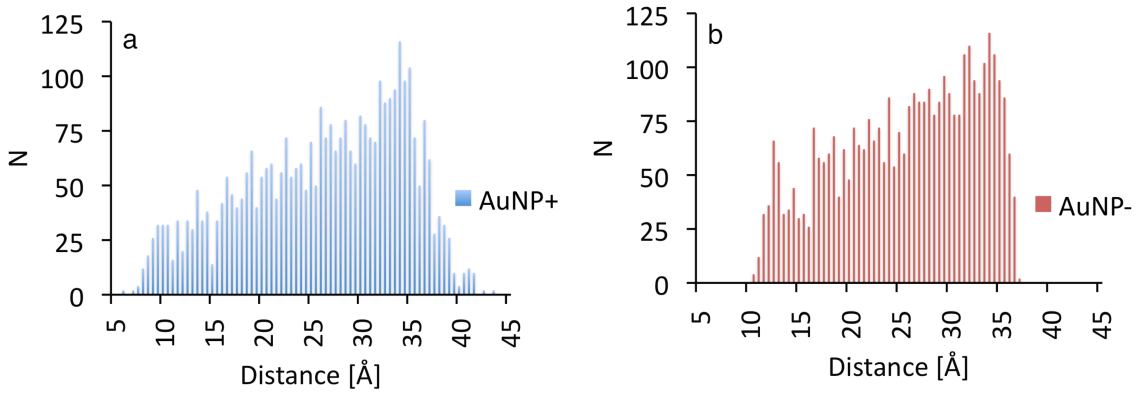

Figure 5.3: Terminal group distance distributions in AuNP solutions. The histograms present the number distributions as a function of distance between terminal groups. The bin width is 0.5 Å. Figures (a) and (b) present NH_3^+ groups of $AuNP^+$ and COO^- groups of $AuNP^-$, respectively — distances are measured between amine nitrogens for $AuNP^+$ and between carboxylic carbons for $AuNP^-$.

gyration, R_g, and the MOI-vector ACF, $C(t)$, of AuNPs are shown in Figure 5.5. The radius of gyration is $R_g = 0.946 \pm 0.004$ nm and $R_g = 0.995 \pm 0.005$ nm for $AuNP^+$ and $AuNP^-$, respectively. These values are biased towards the Au core because of the large atomic mass of gold. MOI-ACFs show shape relaxation at ∼10 ns. The phase sampling of the data can be considered sufficient for the properties analyzed here because of the fast decay of the autocorrelation function. However, the quality of sampling depends on the property considered, and can, of course, be different for some other degrees of freedom.

The RCF of the AuNP was calculated using three Au atoms (i, j, k) as reference

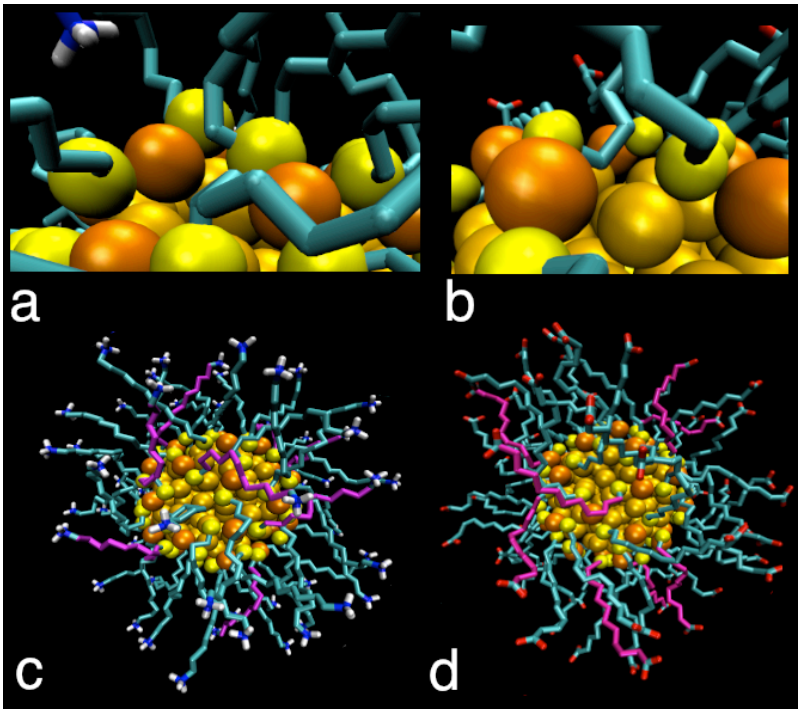

Figure 5.4: Alkyl chains close to the Au core in AuNP solutions. Figures (a) and (b) present the Au core surface of $AuNP^+$ and $AuNP^-$, and Figures (c) and (d) present $AuNP^+$ and $AuNP^-$, respectively. Alkyl chains are slightly bent close to the Au core surface in (b) – this does not occur in (a). In Figures (c) and (d) the magenta-colored alkyl chains' surface groups are within a distance of 10.5 Å from the surface Au atoms.

for defining two vectors $\vec{r}_{ij}$ and $\vec{r}_{jk}$ at the inner gold core (see Figure 5.6 inset). The vector cross product $\vec{r}_n = \vec{r}_{ij} \times \vec{r}_{jk}$ was used for computing RCF with respect to the vector $\vec{r}_n$ (zero time). The RCFs of the AuNPs calculated using a first order Legendre polynomial are presented in Figure 5.6. The RCFs show a decaying trend during the 200-ns simulation. Since the rotational movement takes place slower than fluctuations of MOI, the correlation time is shorter in the latter case.

ESP and the radially integrated charge of the AuNP solutions are presented in Figures 5.7, 5.8 and 5.9. Both particles comprise the same Au_{114} core and Au-S interface, and they essentially display the same distribution of accumulated charge in the core region (<1 nm, Figure 5.7, inset). Small differences can be detected due to the mobility of the interfacial Au and S atoms. Between 1.0–1.3 nm, a small flat region is observed accounting to the neutral carbons (united atoms, see Figure 4.2) of the alkyl chain. After this, the COO^- and NH_3^+ terminal groups start to contribute, and the graphs substantially differ. These differences can be understood by comparing the individual RDFs of the terminal groups and their

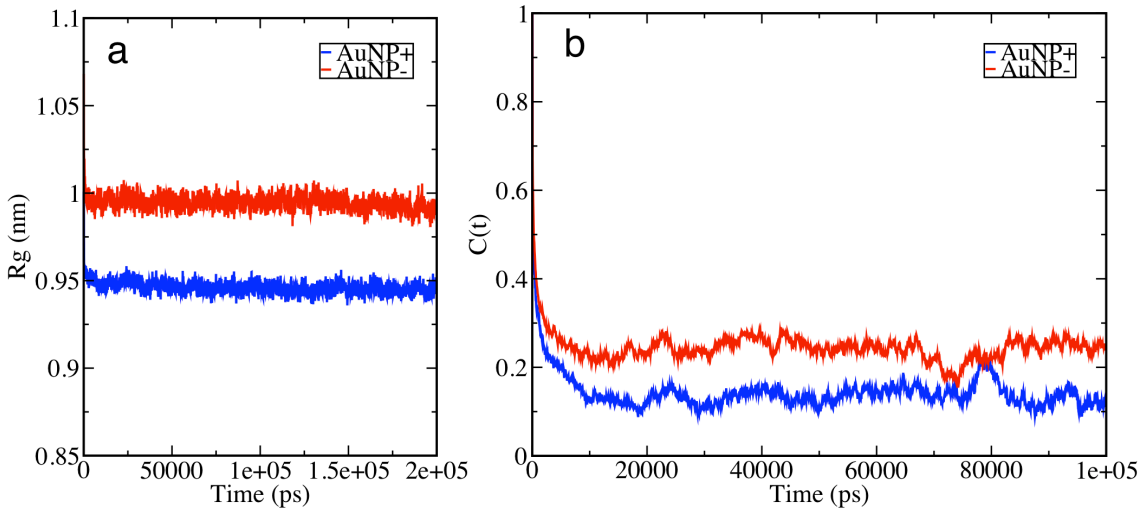

Figure 5.5: Radius of gyration and the MOI-ACF of AuNPs in solution. (a) Radius of gyration and (b) MOI-ACF. The graphs of the $AuNP^+$ and $AuNP^-$ are drawn using blue and red lines, respectively.

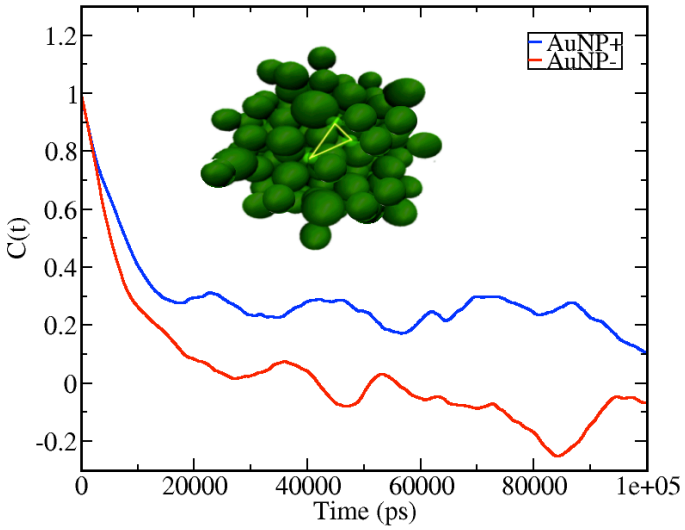

Figure 5.6: RCFs of the AuNP in solution. The cationic and anionic AuNPs are drawn with blue and red colors, respectively. RCF was calculated using three Au atoms (i, j, k) defining two vectors $\vec{r}_{ij}$ and $\vec{r}_{jk}$ at the inner gold core – all the three possible $\vec{r}_{lm}$ $(l \neq m)$ vectors of the atoms spanning a plane are drawn in the figure.

respective partial charges (Figures 4.2 and 5.1).

The ESP analysis shows that in the $AuNP^-$ system the counter-ions (Na^+) are likely to accumulate around 2.0 nm from the AuNP COM. For $AuNP^+$ the counter-ions (Cl^-) experience an increasingly attractive ESP towards the center with a small maximum. The curve is to be inverted when testing the effects for negative counter-ions. It clearly shows in the graph that ESP accounts for the electrostatic forces and neglects details at the atomic level. The RDFs of the counter-ions in Figure 5.1

show that both curves mainly overlap instead of finding Cl^- significantly closer to the AuNP core as one would expect based on ESP. The underlying reason is that despite the stronger attractive electrostatic force towards the core, Cl^- is also substantially larger than Na^+ in size (the atomic radii, 0.098 nm in Na^+ and 0.181 nm in Cl^-). As a consequence, Cl^- experiences a stronger repulsion when trying to penetrate inside the hydrocarbon chain region. The ion-size effect and ESP balance each other leading to rather similar RDF behavior for both AuNPs.

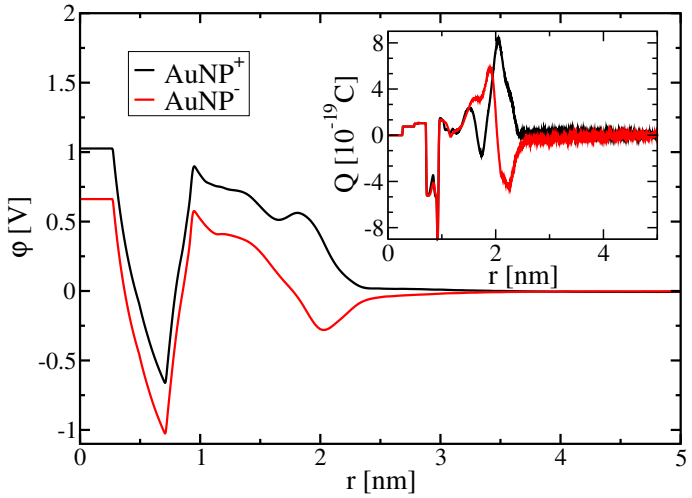

Figure 5.7: Radially integrated electrostatic potential and charge (the latter shown in the inset) in AuNP solutions. $AuNP^+$ and $AuNP^-$ are drawn using solid black and red line, respectively.

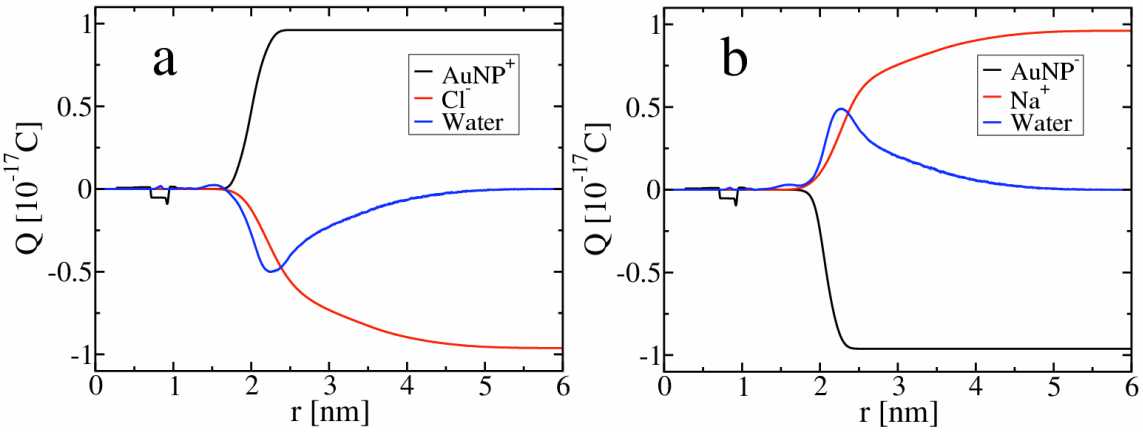

Figure 5.8: Radially integrated charge in AuNP solutions decomposed into the different components. $AuNP^+$ and $AuNP^-$ are drawn using black and red behaviors, respectively. Water is drawn using blue solid line.

When the radially integrated charge is decomposed into different components for AuNP, water, and ions (see Figure 5.8) it can be seen that the contribution due to

AuNP competes against the other two components of the system. The contribution of ions decays slowly as in the RDF data. There is a peak for water with a width of about 2 nm, the peak position being close to the maximum of ion distribution (see Figure 5.1). As further results for the distribution of water orientation show below, the water behavior in Figure 5.8 arises from the complexity of the ordering of water (see a schematic figure of the orientation of water around $AuNP^+$ in Figure 5.10). Even though water molecules are neutral, they can cause local contributions to the radial charge, since they dipolar. Similar features over similar scales have been observed for water close to its interface with charged lipid membranes [150].

In the present case with AuNP and counter-ions, the proper theoretical context is given by the mean-field Debye-Hückel theory, where for counter-ions around a charged particle, one combines the Poisson equation to specify the electrostatic potential of an ion with the Boltzmann equation for charge distribution. The theoretical background of the analysis of the electric double layer structure was discussed in Chapter 3.2.6. In radial symmetry, the Debye-Hückel description for the counter-ion distribution around a charged spherical AuNP can be written as $Ae^{-Br}/r + C$, where A, B, and C are positive constants. The constant C is included due to the finite system size. The most relevant parameter of these is the Debye screening length $\lambda_D = B^{-1}$. To analyse the charged surface of the AuNP surrounded with counter-ions, the counter-ion distributions were fitted to the Debye-Hückel theory, presented in Figure 5.11. In the simulations, the number of counter-ions was set 60 to correspond and cancel out the AuNP charge $\pm 60\, e$. Despite this statistical limitation, the statistics of the 200-ns simulations for the ion distributions was considered sufficient. The following analysis of the ion-AuNP contact lifetimes (see Table 5.1) shows that the contacts between the AuNP and ions have short life-times, and the diffusion of ions is fast (see below, Table 5.2). Based on the results, the agreement with Debye-Hückel theory was found to be very good at large distances.

The deviations between the ion distribution data and the Debye-Hückel descriptions emerge around 2.4 nm from AuNP-COM, which can be considered as an approximate location for the electric double layer interface between AuNP-bound and loosely associated counter-ions, the latter being able to move rather freely in the

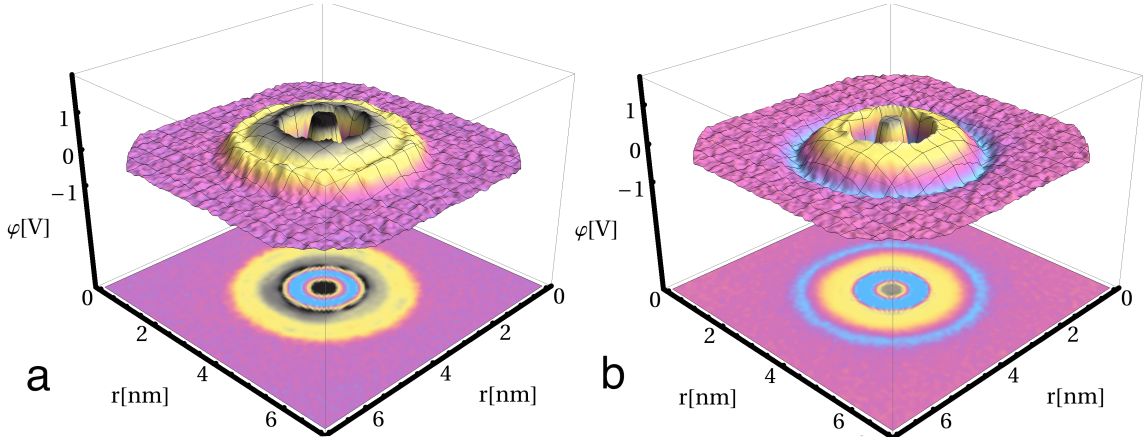

Figure 5.9: ESPs in AuNP solutions. (a) $AuNP^+$ and (b) $AuNP^-$ solutions. Shown here is a two-dimensional slice (in this case in the xy-plane) of ESP passing through the center of the nanoparticle in AuNP solutions. Any chosen plane through the origin leads to the same result due to the spherical symmetry of the nanoparticle.

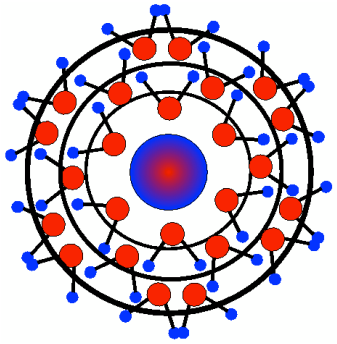

Figure 5.10: Schematic figure of the orientation of water spheres in $AuNP^+$ solution.

system despite the presence of AuNP. The fits shown in Figure 5.11 yield values of 0.27 and 0.20 nm for the Debye length in $AuNP^+$ and $AuNP^-$, respectively. These lengths are one order of magnitude smaller than the AuNP size, which implies that the assumptions of the Smoluchowski theory for zeta potential determination are valid in the present case. Based on the counter-ion fits, the position of the interface between AuNP-bound and loosely bound ions was estimated to be approximately 2.4 nm. At this distance, the ESP gives an estimate for the zeta potential: 26 mV for $AuNP^+$ and -59 mV for $AuNP^-$ (Figure 5.12).

The AuNP terminal group contacts with water and counter-ions are visualized in Figure 5.13. The average number of H-bonds and ion contacts per 0.5 ps time frame and their lifetimes are shown in Table 5.1. The analysis of H-bonds and ion contacts with the terminal groups reveal differences between the two AuNP systems. The ter-

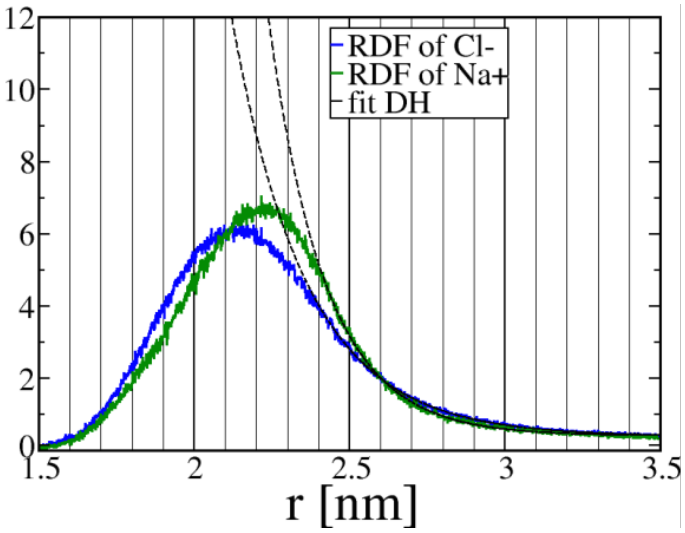

Figure 5.11: Counter-ion distribution profiles fitted to the Debye-Hückel description in the AuNP solutions. The RDFs of counter-ions Cl^- and Na^+ are drawn using blue and green color, respectively. The exponential fits based on the Debye-Hückel theory, $Ae^{-Br}/r + C$ with constants A, B and C are drawn using black dashed lines. The fits were made for data with $r \geq 2.5$ nm.

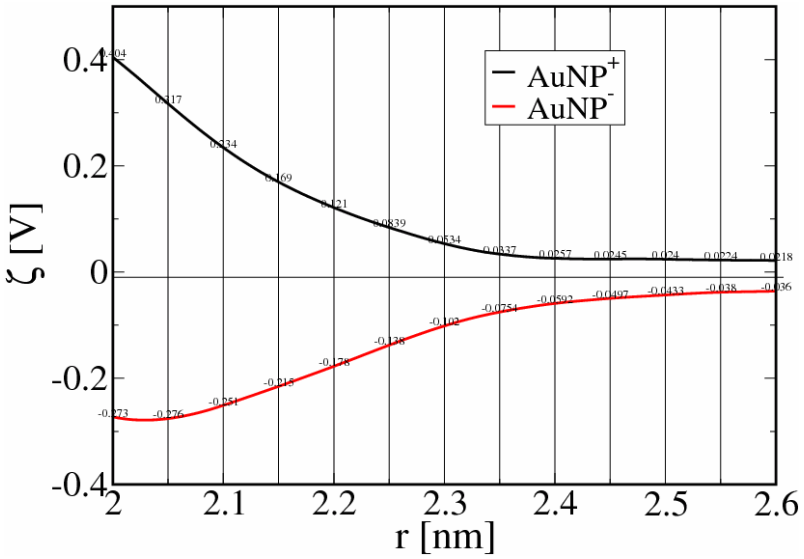

Figure 5.12: ζ potential in AuNP solutions. ESPs of $AuNP^+$ and $AuNP^-$ are drawn using black and red lines, respectively.

minal amine groups of $AuNP^+$ form three contacts with the solvent each. There are two possible configurations: First, one hydrogen of $NH_3{}^+$ connects to a counter-ion Cl^- and the other two form H-bonds with water oxygens (Figure 5.13(b)), and second, the amine hydrogens make three H-bonds with water oxygens (Figure 5.13(c)). The solvent configurations around the terminal carboxyl groups of $AuNP^-$ appear more complicated, as they form six or seven contacts (Figure 5.13(d-f)). One fre-

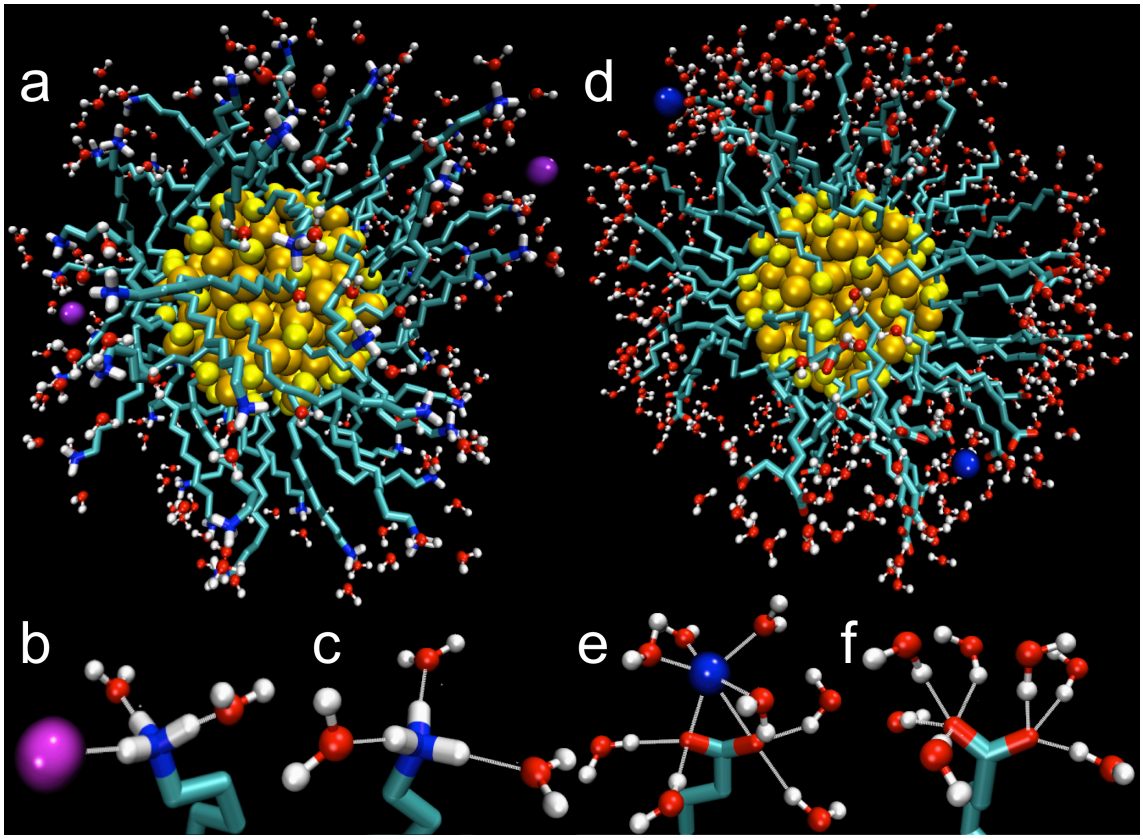

Figure 5.13: The first solvation shell in AuNP solutions. $AuNP^+$: Amine terminal groups NH_3^+ with Cl^- counter-ions and water; and $AuNP^-$: Carboxylic terminal groups COO^- with Na^+ counter-ions and water. (a) $AuNP^+$ and solvent molecules within a cut-off distance of 0.34 nm with respect to the amine terminal group. (b) NH_3^+ terminal group (color key: N, blue; and H, white) forming three contacts: one ionic bond with Cl^- (violet) and two H-bonds with water molecules (O, red). (c) NH_3^+ group forming H-bonds with three water molecules. (d) $AuNP^-$ and solvent molecules within a cut-off distance of 0.36 nm with respect to the carboxylic terminal group. (e) Na^+ ion (color: blue) is coordinated by four water molecules (O, red; H, white) and COO^-, and the two carboxylic group oxygens form H-bonds with four waters. (f) COO^- group and seven water molecules; three and four H-bonds for each carboxylic oxygen.

quently observed case is a configuration of seven H-bonds between the carboxyl group and seven waters. Another relevant configuration involves contacts between Na^+, COO^-, and water in such a way that the two carboxylic oxygens form H-bonds with four waters and two (ionic) Na-O bonds with the counter-ion, and in addition, Na^+ forms four ionic Na-O bonds with the waters nearby (Figure 5.13(e-f)).

The average number and lifetime of H-bonds and ion contacts (Table 5.1) show significant differences between the two AuNP solutions: The total number of H-bonds between water and AuNP is 170.8 ± 0.2 and 404.4 ± 0.5 for the cationic and anionic AuNP, respectively, and the number of contacts for the anionic case is over

Table 5.1: Hydrogen bonds and ionic contacts between AuNP and the solvent in the AuNP solutions. N_A is the average number of hydrogen bonds and contacts and τ_A is the average lifetime of the contacts.

A	N_A	τ_A [ps]
Water ($AuNP^+$)	170.8 ± 0.2	6.5 ± 0.2
Cl^-	4.7 ± 0.4	5.0 ± 0.1
Water ($AuNP^-$)	404.4 ± 0.5	3.5 ± 0.1
Na^+	4.4 ± 0.4	10.1 ± 1.1

two times larger. However, the total number of ion contacts does not differ considerably (4.7 ± 0.4 and 4.4 ± 0.4 for $AuNP^+$ and $AuNP^-$, respectively). These results are consistent with the details of the atomic configurations around the terminal groups as discussed above — the number of contacts with water is over two times larger for the COO^- groups ($AuNP^-$) because each carboxyl oxygen is able to make several H-bonds simultaneously. The number of counter-ions around terminal groups is similar, but when it comes to contact lifetimes, the results reveal differences in counter-ion coordination. The AuNP/counter-ion contact lifetime is 5.0 ± 0.1 and 10.1 ± 1.1 ps for the cationic and anionic AuNP, respectively. The Na^+ ions (with $AuNP^-$) are more tightly bound, between two COO^- oxygens and surrounded by water molecules (Figure 5.13(d-f)), whereas the Cl^- ions ($AuNP^+$) are more mobile as they are bound to only one $NH_3{}^+$ hydrogen (Figure 5.13(a-c)). The water contact lifetimes are longer for the cationic nanoparticle, 6.5 ± 0.2 vs. 3.5 ± 0.1 ps, and this appears to be coupled to the ion coordination. The water contacts of $AuNP^+$ are less disturbed by counter-ion movements because of weaker ion binding of the $NH_3{}^+$ group and fewer H-bonds. Consequently, the lifetime value for water is larger than in the case of $AuNP^-$.

The self-diffusion coefficients of the AuNP solution in the *NPT* ensemble are presented in Table 5.2. The diffusion coefficients of the *NPT* and the *NVT* ensembles show no significant difference for water. The water molecules were represented using the SPC model in the simulation setup, and the previously reported diffusion coefficient for pure SPC water 4.40×10^{-5} cm^2 s^{-1} is smaller than for the AuNP solutions [151], but so is also the temperature 300 K compared to the one in our work (310 K). The minor difference therefore arises in part from thermal fluctuations and

Table 5.2: Self-diffusion coefficients D_A of particles A in AuNP solutions in the NPT ensemble.

A	$D_A[\times 10^{-5}$ cm^2 s$^{-1}]$
$Au_{144}(SRNH_3^+)_{60}$	0.2 ± 0.1
Water	4.7 ± 0.1
Cl^-	1.6 ± 0.2
$Au_{144}(SRCOO^-)_{60}$	0.1 ± 0.1
Water	4.7 ± 0.1
Na^+	1.0 ± 0.1

the presence of AuNP and counter-ions. Furthermore, the diffusion coefficient of Cl^- counter-ions ($AuNP^+$) is approximately 20% higher than that for Na^+ ($AuNP^-$). This shows that the counter-ions of $AuNP^-$ are not able to move as freely as in $AuNP^+$, which is consistent with the stronger ionic binding between the carboxylate groups ($AuNP^-$) and Na^+. This also correlates with the fact that the first hydration shell around a Na^+ ion is more ordered than that for a Cl^- ion [152]. The diffusion coefficients of $AuNP^+$ and $AuNP^-$ are almost identical given their error limits.

The short-time diffusion factors of water molecules and counter-ions were calculated inside spherical 0.5 nm shells around AuNPs, and they are shown in Figure 5.14. Apart from the slight deviation at 1.5–2.5 nm, the results show little difference for water (as for the self-diffusion coefficients, Table 5.2), but there is a significant deviation for the counter-ions. The Cl^- ions ($AuNP^+$) have higher values than those (Na^+) of the anionic nanoparticle. In general, the short-time diffusion values increase as a function of radius, which is caused by the water/ion interactions with AuNPs. The presence of AuNP slows down the diffusion of water molecules and ions. Water forms a network of H-bonds around the terminal groups of AuNP and counter-ions, and this makes the H_2O positions more restricted close to AuNP. For water, the rate of increase in short-time diffusion factors as a function of distance is lower than for the counter-ions. This can be explained by the type of bonds, which water and ions form with AuNP: An H-bond between AuNP and an H_2O molecule is weaker and of shorter range than the electrostatic interaction between a AuNP terminal group and a counter-ion.

The effect of AuNP in solvent diffusion extends at least to 5 nm from the AuNP

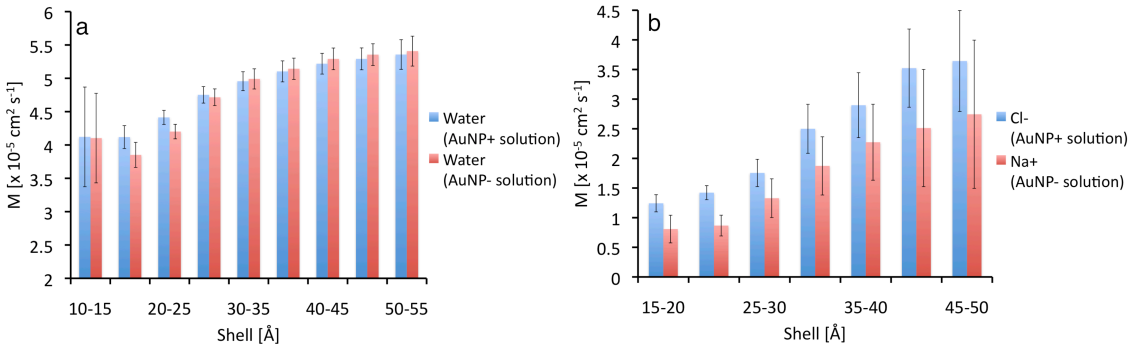

Figure 5.14: Solvent mobility around AuNPs for spherical shells in the AuNP solutions. (a) Mobility of water and (b) counter-ions located at AuNP centered $\Delta r = 0.5$ nm shells for time windows of $\Delta t = 200$ ps (water) and $\Delta t = 500$ ps (counter-ions) averaged over the 0–200 ns simulation time. The $AuNP^+$ and $AuNP^-$ histograms are presented using blue and red colors, respectively. The error bars correspond to standard deviation.

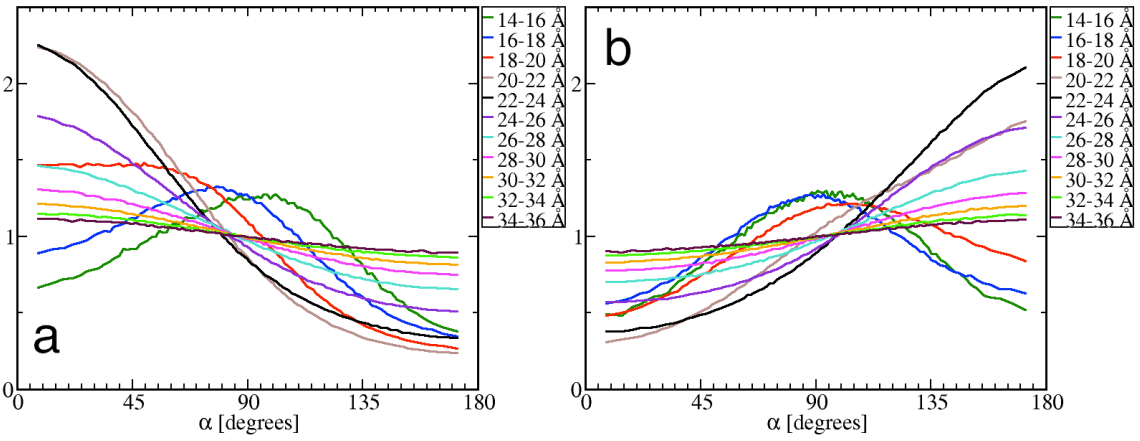

Figure 5.15: Distribution of water orientation for different distances from the AuNP center: (a) $AuNP^+$ and (b) $AuNP^-$. Orientation is characterized by the angle α, which is defined by a vector from the AuNP center to a water oxygen and a vector from this oxygen to a midpoint between two H atoms in the same H_2O molecule. If the two vectors are aligned pointing in the same direction, then the angle $\alpha = 0$. Solvent orientation is calculated for AuNP-centered spherical shells of thickness $\Delta r = 0.2$ nm over the simulation simulation time 0–200 ns. Note that the most likely location for the terminal groups is between 1.8–2.2 nm, (see Figure 5.1).

COM (this distance corresponds to 3 nm from the surface, Figure 5.14), which indicates that the solvent transmits the interaction shell-by-shell by intermediating the orientation of water molecules. This phenomenon is evident in the solvent orientation data shown for the AuNP solutions in Figure 5.15. Schematic figure of orientation of water spheres in $AuNP^+$ solution is presented in Figure 5.10. As for the short-time diffusion analysis, the water orientations also depend strongly on distance: The first shell surrounding the NH_3^+ terminal groups aligns water molecules

in such a manner that oxygen is closer to $AuNP^+$ than the H atoms, and vice versa for $AuNP^-$. This effect arises from the electrostatic forces (of H-bonding) between the oppositely charged terminal groups of AuNPs and polarized water molecules, and it results in opposite trends for the two AuNPs.

5.2 Interplay between AuNPs and Membranes

AuNPs were simulated both in the EC and IC compartments. Visualizations of AuNP-membrane systems are presented in Figure 4.4. Five different 200-ns simulation setups were prepared for $AuNP^+$: EC, EC with salt, EC constraint-released, IC and IC with salt; and three for $AuNP^-$: EC, EC with salt and IC (see Table 4.1 for simulations).

Partial densities for relevant groups in the AuNP-membrane systems are presented in Figures 5.16(a-e) and 5.16(e-f) for $AuNP^+$ and $AuNP^-$, respectively. The partial density profiles demonstrate that once the AuNP-membrane binding occurs, AuNP is in a stable contact with the membrane interacting with the lipid head groups ($AuNP^+$-IC: Figures 5.16(a-b) and $AuNP^-$ in EC: Figures 5.16(f-g)). In contrast, when AuNPs are not attached to the membrane surface, the density profile shows a broader distribution for AuNPs around the compartment center ($AuNP^+$-EC: Figures 5.16(c-d) and $AuNP^-$ in IC: Figure 5.16(h)), reflecting fluctuations of the nanoparticle in the bulk water phase.

In the EC compartment, the ionic cloud of Na^+ around $AuNP^-$ is rather compact, but strongly biased towards the neighbouring leaflet of the membrane (see Figure 5.16(f)). The counter-ions have small maxima overlapping with the membrane due to contacts with negative POPC phosphate groups, but there are no counter-ions between $AuNP^-$ and the membrane. The $AuNP^-$ in EC system with added 150 mM NaCl (Figure 5.16(g)) shows that both Na^+ counter-ions and Cl^- ions have accumulated close to the opposite membrane surface with respect to the nanoparticle. The behaviour of Cl^- ions occurs due to the high surface charge density of $AuNP^-$, which repels Cl^-. The accumulation of Na^+ to the opposite leaflet arises from the electrostatic attraction between the ions and negatively charged POPC lipid head groups. Obviously, the electrostatic interactions are mediated through the whole

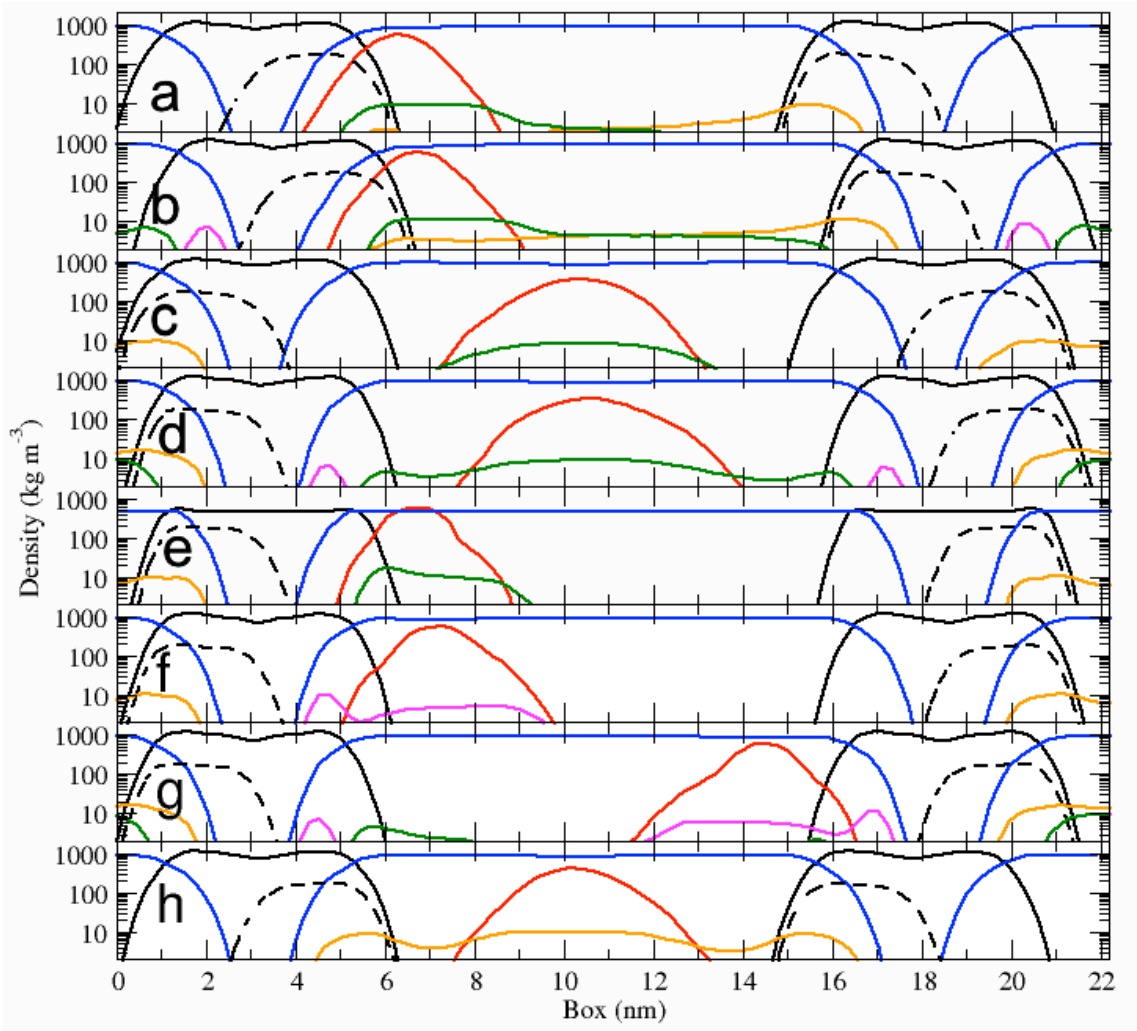

Figure 5.16: Partial densities in AuNP-membrane simulations. Partial density profiles of $AuNP^+$ systems in (a) IC (b) IC with salt (c) EC (d) EC with salt (e) EC constraint-released, and $AuNP^-$ systems in (f) EC (g) EC with salt (h) IC. $x = 0$ is at the box end. Color code: membrane: black solid; NP: red solid; water: blue solid; POPS: black striped; K^+: orange solid; Cl^-: green solid; Na^+: magenta solid. (See Figure 4.4 for visualisations of systems and Table 4.1 for simulations.)

compartment, and the nanoparticle attachment is a co-operative process, which involves all components in the solvent. The K^+ content on the IC side is already rather substantial without additional salt as the $AuNP^-$ and POPS counter-ions add up in a continuous distribution across the whole compartment, which screens both the nanoparticle and the membrane surface.

The calculation of nanoparticle size confirmed same results as in the case of AuNPs in aqueous solution. The radius of gyration, R_g, and the MOI-ACF, $C(t)$, of AuNPs are shown in Figure 5.17. The RCFs of the AuNPs are presented in Fig-

ure 5.18. The radius of gyration of AuNP in EC solution is $R_g = 0.948 \pm 0.001$ nm and $R_g = 0.999 \pm 0.001$ nm for $AuNP^+$ and $AuNP^-$, respectively. The radius of gyration of AuNP in IC solution is $R_g = 0.948 \pm 0.003$ nm and $R_g = 0.998 \pm 0.004$ nm for $AuNP^+$ and $AuNP^-$, respectively. The values are similar to those of the same AuNPs in aqueous solution (Figure 5.5), which indicates that the nanoparticles are able to maintain their compactness of structure in the presence of membranes. The MOI-ACF analysis shows significant difference only in the case where $AuNP^+$ attaches to the IC leaflet (Figure 5.17(d)), indicating that the presence of the membrane affects the moment of inertia of the AuNP, since side groups deform. The AuNP-membrane contact is reflected to the RCF, as well, which shows a long-range correlation for the rotation of $AuNP^+$ in IC (Figure 5.18(b)). According to the results, it is evident that after embedding into the membrane, the rotational degree of freedom $AuNP^+$ is highly restricted by the presence of the membrane, and the phase space sampling is limited to that particular embedding conformation, as can be seen by constant autocorrelation function. A slight effect can be seen also in the case where $AuNP^-$ approaches the EC leaflet (Figure 5.18(a)) in comparison to $AuNP^-$ in aqueous solution (Figure 5.6); the contacts with the membrane surface slow down the rotation of $AuNP^-$, and, consequently, the decay of the RCF in aqueous solution is faster than in the presence of membranes. The RCFs of $AuNP^+$ in aqueous solution and in EC are somewhat the same, indicating that the AuNP is able to rotate in the EC compartment rather freely. The differences between $AuNP^-$ in aqueous solution and in IC were concluded to arise from the high counter-ion concentration of the IC compartment. The large number of contacts with counter-ions slows down the rotational movement of the AuNP, and the autocorrelation time is of order of the simulation time. However, even though the extended autocorrelation times of some of the simulated systems would require performing longer simulations to study the rotational movements of the membrane-bound AuNP, in this study, the focus was on a particular process of AuNP embedding to the surface, for which the available data gives a good insight. Furthermore, since the particle is symmetric, and the observed degree of freedom is not directly responsible for any binding mechanism, the phase space sampling can be considered sufficient also in these cases.

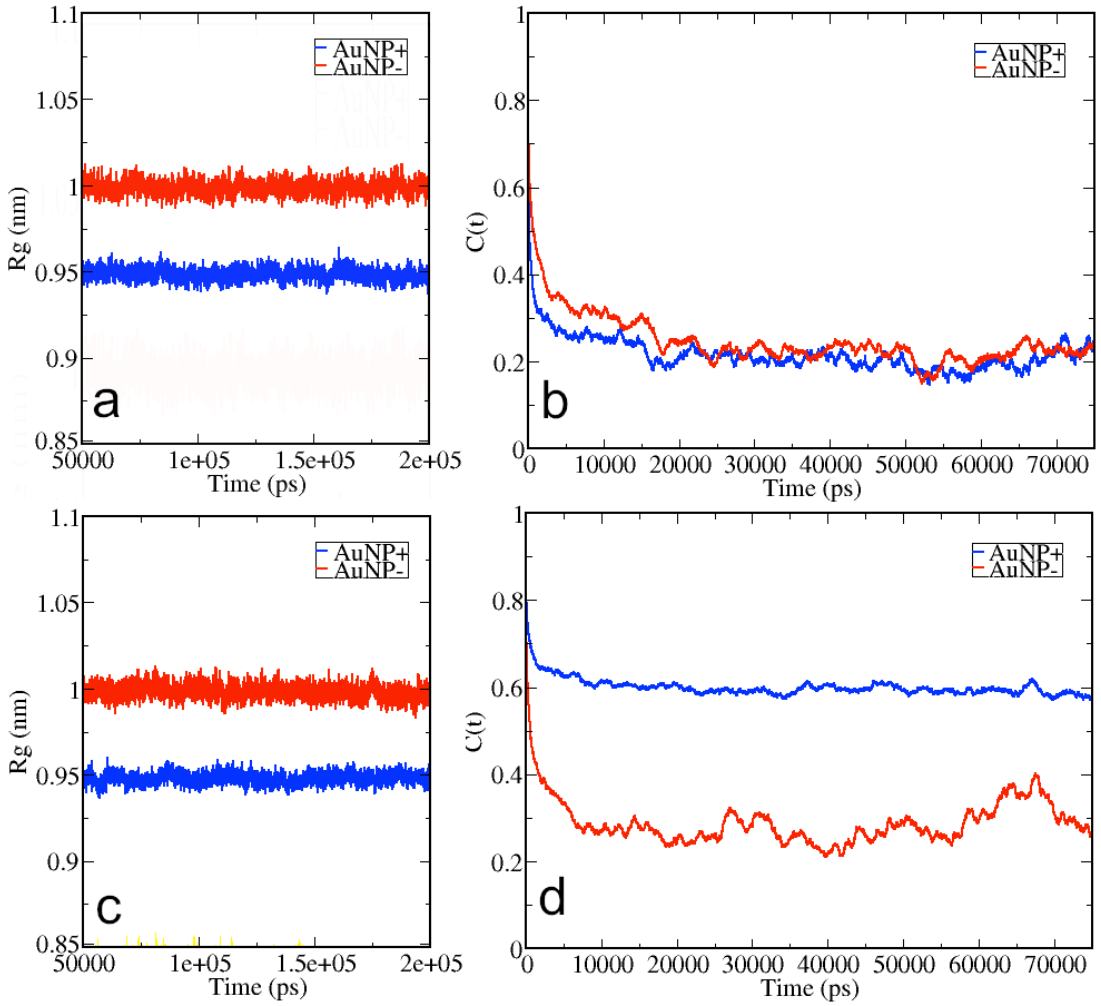

Figure 5.17: Radius of gyration and MOI-ACF in the AuNP-membrane simulations.The graphs of $AuNP^{+}$ and $AuNP^{-}$ in (a,b) EC and (c,d) IC compartments are drawn using blue and red colors, respectively.

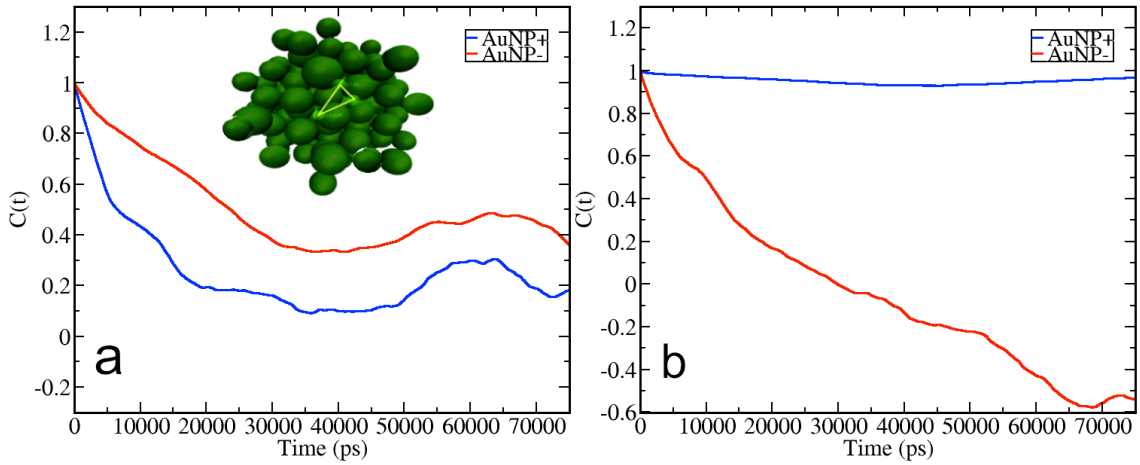

Figure 5.18: RCFs of the AuNPs. RCFs in (a) EC and (b) IC of $AuNP^{+}$ and $AuNP^{-}$ are drawn using blue and red colors, respectively. RCF was calculated using three Au atoms (i, j, k) defining two vectors $\vec{r}_{ij}$ and $\vec{r}_{jk}$ at the inner gold core – all the three possible $\vec{r}_{lm}$ $(l \neq m)$ vectors of the atoms spanning a plane are drawn in the figure.

Distance between AuNP-COM and the closest membrane surface along the bilayer surface normal is shown in Figure 5.19. Five repeated 100-ns simulations with the same initial coordinates and arbitrary initial velocities were performed for both AuNP in EC (Figures 5.19(a-b)) and in IC (Figures 5.19(c-d). AuNP radius is approximately 2 nm. Hence, in the figures the AuNP-membrane distance of ∼1–2 nm means that the AuNP is attached to the bilayer surface and that AuNP's functional groups and membrane surface groups are in contact. With distances less than 2 nm, the AuNP is embedded into the membrane. As seen in Figure 5.19(b), $AuNP^-$ approaches the EC leaflet of the membrane in all five EC simulations within few tens of nanoseconds and after that stays on the bilayer surface, whereas $AuNP^+$ stays at the center of the simulation box between the membranes (Figure 5.19(a)) in all simulations I-IV. The AuNP-membrane distance data of the EC contraint-released simulation of $AuNP^+$ showed that after releasing the constraint, the AuNP stayed bound to the surface during the 300-ns simulation (Figure 5.19(a)). In IC, $AuNP^+$ attaches to the cytosolic leaflet of the membrane within 10 ns in all 5 simulations (Figure 5.19(c)), whereas $AuNP^-$ remains fluctuating in the compartment center between the membranes. AuNPs' charge-dependent tendency to approach the membrane was concluded to arise from the electrostatics of the systems.

$AuNP^+$ in IC penetrates deeper into the IC leaflet than $AuNP^-$ into the extracellular leaflet in EC. $AuNP^-$ interacts with the zwitterionic POPC head groups, in particular with positively charged choline, but in the same time it feels a repulsive force arising from the presence of negatively charged phosphates right below these, and therefore, it will stay on the surface of the EC membrane, close to the positively charged surface groups of the POPC lipids. The negatively charged POPS lipids are at the IC leaflet, and $AuNP^+$ in IC feels stronger attractive force towards the membrane than $AuNP^-$ in EC. Moreover, it is obvious that $AuNP^-$ in IC (Figure 5.19(d)) does not approach the membrane because of POPS lipids. For the cases when the AuNPs do not approach the membrane, stronger repulsive forces for $AuNP^-$ in IC show up as narrower partial density profiles for AuNP as well as smaller variation in AuNP-membrane distances in comparison with $AuNP^+$ in EC.

Since $AuNP^+$ did not spontaneously bind to the EC leaflet, the binding process

was taken into more detailed consideration through free-energy simulations using umbrella sampling. The results of free-energy calculation showed a free-energy barrier of about 11.7 kJ/mol (4.7 $k_B T$) for the binding of $AuNP^+$ to the EC leaflet and that once the barrier is crossed, the AuNP is bound to the EC leaflet in a stable manner at the membrane-water interface, about 1.7 nm from the membrane center, with a well depth of about −18.3 kJ/mol (−7.4 $k_B T$) with respect to unbound $AuNP^+$. These values are comparable to thermal fluctuations of few $k_B T$.

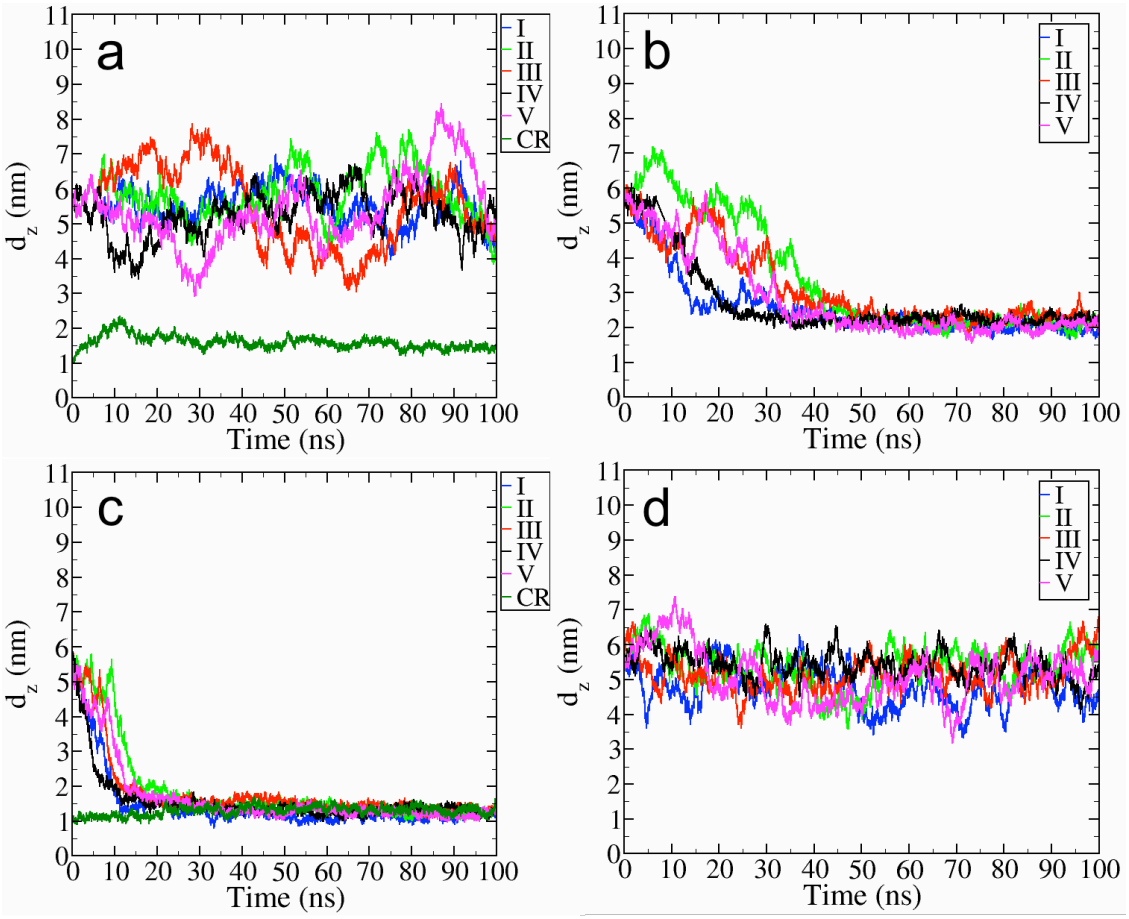

Figure 5.19: Distances between AuNP and the closest membrane surface phosphate group COMs along the z-axis of the box (bilayer surface normal) as a function of time in five repeated runs I-V for each system: (a) $AuNP^+$ in EC, (b) $AuNP^-$ in EC, (c) $AuNP^+$ in IC and (d) $AuNP^-$ in IC. Constraint-released simulations, CR, are drawn using green solid lines in the figures. The AuNP diameter is approximately 2 nm and in the figures the AuNP-membrane surface distance of 2 nm corresponds to a situation, where AuNP is attached to the bilayer surface and its terminal groups and membrane surface groups are in close contact.

The trends in hydrogen bonding and ion contacts in AuNP-membrane systems are similar to those for AuNPs in aqueous solution. Differences in AuNP-solvent

Table 5.3: Hydrogen bonds and ionic contacts between AuNPs and solvent/lipids. N_A is the average number of hydrogen bonds and contacts and τ_A is the average lifetime of the contacts, per solvent molecule/lipid. EC and IC are extracellular and intracellular compartments, respectively. C.R. refers to the EC constraint-released case.

Compartment	AuNP	A	N_A	τ_A [ps]
EC	$AuNP^+$	H_2O	169.7 ± 0.1	5.8 ± 0.2
		Cl^-	4.9 ± 0.2	5.5 ± 0.3
		lipid	–	–
EC	$AuNP^-$	H_2O	397.7 ± 1.6	4.7 ± 0.3
		Na^+	3.0 ± 0.3	9.8 ± 0.5
		lipid	5.0 ± 2.5	15.3 ± 2.2
EC (0.15 M NaCl)	$AuNP^+$	H_2O	169.7 ± 0.1	5.8 ± 0.1
		Cl^-	3.4 ± 0.2	5.0 ± 0.6
		lipid	–	–
EC (0.15 M NaCl)	$AuNP^-$	H_2O	399.4 ± 0.7	4.2 ± 0.2
		Na^+	3.6 ± 0.4	10.3 ± 1.9
		lipid	4.6 ± 0.5	15.3 ± 1.4
EC (C.R.)	$AuNP^+$	H_2O	138.6 ± 1.7	11.9 ± 0.7
		Cl^-	7.3 ± 0.3	8.0 ± 1.0
		lipid	18 ± 6	224.3 ± 42.7
IC	$AuNP^+$	H_2O	141.2 ± 3.7	10.3 ± 0.8
		Cl^-	1.4 ± 0.8	11.3 ± 2.5
		lipid	78 ± 12	99.9 ± 19.7
IC	$AuNP^-$	H_2O	371.1 ± 1.1	3.3 ± 0.1
		K^+	42.7 ± 1.2	20.9 ± 0.2
		lipid	–	–
IC (0.15 M KCl)	$AuNP^+$	H_2O	137.3 ± 4.1	9.5 ± 1.3
		Cl^-	3.6 ± 0.8	6.4 ± 1.4
		lipid	96 ± 12	102.6 ± 15.0

contacts between the two considered types of AuNPs were discussed already in detail in the case of AuNPs in aqueous solution (Chapter 5.1). The solvent orientation in presence of membranes (Figure 5.20) is similar to the data shown for the AuNP solutions (Figure 5.15). The average number and the lifetime of H-bonds and ion contacts between AuNP and solvent in the AuNP-membrane systems are presented in Table 5.3. The total number of H-bonds between water and AuNP in EC are 169.7 ± 0.1 and 397.7 ± 1.6, and in IC 141.2 ± 3.7 and 371.1 ± 1.1 for $AuNP^+$ and $AuNP^-$, respectively. For the same AuNPs in aqueous solution (in absence of bilayers), the values are 170.8 ± 0.2 and 404.4 ± 0.5 for $AuNP^+$ and $AuNP^-$, respectively (Table 5.1). In both EC and IC compartments, the values for the

number of contacts with water for $AuNP^-$ are over two times larger than for $AuNP^+$. As discussed in the case of AuNPs in aqueous solution, this is because carboxyl oxygens of COO^- terminal groups can form more H-bonds than the NH_3^+ terminal groups of $AuNP^+$.

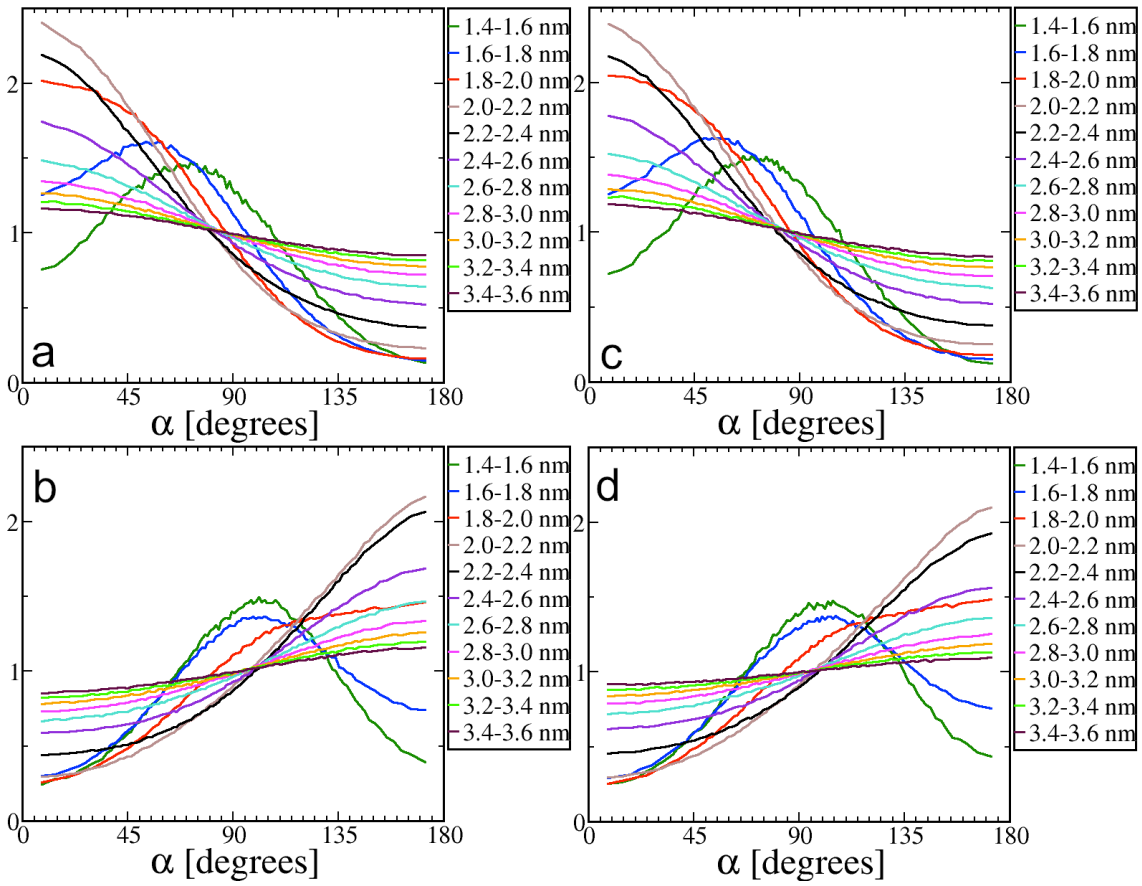

Figure 5.20: Distribution of water orientation for different distances from the AuNP center: (a) $AuNP^+$ in EC, (b) $AuNP^-$ in EC, (c) $AuNP^+$ in IC and (d) $AuNP^-$ in IC solution (with counter-ions and water). Orientation is characterized by the angle α, which is defined by a vector from the AuNP center to a water oxygen and a vector from this oxygen to a midpoint between two H atoms in the same H_2O molecule. If the two vectors are aligned pointing in the same direction, then the angle $\alpha = 0$. Solvent orientation is calculated for AuNP centered spherical shells of thickness $\Delta r = 0.2$ nm over the simulation time 50–200 ns.

The values of the number of contacts for AuNPs in EC compartment are close to the values of AuNPs in aqueous solution. In the case of $AuNP^+$ in IC, the values are smaller than those of AuNPs in aqueous solution (in the absence of membrane) and $AuNP^+$ in EC. In the IC compartment, $AuNP^+$ attaches to the membrane surface making contacts with lipids, and consequently, is able to form less contacts with water and counter-ions in IC than in EC where all the head groups are available

for water contacts. In contrast, the difference in the values between EC and IC for $AuNP^-$ are small. $AuNP^-$ approaches the membrane in EC, but since it is not embedding into the surface as $AuNP^+$, its ability to form contacts with water is not restricted by the presence of the membrane. The effect of membrane attachment and the subsequent decrease in the size of the solvent interface can be clearly seen also in the number of water contacts in the EC constraint-released case for $AuNP^+$ — the number of contacts for freely fluctuating $AuNP^+$ in EC, 169.7 ± 0.1, decreases to 138.6 ± 1.7 when the nanoparticle is attached to the membrane in the constraint-released simulation. The water contact lifetimes are considerably larger in the cases where $AuNP^+$ is bound to the membrane where the contacts are less interrupted and consequently last longer. Adding 150 mM salt into the EC and IC compartments does not affect the number of water contacts or contact lifetimes significantly.

The number of contacts with lipids goes together with the results of AuNP-membrane distance (Figure 5.19) and water contact analysis discussed above. The number of lipid contacts differs significantly for the two types of AuNPs and varies for the same AuNP depending on which leaflet (EC/IC) the nanoparticle is attached to, highlighting that the difference arises from the degree of attachment at the membrane surface. The number of contacts with lipids for $AuNP^-$ at EC leaflet are orders of magnitude smaller than those of $AuNP^+$ in EC and IC compartments (see Table 5.3). $AuNP^-$ is practically floating at the surface of the membrane, forming only a few short contacts with the lipids. This shows at the lipid contact lifetimes: The $AuNP^-$-EC leaflet lipid contacts last for 15 ps, while contacts between $AuNP^+$ and lipids have values ranging from 100 ps (IC) up to 224 ps (EC C.R.). Namely, $AuNP^-$ is relatively free to move at the membrane surface and its movement is not restricted by the interactions with the membrane, while $AuNP^+$ moves relatively slowly along the membrane surface. For $AuNP^+$ in IC, the number of lipid contacts is 78 ± 12 and it increases with added 150 mM KCl to 96 ± 12, while in the EC constraint-released case the value is 18 ± 6. These results indicate that when $AuNP^+$ is bound to the membrane, it is more stable at the IC leaflet in comparison to the EC side.

The average number and lifetime of ion contacts between AuNPs and solvent show

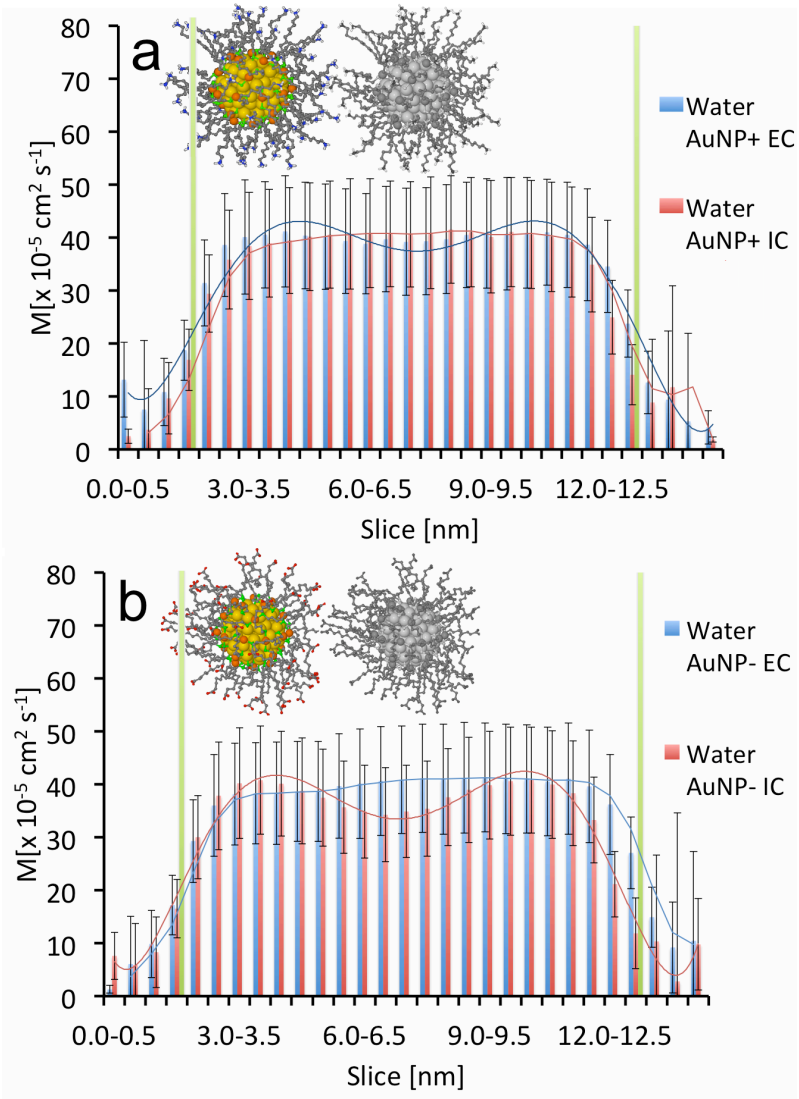

Figure 5.21: Water mobility in AuNP-membrane simulations. The mobility presented in (a) $AuNP^+$ and (b) $AuNP^-$ has been calculated for solvent molecules inside $\Delta r = 0.5$ nm slices along the membrane surface normal starting from the center of the membrane closer to the AuNP and ending at the surface of the other one for time windows of $\Delta t = 20$ ps and averaged over 10×1-ns trajectories. The EC and IC solution histograms are presented using blue and red colors, respectively. Green bars present the approximate positions of membrane leaflet surfaces. The mobility error is the standard average error. The colored nanoparticle z-position is similar to the case where the AuNP is attached to the membrane surface ($AuNP^+$ IC and $AuNP^-$ EC) and black-and-white nanoparticle position corresponds to the situation, in which AuNP is not attached to the membrane ($AuNP^+$-EC and $AuNP^-$-IC).

clear differences between the EC and IC compartments. The number of counter-ion contacts are 4.9 ± 0.2 and 3.0 ± 0.3 in EC, and 1.4 ± 0.8 and 42.7 ± 1.2 for $AuNP^+$ and $AuNP^-$ in IC, respectively. For AuNPs in aqueous solution (Table 5.1) the number of ion contacts were 4.7 ± 0.4 and 4.4 ± 0.4 for $AuNP^+$ and $AuNP^-$,

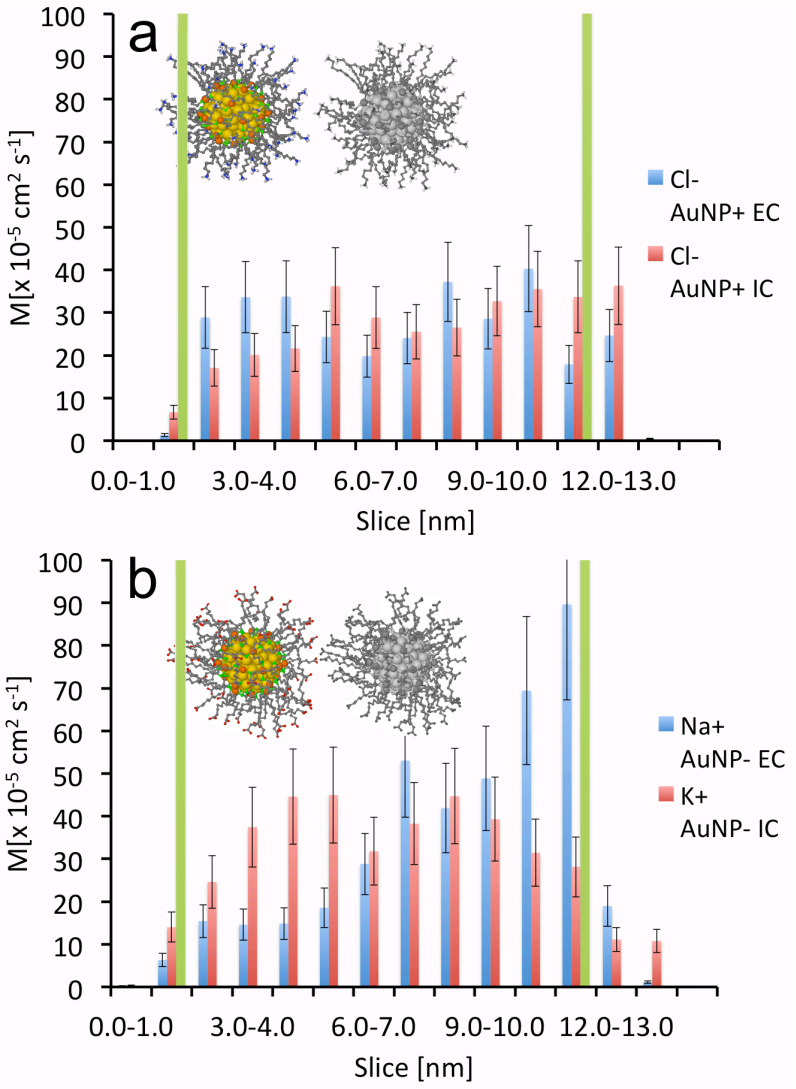

Figure 5.22: Counter-ion mobility in AuNP-membrane simulations. The mobility presented for counter-ions of (a) $AuNP^+$ and (b) $AuNP^-$ has been calculated for solvent ions inside $\Delta r = 0.5$ nm slices along box membrane surface normal starting from the center of the membrane closer to the AuNP and ending at the surface of the other one for time windows of $\Delta t = 20$ ps and averaged over 10×1-ns trajectories. The EC and IC solution histograms are presented using blue and red colors, respectively. Green bars present the approximative positions of membrane leaflet surfaces. The mobility error is the standard average error. The colored nanoparticle z-position is similar to the case where AuNP is attached to the membrane surface ($AuNP^+$ IC and $AuNP^-$ EC) and black-and-white nanoparticle position corresponds to the situation, in which AuNP is not attached to the membrane ($AuNP^+$-EC and $AuNP^-$-IC).

respectively. There is a significant difference in the number of ion contacts for $AuNP^-$ between EC and IC, arising from the increased counter-ion concentration in IC: 3.0 ± 0.3 for Na^+ in EC and 42.7 ± 1.2 for K^+ in IC. The positively charged counter-ions of POPS lipids ($48\,K^+$) and $AuNP^-$ ($60\,K^+$) are both present at the IC

compartment, whereas in the EC compartment there are only the counter-ions of $AuNP^-$ ($60\,Na^+$). The high concentration of counter-ions affects the lifetimes of the contacts, as well, doubling the lifetime values as the repulsive ion-ion interactions stabilize the AuNP-ion contacts together with the AuNP-membrane repulsion, which was observed to restrict the AuNP fluctuation along the membrane surface normal direction in the AuNP-membrane distance analysis. The increase in the number of $AuNP^-$-ion contacts in IC results in the decreased values of the water contacts and their lifetimes compared to the EC compartment — counter-ions occupy terminal groups preventing water molecules from H-bonding and disturb the formed H-bonds. The numbers of ion contacts for $AuNP^+$ do not differ considerably between aqueous solution and EC, as expected, since in both cases $AuNP^+$ fluctuates freely in the solvent.

In contrast, there is a noticeable difference in the number of ion contacts for $AuNP^-$, which approaches the membrane in EC: The number of ion contacts is 47% larger in aqueous solution than in EC. The same phenomenon occurs for $AuNP^+$ in IC, amplified: The number of ion contacts in IC is more than two times larger than in aqueous solution in the absence of bilayers despite the ionic cloud around the nanoparticle (see Figure 6.1). When the AuNP is in contact with the bilayer, it has less available terminal groups to make contacts with counter-ions. This is reflected in the contact lifetimes, as well, which are larger in the cases where the AuNPs are attached to the membrane. As in the case of H-bonds with water, the ion contacts are less disturbed, resulting in higher contact lifetime values. The role of counter-ions will be summarized in Chapter 6.2

The results of mobility calculations for water and ions are shown in Figures 5.21 and 5.22. The mobility of solvent molecules in the AuNP-membrane simulations was calculated as short-time diffusion factors of water molecules and counter-ions inside 0.5 nm thick slices along the membrane surface normal starting at the AuNP-closest leaflet across the box and ending at the other one for time windows of $\Delta t = 20$ ps averaging over 10×1-ns trajectories. The results show clearly that the solvent mobility is reduced both close to the membrane surfaces and in the AuNP surroundings. Water forms an H-bond network around the terminal groups of AuNPs (with

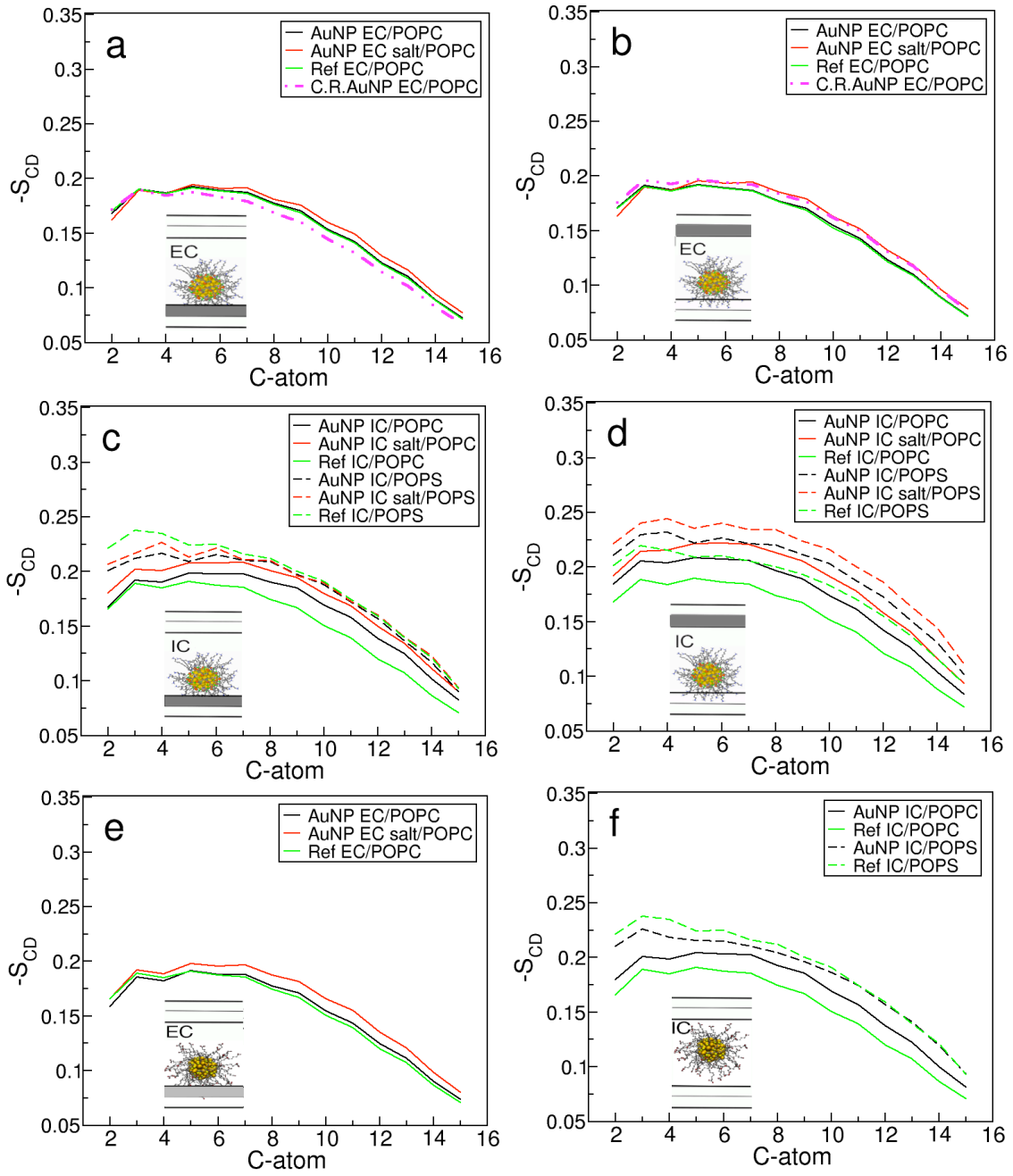

Figure 5.23: Order parameters of membrane in the presence/absence of AuNP. $AuNP^{+}$ simulations: (a) Closest membrane at EC: POPCs of the closest extracellular leaflet; (b) farther membrane at EC: POPCs of the extracellular leaflet; (c) closest membrane at IC: POPCs and POPSs of the closest cytosolic leaflet and (d) farther membrane at IC: POPCs and POPSs of the cytosolic leaflet. $AuNP^{-}$ simulations: (e) Closest membrane at EC: POPCs of the closest extracellular leaflet, and (f) closest membrane at IC: POPCs and POPSs of the closest cytosolic leaflet. Order parameters in the AuNP system without added salt, AuNP system with added salt, and reference system are drawn using black, red and green colors, respectively. POPC lipids are drawn using solid lines and POPS lipids using dashed lines. Constraint-released (C.R.) simulation is drawn using dashed magenta line. Parameters were calculated for 150-ns simulations after skipping 50 ns for equilibration. Each extracellular leaflet contains 124 POPC lipids, and the cytosolic leaflets are mixtures of 104 POPC and 24 POPS lipids, each.

counter-ions, see Figure 5.13), and this makes the water molecule positions more restricted close to the nanoparticle. The same effect is also visible for the counter-ions. For water, the change in mobility as a function of distance is smaller than for counter-ions. This can be explained by the type of bonds/contacts that water and ions form with AuNPs: H-bonds between the terminal groups and water are weaker and of shorter range than the electrostatic interactions between AuNP and counter-ions. At the membrane surface, the mobility of solvent molecules reduces because of contacts with charged lipid head groups. AuNP-membrane binding results in an increase in mobility at the opposite membrane surface, highlighting the fact that the AuNP movement is reflected throughout the whole compartment and not just the leaflet it is attached to, also in terms of the dynamics.

The AuNP-membrane interactions discussed above are reflected in the order parameters of lipids, as well, shown in Figure 5.23. The results for $AuNP^+$ and $AuNP^-$ are presented in Figures 5.23(a-d) and 5.23(e-f), respectively. AuNP-induced perturbations in the membrane structure were determined by considering changes in the lipid hydrocarbon chain order parameter, S_{CD}. The order parameters for the saturated palmitoyl tail (*sn*-1) of both POPC and POPS were calculated for both leaflets sharing the compartment with AuNP and compared with the reference system without AuNPs. The oleoyl (*sn*-2) tail provided qualitatively the same information. The order parameters of the bilayer lipids were calculated using the angle between bilayer surface normal and two lipid carbon palmitoyl tail atoms C_{n-1} and C_{n+1} as in Equation (3.45).

The order parameter profiles show that $AuNP^+$ in IC induces increasing order for POPC (Figure 5.23(c)), and also that adding 150 mM KCl increases the ordering further. The ordering effects of $AuNP^+$ in IC on POPC and POPS depend on the region considered. In the contact layer $AuNP^+$ induces clear ordering in POPC alkyl chains, while POPS lipids actually become slightly disordered close to the head groups (Figure 5.23(c)). The underlying reason for this is the interdigitation of the $AuNP^+$ side chains in the contact layer, especially with POPS accumulated underneath the nanoparticle. In the opposite layer that is farther from the nanoparticle, the ordering was observed to take place when $AuNP^+$ is present, and this effect is

amplified with added salt (Figure 5.23(d)). This phenomenon was concluded to arise from the increased concentration of K^+ ions at the membrane surface surroundings [152, 153]. The results also show that $AuNP^+$ affects the POPC order only slightly on the EC side (Figure 5.23(a)). Only for the constraint-released case, where $AuNP^+$ is in direct contact with the leaflet, a small effect can be observed (Figure 5.23(a)).

In the case of $AuNP^-$ in EC (Figure 5.23(e)), the POPC order parameter is largely the same regardless of the presence of AuNP. With added 150 mM of NaCl, the order parameter increases about $5-10\,\%$ compared to the reference system, but this is likely due to monovalent salt that is known to decrease the area per lipid in the membrane, thereby increasing membrane order, and stems from salt ion-induced lipid clustering [152, 154, 155]. In the IC compartment without additional salt (Figure 5.23(f)), the results show that the ordering of POPCs increases and the ordering of POPS lipids decreases due to the presence of $AuNP^-$. It was concluded that the repulsive interactions between $AuNP^-$ and POPS result in lateral lipid reorganization, since POPS lipids are displaced nearby $AuNP^-$, making room for a POPC-rich lipid region right underneath the nanoparticle.

6. DISCUSSION

6.1 Water-Mediated Effects in AuNP-Solutions Are Long-Ranged

The first part of this work concentrated on studying charged gold nanoparticles in aqueous solution with counter-ions. Cationic and anionic AuNPs were modeled with amine (NH_3^+) and carboxyl (COO^-) terminal groups and Na^+/Cl^- counter-ions, respectively. The comparison of properties of the AuNPs revealed both differences and similarities in their behavior in aqueous environment. For the two systems, RDFs (Figure 5.1) were found to be rather similar. The side chains and terminal groups showed significant flexibility and the water/counter-ion profiles had the same characteristics. However, the distance distributions of terminal groups (Figure 5.2) showed that the NH_3^+-terminated alkyl thiols displayed a wider range of fluctuations with respect to each other (Figure 5.3), and the atomic configurations (water/counter-ions) were significantly different around the NH_3^+ and COO^- terminal groups. The orientation of water was observed to be distinct for both AuNPs in the first solvation shell (Figures 5.13 and 5.15), and the AuNPs clearly caused a long-range effect in the solvent structure. This effect was particularly strong for counter-ions, emphasizing the importance of long-range electrostatic interactions in the systems.

The radial electrostatic potential profiles (Figures 5.7 and 5.8) displayed a minimum for $AuNP^-$ at about 2.0 nm from the AuNP center, marking a preferable location for Na^+, while the electrostatic potential of $AuNP^+$ rose almost monotonically and attracted Cl^- further inside. However, other factors (such as reduced water concentration and larger ionic radius) exhibit Cl^- from entering inside $AuNP^+$. Despite its larger atomic mass, the self-diffusion coefficient of Cl^- was about 20 % larger than that of Na^+, which is related to the details in ionic bonding with the termi-

nal carboxylate/amine groups (reduced life time for Cl^- contacts). The short-time diffusion analysis around AuNPs revealed that the solvent diffusion is slower near AuNP due to H-bonds and ionic contacts with the terminal groups, and that the effect extends over 3 nm from the AuNP surface because of several solvation shells that transmit the effect.

The data of counter-ion distributions was is in good agreement with the Debye-Hückel theory [131, 135] (Figure 5.11). The interface between AuNP-bound and loosely associated counter-ions was observed to be around 2.4 nm from the AuNP-COM, and a fit to the ion density distributions at distances larger than this one resulted in values of 0.27 and 0.20 nm for the Debye length in $AuNP^+$ and $AuNP^-$, respectively. The Debye lengths are small, and about an order of magnitude smaller than the AuNP size, allowing to use the Smoluchowski theory [123, 131, 134] for zeta potential determination. The magnitudes of zeta potentials were determined to be of approximately 26 mV for $AuNP^+$ and -59 mV for $AuNP^-$ (Figure 5.12). The difference in zeta potential implies that cationic and anionic AuNPs respond to an external field with different strengths. Furthermore, even if our assumption of the location of the interface was partly inaccurate, it can still be concluded that the zeta potential in the present systems without salt is approximately 25 mV, or larger than this value, which is often considered as a threshold value for coagulation/aggregation. Furthermore, if there was added salt present, the Debye length would decrease for increasing ion concentration, which would show up as an increase in the zeta potential (see Figure 5.12). Recent experimental data by Verma *et al.* [53] for gold nanoparticles protected by a number of different organic ligands is in agreement with this view, since they found the (absolute value of) zeta potential to vary between 31–38 mV. Hence, the results imply that the AuNPs of this type do not coagulate.

The self-diffusion coefficients of the AuNPs were around 1×10^{-6} cm^2 s^{-1}. These values are comparable with experimental values (range $\sim 10^{-6}$ cm^2 s^{-1}) of MPC AuNPs of size $\sim$ 1–5 nm in water [156]. The solvent diffusion is slower near AuNPs, and Cl^- is more mobile than Na^+, which is related to the details in ionic/hydrogen bonding with the terminal carboxylate/amine groups. The results highlight the im-

portance of long-range electrostatic interactions in determining nanoparticle properties in aqueous solutions. They suggest that electrostatics is one of the central factors in complexation of AuNPs with other nanomaterials and biological systems, and that effects of electrostatics as water-mediated interactions are relatively long-ranged.

The results highlight the importance of electrostatics and the nanoparticle-solvent interface in determining the properties of AuNPs considered in this work and provide a great deal of insight into the properties of charged and functionalized NPs in aqueous surroundings. Considering that the model used in this work is particularly realistic and is in agreement with a wide range of experiments, its predictions for AuNPs are expected to be highly useful in follow-up considerations of NP effects on biological systems.

The outcome of studying AuNPs in aqueous solution shows that NPs of this type cannot be considered as distinct bodies, but on the contrary, due to long-range interactions they form complexes together with the ions and solvent molecules surrounding them. This implies that in NP solutions, there are interactions between the nanoparticles due to the ordering effects of water and ions around the NPs, which give rise to long-range solvent-mediated interactions that complement those due to hydrodynamics (conservation of momentum). Based on the results, the characteristic length over which charged AuNPs affects biological molecules or complexes in terms of water-mediated interactions may extend up to 10 nm.

6.2 AuNP-Membrane Interface

To study the AuNP-membrane interactions, several model systems were built placing the AuNPs in extracellular (EC) and cytosolic/intracellular (IC) compartments, with and without salt (see Figure 4.4 and Table 4.1). The extracellular (EC) and intracellular/cytosolic (IC) environments were modeled using asymmetric bilayers with lipid compositions resembling eukaryotic plasma membranes with different ion compositions in each compartment. The outer EC leaflet consisted of zwitterionic POPC lipids, and lipid composition of the inner IC leaflet was a mixture of POPC (81.25%) and negatively charged POPS (18.75%). AuNPs with counter-ions were

placed in either the EC or IC compartment. The negative charge of POPS was compensated by including additional K^+ ions in the IC compartment. Simulations were performed also with added salt by placing 150 mM of NaCl and KCl in the EC and IC compartments, respectively. Systems were simulated for extensive periods up to 200 ns at physiological temperature, 310 K.

The results show a distinguishable difference in the behavior of the cationic and anionic AuNP in the presence of membranes. $AuNP^+$ approaches the membrane in the IC compartment within $10 - 20$ ns in simulations with and without added salt and attaches rapidly to the membrane in a manner where the functional amine groups are in contact with the membrane surface (Figure 5.19(c)), whereas in the EC compartment $AuNP^+$ fluctuates between the bilayers and does not approach or form direct contacts with the membrane in the time scale of simulations with or without added salt (Figure 5.19(a)). The behavior is opposite to $AuNP^-$, which approaches the membrane in the EC compartment (Figure 5.19(b)), while in the IC compartment $AuNP^-$ stays in between the membranes, not forming contacts with the membrane (Figure 5.19(d)). In the cases where AuNPs approach the surface, $AuNP^+$ binds tighter to the IC leaflet than $AuNP^-$ binds at the EC leaflet. Four shorter 100-ns simulation replicas were performed to validate the results, for systems without extra salt and with arbitrary initial velocities, and they provided the same outcome.

The fact that $AuNP^-$ binds to the EC leaflet of a negatively charged membrane and $AuNP^+$ does not, is interesting. At the EC leaflet, $AuNP^-$ feels the attractive force of positively charged POPC lipid head groups (with a positive choline group pointing towards the aqueous region), whereas for $AuNP^+$ these same head groups form a potential barrier. These lipid head groups effectively create a positively charged layer to the membrane surface, inducing an attractive interaction with $AuNP^-$ and repulsive with $AuNP^+$. The zwitterionic POPC lipids of the EC leaflet are neutral and the negatively charged POPS lipids are at the IC leaflet. This makes it possible for $AuNP^-$ to attach the membrane at the EC side, even though the net charge of the membrane is negative. The role of solvent molecules and ions in the binding process is, of course, meaningful and will be discussed in the following.

In contrast to the findings of the EC simulations, it is more obvious what happens in the IC compartment. There is a strong electrostatic force driving $AuNP^+$ towards the surface of the IC leaflet and its negatively charged POPS lipids, while $AuNP^-$ feels repulsive force acting between objects of the same charge.

The partial density profiles show that $AuNP^+$ forms a stable contact with the membrane in IC (Figures 5.16(a-b)). The Cl^- counter-ions screen $AuNP^+$ but do not inhibit binding to the IC leaflet. The profiles show a broader distribution for $AuNP^+$ in EC (Figures 5.16(c-d)), since it fluctuates between the membranes. In EC, $AuNP^-$ approaches the membrane surface (Figures 5.16(f-g)), whereas in IC it stays around the center of the compartment (Figure 5.16(h)). Each case shows an ionic cloud of counter-ions around AuNPs, screening their charge.

The halo-pattern of counter-ions is highlighted in Figure 6.1, where the counter-ion concentration has been visualized for the EC and IC cases. The distribution of Cl^- counter-ions of $AuNP^+$ in the IC compartment is not as symmetric as in EC, since the ion concentration has been reduced in the membrane contact area. The K^+ ions have accumulated close to the opposite membrane surface with respect to $AuNP^+$ in the IC compartment, and the net negative charge of the cytosolic leaflet is more exposed to the nanoparticle. The source of the observed K^+ asymmetry is the overcharging effect caused by the high surface charge density of $AuNP^+$. For $AuNP^+$ in IC, the limited number of contacts of Cl^- with the membrane, and in particular with POPS lipids, becomes evident despite the fact that there are also K^+ ions around. As expected, there are no Cl^- counter-ions between the nanoparticle and the membrane as the negative charge of POPS causes repulsion.

In the case of $AuNP^-$ in IC, there are only K^+ counter-ions present, and the counter-ions are distributed both at the $AuNP^-$ and membrane surroundings. The tight space between the thiol chains of AuNPs together with a less hydrated environment makes it difficult for the relatively voluminous counter-ions to penetrate into the surface region of AuNPs, allowing the nanoparticle surface to behave effectively as a charged wall. The terminal groups of AuNPs are distributed in somewhat equidistant positions, which causes fluctuation in the counter-ion concentration. The surface charge density of the AuNP is not large enough to fully condense the

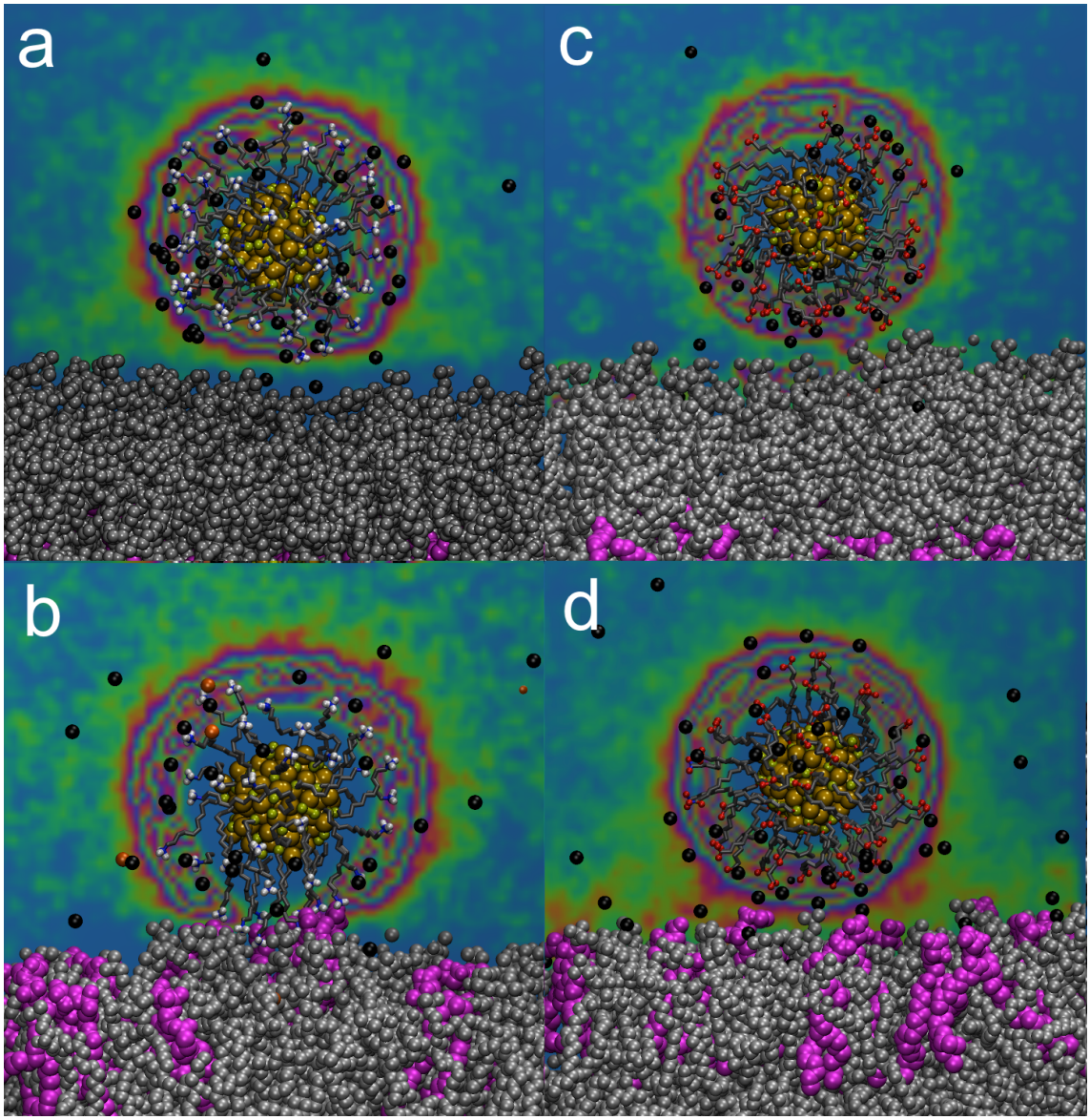

Figure 6.1: Visualization of AuNPs and counter-ions: (a) $AuNP^+$ and Cl^- in EC, (b) $AuNP^+$ and Cl^- in IC, (c) $AuNP^-$ and Na^+ in EC and (d) $AuNP^-$ and K^+ in IC compartments. Distance between the center of the nanoparticle and the headgroups of the POPC of the nearest leaflet has been fixed to 2.8 nm in all cases. The counter-ion concentration are averaged over 60 ns simulations. Color code: counter-ions, black; other ions, orange; POPS lipids, magenta.

counter-ions to the surface. This is expected as both counter-ions and terminal groups are monovalent and relatively small [157]. Under these conditions, and in agreement with the Gouy-Chapman model [131–133], one expects the formation of a diffuse ionic cloud around the AuNPs, and this is clearly visible in the partial density profiles of counter-ions.

In order to discuss the stability of the AuNP contacts at the membrane interface,

consideration of the interaction of AuNP with water, lipids, and ions is of importance. The topic is largely related to hydrogen bonding at atomic resolution and electrostatic interactions. The average number and the lifetime of H-bonds and ion contacts between $AuNP^-$ and solvent (Table 5.3) showed small differences between the EC and IC solutions: The total number of H-bonds between $AuNP^-$ terminal carboxylate groups and water was reduced from 397.7 ± 1.6 to 371.1 ± 1.1 by a change from EC to IC, and the corresponding lifetimes decrease similarly from 4.7 ± 0.3 ps to 3.3 ± 0.1 ps. Longer H-bond lifetime values for water in EC can be explained by the $AuNP^-$-membrane interactions: The movement of $AuNP^-$ is restricted in EC due to the membrane attachment, and this causes its water solvation shell to be less interrupted, and consequently, the H-bonds live longer. Furthermore, the water mobility itself is reduced close to the membrane surface.

The number of ion contacts differed by an order of magnitude between EC and IC: 3.0 ± 0.3 for Na^+ in EC and 42.7 ± 1.2 for K^+ in IC. The difference is partially explained by the fact that there were K^+ counter-ions present for both POPS lipids and $AuNP^-$ in the IC compartment. The ion contact lifetimes in IC were twice the lifetimes in EC, which is presumably related to the number of counter-ions in the solution and repulsive ion-ion interactions in the $AuNP^-$ surroundings.

The counter-ion concentration affects the H-bonds as well, and the number of H-bonds with water is smaller in IC than in EC as the numerous contacts with ions diminish the number of H-bonds between the $AuNP^-$ terminal groups and water. For EC, the number of Na^+ ion contacts and lifetimes were similar to those observed for the same $AuNP^-$ in an aqueous solution without the presence of bilayers, 4.4 ± 0.4 and 10.1 ± 1.1 ps (Table 5.1). The same applied for H-bonds where the corresponding values were 404.4 ± 0.5 and 3.5 ± 0.1 ps in an aqueous environment.

The results of $AuNP^-$-lipid contacts showed rather short lifetimes, approximately 15 ps, which indicate that $AuNP^-$ diffuses relatively freely along the membrane surface. Small values for the membrane contacts indicate that $AuNP^-$ remains close to the surface of the EC leaflet, not penetrating deeply inside the membrane, since it feels the electrostatic repulsive force caused by the negatively charged POPS lipids in the cytosolic leaflet. Concerning the number of water-membrane contacts,

there were more of those in the IC compartment where $AuNP^-$ is not attached, as this leaves more lipid surface groups exposed to the water solvent.

Hydrogen bonding shows binding of $AuNP^+$ with the IC leaflet to be more stable than with the EC leaflet. The average number and the lifetime of hydrogen bonds (H-bonds) and ion contacts between $AuNP^+$ and solvent (Table 5.3) showed clear differences between the IC and EC solutions: The total number of H-bonds between water and $AuNP^+$ were 141.2 $\pm$3.7 and 169.7 $\pm$0.1, respectively, and also the number of ion contacts differs, 1.4 $\pm$0.8. and 4.9 $\pm$0.2. The number of water contacts is close to three per amine group in EC, as expected, but the number of direct ion contacts is relatively small despite the counter-ion cloud around the nanoparticle (see Figure 6.1). $AuNP^+$ attaches to the cytosolic leaflet in IC, and hence it has less available terminal groups to make contacts with water and/or counter-ions. This is reflected not only in the number of H-bonds but also in contact lifetimes, which were considerably larger in IC. $AuNP^+$ moves freely in EC, whereas its movement is restricted in IC by the interactions with the membrane — the contacts are less interrupted, and consequently, last longer.

For the EC compartment, the values of the number of contacts and lifetimes were similar to those of the same $AuNP^+$ in aqueous solution without the presence of bilayers, 170.8$\pm$0.2 and 6.5 $\pm$0.2 ps, for water and counter-ions, respectively (see Table 5.1). The situation changes in EC when $AuNP^+$ is pulled onto the POPC leaflet (constraint-released case). The interaction with water has decreased as the effective solvent interface of $AuNP^+$ is smaller, whereas the number of Cl^- contacts is larger reflecting changes in the dielectric medium (water/membrane) and $AuNP^+$ screening charge. Comparing with the IC case, Cl^- contact values are significantly higher, corresponding to a tighter Cl^- cloud around $AuNP^+$ in the EC constraint-released system. The AuNP-membrane contacts were numerous due to the $NH_3{}^+$ terminal groups, and their lifetimes were of the order 100 ps, illustrating that the AuNP moves relatively slowly along the membrane surface. Despite being attached to the membrane, there are not many H-bonds forming between $AuNP^+$ and the lipid head groups.

Summarizing, the analysis based on H-bonding and contacts indicates that when

AuNP$^+$ is bound to a membrane, it is more stable at the IC side compared to the EC leaflet. Despite the fact that AuNP$^-$ formed contacts with the membrane in EC, it was still able to fluctuatate relatively freely along the membrane surface. In the IC compartment, the high counter-ion concentration together with POPS repulsion restricted AuNP$^-$ to the compartment center. Adding 150 mM of salt (KCl, NaCl) to the systems did not significantly affect the H-bonds between AuNPs and solvent.

6.3 Why No Spontaneous Permeation for AuNP$^+$?

The findings that AuNP$^+$ did not bind spontaneously to the EC leaflet are something one would not expect. The membrane is negatively charged, and spontaneous binding of cationic nanoparticles can be seen in the experiments. The results discussed above do not seem to support the current experimental evidence that AuNP$^+$ outside a cell could spontaneously reach the cytoplasmic region [51, 55, 58, 158–160], or self-penetrate to a cell [63], since in the EC compartment AuNP$^+$ resists the formation of a contact with the membrane. As discussed above, the barrier was concluded to arise from the positive charged layer at the membrane surface created by the POPC lipid head groups. The results of free-energy calculation showed a free-energy barrier of about 11.7 kJ/mol (4.7 $k_B T$) for the binding of AuNP$^+$ to the EC leaflet and that once the barrier is crossed, the AuNP is stably bound to the EC leaflet at the membrane-water interface, about 1.7 nm from the membrane surface plane, with a well depth of about -18.3 kJ/mol (-7.4 $k_B T$) in the unbound case. These values are comparable to thermal fluctuations of few $k_B T$.

The results of free-energy calculation are in agreement with recent experimental findings of Tatur *et al.* [63]. These evidence on pure synthetic DSPC membranes suggested that there is a free-energy barrier for approaching AuNP$^+$. In these experiments, the temperature of the model system had to be risen up to 326 K in order to activate AuNP$^+$ to bind with the membrane. Experiments also showed that subsequent cooling down of the sample to a working temperature of 298 K did not terminate the binding. This suggests that once the free-energy barrier has been crossed, there is a net attraction between AuNP$^+$ and the membrane. Similarly, the MD simulations presented here highlight the presence of a free-energy barrier when

$AuNP^+$ approaches the EC leaflet comprised of POPC lipids.

Why spontaneous permeation was not observed in the simulations? It is clear that this is, in part, due to the high charge of $AuNP^+$ studied here. Regardless of the environment, $AuNP^+$ is always equally charged (+60 e). A more realistic model to consider penetration would include deprotonation of the amine groups while $AuNP^+$ passes through the low dielectric lipid tail region. Based on earlier simulations it is clear that neutralization of the nanoparticle would strongly promote permeation across the membrane [161]. The substantial charge of the nanoparticle is a seemingly simple reason to explain why no translocation was observed in simulations. This view is supported by the fact that in experiments the coverage of positively charged alkyl chains rarely exceeds 70%, in contrast to 100% of present work. Also the terminal choline terminal groups of the experiments are significantly more bulky than the small amine groups of the model presented here, and the positive charge is more delocalized. However, according to experimental results, also cationic AuNPs with terminal (choline) group,s which cannot deprotonate have proven to be capable of trespassing the membrane [63]. Therefore, deprotonation of the amine groups can explain the experimentally observed translocation rate only partially.

As for methodological matters related to simulations only, the use of the double bilayer setup hampers the penetration process as the lateral dimensions of the two membranes are coupled to each other via the simulation box and the periodic boundary conditions used (lateral strain). These imply that in the simulations presented here, the bilayer through which the nanoparticle is translocating is not in a tensionless state, as it should be, and the tension arising from the use of the double bilayer setup will certainly increase the translocation free-energy barrier. This issue could be minimized by using membrane systems much larger than the one employed in this work. It should be noted that recent coarse-grained simulations using a double bilayer model (1032 lipids per membrane) achieved $AuNP^+$ translocation by using an external electric field of -1.5 eV, mimicking the transmembrane potential [70], in favour of the views discussed here.

6.4 AuNP$^-$ Appears to Have Less Effect on Membranes

Based on the results presented here, AuNP$^-$ appears to have less effect on membranes. It was observed that AuNP$^-$ attaches to the EC leaflet, but the interaction mediated by hydrogen bonds is rather weak and does not lead to nanoparticle immersion to the membrane, thus also structural perturbations of the membrane remained limited. AuNP$^-$ floats on top of the EC leaflet, diffusing laterally along the membrane surface plane. Spontaneous desorption of the nanoparticle back to the water phase was not observed in the simulation, indicating that there is a considerably deep free-energy barrier at the membrane-water interface region. However, AuNP$^-$ was found to alter some of the structural and dynamical properties of the membrane.

In the IC compartment, AuNP$^-$ did not bind to the membrane due to the repulsive interaction with the negatively charged POPS lipids. The results are in agreement with recent experiments [63]. Anionic AuNPs seem to have less effect on membranes than cationic AuNPs. In neutron reflectometry measurements, cationic AuNPs penetrated into membrane interior, causing disruption at increased concentrations, but no such effect was observed for anionic AuNPs, which stayed outside the lipid bilayers [63]. However, recently, it was also demonstrated that anionic striped AuNPs, which comprise an amphiphilic surface, can permeate non-disruptively through model membranes with size-dependent activity [62]. One of the next steps from here would be performing detailed simulations with anionic AuNPs with altered surface structure.

6.5 Potential Mechanism for AuNP$^+$ Translocation

Having confirmed the activated binding on the EC side, AuNP$^+$ was gradually pulled closer to the membrane using a harmonic potential. Once in contact, 0.9 nm from AuNP$^+$ COM to the membrane surface, the constraint was released and the system was simulated for 300 ns. During this "EC constraint-released" 300-ns simulation, AuNP$^+$ remained attached to the membrane (as seen in the corresponding partial density profile over the last 150 ns, Figure 5.16(e)). It was now observed that AuNP$^+$ binds to the extracellular leaflet once the free-energy barrier has been overcome, and the binding is stable and suggestive of pore formation. Furthermore, AuNP$^+$

attaches to both IC (mixture of POPC/POPS) and EC (pure POPC) layers, the latter being an activated process.

Comparing the contact areas between $AuNP^+$ and each of the two layers it is attached to, revealed a convex bending towards $AuNP^+$ in IC, and a minor concave deformation at the EC leaflet. On the IC side, the contact layer shows slightly convex bending towards $AuNP^+$, allowing the system to maximize the number of POPS-$AuNP^+$ contacts. $AuNP^+$ then floats over the membrane surface with occasional but clear interdigitation between the $AuNP^+$ side chains and lipid head groups. The convex deformation on the IC side is caused by the energetically favorable POPS-$AuNP^+$ contact. Using such deformation topology, the system can maximize the POPS-$AuNP^+$ contacts. In the IC leaflet, the average equilibrium distance between the $AuNP^+$-COM and the POPC/POPS leaflet (phosphorous atom in POPC) is 1.4±0.2 nm and at this distance $AuNP^+$ seems to float and roll just on top of the surface. If a positive side chain of $AuNP^+$ manages to cross the positively charged POPC choline region with the help of the negatively charged POPS groups, it immediately becomes trapped deeper in the membrane due to the attraction of the underlying negatively charged region of the phosphate groups. However, it was found that $AuNP^+$ does not considerably perturb the contact leaflet, besides slowly recruiting POPS lipids underneath itself.

In the EC compartment, while having a larger separation distance than in IC, the nanoparticle appears to be embedded deeper in the induced concave curvature of the underlying layer. The concave deformation in the EC is largely due to the dense packing of POPC head groups around the immersed $AuNP^+$. This slight deformation allows the system to reduce the repulsion between head groups around $AuNP^+$, without exposing the hydrophobic membrane acyl chains to the water solvent. $AuNP^+$ positions itself partly embedded in the pure POPC layer at a distance of 1.6±0.2 nm (phosphorous atom in POPC). In this case no side chain interdigitation is observed, and the lipid head groups are clearly pushed away underneath $AuNP^+$. Similarly, the facing $AuNP^+$ side chains bend towards the membrane plane, maximizing the number of contacts with the ring of the negatively charged phosphate groups. This ring emerges because phosphatidylcholine groups strongly orient

themselves, with the phosphates pointing towards $AuNP^+$.

Based on the results, a potential mechanism for $AuNP^+$ translocation is being suggested as follows. In the EC system, not a single $AuNP^+$ side chain points towards the hydrophobic lipid core area of the membrane, and this could be a favourable initial stage for self-penetration. The fact that $AuNP^+$ manages to isolate its charged side groups from the hydrophobic (low dielectric constant) lipid tail groups allows it to move across the membrane without a large energy penalty. The lipids in contact with $AuNP^+$ can bend towards the membrane plane as $AuNP^+$ passes through the membrane, forming a pore. Recently reported coarse-grained simulations of $AuNP^+$s in symmetric bilayers are in favour of this view, suggesting the formation of torus-like pores [70]. In the present case, in the absence of an artificially created electrostatic potential, the driving force pulling $AuNP^+$ into the membrane is the electrostatic attraction from the negatively charged POPS lipids on the IC side, and the described mechanism should evolve until $AuNP^+$ is fully embedded in the membrane. There are studies showing that the translocation of drugs and other charged compounds across lipid membranes has a very high free-energy barrier that is lowered substantially through neutralization [161]. Hence, it was concluded that to undergo the translocation process, $AuNP^+$ has to at least partly neutralize/deprotonate. Even though the observations are consistent with the formation of holes [43] observed in toxicity experiments [51, 55, 58, 158–160], they are not fully conclusive as no $AuNP^+$ penetration was observed during the simulations. This is due in part to the high charge concentration of the nanoparticle, +60 e, as well as the geometrical constrains inherent to the double bilayer setup used in the simulations.

Structural changes at the EC and IC leaflets are consistent with the proposed mechanism. All the order parameter profiles showed that on the IC side, $AuNP^+$ induces rather substantial increasing order for POPC (Figure 5.23(a)). Increasing the salt concentration to match the biological condition (150 mM) increases the ordering further. The results also show that $AuNP^+$ affects the POPC order only slightly on the EC leaflet (Figure 5.23(c)). Only for the constraint-released case where the nanoparticle is in direct contact with the leaflet, a small effect can be ob-

served (Figure 5.23(a)). For the IC compartment, the ordering effects of $AuNP^+$ and salt are significantly amplified for both POPC and POPS, but the effect depends on the region considered. In the contact layer $AuNP^+$ induces clear ordering in POPC alkyl chains, while POPS lipids actually become slightly disordered close to the head groups (Figure 5.23(c)). The underlying reason for this is the interdigitation of the $AuNP^+$ side chains in the contact layer, especially with POPS accumulated beneath the nanoparticle. In the opposite layer that is farther from the nanoparticle, the ordering was observed to take place when $AuNP^+$ is present, and this effect is amplified with added salt (Figure 5.23(d)). The increased K^+ concentration (see Figure 5.16(a)) close to the membrane causes this phenomenon [152, 153].

The results are in agreement with the self-penetration mechanism. When $AuNP^+$ approaches the EC leaflet, the high fluidity of the lipid layer remains unaffected, and this allows quick reordering of the lipids to form a hole around $AuNP^+$ [51, 55, 58, 158–160]. Instead, on the IC side the ordering increases in the contact layer, rendering this layer more impermeable. Based on this finding and the attractive electrostatic interaction, one should expect $AuNP^+$ accumulation on the cytosolic layer.

6.6 Concluding Remarks for $AuNP^+$-Membrane Interactions

All simulations show that electrostatics drives $AuNP^+$ to move fast towards the negatively charged surface of the cytosolic leaflet, while it experiences a free-energy barrier to bind with the extracellular leaflet, in agreement with experiments [63]. These results are understandable, considering the opposite overall surface charge in the two leaflets. While the surface charge in the IC leaflet is dominated by the negative charge of the POPS head group (20% of the lipids in the leaflet), in the case of the EC leaflet constituted by pure zwitterionic POPC, there is a local positive surface charge due to the positively charged choline groups facing water solvent. In other words, the distinct behavior, selectivity, arises from the specific lipid composition of each leaflet.

The results also highlight the active role of ions regulating the binding with a membrane. The counter-ions not only play a critical role by shielding the large

charge of $AuNP^+$ during the transit to the membrane, but they also foster the process by migration to compensate for electrostatic potential imbalances. The role of counter-ions in this context was most evident on the IC side, and this process was further supported by POPS lipids that were observed to play an active role by slightly popping out of the membrane and capturing the nanoparticle, as the membrane reorganized through lateral diffusion of POPS to concentrate right underneath $AuNP^+$.

As mentioned above, $AuNP^+$ was found to experience a free-energy barrier to bind with the EC leaflet, in agreement with experiments [63]. However, several *in vivo* experiments have shown $AuNP^+$ to interact with the EC layer spontaneously [51, 55, 58, 158–160]. In real plasma membranes other membrane bound components, such as the negatively charged glycocalyx [162] can play a similar role as POPS in the cytosolic compartment, thus facilitating the contact of $AuNP^+$ and the EC layer.

Based on the results, one possible mechanism for $AuNP^+$ permeation is pore-formation. $AuNP^+$ attaches to both the IC (POPC/POPS) and EC (POPC) layers in a stable manner, the latter taking place after the crossing of a free-energy barrier. However, the nature of $AuNP^+$ membrane interaction differs significantly. On the EC side, there are no lipid head groups underneath the nanoparticle, as they migrate to the boundary of the $AuNP^+$ contact region and orient themselves with the phosphate groups pointing towards $AuNP^+$. The side chains of $AuNP^+$ also bend towards the membrane plane to be in contact with the surface phosphates. As a result, the $AuNP^+$ interacts with the EC membrane in a very singular way: Below the nanoparticle, hydrophobic interactions of the lipid tails and the mainly hydrophobic alkanethiol tails of $AuNP^+$ prevail, while in the borders of its projection there are ionic contacts between $AuNP^+$ amine terminal groups and oriented phosphate groups of POPC. This membrane reorganization gives room for the formation of a patch that is largely hydrophobic. Meanwhile, on the IC side, there is interdigitation between $AuNP^+$ sidechains and lipid head groups, and considerable enrichment of phosphatidylserines under $AuNP^+$. Together these could constitute the initial stage for pore formation, possibly having the torus shape [43, 70] seen in experiments [51, 55, 58, 158–160].

After $AuNP^+$ has adsorbed to the EC leaflet, at least a partial deprotonation of the amine groups will occur before permeation takes place through formation of a pore. The proposed mechanism could be tested in experiments by decreasing the length of $AuNP^+$ side chains and monitoring the hole formation and toxicity. It is likely that shorter side chains would result in smaller amount of holes and lower toxicity as the initial stages of the pore formation would be hampered.

Summarizing the results, it is proposed that $AuNP^+$ is able to approach and attach to the plasma membrane aided by negatively charged membrane-bound components, *e.g.,* glycocalyx. After this, $AuNP^+$ can form a large pore while moving towards the cytosolic layer, and it is concluded that the cytotoxicity of $AuNP^+$ arises here. The nanoparticle can simply destabilize the membrane as seen in experiments [63] or favour the diffusion of phosphatidylserine lipids from the cytoplasmic leaflet to the extracellular one through the pore boundaries, which can potentially initiate apoptosis. Finally, in case $AuNP^+$ manages to permeate all the way to the cytoplasm, it will strongly attach to the inner IC leaflet and accumulate. At this point, increasing nanoparticle concentration is expected to disturb many critical molecular functions due to the high $AuNP^+$ charge, which can alter membrane protein conformations.

7. CONCLUSION

Gold nanoparticles are being used for the purposes of bio- and nanotechnology. Understanding details of their interactions with biological fluids and with cell membranes is important — gold nanoparticles have biomedical applications and studying potential toxic effects of nanoparticles is relevant, as well.

In this work, functional monolayer-protected AuNPs were studied in aqueous solution and in the presence of animal plasma-like cell membranes by performing atomistic molecular dynamics simulations at physiological temperature. The aim was to study the properties of AuNPs in biological environment, and to test their tendency to penetrate to cell membrane as well as to shed light on the mechanisms involved.

The gold nanoparticles studied were Au_{144} nanoparticles that comprise a nearly-spherical Au core (diameter ~ 2 nm), a passivating Au-S interface, and functionalized alkanethiol chains. The AuNP composition matches one of the most ubiquitous synthesised AuNP sizes. Cationic and anionic AuNPs were modeled with amine and carboxyl terminal groups (NH_3^+ and COO^-) and Cl^-/Na^+ counter-ions, respectively. To study nanoparticle-membrane interactions the AuNPs were simulated both in extracellular (EC) and intracellular fluid (IC) using realistic model cell membranes. The theoretical approach in this study was unique. The atomistic simulations differed from the previous coarse-grained methods, and enabled studying cellular level interactions in a considerable detail.

The study of AuNPs in aqueous solution showed that the radial distribution functions were similar for the two AuNPs. The side chains and terminal groups were significantly flexible, and the water/counter-ion profiles had similar characteristics. In contrast, the atomic configurations (water and counter-ions) were remarkably different around the head groups, NH_3^+ and COO^-, of the AuNPs. The orientation of water was distinct in the first solvation shell, and AuNPs caused a long-range effect

in the solvent structure. The effect was strong for counter-ions and emphasised the importance of long-range electrostatic interactions. The short-time diffusion analysis revealed that contacts with AuNP slows down solvent diffusion around AuNP, and this effect extended over 3 nm from the surface of AuNP transmitted by several solvation shells. According to the analysis of Debye length and zeta potential, AuNPs of the considered type do not coagulate.

The results of the study of AuNPs in aqueous solution highlighted the importance of electrostatic interactions and the nanoparticle-solvent interface in determining the properties of AuNPs considered in this work. The analysis showed that AuNPs of this type cannot be considered as distinct bodies — due to long-ranged electrostatic interactions they form complexes with ions and water molecules around them. The interactions in AuNP solutions were concluded to be long-range and solvent-mediated, due to ordering of ions and solvent molecules around them. The characteristic length over which charged AuNPs may affect biological molecules or complexes was concluded to be at least 10 nm. Since NPs synthesised for technology are usually charged or polar, the results may have generic relevance in conditions were NPs interact with cells or biomolecules.

Electrostatic interactions turned out to play an important role also in the case of AuNPs in presence of cell membranes. $AuNP^+$ attached to both the cytosolic (POPC/POPS) and extracellular (POPC) layers in a stable manner, the latter taking place after the crossing of a free-energy barrier. However, the nature of $AuNP^+$ membrane interaction differed significantly. $AuNP^-$ attached to the cytosolic leaflet within a few tens of nanoseconds, while it avoided contact with the membrane on the cytosolic side. This behavior was concluded to arise from several factors. When the nanoparticle interacts with lipids in the EC compartment, it forms relatively weak contacts with the zwitterionic headgroups of the POPC lipids. Consequently, $AuNP^-$ does not immerse deeply in the leaflet, enabling relatively free lateral diffusion of the nanoparticle along the membrane surface. On the IC side, $AuNP^-$ remains in the water phase as there is no attractive interaction due to the Coulomb repulsion arising from negatively charged POPS lipids. Cationic $AuNP^+$ was driven towards the membrane at the cytosolic side of the cell, because of electro-

statics, whereas in contrast, anionic $AuNP^-$ was repelled by the negatively charged phophaditylserine lipids of the cytosolic leaflet. In the extracellular compartment, the membrane has effectively positive surface charge due to the positively charged choline groups of POPC lipids of the extracellular leaflet. Consequently, $AuNP^+$ experienced a free-energy barrier to bind with the extracellular leaflet, while the same leaflet appeared attractive to $AuNP^-$. The binding selectivity was concluded to rise from the specific lipid composition of the membrane leaflets.

Nanoparticle charge-sign dependent component in the cytotoxity of AuNPs was visible in the simulations. $AuNP^-$ appeared to have less effect on membranes than $AuNP^+$. The cytotoxity of $AuNP^+$ was concluded to arise from its ability to approach and attach negatively charged cell membrane components. After binding to the extracellular membrane surface, $AuNP^+$ can form a pore, while moving towards the cytosolic layer driven by electrostatics. The results pointed to few possible scenarios for AuNP-induced disruption of membranes. One option is that the nanoparticle simply destabilizes the membrane and its critical molecular functions. NP-induced membrane destabilization has been seen in the experiments [63]. The binding of $AuNP^+$ could cause diffusion of negatively charged phophaditylserines from the cytoplasmic leaflet to the extracellular one, resulting in translocation of phosphaditylserines. This is one possible trigger for apoptosis. If the $AuNP^+$ manages to permeate all the way through to the cytoplasm, it will attach to the cytosolic leaflet and accumulate, which will considerably affect the normal function of the membrane, *e.g.,* altering the membrane protein conformations due to high charge, especially at higher nanoparticle concentrations.

The work presented here provides novel aspects on the interactions of functional AuNPs on cellular level with the use of atomistic MD simulations. A further step from here would be studying membrane with negatively charged components (*e.g.,* glycocalyx), since they may facilitate the contact of $AuNP^+$ and the extracellular leaflet in similar manner as phosphaditylserine lipids used in this study did for the AuNP-membrane binding in the cytosolic leaflet. Further developments could also involve including other essential lipid components into the membrane model, such as sphingomyelin, phosphatidylethanolamine, and cholesterol. Altering AuNP

surface structure would be interesting future research topic, as well. The present work provides a basis for further investigations of NP-induced pore-formation. The proposed mechanism could be tested in experiments by decreasing the length of $AuNP^+$ side chains and monitoring the hole formation and toxicity.

REFERENCES

1. http://www.nanotechproject.org [Online; accessed 19-May-2014].

2. http://www.reportlinker.com [Online; accessed 19-May-2014].

3. N. Lewinski, V. Colvin, and R. Drezek. Cytotoxicity of Nanoparticles. *Small*, 4(1):26–49, 2008.

4. N. S. Allen, M. Edge, J. Verran, J. Stratton, J. Maltby, and C. Bygott. Photocatalytic Titania Based Surfaces: Environmental Benefits. *Polym. Degrad. Stab.*, 93:1632–1646, 2008.

5. N. S. Allen, M. Edge, A. Ortega, C. M. Liauw, J. Stratton, and R. B. McIntyre. Behaviour of Nanoparticle (Ultrafine) Titanium Dioxide Pigments and Stabilisers on the Photooxidative Stability of Water Based Acrylic and Isocyanate Based Acrylic Coatings. *Polym. Degrad. Stab.*, 78(3):467–478, 2002.

6. B. Luppi, T. Cerchiara, F Bigcucci, R. Basile, and V. Zecchi. Polymeric Nanoparticles Composed of Fatty Acids and Polyvinylalcohol for Topical Application of Sunscreens. *J. Pharm. Pharmacol.*, 56(3):407–411, 2004.

7. R. Beck, S. Guterres, and A. Pohlmann, editors. *Nanocosmetics and Nanomedicines: New Approaches for Skin Care*. Springer-Verlag, Berlin, 2011.

8. A. Leifert, Y. Pan-Bartnek, U. Simona, and W. Jahnen-Dechent. Molecularly Stabilised Ultrasmall Gold Nanoparticles: Synthesis, Characterization and Bioactivity. *Nanoscale*, 5:6224–6242, 2013.

9. E. C. Dreaden, A. M. Alkilany, X. Huang, C. J. Murphy, and M. A. El-Sayed. The Golden Age: Gold Nanoparticles for Biomedicine. *Chem. Soc. Rev.*, 41:2740–2779, 2012.

10. M. C. Daniel and D. Astruc. Gold Nanoparticles: Assembly, Supramolecular Chemistry, Quantum-Size-Related Properties, and Applications Toward Biology, Catalysis, and Nanotechnology. *Chem. Rev.*, 104:293–346, 2004.

11. R. W. Murray. Nanoelectrochemistry: Metal Nanoparticles, Nanoelectrodes and Nanopores. *Chem. Rev.*, 108:2688–2720, 2008.

12. M. Walter, J. Akola, O. Lopez-Acevedo, P.D. Jadzinsky, G. Calero, C.J. Ackerson, R.L. Whetten, H. Grönbeck, and H. Häkkinen. A Unified View of Ligand-Protected Gold Clusters as Superatoms. *Proc. Natl. Acad. Sci.*, 105(27):9157–9162, 2008.

13. O. Lopez-Acevedo, A. K. Kacprzak, J. Akola, and H. Häkkinen. Quantum Size Effects in Ambient CO Oxidation Catalysed by Ligand-Protected Gold Clusters. *Nat. Chem.*, 2:329–334, 2010.

14. Y. Shichibu, Y. Negishi, H. Tsunoyama, M. Kanehara, T. Teranishi, and T. Tsukuda. Extremely High Stability of Glutathionate-Protected Au_{25} Clusters Against Core Etching. *Small*, 3(5):835–839, 2007.

15. C. J. Murphy, M. G. Anand, J. W. Stone, P. N. Sisco, A. M. Alkinaly, E. C. Goldsmith, and S. C. Baxter. Gold Nanoparticles in Biology: Beyond Toxicity to Cellular Imaging. *Acc. Chem. Res.*, 41(12):1721–1730, 2008.

16. W. J. E. Beek, M. M. Wienk, and R. A. J. Janssen. Efficient Hybrid Solar Cells from Zinc Oxide Nanoparticles and a Conjugated Polymer. *Adv. Mater.*, 16(12):1009–1013, 2004.

17. M. A. Caldwell, S. Raoux, R. Y. Wang, H. S. P. Wong, and D.J. Milliron. Synthesis and Size-Dependent Crystallization of Colloidal Germanium Telluride Nanoparticles. *J. Mater. Chem.*, 20(7):1285–1291, 2010.

18. K. L. Kelly, E. Coronado, L. L. Zhao, and G. C. Schatz. The Optical Properties of Metal Nanoparticles: The Influence of Size, Shape and Dielectric Environment. *J. Phys. Chem. B*, 107(3):668–677, 2003.

19. P. Peng, D. J. Milliron, S. M. Hughes, J. C. Johnson, A. P. Alivisatos, and R. J. Saykally. Femtosecond Spectroscopy of Carrier Relaxation Dynamics in Type II CdSe/CdTe Tetrapod Heteronanostructures. *Nano Lett.*, 5(9):1809–1813, 2005.

20. S. Biswas, K. D. Belfield, R. K. Das, S. Ghosh, and A. F. Hebard. Block Copolymer-Mediated Formation of Superparamagnetic Nanocomposites. *Chem. Mat.*, 21:5644–5653, 2009.

21. G. C. Papaefthymiou. Nanoparticle Magnetism. *Nano Today*, 4:438–447, 2009.

22. T.-H. Chung, S.-H. Wu, M. Yao, C.-W. Lu, Y.-S. Lin, Y. Hung, C.-Y. Mou, Y.C. Chen, and D.-M. Huang. The Effect of Surface Charge on the Uptake and Biological Function of Mesoporous Silica Nanoparticles in 3t3-L1 Cells and Human Mesenchymal Stem Cells. *Biomat.*, 28:2959–2966, 2007.

23. P. V. AshaRani, G. L. K. Mun, M. P. Hande, and S. Valiyaveetti. Cytotoxicity and Genotoxicity of Silver Nanoparticles in Human Cells. *ACS Nano*, 3(2):279–290, 2009.

24. Y. Zhang, M. Yang, J.-H. Park, J. Singelyn, H. Ma, M. J. Sailor, E. Ruoslahti, M. Ozkan, and C. Ozkan. A Surface-Charge Study on Cellular-Uptake Behavior of F_3-Peptide-Conjugated Iron Oxide Nanoparticles. *Small*, 5(17):1990–1996, 2009.

25. C.-A. J Lin, T.-Y. Yang, C. H. Lee, S. H. Huang, R. A. Sperling, M. Zanella, J. K Li, J.-L. Shen, H. H. Wang, H.-I. Yeh, W. J. Parak, and W. H. Chang. Synthesis, Characterization, and Bioconjugation of Fluorescent Gold Nanoclusters toward Biological Labeling Applications. *ACS Nano*, 3(2):395–401, 2009.

26. C. J. Ackerson, P. D. Jadzinsky, J. Z. Sexton, D. A. Bushnell, and R. D. Kornberg. Synthesis and Bioconjugation of 2 and 3 nm-Diameter Gold Nanoparticles. *Bioconjugate Chem.*, 21(2):214–218, 2010.

27. M. C. Bowman, T. E. Ballard, C. J. Ackerson, D. L. Feldheim, D. M. Margolis, and C. Melander. Inhibition of HIV Fusion with Multivalent Gold Nanoparticles. *J. Am. Chem. Soc.*, 130(22):6896–6897, 2008.

28. R. Chen, T. A. Ratnikova, M. B. Stone, S. Lin, M. Lard, G. Huang, J. A. S. Hudson, and P. C. Ke. Differential Uptake of Carbon Nanoparticles by Plant and Mammalian Cells. *Small*, 6(5):612–617, 2010.

29. E. C. Cho, J. Xie, P. A. Wurm, and Y. Xia. Understanding the Role of Surface Charges in Cellular Absorption versus Internalization by Selectively Removing Gold Nanoparticles on the Cell Surface with a I/Kl Etchant. *Nano Lett.*, 9(3):1080–1084, 2009.

30. E. C. Cho, L. Au, Q. Zhang, and Y Xia. The Effects of Size, Shape, and Surface Functional Group of Gold Nanostructures on Their Adsorption and Internalization by Cells. *Small*, 6(4):517–522, 2009.

31. C. Kim, S. S. Agasti, Z. Zhu, L. Isaacs, and V. M. Rotello. Recognition-Mediated Activation of Therapeutic Gold Nano-Particles Inside Living Cells. *Nature Chem.*, 2:962–966, 2010.

32. J. Bresee, K. E. Maier, A. E. Boncella, C. Melander, and D. L. Feldheim. Growth Inhibition of Staphylococcus aureus by Mixed Monolayer Gold Nanoparticles. *Small*, 7(14):2027–2031, 2011.

33. R. A. Sperling, P. R. Gil, F. Zhang, M. Zanella, and W. J. Parak. Biological Applications of Gold Nanoparticles. *Chem. Soc. Rev.*, 37:1896–1908, 2008.

34. R. Jin. Quantum Sized Thiolate-Protected Gold Nanoclusters. *Nanoscale*, 2:343–362, 2010.

35. L. Dykman and N. Khlebtsov. Gold Nanoparticles in Biomedical Applications: Recent Advances and Perspectives. *Chem. Soc. Rev.*, 41:2256–2282, 2012.

36. A. Verma and F. Stellacci. Effect of Surface Properties on Nanoparticle-Cell Interactions. *Small*, 6(1):12–21, 2010.

37. B. D. Chithrani, A. A. Ghazani, and W. C. W Chan. Determining the Size and Shape Dependence of Gold Nanoparticle Uptake into Mammalian Cells. *Nano Lett.*, 6(4):662–668, 2006.

38. Y. Roiter, M. Ornatska, A. R. Rammohan, J. Balakrishnan, D. R. Heine, and S. Minko. Interaction of Nanoparticles with Lipid Membrane. *Nano Lett.*, 8(3):941–944, 2008.

39. J. Lin, H. Zhang, Z. Chen, and Y. Zheng. Penetration of Lipid Membranes by Gold Nanoparticles: Insights into Cellular Uptake, Cytotoxicity, and Their Relationship. *ACS Nano*, 4(9):5421–5429, 2010.

40. A.-C. Yang and C.-J. Weng. Structural and Dynamic Properties of Water near Monolayer-Protected Gold Clusters with Various Alkanethiol Tail Groups. *J. Chem. Phys.*, 114(19):8697–8709, 2010.

41. S. Zhang, G. Lykotrafitis, G. Bao, and S. Suresh. Size-Dependent Endocytosis of Nanoparticles. *Adv. Mater.*, 21:419–424, 2009.

42. J.-Q. Lin, Y.-G. Zheng, H.-W. Zhang, and Z. Chen. A Simulation Study on Nanoscale Holes Generated by Gold Nanoparticles on Negative Lipid Bilayers. *Langmuir*, 27:8323–8332, 2011.

43. A. A. Gurtovenko, J. Anwar, and I. Vattulainen. Defect-Mediated Trafficking across Cell Membranes: Insights from *In Silico* Modelling. *Chem. Rev.*, 110(10):6077–6103, 2010.

44. A. A. Gurtovenko and I. Vattulainen. Lipid Transmembrane Asymmetry and Intrinsic Membrane Potential: Two Sides of the Same Coin. *J. Am. Chem. Soc.*, 129:5358–5359, 2007.

45. A. A. Gurtovenko and I. Vattulainen. Membrane Potential and Electrostatics of Phospholipid Bilayers with Asymmetric Transmembrane Distribution of Anionic Lipids. *J. Phys. Chem. B*, 112:4629–4634, 2008.

46. R. Vácha, M.L. Berkowitz, and P. Jungwirth. Molecular Model of a Cell Plasma Membrane With an Asymmetric Multicomponent Composition: Water Permeation and Ion Effects. *Biophys. J.*, 96(11):4493–4501, 2009.

47. A. A. Gurtovenko. Asymmetry of Lipid Bilayers Induced by Monovalent Salt: Atomistic Molecular Dynamics Study. *J. Chem. Phys.*, 122:244902, 2005.

48. S. J. Lee, Y. Song, and N. A. Baker. Molecular Dynamics Simulations of Asymmetric NaCl and KCl Solutions Separated by Phosphatidylcholine Bilayers: Potential Drops and Structural Changes Induced by Strong Na^+-Lipid Interactions and Finite Size Effects. *Biophys. J.*, 94(9):3565–3576, 2008.

49. A. A. Gurtovenko and I. Vattulainen. Intrinsic Potential of Cell Membranes: Opposite Effects of Lipid Transmembrane Asymmetry and Asymmetric Salt Ion Distribution. *J. Phys. Chem. B*, 113(20):7194–7198, 2009.

50. A. Nel, T. Xia, L. Mädler, and N. Li. Toxic Potential of Materials at the Nanolevel. *Science*, 311:622–627, 2006.

51. A. Hirano, H. Yoshikawa, S. Matsushita, Y. Yamada, and K. Shiraki. Adsorption and Disruption of Lipid Bilayers by Nanoscale Protein aggregates. *Langmuir*, 28(8):3887–3895, 2012.

52. J. A. Álvarez, Y. D. Fauerbach, V. Pellegrotti, T .M. Jovin, E. A. Jares-Erijman, and F. D. Stefani. Influence of Gold Nanoparticles on the Kinetics of α-Synuclein Aggregation. *Nano Lett.*, 13:6156–6163, 2013.

53. A. Verma, O. Uzun, Y. Hu, Y. Hu, H.-S. Han, N. Watson, S. Chen, Irvine D.J., and F. Stellacci. Surface-Structure-Regulated Cell-Membrane Penetration by Monolayer-Protected Nanoparticles. *Nature Mat.*, 7:588–595, 2008.

54. P. R. Leroueil, S. A. Berry, K. Duthie, G. Han, V. M. Rotello, D. Q. McNerny, J. R. Baker Jr., B. G. Orr, and M. M. Banaszak Holl. Wide Varieties of Cationic Nanoparticles Induce Defects in Supported Lipid Bilayers. *Nano Lett.*, 8(2):420–424, 2008.

55. C. M. Goodman, C. D. McCusker, T. Yilmaz, and V. M. Rotello. Toxicity of Gold Nanoparticles Functionalized with Cationic and Anionic Side Chains. *Bioconjugate Chem.*, 15(4):897–900, 2004.

56. A. M. Alkilany, P. K. Nagaria, C. R. Hexel, T. J. Shaw, C. J. Murphy, and M. D. Wyatt. Cellular Uptake and Cytotoxicity of Gold Nanorods: Molecular Origin of Cytotoxicity and Surface Effects. *Small*, 5(6):701–708, 2009.

57. Y. Pan, A. Leifert, D. Ruau, S. Neuss, J. Bornemann, G. Schmid, W.; Brandau, U. Simon, and W. Jahnen-Dechent. Gold Nanoparticles of Diameter 1.4 nm Trigger Necrosis by Oxidative Stress and Mitochondrial Damage. *Small*, 5:2067–2076, 2009.

58. A. Mecke, D.-Kuk. Lee, A. Ramamoorthy, B. G. Orr, and M. M. Banaszak Holl. Synthetic and Natural Polycationic Polymer Nanoparticles Interact Selectively with Fluid-Phase Domains of DMPC Lipid Bilayers. *Langmuir*, 21(19):8588–8590, 2005.

59. J. Chen, J. A. Hessler, K. Putchakayala, B. K. Panama, D. P. Khan, S. Hong, D. G. Mullen, S. C. DiMaggio, A. Som, G. N. Tew, A. N. Lopatin, J. R. Baker, M. M. Banaszak Holl, and B. G. Orr. Cationic Nanoparticles Induce Nanoscale Disruption in Living Cell Plasma Membranes. *J. Phys. Chem. B*, 113:11179–11185, 2009.

60. R. R. Arvizo, O. R. Miranda, M. A. Thompson, C. M. Pabelick, R. Bhattacharya, J. D. Robertson, V. M. Rotello, Y. S. Prakash, and P. Mukherjee. Effect of Nanoparticle Surface Charge at the Plasma Membrane and Beyond. *Nano Lett.*, 10:2543–2548, 2010.

61. E. Salonen, S. Lin, M. L. Reid, M. S. Allegood, X. Wang, A. M. Rao, I. Vattulainen, and P. C. Ke. Real-Time Translocation of Fullerene Reveals Cell Contraction. *Small*, 4(11):1986–1992, 2008.

62. R. C. Van Lehn, P. U. Atukorale, R. P. Carney, Y.-S. Yang, F. Stellacci, D. J. Irvine, and A. Alexander-Katz. Effect of Particle Diameter and Surface Composition on the Spontaneous Fusion of Monolayer-Protected Gold Nanoparticles with Lipid Bilayers. *Nano Lett.*, 13:4060–4067, 2013.

63. S. Tatur, M. Maccarini, R. Barker, A. Nelson, and G. Fragneto. Effect of Functionalized Gold Nanoparticles on Floating Lipid Bilayers. *Langmuir*, 29:6606–6614, 2013.

64. A. C. T. Van Duin, S. Dasgupta, F. Lorant, and W. A. Goddard. ReaxFF: A Reactive Force Field for Hydrocarbons. *J. Phys. Chem. A*, 105:9396–9409, 2001.

65. A. Warshel and M. Levitt. Theoretical Studies of Eenzymic Reactions: Dielectric, Electrostatic and Steric Stabilization of the Carbonium Ion in the Reaction Lysozyme. *J. Mol. Biol.*, 103:227–249, 1976.

66. Royal Swedish Academy of Sciences. The Nobel Prize in Chemistry 2013, *Press release*. `http://www.nobelprize.org/nobel_prizes/chemistry/laureates/2013/` [Online; accessed 20-May-2014].

67. R. C. Van Lehn and A. Alexander-Katz. Structure of Mixed-Monolayer-Protected Nanoparticles in Aqueous Salt Solution from Atomistic Molecular Dynamics Simulations. *J. Phys. Chem. C*, 117:20104–20115, 2013.

68. Y. Li, Z. Yang, N. Hu, R. Zhou, and X. Chen. Insights into Hydrogen Bond Dynamics at the Interface of the Charged Monolayer-Protected Au Nanoparticle from Molecular Dynamics Simulation. *J. Chem. Phys.*, 138:184703–184709, 2013.

69. G. Milano, G. Santangelo, F. Ragone, L. Cavallo, and A. Di Matteo. Gold Nanoparticle/Polymer Interfaces: All Atom Structures from Molecular Dynamics Simulations. *J. Phys. Chem. C*, 115:15154–15163, 2011.

70. J. Lin and A. Alexander-Katz. Cell Membranes Open "Doors" for Cationic Nanoparticles/Biomolecules: Insights into Uptake Kinetics. *ACS Nano*, 7:10799–10808, 2013.

71. R. C. Van Lehn and A. Alexander-Katz. Free Energy Change for Insertion of Charged, Monolayer-Protected Nanoparticles into Lipid Bilayers. *Soft Matter*, 10:648–658, 2014.

72. L. Monticelli, E. Salonen, P. C. Ke, and I. Vattulainen. Effects of Carbon-nanoparticles on Lipidmembranes: A Molecular Dynamics Simulation Perspective. *Soft Matter*, 5:4433–4445, 2009.

73. W.-D. Tian and Y.-Q. Ma. pH-Responsive Dendrimers Interacting with Lipid Membranes. *Soft Matter*, 8:2627–2632, 2012.

74. C. L. Ting and Z.-G. Wang. Interactions of a Charged Nanoparticle with a Lipid Membrane: Implications for Gene Delivery. *Biophys. J.*, 100:1288–1297, 2011.

75. K. Huang and A. E. Garcia. Free Energy of Translocating an Arginine-Rich Cell-Penetrating Peptide across a Lipid Bilayer Suggests Pore Formation. *Biophys. J.*, 104:412–420, 2013.

76. S. L. Fiedler and A. Violi. Simulation of Nanoparticle Permeation through a Lipid Membrane. *Biophys. J.*, 99:144–152, 2010.

77. K. Yang and Y.-Q. Ma. Computer Simulation of the Translocation of Nanoparticles with Different Shapes across a Lipid Bilayer. *Nat. Nanotech.*, 5:579–583, 2010.

78. B. Song, H. Yuan, C. J. Jameson, and S. Murad. Role of Surface Ligands in Nanoparticle Permeation through a Model Membrane: A Coarse-Grained Molecular Dynamics Simulation Study. *Mol. Phys.*, 110(18):2181–2195, 2012.

79. P. Gkeka and P. Angelikopoulos. The Role of Patterned Hydrophilic Domains in Nanoparticle-Membrane Interactions. *Curr. Nanosci.*, 7:690–698, 2011.

80. Y. Li, X. Li, Z. Li, and H. Gao. Surface-Structure-Regulated Penetration of Nanoparticles across a Cell Membrane. *Nanoscale*, 4:3768–3775, 2012.

81. Y. Li, X. Chen, and N. Gu. Computational Investigation of Interaction between Nanoparticles and Membranes: Hydrophobic/Hydrophilic Effect. *J. Phys. Chem. B*, 112(51):16647–16653, 2008.

82. C. L. Ting and Z.-G. Wang. Minimum Free Energy Paths for a Nanoparticle Crossing the Lipid Membrane. *Soft Matter*, 8:12066, 2012.

83. H.-M. Ding, W.-D. Tian, and Y.-Q. Ma. Designing Nanoparticle Translocation through Membranes by Computer Simulations. *ACS Nano*, 6(2):1230–1238, 2012.

84. V. V. Ginzburg and S. Balijepalli. Modeling the Thermodynamics of the Interaction of Nanoparticles with Cell Membranes. *Nano Lett.*, 7(12):3716–3722, 2007.

85. Y. Li and N. Gu. Thermodynamics of Charged Nanoparticle Adsorption on Charge-Neutral Membranes: A Simulation Study. *J. Phys. Chem. B*, 114:2749–2754, 2010.

86. K. Lai, B. Wang, Y. Zhang, and Y. Zheng. Computer Simulation Study of Nanoparticle Interaction with a Lipid Membrane Under Mechanical Stress. *Phys. Chem. Chem. Phys.*, 15:270–278, 2013.

87. N. K. Chaki, Y. Negishi, H. Tsunoyama, Y. Shichibu, and T. Tsukuda. Ubiquitous 8 and 29 kDa Gold: Alkanethiolate Cluster Compounds: Mass-Spectrometric Determination of Molecular Formulas and Structural Implications. *J. Am. Chem. Soc.*, 130:8608–8610, 2008.

88. H. Qian and R. Jin. Controlling Nanoparticles with Atomic Precision: The Case of $Au_{144}(SCH_2CH_2Ph)_{60}$. *Nano Lett.*, 9(12):4083–4087, 2009.

89. C. A. Fields-Zinna, R. Sardar, C. A. Beasley, and R. W. Murray. Electrospray Ionization Mass Spectrometry of Intrinsically Cationized Nanoparticles $[Au_{144/146}(SC_{11}H_{22}N(CH_2CH_3)_3{}^+)_x(S(CH_2)_5CH_3)_y]^{x+}$. *J. Am. Chem. Soc.*, 131:16266–16271, 2009.

90. H. Qian and R. Jin. Ambient Synthesis of $Au_{144}(SR)_{60}$ Nanoclusters in Methanol. *Chem. Mat.*, 23:2209–2217, 2011.

91. P. D. Jadzinsky, G. Calero, C. J. Ackerson, D. A. Bushnell, and R. D. Kornberg. Structure of a Thiol Monolayer-Protected Gold Nanoparticle at 1.1 Å Resolution. *Science*, 318(5849):430–433, 2007.

92. M. W. Heaven, A. Dass, P. S. White, K. M. Holt, and R. W. Murray. Crystal Structure of the Gold Nanoparticle $[N(C_8H_{17})_4][Au_{25}(SCH_2CH_2Ph)_{18}]$. *J. Am. Chem. Soc.*, 130:3754–3755, 2008.

93. J. Akola, M. Walter, R.L. Whetten, H. Häkkinen, and H. Grönbeck. On the Structure of Thiolate-Protected Au_{25}. *J. Am. Chem. Soc.*, 130:3756–3757, 2008.

94. H. Qian, W.T. Eckenhoff, Y. Zhu, T. Pintauer, and R. Jin. Total Structure Determination of Thiolate-Protected Au_{38} Nanoparticles. *J. Am. Chem. Soc.*, 132(24):8280–8281, 2010.

95. O. Lopez-Acevedo, J. Akola, R.L. Whetten, H. Grönbeck, and H. Häkkinen. Structure and Bonding in the Ubiquitous Icosahedral Metallic Gold Cluster $Au_{144}(SR)_{60}$. *J. Phys. Chem. C.*, 113:5035–5038, 2009.

96. T. G. Schaaff, M. N. Shafigullin, J. T. Khoury, I. Vezmar, and R. L. Whetten. Properties of a Ubiquitous 29 kDa Au:SR Cluster Compund. *J. Phys. Chem. B*, 105:8785–8796, 2001.

97. J. F. Hicks, D. T. Miles, and R. W. Murray. Quantized Double-Layer Charging of Highly Monodisperse Metal Nanoparticles. *J. Am. Chem. Soc.*, 124:13322–13328, 2002.

98. T. Laaksonen, V. Ruiz, P. Liljeroth, and B. M. Quinn. Quantised Charging of Monolayer-Protected Nanoparticles. *Chem. Soc. Rev.*, 37:1836–1846, 2008.

99. T. Schlick. *Molecular Modelling and Simulations.* Springer, New York, 2002.

100. S. T. Thornton and J. B. Marion. *Classical Dynamics of Particles and Systems.* Thomson, USA, 2004.

101. *GROMACS User Manual Version 4.5.4.* `http://www.gromacs.org`.

102. L. Verlet. Computer "Experiments" on Classical Fluids: I. Thermodynamical Properties of Lennard-Jones Molecules. *Physical Review*, 159:98–103, 1967.

103. J.-P. Ryckaert, G. Ciccotti, and H. J. C. Berendsen. Numerical Integration of the Cartesian Equations of Motion of a System with Constraints: Molecular Dynamics of *n*-Alkanes. *J. Comp. Phys.*, 23(3):327–341, 1977.

104. U. L. Essmann, L. Perera, M. L. Berkowitz, T. Darden, H. Lee, and L. G. A Pedersen. Smooth Particle Mesh Ewald Method. *J. Chem. Phys.*, 103(19):8577–8593, 1995.

105. D. P. Tieleman and H. J. C. Berendsen. Molecular Dynamics Simulations of a Fully Hydrated Dipalmitoylphosphatidylcholine Bilayer with Different Macroscopic Boundary Conditions and Parameters. *J. Chem. Phys.*, 105(11):4871–4880, 1996.

106. B. R. Brooks, R. E. Bruccoleri, B. D. Olafson, D. J. States, S. Swaminathan, and M. Karplus. CHARMM: A Program for Macromolecular Energy, Minimization, and Dynamics Calculations. *J. Comp. Chem.*, 4(2):187–217, 1983.

107. W. D. Cornell, P. Cieplak, C. I. Bayly, I. R. Gould, K. M. Merz, D. M. Ferguson, D. C. Spellmeyer, T. Fox, J. W. Caldwell, and P. A. Kollman. A Second Generation Force Field for the Simulation of Proteins, Nucleic Acids, and Organic Molecules. *J. Am. Chem. Soc.*, 117:5179–5197, 1995.

108. W. L. Jorgensen and J. Tirado-Rives. The OPLS Force Field for Proteins — Energy Minimizations for Crystals of Cyclic Peptides and Crambin. *J. Am. Chem. Soc.*, 110(6):1657–1666, 1988.

109. W. L. Jorgensen, D. S. Maxwell, and J. Tirado-Rives. Development and Testing of the OPLS All-Atom Force Field on Conformational Energetics and Properties of Organic Liquids. *J. Am. Chem. Soc.*, 118(45):11225–11236, 1996.

110. H. J. C. Berendsen, D. van der Spoel, and R. van Drunen. GROMACS: A Message-Passing Parallel Molecular Dynamics Implementation. *Comp. Phys. Comm.*, 91(1–3):43–56, 1995.

111. H. Heinz, R. A. Vaia, B. L. Farmer, and R. R. Naik. Accurate Simulation of Surfaces and Interfaces of Face-Centered Cubic Metals Using 12-6 and 9-6 Lennard-Jones Potentials. *J. Phys. Chem. B*, 112(44):17281–17290, 2008.

112. H. J. C. Berendsen, J. P. M. Postma, W. F. van Gunsteren, and J. Hermans. *Intermolecular Forces*, chapter Interaction Models for Water in Relation to Protein Hydration. Reidel, Dordrecht, 1981.

113. M. P. Allen and D. J. Tildesley. *Computer Simulations of Liquids*. Oxford University Press, New York, 1987.

114. H. J. C. Berendsen, J. P. M. Postma, W. F. Van Gunsteren, A. Dinola, and J. R. Haak. Molecular Dynamics with Coupling to an External Bath. *J. Chem. Phys.*, 81(8):3684–3690, 1984.

115. S. Nóse and M. L. Klein. Constant Pressure Molecular Dynamics for Molecular Systems. *Mol. Phys.*, 50:1055–1076, 1983.

116. M. Parrinello and A. Rahman. Polymorphic Transitions in Single Crystals: A New Molecular Dynamics Method. *J. Appl. Phys.*, 52:7182–7190, 1981.

117. R. Bowley and M. Sánchez. *Introductory to Statistical Mechanics.* Oxford University Press, New York, 2^{nd} edition, 1996.

118. P. H. Hünenberger. Thermostat Algorithms for Molecular Dynamics Simulations. *Adv. Polym. Sci.*, 173:105–149, 2005.

119. M. Von Essen. Comparison of Temperature Coupling Algorithms in SMD simulations and Mutation Design in Talin I/LWEQ Domain. Master's thesis, Institute of Biomedical Technology, University of Tampere, Finland, 2013. urn:nbn:fi:uta-1-24067.

120. *GROMACS User Manual Version 4.0.* `http://www.gromacs.org`.

121. P. Chaikin and T. Lubensky. *Principles of Condensed Matter Physics.* Cambridge University Press, Cambridge, 1995.

122. Zeta Potential for a Particle in Dispersion Medium. `http://en.wikipedia.org/wiki/File:Zeta_Potential_for_a_particle_in_dispersion_medium.png` [Online; accessed 18-May-2014].

123. M. Smoluchowski. Drei Vorträge über Diffusion, Brownsche Molekularbewegung und Koagulation von Kolloidteilchen. *Physik. Z.*, 17:557–571,585–599, 1916.

124. F. M. Tiller, L. Wenping, and W. Chen. *Albright's Chemical Engineering Handbook.* CRC Press, USA, 2009.

125. T. Pradeep. *A Textbook of Nanoscience and Nanotechnology.* Tata McGraw-Hill, New Delhi, 2012.

126. R. Xu. *Particle Characterization: Light Scattering Methods.* Kluwer Academic Publishers, Netherlands, 2000.

127. nanoComposix. Zeta Potential Analysis of Nanoparticles. `http://nanoComposix.com` [Online; accessed 15-May-2014].

128. Colloidal Dynamics. The Zeta Potential. `http://www.colloidal-dynamics.com` [Online; accessed 15-May-2014].

129. Sympatec. Zeta Potential, 2014. `http://api.ning.com` [Online; accessed 15-May-2014].

130. R. A. L. Jones. *Soft Condensed Matter*. Oxford University Press, New York, 2002.

131. A. J. Bard and L. R. Faulkner. *Electrochemical Methods*. Wiley, New York, 2^{nd} edition, 2001.

132. M. Gouy. Sur la Constitution la Charge Électrique a la Surface d'un Électrolyte. *J. de Phys.*, 9:457–468, 1910.

133. D. L. Chapman. A Contribution to the Theory of Electrocapillarity. *Philos. Mag.*, 25:475–481, 1913.

134. T. M. Squires and S. R. Quake. Microfluidics: Fluid Physics at the Nanoliter Scale. *Rev. Mod. Phys.*, 77:977–1026, 2005.

135. P. Debye and E. Hückel. Zur Theorie der Elektrolyte. *Phys. Z.*, 24(9):185–206, 1923.

136. P. Nelson. *Biological Physics*. Freeman, New York, 2008.

137. D. Van der Spoel, P.J. Van Maaren, P. Larsson, and N. Tîmneanu. Thermodynamics of Hydrogen Bonding in Hydrophilic and Hydrophobic Media. *J. Phys. Chem. B*, 110:4393–4398, 2006.

138. P. L. Chau and A. J. Hardwick. A New Order Parameter for Tetrahedral Configurations. *Mol. Phys.*, 93(3):511–518, 1998.

139. D. P. Tieleman and H. J. C. Berendsen. A Molecular Dynamics Study of the Pores Formed by *Escherichia coli* OmpF Porin in a Fully Hydrated Palmitoyloleoylphosphatidylcholine Bilayer. *Biophys. J.*, 74:2786–2801, 1998.

140. P. Mukhopadhyay, L. Monticelli, and D. P. Tieleman. Molecular Dynamics Simulation of a Palmitoyl-Oleoyl Phosphatidylserine Bilayer with Na^+ Counterions and NaCl. *Biophys. J.*, 86(3):1601–1609, 2004.

141. W. Tang, E. Sanville, and G. Henkelman. A Grid-Based Bader Analysis Algorithm without Lattice Bias. *J. Phys. Condens. Matter*, 21(8):084204, 2009.

142. D. Van der Spoel, E. Lindahl, B. Hess, G. Groenhof, A. E. Mark, and H. J. C. Berendsen. GROMACS: Fast, Flexible and Free. *J. Comput. Chem.*, 26:1701–1718, 2005.

143. L. L. M. Van Deenen, J. A. F. O. Op den Kamp, B. Roelofsen, and K. W. A. Wirtz. On Membrane Phospholipids and Protein-Lipid Association. *Pure Appl. Chem.*, 54:2443–2454, 1982.

144. A. A. Spector and M. A. Yorek. Membrane Lipid Composition and Cellular Function. *J. Lipid Res.*, 26:1015–1035, 1985.

145. O. Berger, O. Edholm, and F. Jähnig. Molecular Dynamics Simulations of a Fluid Bilayer of Dipalmitoylphosphatidylcholine at Full Hydration, Constant Pressure, and Constant Temperature. *Biophys. J.*, 72(5):2002–2013, 1997.

146. M. Bachar, P. Brunelle, D. P. Tieleman, and A. Rauk. Molecular Dynamics Simulation of a Polyunsaturated Lipid Bilayer Susceptible to Lipid Peroxidation. *J. Phys. Chem. B*, 108(22):7170–7179, 2004.

147. T. R. Oliveira, M. T. Lamy, U. M. De Paula, L. L. Guimar aes, M. S. Toledo, H. K. Takahashi, A. H. Straus, C. J. Lindsey, and T. B. Paiva. Structural Properties of Lipid Reconstructs and Lipid Composition of Normotensive and Hypertensive Rat Vascular Smooth Muscle Cell Membranes. *Braz. J. Med. Biol. Res.*, 42(9):844–853, 2009.

148. G. M. Torrie and J. P. Valleau. Nonphysical Sampling Distributions in Monte Carlo Free-Energy Estimation: Umbrella Sampling. *Biophys. J.*, 23:187–199, 1977.

149. J. S. Hub, B. L. de Groot, and D. van der Spoel. g_wham — A Free Weighted Histogram Analysis Implementation Including Robust Error and Autocorrelation Estimates. *J. Chem. Theory Comput.*, 6:3713–3720, 2010.

150. A. A. Gurtovenko, M. Patra, M. Karttunen, and I. Vattulainen. Cationic DMPC/DMTAP Lipid Bilayers: Molecular Dynamics Study. *Biophys. J.*, 86:3461–3472, 2004.

151. P. Mark and L. Nilsson. Structure and Dynamics of the TIP3P, SPC and SPC/E Water Models at 298 K. *J. Phys. Chem. A*, 105(43):9954–9960, 2001.

152. A. A. Gurtovenko and I. Vattulainen. Effect of NaCl and KCl on Phosphatidylcholine and Phosphatidylethanolamine Lipid Membranes: Insight from Atomic-Scale Simulations for Understanding Salt-Induced Effects in the Plasma Membrane. *J. Phys. Chem. B*, 112:1953–1962, 2008.

153. A. Magarkar, E. Karakas, M. Stepniewski, T. Róg, and A. Bunker. Molecular Dynamics Simulation of PEGylated Bilayer Interacting with Salt Ions: A Model of the Liposome Surface in the Bloodstream. *J. Phys. Chem. B*, 116(14):4212–4219, 2012.

154. R. A. Böckmann, A. Hac, T. Heimburg, and H. Grubm uller. Effect of Sodium Chloride on a Lipid Bilayer. *Biophys. J.*, 85:1647–1655, 2003.

155. A. Cordomi, O. Edholm, and J. J. Perez. Effect of Force Field Parameters on Sodium and Potassium Ion Binding to Dipalmitoyl Phosphatidylcholine Bilayers. *J. Chem. Theory Comput.*, 5:2125–2134, 2009.

156. W. P. Wuelfing, A. C. Templeton, J. F. Hicks, and R. W. Murray. Taylor Dispersion Measurements of Monolayer Protected Clusters:? A Physicochemical Determination of Nanoparticle Size. *Anal. Chem.*, 71:4069–4074, 1999.

157. M. Lund, B. Jagoda-Cwiklik, C. E. Woodward, R. Vácha, and P. Jungwirth. Dielectric Interpretation of Specificity of Ion Pairing in Water. *J. Phys. Chem. Lett.*, 1(1):300–303, 2010.

158. N. Khlebtsov and L. Dykman. Biodistribution and Toxicity of Engineered Gold Nanoparticles: A Review of *In Vitro* and *In Vivo* Studies. *Chem. Soc. Rev.*, 40(3):1647–1671, 2011.

159. P. Ruenraroengsak, P. Novak, D. Berhanu, A. J. Thorley, E. Valsami-Jones, J. Gorelik, Y. E. Korchev, and T. D. Tetley. Respiratory Epithelial Cytotoxicity and Membrane Damage (holes) Caused by Amine-Modified Nanoparticles. *Nanotoxicology*, 6(1):94–108, 2012.

160. M. M. B. Holl. Nanotoxicology: A Personal Perspective. *Wiley Interdisciplinary Rev.: Nanomedicine and Nanobiotechnology*, 1(4):353–359, 2009.

161. O. Cramariuc, T. Róg, M. Javanainen, L. Monticelli, A. Polishchuk, and I. Vattulainen. Mechanism for Translocation of Fluoroquinolones across Lipid Membranes. *Biochim. Biophys. Acta*, 1818:2563–2571, 2012.

162. J. M. Tarbell and M. Y. Pahakis. Mechanotransduction and the Glycocalyx. *J. Intern. Med.*, 259(4):339–350, 2006.

PUBLICATIONS

I

THE JOURNAL OF PHYSICAL CHEMISTRY C

Article

pubs.acs.org/JPCC

Atomistic Simulations of Functional $Au_{144}(SR)_{60}$ Gold Nanoparticles in Aqueous Environment

Elena Heikkilä,[†] Andrey A. Gurtovenko,[‡,§] Hector Martinez-Seara,[†] Hannu Häkkinen,[∥] Ilpo Vattulainen,[†,⊥] and Jaakko Akola*[,†,∥,#]

[†]Department of Physics, Tampere University of Technology, P.O. Box 692, FI-33101 Tampere, Finland

[‡]Institute of Macromolecular Compounds, Russian Academy of Sciences, Bolshoi Prospect 31, V.O., St. Petersburg, 199004, Russia

[§]Department of Molecular Biophysics, Faculty of Physics, St. Petersburg State University, St. Petersburg, 198504, Russia

[∥]Departments of Physics and Chemistry, Nanoscience Center, University of Jyväskylä, FI-40014 Jyväskylä, Finland

[⊥]Center for Biomembrane Physics (MEMPHYS), University of Southern Denmark, Odense, DK-5230 Denmark

[#]Institut für Festkörperforschung, Forschungszentrum Jülich, D-52425 Jülich, Germany

Supporting Information

ABSTRACT: Charged monolayer-protected gold nanoparticles (AuNPs) have been studied in aqueous solution by performing atomistic molecular dynamics simulations at physiological temperature (310 K). Particular attention has been paid to electrostatic properties that modulate the formation of a complex comprised of the nanoparticle together with surrounding ions and water. We focus on Au_{144} nanoparticles that comprise a nearly spherical Au core (diameter ∼2 nm), a passivating Au−S interface, and functionalized alkanethiol chains. Cationic and anionic AuNPs have been modeled with amine and carboxyl terminal groups and Cl^-/Na^+ counterions, respectively. The radial distribution functions show that the side chains and terminal groups show significant flexibility. The orientation of water is distinct in the first solvation shell, and AuNPs cause a long-range effect in the solvent structure. The radial electrostatic potential displays a minimum for $AuNP^-$ at 1.9 nm from the center of the nanoparticle, marking a preferable location for Na^+, while the $AuNP^+$ potential (affecting the distribution of Cl^-) rises almost monotonically with a local maximum. Comparison to Debye−Hückel theory shows very good agreement for radial ion distribution, as expected, with a Debye screening length of about 0.2−0.3 nm. Considerations of zeta potential predict that both anionic and cationic AuNPs avoid coagulation. The results highlight the importance of long-range electrostatic interactions in determining nanoparticle properties in aqueous solutions. They suggest that electrostatics is one of the central factors in complexation of AuNPs with other nanomaterials and biological systems, and that effects of electrostatics as water-mediated interactions are relatively long-ranged, which likely plays a role in, e.g., the interplay between nanoparticles and lipid membranes that surround cells.

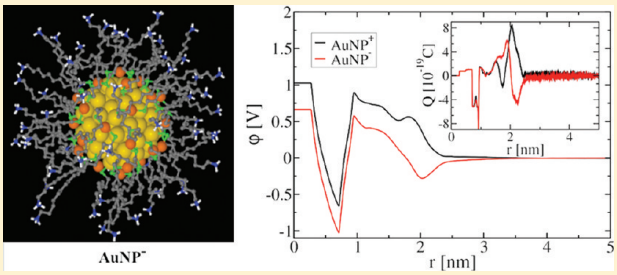

INTRODUCTION

Nanoparticles (NPs, size range 1−100 nm) have many interesting properties, as they bridge the gap between bulk materials and atomic or molecular structures.[1,2] Typically, the physical properties of bulk materials do not depend on the size of the sample, while at the nanoscale size-dependent properties are frequently encountered. Two contributing factors for the size dependence are (a) number of surface atoms whose percentage reduces as the NP size increases toward the bulk limit and (b) quantum confinement effects at the smallest length scales (<10 nm) where the electronic structure plays a significant role in determining the composition, stability, structure, and function of NPs.[3,4]

Nanoparticles often display fascinating optical properties because of quantum effects, and, e.g., gold nanoparticles (AuNPs) appear from yellow to deep red and black in solution depending on their size.[5] In photovoltaic cells, absorption of solar radiation is much higher for semiconductor materials comprised of NPs than for continuous sheets of thin films (e.g., CdTe, ZnO).[6] For phase-change materials used in optical data storage and nonvolatile computer memory, chalcogenide (e.g., GeTe) NPs offer an intriguing route of manufacturing composite materials with tuned (size-dependent) melting point and recrystallization temperature.[7] Other size-dependent properties include surface plasmon resonance in metal NPs,[8] quantum confinement effects in semiconductor NPs (quantum dots),[9] and superparamagnetism in magnetic materials.[10] The changes in physical properties are not always desirable, and,

Received: February 2, 2012
Revised: April 6, 2012
Published: April 9, 2012

e.g., the magnetization direction of small ferromagnetic NPs can switch at low temperature, making them unsuitable for applications.[11]

Several nanoparticles are used in nanomedicine and biochemistry for drug delivery, diagnostics, therapeutics, and bioimaging.[12−17] AuNPs are one type of nanoagents that are being employed for such purposes,[18−22] and they have nowadays a variety of useful applications in these fields. Meanwhile, according to recent experimental findings, AuNPs may also have cytotoxic properties (among other particle types).[23,24] In this context, the interaction between NPs and cell membranes is very relevant,[18,25−31] since all trafficking between the cell interior and the extracellular space takes place through the cell membrane.[32] The permeation rates of particles translocating through a membrane are therefore affected by the membrane potential, which in mammalian cells is known to be rather complicated and arises from asymmetric lipid[33−35] and ion distributions[34−38] on the extracellular and cytosolic sides of a cell.

Interactions of charged or polar NPs with the cell membrane are expected to be strong and long-ranged. This view is quite relevant, since NPs are often layered (protected, passivated) for medical applications, and, e.g., grafting polar surface groups onto AuNPs affects their water solubility and ability to penetrate cell membranes.[23] Extracellular positively charged NPs (e.g., SiO_2, TiO_2, AuNPs) have also been reported to intrude through cell membranes, and, in some cases, to cause a large-scale cell death in comparison with the negatively charged particles which remain on the extracellular side.[12,13,19,20,23,24] It has been concluded that, among other factors, such as NP size/shape and hydrophobicity of grafted side chains, toxicity of nanoparticles depends on the sign of charge.[24,39] Also important to stress is the interaction of NPs with native biological molecules in the context of natural organic matter (NOM), since, e.g., carbon nanoparticles have been found to induce cell death when cells have been exposed to fullerenes together with NOM.[40]

A particularly suitable strategy to gain a better understanding of NP properties in aqueous and biological environments is to employ atomic-scale computer simulations to characterize the properties of the commonly used nanomaterials. In this spirit, not only the novelty of the topic but also the importance of revealing the details of interactions at the cellular level makes studies of *monolayer-protected AuNPs* interesting. Recently, a few molecular dynamics (MD) simulations have been performed for related systems: The properties of monolayer-protected AuNPs in water have been studied by 1 ns MD simulations,[29] and the interface between AuNP and polymers has been simulated in order to achieve all-atom models for AuNP−polymer nanocomposites (polymeric memory devices).[41] AuNP penetration in lipid bilayers has been simulated with coarse-grained (CG) MD by enforcing AuNP intrusion via external potentials, and considerable disruptions of cell membranes have been reported, including a large hole of ∼5.5 nm diameter with a positively charged AuNP.[28,31] Furthermore, while the knowledge of the effects of AuNPs on lipid membranes is rather limited, quite a lot of potentially useful insight is available from recent MD simulations of lipid membranes interacting with carbon NPs.[42]

In this work, we have performed a series of MD simulations for monolayer-protected AuNPs in aqueous solution with functionalized (charged) alkanethiol side groups [$Au_{144}(SR)_{60}$, where R = $C_{11}H_{22}$ + amine/carboxylate terminal group] to study their structural and dynamical properties, and the interaction with solvent (water, counterions). Both the cationic and anionic AuNPs were simulated over an extensive period of 200 ns, allowing us to compare the two cases on equal footing and without considerable concerns of sufficient sampling. The nanoparticle composition corresponds to one of the most ubiquitous synthesized AuNP sizes (29 kDa, core diameter ∼2 nm), matching also its mass-spectrometrical analysis for $Au_{144}(SR)_{60}$.[43−46] Also, the AuNP structure incorporates the common structural details reported for several cluster sizes in this size regime ($d \leq 2$ nm).[3,47−50] The structural model of $Au_{144}(SR)_{60}$ is based on the recent theoretical model by Lopez-Acevedo et al.[51] which was shown to be in very good agreement with the experimental X-ray powder diffraction measurements,[52] and the AuNP electronic structure is consistent with the chemical voltammetry measurements and optical properties.[43,53,54]

We discuss several aspects of electrostatics in systems comprised of charged nanoparticles and ions in aqueous environments. We consider the ordering and dynamics of ions and water around AuNPs, and the range of water-mediated interactions between AuNPs and other objects. We also discuss ions' distributions in terms of the Debye−Hückel description and use this treatment for consideration of nanoparticle coagulation in terms of the zeta potential. Overall, our results emphasize the importance of electrostatics and the interface between AuNP and solvent as decisive factors in determining the properties of nanoparticle complexes in aqueous environments. In this spirit, the present work provides a basis for further investigations of the $Au_{144}(SR)_{60}$ nanoparticles in biologically relevant interface systems such as lipid membranes.

MATERIALS AND METHODS

Descriptions of Model Systems. Monolayer-protected gold nanoparticles (AuNPs) of 144 Au atoms have been modeled with functionalized alkanethiol side groups (undecanyl chain, R = $C_{11}H_{22}$, and a terminal group), shown in Figure 1. The alkanethiol chains are modeled on the basis of the united atom concept that describes a CH_2 group as a single "united" bead. The rigid 114-atom gold core possesses a nearly-spherical polyhedral geometry (rhombicosidodecahedron) based on the previous theoretical suggestion.[51] The monolayer covering the Au core consists of 30 "oxidized" surface gold atoms and 60 alkylthiol ligands (SR−, with R = $C_{11}H_{22}$) with polar terminal groups, and two ligands attached to each surface gold atom (Figure 2). (As a remark, let us mention that rigorously speaking there is no "alkyl" chain here in a traditional sense due to the S atom in the given functional group, but we use this naming convention here.) This feature of the Au−S interface, which exists also for self-assembled monolayers on bulk Au, has not been incorporated previously for AuNP simulations with classical force fields.[28,29,31,41] Two types of Au nanoparticles were prepared: one with a terminal amine group (NH_3^+) and the other with a carboxylic group (COO^-) attached to each hydrocarbon chain (Figure 1). The molecular formulas of the corresponding particles can be represented as $Au_{144}(SRNH_3^+)_{60}$ and $Au_{144}(SRCOO^-)_{60}$ for $AuNP^+$ and $AuNP^-$, respectively.

The simulation box dimensions were adjusted for all systems to 7.06 × 7.06 × 7.06 nm^3. After placing the AuNP inside the box, the box was filled with water, and 60 counterions were added for each AuNP: Cl^- ions for $AuNP^+$ and Na^+ ions for $AuNP^-$. The chosen system size was confirmed to be consistent

dx.doi.org/10.1021/jp301094m | J. Phys. Chem. C 2012, 116, 9805−9815

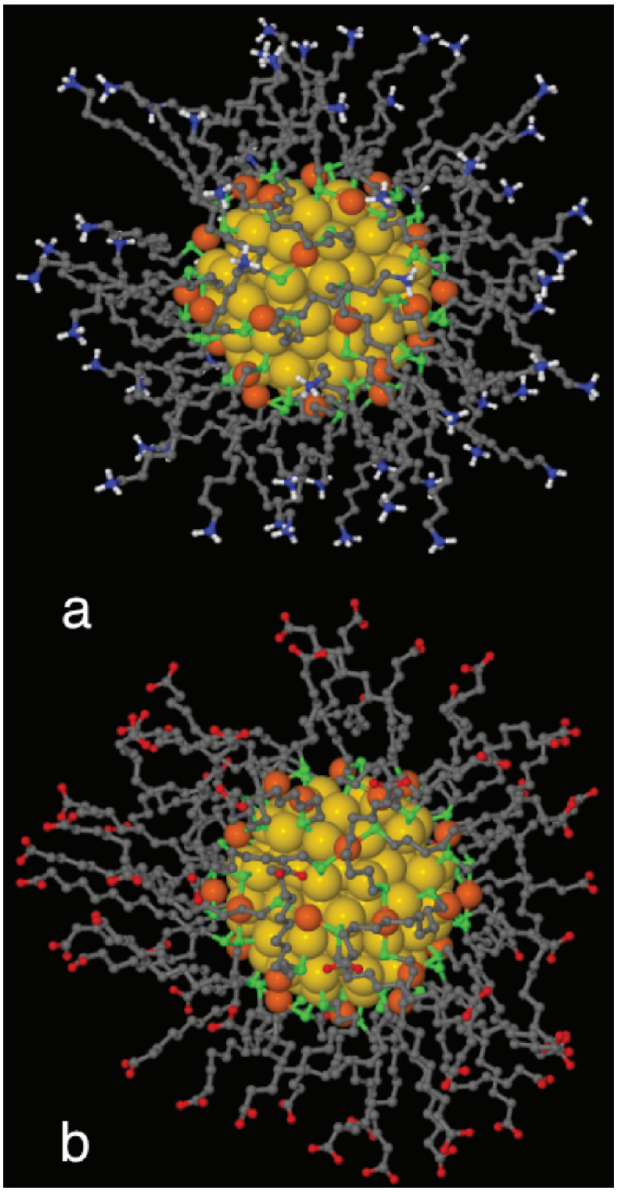

Figure 1. Visualization of Au nanoparticles: (a) the cationic $Au_{144}(SRNH_3^+)_{60}$ and (b) the anionic $Au_{144}(SRCOO^-)_{60}$, where R = $C_{11}H_{22}$. Color code: Au (core), gold; Au (interface), orange; S, green; C (united atom), gray; N, blue; O, red; and H, white.

with the water density at the given temperature. The overall number of atoms in the simulated systems was around 33 000.

Our long-term goal is to model interactions of functionalized AuNPs with cell (lipid) membranes, and the AuNP force-field has to be consistent with the force-field for lipid membranes. As follow-up simulations of AuNPs with lipid membranes are currently in progress, we here describe the background related to both simulation projects. We employ the well-known united-atom force-field by Berger et al.[55] for the alkythiol side groups. The force-field is essentially a mixture of OPLS (nonbonded interactions) and GROMOS (bonded interactions) force-fields. Partial charges for the ionized head groups of $AuNP^+$ and $AuNP^-$ were taken from the appropriate parts of POPE[55,56] and POPS[57] lipids, respectively. A common problem for metallic NPs in a biologically relevant environment is the fact

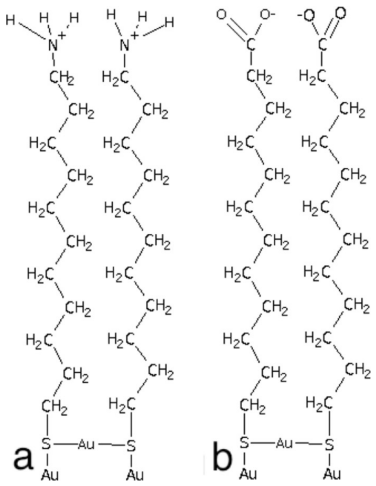

Figure 2. Schematic description of the atom nomenclature of alkanethiol groups: (a) $AuNP^+$ with amine and (b) $AuNP^-$ with carboxylic terminal group (charged). Pairs of hydrocarbon chains are connected via one Au (surface) in each case, and the RS−Au−SR oligomers (R standing for the hydrocarbon chain) make additional Au−S bonds with the Au core. CH_2 groups are treated using the united-atom description.

that metals are not normally included in biomolecular force-fields. Recently, Lennard-Jones (LJ) parameters for several metals were developed,[58] and the parameters are compatible with some widely used empirical force-fields, such as Charmm, Amber, and OPLS. Therefore, the corresponding OPLS-compatible LJ parameters for Au atoms were taken from ref 58. Partial charges of the AuNP core (144 Au and 60 S atoms) were evaluated from the density functional (DF) calculations of ref 51 by using electron density and the method of Bader charges. The rigidity of the gold core was preserved by introducing a number of virtual constant bonds and constraint potentials between Au atoms of the core. Additional bonds and constraint potentials were set for the Au−S interface structure in order to maintain the correct geometry of the NP interior (details given in the Supporting Information).

Water molecules were represented using the SPC model.[59] The particle-mesh Ewald summation (PME) method[60] was used for the electrostatic interactions with a real space cutoff of 1.0 nm and a reciprocal grid of 60 × 60 × 60 cells with a fourth-order *B*-spline interpolation. For van der Waals interactions, we used a cutoff distance of 1.0 nm. All MD simulations were performed by using the GROMACS package (version 4.0.5).[61]

Prior to actual simulations, the systems were energy minimized and equilibrated by short 20 ns MD runs. The production simulations were performed over a period of 200 ns for each AuNP. For comparison, previous simulation studies of related systems covered time scales of the order of 1 ns.[29] The time step was set to 1 fs, and the neighbor list (cutoff 1.0 nm) was updated for every frame. The simulations were performed both in the *NVT* and *NPT* ensembles for 200 ns, respectively. For the *NVT* ensemble, the temperature was set to 310 K using the Berendsen thermostat[62] with a time constant of 0.1 ps. In addition, for the *NPT* ensemble, the Berendsen algorithm[62] with a compressibility of 4.5×10^{-5} bar^{-1}, time constant of 5 ps, and reference pressure of 1 bar was used for isotropic pressure coupling. The variable cell size in *NPT* resulted in 0.02−0.03 nm changes in the simulation box dimensions (7.06 nm). However, most of the analysis was performed using the

dx.doi.org/10.1021/jp301094m | *J. Phys. Chem. C* 2012, 116, 9805−9815

NVT simulation data (constant simulation box size) for practical reasons, mainly due to determination of the electrostatic potential (see below) where a constant system size is most appropriate. In practice, several tests showed that the difference between the *NVT* and *NPT* simulation data was negligibly small. Self-diffusion coefficient values shown in this article are calculated using *NPT*, since the movement of the molecules and particles is considered to be more realistic under constant pressure. The diffusion coefficients of the *NVT* ensemble are shown in Table 1 in the Supporting Information.

Analysis. Data for analysis was stored every 10 ps (RDF, ESP, diffusion coefficients, water orientation). Furthermore, in order to study particularly rapid processes related to hydrogen bonds (water) and other contacts (counterions) between the AuNPs and the surrounding solution, a set of five 1 ns MD simulations starting at 80 ns were performed storing data every 0.5 ps. The GROMACS suite of programs was used for the data analysis,[61,63] complemented by analysis codes of our own.

The NP size was calculated as a time average of the average distance per time frame between the center of mass of the Au core and the terminal groups. The terminal group atoms for the cationic and anionic NP are the amine hydrogens and the carboxylic oxygens, respectively. The Au core size was calculated in a similar manner as an average distance between the center of mass of the core and the surface Au atoms.

The electrostatic potential (ESP) of the systems was calculated in two ways to ensure the consistency of results. The first method takes advantage of the spherically symmetric topology of the system. In this case, the radial electrostatic potential (φ) is calculated as follows:

$$\varphi(r) = \int_0^r \mathbf{E}(r')\, \mathrm{d}r' \tag{1}$$

where $\mathbf{E}(r)$ can be calculated as follows using the Gauss theorem:

$$\mathbf{E}(r) = \frac{Q_r}{4\pi\varepsilon_0 r^2} \tag{2}$$

Here, Q_r is the total charge enclosed by a sphere of radius r from the AuNP center and ε_0 stands for the dielectric constant. The used grid size has been 0.001 nm to calculate Q_r. No significant changes were observed when decreasing the grid size further.

The second method consists of the direct solution of the Poisson equation by using discrete Fourier transforms. Here, AuNP is centered in a three-dimensional grid where the atomic charges are placed by linear interpolation. The charge density grid is Fourier transformed afterward. By applying eq 2 and inverse-Fourier-transforming the potential in the reciprocal space (with wave vectors $\mathbf{k}_x$, $\mathbf{k}_y$, $\mathbf{k}_z$), one obtains the three-dimensional electrostatic potential of the system:

$$\hat{\varphi}(\mathbf{k}_x, \mathbf{k}_y, \mathbf{k}_z) = \frac{\hat{\rho}(x, y, z)}{\varepsilon_0(-k_x^2 - k_y^2 - k_z^2)} \tag{3}$$

where $\hat{\rho}$ stands for the charge density, and in the computation one has used an equally spaced grid of 100 nodes in each direction (grid spacing being 0.07 nm). This method is significantly less sensitive to the grid size than the double integration above, and grids of 50 (0.14 nm) or 200 nodes (0.035 nm) were found to provide essentially the same results. As for the two methodologies for ESP calculation, in both cases, averages over all MD frames were performed. Importantly, the two approaches to compute ESP provided consistent results in every case. The data presented in this paper is based on the first (radial integration) technique presented in eqs 1 and 2.

Radial distribution functions (RDFs) were calculated as a function of the radial distance from the center of mass (COM) of the Au core, r. The radius of gyration, $R_g(t)$, and the moment of inertia (MOI) vector autocorrelation function (ACF), $C(t)$, were computed for the AuNP's x, y and z axes as a function of time, and for explicitly mass weighted atoms (Figure 1, Supporting Information). Similarly, the rotational correlation function (Figure 2, Supporting Information) was evaluated as a function of time, and it shows a decaying trend during the 200 ns simulation.

The analysis of hydrogen bonds (H-bonds) and ionic contacts of the AuNP terminal groups and solution was carried out by averaging over five time windows using five snapshots of the total trajectory as starting structures for 1 ns simulations with a data storage rate of 1/(0.5) ps. Contacts between the AuNP terminal groups and water molecules were considered within a cutoff distance of 0.35 nm for non-hydrogen atoms and a H-bond angle of 30°. Ion contact analysis of the AuNP solutions was performed considering ions within a cutoff distance of 0.35 nm from AuNP terminal groups.

To determine the lifetimes of hydrogen bonds, we used the approach suggested by van der Spoel et al.[63] In essence, the lifetime of a hydrogen bond τ_{HB} was given by inverse forward rate constant k through $\tau_{HB} = 1/k$. The parameter k was determined as follows. The hydrogen bonds during the simulations were allowed to break and reform, allowing us to analyze lifetimes by using binary function $h(t)$, which is 1 when a hydrogen bond is present and 0 otherwise. Then, the forward rate constant k for hydrogen bond breakage and the backward rate constant k' for hydrogen bond formation were determined from the reactive flux correlation $K(t) = kc(t) - k'n(t)$, where $c(t)$ is the autocorrelation function of $h(t)$ and $n(t)$ is the probability that a hydrogen bond that existed at $t = 0$ is broken, but the groups forming the hydrogen bond are still within the hydrogen bonding distance. For details of the lifetime determination, see ref 63.

Self-diffusion coefficients D_A of particles A were calculated by using the Einstein relation.[64] One first defines the mean-squared displacement $\mathrm{MSD}_A(t)$ as follows:

$$\mathrm{MSD}_A(t) = \langle |\mathbf{r}_i(t) - \mathbf{r}_i(0)|^2 \rangle_{i \in A} \tag{4}$$

and then the diffusion coefficient is given by

$$D_A = \lim_{t \to \infty} \frac{\mathrm{MSD}_A(t)}{6t} \tag{5}$$

where in practice we have carried out a linear fitting of the mean-squared displacement between a time interval of 20−180 ns. The error estimate is the difference of the diffusion coefficients obtained from fits over two halves of the initial fitting interval.

To characterize the diffusive motion of water and ions around AuNP, we computed their short-time diffusion factor M radially inside AuNP-centered spherical shells of thickness Δr = 0.5 nm. That is, at every time t during the simulation, we determined the water molecules and ions that at this moment t were at a given distance from the center of AuNP, after which we determined their mean-squared displacement over a short period of time; the width of the time window was Δt = 200 ps and Δt = 500 ps for water and counterions, respectively. The

dx.doi.org/10.1021/jp301094m | J. Phys. Chem. C 2012, 116, 9805−9815

data for MSD(t) in every shell (representing a fixed distance from the AuNP center) was averaged separately for water molecules and ions over the total simulation time of 200 ns. Finally, we computed the short-time diffusion factor M as an effective slope of the mean-squared displacement over the short time window. Hence, the factor M is computed largely in a similar manner as the hydrodynamic diffusion coefficient in eq 5 but now without the long-time limit. For the same reason, since M is not defined in the hydrodynamic long-time limit, we call it a diffusion factor instead of a true diffusion coefficient.

The orientation of water molecules was calculated for a time window of 0−200 ns for AuNP-centered spherical shells of thickness Δr = 0.2 nm using the angle α between a vector from the AuNP center to a water oxygen and a vector from the oxygen to a midpoint between two water hydrogens in the same molecule.

RESULTS

Structural details around AuNPs can be extracted from analyzing the three-dimensional radial distribution functions (RDFs) shown in Figure 3. Each panel depicts the RDFs with

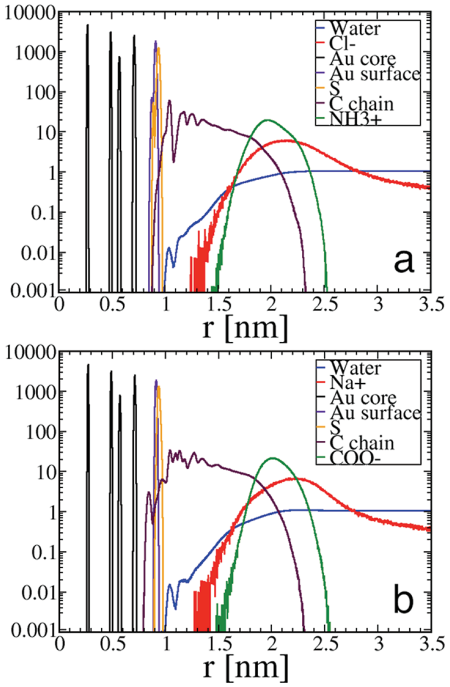

Figure 3. Radial distribution functions (RDFs) averaged over a time window of 200 ns: (a) $AuNP^+$ and (b) $AuNP^-$ solutions. The distance of r = 0 corresponds to the center of the nanoparticle.

respect to the AuNP center for relevant groups in the $AuNP^+$ (Figure 3a) and $AuNP^-$ (Figure 3b) solutions. The size (diameter) of the Au-rich part is d = 1.82 nm, and the average overall diameter is 4.06 and 4.13 nm for $AuNP^+$ and $AuNP^-$, respectively, including the alkanethiol chains and terminal groups.

The three stacked polyhedral Au layers that constitute the metallic core (114 atoms, rhombicosidodecahedron) can be clearly identified. The first two shells of the core consist of 12 and 42 atoms, respectively. One should note that the first peak corresponds to the first Au layer, while the second and third peaks reflect the second Au layer (MacKay icosahedron). The fourth peak at 0.7 nm corresponds to the outer layer of the Au core and gives an estimate for the metallic core. Between 0.9 and 1.0 nm, we find S and Au (surface) atoms according to their colinear positioning in the RS−Au−SR oligomers (Figure 2), as suggested by electronic structure calculations and X-ray diffraction measurements for AuNPs.[3] In our model, additional constraints (together with added nonbonded parameters) maintain the correct surface structure of the Au core, Au surface atoms, and S atoms (see the Supporting Information). Otherwise, these atoms would overlap because of lacking repulsive forces.

The average hydrocarbon chain length is 1.16 and 1.17 nm for $AuNP^+$ and $AuNP^-$, respectively, measured as the distance between the first carbon (connected to S) and the amine nitrogen or carboxylic carbon, respectively. Correspondingly, for a single unit of the alkyl chain, CH_2, the segment length is 0.096 nm for both AuNPs. The radius of gyration is R_g = 0.946 ± 0.004 nm and R_g = 0.995 ± 0.005 nm for $AuNP^+$ and $AuNP^-$, respectively. These values are biased toward the Au core because of the large atomic mass of gold.

ESP and the radially integrated charge of the AuNP solutions are presented in Figures 4 and 5 (see also Figures 6 and 7 in the

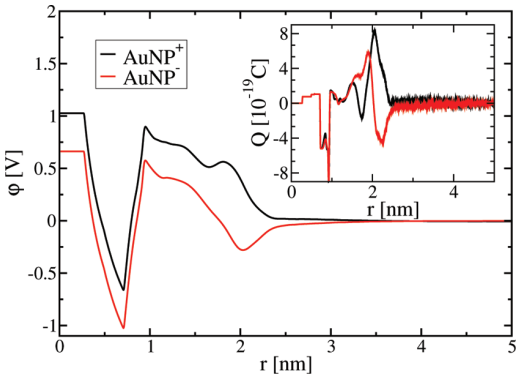

Figure 4. Radially integrated electrostatic potential and charge (the latter shown in the inset) in AuNP solutions.

Supporting Information). Both particles comprise the same Au_{114} core and Au−S interface, and they essentially display the same distribution of accumulated charge in the core region (<1 nm, Figure 4, inset). Small differences can be detected due to the mobility of the interfacial Au and S atoms. Between 1.0 and 1.3 nm, a small flat region is observed accounting to the neutral carbons (united atoms, Figure 2) of the alkyl chain. After this, the COO^- and NH_3^+ terminal groups start to contribute, and the graphs substantially differ. These differences can be understood by comparing the individual RDFs of the terminal groups and their respective partial charges (Figures 2 and 3).

ESP analysis shows that in the $AuNP^-$ system the counterions (Na^+) are likely to accumulate around 2.0 nm from the AuNP center, where an ESP minimum is observed. For $AuNP^+$, the counterions (Cl^-) experience an almost monotonically increasing (attractive) ESP toward the center with a small maximum. Here, one should remember to invert the curve when testing the effects for negative counterions. Obviously, ESP accounts only for the electrostatic forces and neglects details at the atomic level. The RDFs of the counterions in Figure 3 show that both curves mainly overlap instead of finding Cl^- significantly closer to the AuNP core, as

dx.doi.org/10.1021/jp301094m | J. Phys. Chem. C 2012, 116, 9805−9815

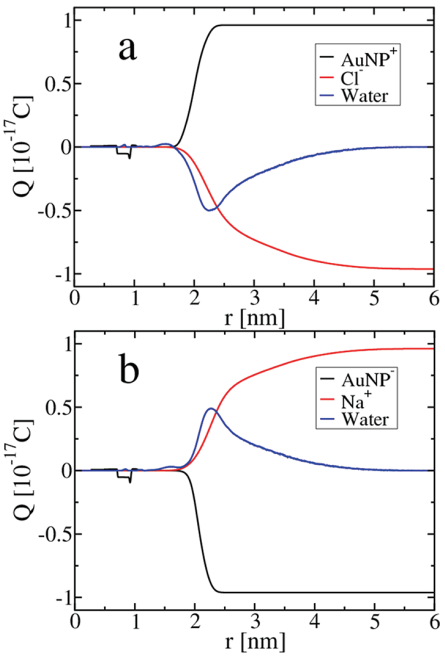

Figure 5. Radially integrated charge in AuNP solutions decomposed into the different components.

one would expect based on ESP. The underlying reason is that, despite the stronger attractive electrostatic force toward the core, Cl^- is also substantially larger than Na^+ in size (cf. the atomic radii, 0.098 nm in Na^+ and 0.181 nm in Cl^-). As a consequence, Cl^- experiences a stronger repulsion when trying to penetrate inside the hydrocarbon chain region. The ion size effect and ESP balance each other, leading to rather similar RDF behavior for both AuNPs.

When the radially integrated charge is decomposed into different components due to the AuNP, water, and ions, one finds (see Figure 5) the contribution due to the nanoparticle to compete against the other two factors. The contribution of ions decays slowly as expected on the basis of the above RDF data. More interesting is the behavior of water, since it shows a peak with a width of about 2 nm, the peak position being close to the maximum of ion distribution (see Figure 3). As further results below for the distribution of water orientation will show, the water behavior in Figure 5 largely arises from the complexity of the ordering of water. Similar features over similar scales have been observed for water close to its interface with charged lipid membranes.[65]

One of the exciting topics in electrolyte solutions concerns the distribution of ions around other charged objects.[66] In the present case with counterions, the proper theoretical context is given by the (mean-field) Debye–Hückel (DH) theory, where for counterions around a charged particle, one combines the Poisson equation to specify the electrostatic potential of an ion with the Boltzmann equation for charge distribution. In radial symmetry, the Debye–Hückel description for the counterion distribution around a charged NP reads as $Ae^{-Br}/r + C$, where A, B, and C are (positive) constants. Here, the constant C is included due to finite system size. However, the most relevant parameter for our purposes is $1/B = \kappa$, known as the Debye screening length.

As our data for counterion distributions were fitted to the DH description, the agreement was found to be very good at large distances (see Figure 6), as expected. Here, it is important to briefly comment on the statistics of the distributions, since

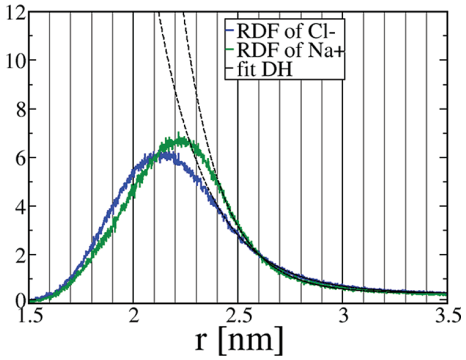

Figure 6. Counterion distribution profiles fitted to the Debye–Hückel description. The RDFs of counterions Cl^- and Na^+ are drawn using blue and green color, respectively. The exponential fits based on the Debye–Hückel theory, $Ae^{-Br}/r + C$ with constants A, B, and C are drawn using black dashed lines. The fits were made for data with $r \geq 2.5$ nm.

the number of ions was limited to 60 to neutralize the functional groups of the AuNP.

The number of ions is not a problem, since the data given below for ion-AuNP lifetimes (Table 1) show that the contacts

Table 1. Hydrogen Bonds and Ionic Contacts between AuNP and Solvent[a]

A	N_A	τ_A (ps)
water ($AuNP^+$)	170.8 ± 0.2	6.5 ± 0.2
Cl^-	4.7 ± 0.4	5.0 ± 0.1
water ($AuNP^-$)	404.4 ± 0.5	3.5 ± 0.1
Na^+	4.4 ± 0.4	10.1 ± 1.1

[a] N_A is the average number of hydrogen bonds and contacts, and τ_A is the average lifetime of the contacts.

between ions and the AuNP are rapid, and the diffusion of ions is also fast (Table 2), indicating that the statistics during the 200 ns simulations for the ion distributions are quite substantial.

Table 2. Self-Diffusion Coefficients D_A of Particles A in AuNP Solutions in the *NPT* Ensemble

A	D_A[× 10^{-5} cm^2 s^{-1}]
$Au_{144}(SRNH_3^+)_{60}$	0.2 ± 0.1
water	4.7 ± 0.1
Cl^-	1.6 ± 0.2
$Au_{144}(SRCOO^-)_{60}$	0.1 ± 0.1
water	4.7 ± 0.1
Na^+	1.0 ± 0.1

The deviations between the ion distribution data and the DH descriptions emerge around 2.4 nm from the AuNP center of mass, which can be considered as an approximate location for the interface (often called a double layer) between NP-bound and loosely associated counterions, the latter being able to move rather freely in the system despite the presence of the NP. The fits shown in Figure 6 yield values of 0.27 and 0.20 nm

dx.doi.org/10.1021/jp301094m | J. Phys. Chem. C 2012, 116, 9805–9815

for the Debye length in $AuNP^+$ and $AuNP^-$, respectively. These lengths are 1 order of magnitude smaller than the NP size, which implies that the assumptions of the Smoluchowski theory for zeta potential determination are valid in the present case.

Now, assuming 2.4 nm to be a safe (that is likely too large) estimate for the position of the interface between NP-bound and loosely bound ions, the ESP gives an approximate estimate for the zeta potential: 26 mV for $AuNP^+$ and −59 mV for $AuNP^-$ (see Figure 8, Supporting Information). The different numbers highlight that cationic and anionic AuNPs respond to an external field with different strengths. Further, even if our assumption of the location of the interface were partly inaccurate, we can still conclude that the zeta potential in the present systems without salt is about 25 mV, or larger than this value, which is often considered as a threshold value for coagulation/aggregation. Further, if there were salt, the Debye length would decrease for increasing ion concentration, which would show up as an increase in the zeta potential (see Figure 8, Supporting Information). Recent experimental data by Verma et al. for gold nanoparticles protected by a number of different organic ligands is in agreement with this view, since they found[23] the (absolute value of) zeta potential to vary between ∼31 and 38 mV. Summarizing, our analysis predicts that the AuNPs considered in this work do not coagulate.

The AuNP terminal group contacts with water and counterions are visualized in Figures 7 and 8. The average number of H-bonds and ion contacts per 0.5 ps time frame and their lifetimes are shown in Table 1. The analysis of H-bonds and ion contacts with the terminal groups reveals differences between the two AuNP systems. The terminal amine groups of $AuNP^+$ form three contacts with the solvent each. There are two possible configurations: First, one hydrogen of NH_3^+ connects to a counterion Cl^- and the other two form H-bonds with water oxygens (Figure 7b), and second, the amine hydrogens make three H-bonds with water oxygens (Figure 7c). The solvent configurations around the terminal carboxyl groups of $AuNP^-$ appear more complicated, as they form six or seven contacts (Figure 8). One frequent case is a configuration of seven H-bonds between the carboxyl group and seven waters. Another relevant configuration involves contacts between Na^+, COO^-, and water in such a way that the two carboxylic oxygens form H-bonds with four waters and two (ionic) Na−O bonds with the counterion, and in addition, Na^+ forms four ionic Na−O bonds with the nearby waters (Figure 8b,c).

The average number and the lifetime of H-bonds and ion contacts (Table 1) show a significant difference between the two AuNP solutions: The total number of H-bonds between water and AuNP is 170.8 ± 0.2 and 404.4 ± 0.5 for the cationic and anionic AuNP, respectively, and the number of contacts for the anionic case is over 2 times larger. Nevertheless, the total number of ion contacts does not differ considerably (4.7 ± 0.4 and 4.4 ± 0.4 for $AuNP^+$ and $AuNP^-$, respectively). These results are consistent with the details of the atomic configurations around the terminal groups (discussion above); the number of contacts with water is over 2 times larger for the COO^- groups ($AuNP^-$) because each carboxyl oxygen is able to make several H-bonds simultaneously. The number of counterions around terminal groups is similar (the total number of opposite charges inside the simulation box is the same, 60), but when it comes to contact lifetimes, the results reveal differences in counterion coordination. The AuNP/counterion contact lifetime is 5.0 ± 0.1 and 10.1 ± 1.1 ps for the cationic and anionic AuNP, respectively. The Na^+ ions (with $AuNP^-$) are more tightly bound, between two COO^- oxygens and surrounded by water molecules (Figure 8), whereas the Cl^- ions ($AuNP^+$) are more mobile, as they are bound to only one NH_3^+ hydrogen (Figure 7). The water contact lifetimes are longer for the cationic nanoparticle, 6.5 ± 0.2 vs 3.5 ± 0.1 ps, and this appears to be coupled to the ion coordination. The water contacts of $AuNP^+$ are less disturbed by counterion movements (weaker ion binding of the NH_3^+ group and fewer H-bonds), and hence, the lifetime value of water is larger.

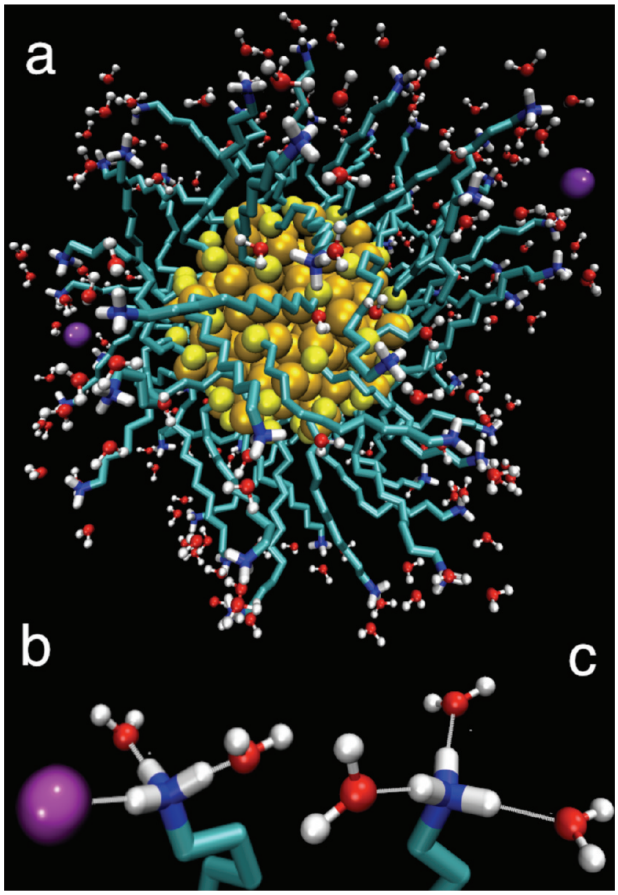

Figure 7. The first solvation shell of $AuNP^+$: Amine terminal groups NH_3^+ with Cl^- counterions and water. (a) The cationic AuNP and solvent molecules within a cutoff distance of 0.34 nm. (b) NH_3^+ terminal group (color key: N, blue; H, white) forming three contacts: one ionic bond with Cl^- (violet) and two H-bonds with water molecules (O, red). (c) NH_3^+ group forming H-bonds with three water molecules.

The self-diffusion coefficients of the AuNP solution in the *NPT* ensemble are presented inTable 2 (see also Table 1 in the Supporting Information for the diffusion coefficients in the *NVT* ensemble), and the corresponding MSD curves are shown in Figure 9 in the Supporting Information. The diffusion coefficients show no significant difference for water. The water molecules were represented using the SPC model in the simulation setup, and the previously reported diffusion coefficient for (pure) SPC water 4.40 × 10^{-5} cm^2 s^{-1} is smaller than that for the AuNP solutions,[67] but so is also the temperature 300 K compared to the one in our work (310 K). The minor difference therefore arises in part from thermal

dx.doi.org/10.1021/jp301094m | J. Phys. Chem. C 2012, 116, 9805−9815

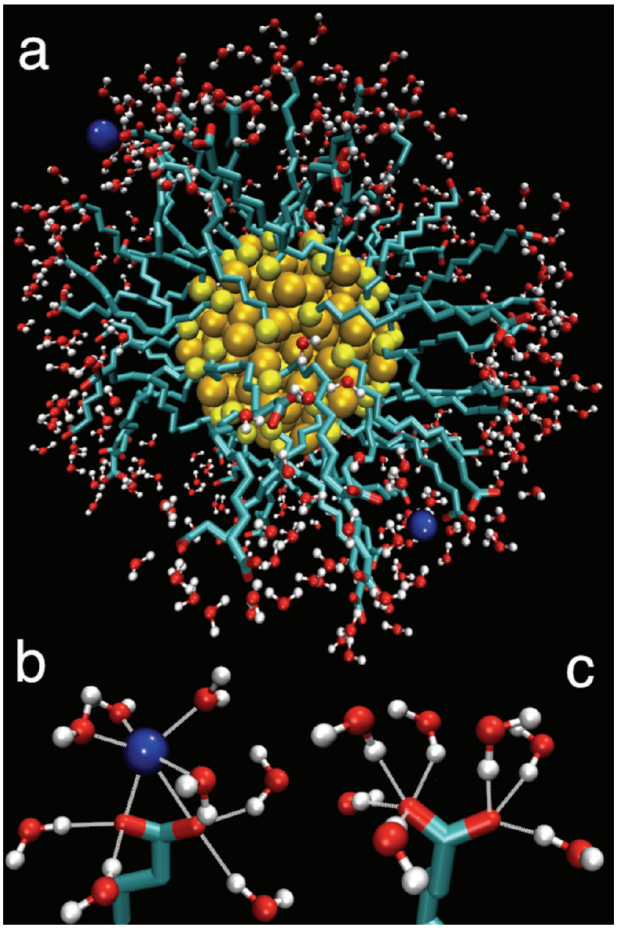

Figure 8. The first solvation shell of $AuNP^-$: Carboxylic terminal groups COO^- with Na^+ counterions and water. (a) The anionic AuNP and solvent molecules within a cutoff distance of 0.36 nm. (b) Na^+ ion (color: blue) is coordinated by four water molecules (O, red; H, white) and COO^-, and the two carboxylic group oxygens form H-bonds with four waters. (c) COO^- group and seven water molecules; three and four H-bonds for each carboxylic oxygen.

fluctuations and the presence of AuNP and the counterions. Furthermore, the diffusion coefficient of Cl^- counterions ($AuNP^+$) is approximately 20% higher than that for Na^+ ($AuNP^-$). This shows that the counterions of $AuNP^-$ are not able to move as freely as in $AuNP^+$, which is consistent with the stronger ionic binding between the carboxylate groups ($AuNP^-$) and Na^+. This also correlates with the fact that the first hydration shell around a Na^+ ion is more ordered than that for a Cl^- ion.[68] The diffusion coefficients of $AuNP^+$ and $AuNP^-$ are almost identical given their error bars.

The short-time diffusion factors of water molecules and counterions have been determined inside spherical 0.5 nm shells around AuNPs, and they are shown in Figure 9. Apart from the slight deviation at 1.5−2.5 nm, the results show little difference for water (as for the self-diffusion coefficients, Table 2), but there is a significant deviation for the counterions. The Cl^- ions ($AuNP^+$) have higher values than those (Na^+) of the anionic nanoparticle. In general, the short-time diffusion values increase as a function of radius, which is caused by the water/ion interactions with AuNPs. The proximity of AuNP slows down the diffusion of water molecules and ions. Water forms an H-bond network around the terminal groups of AuNP (and

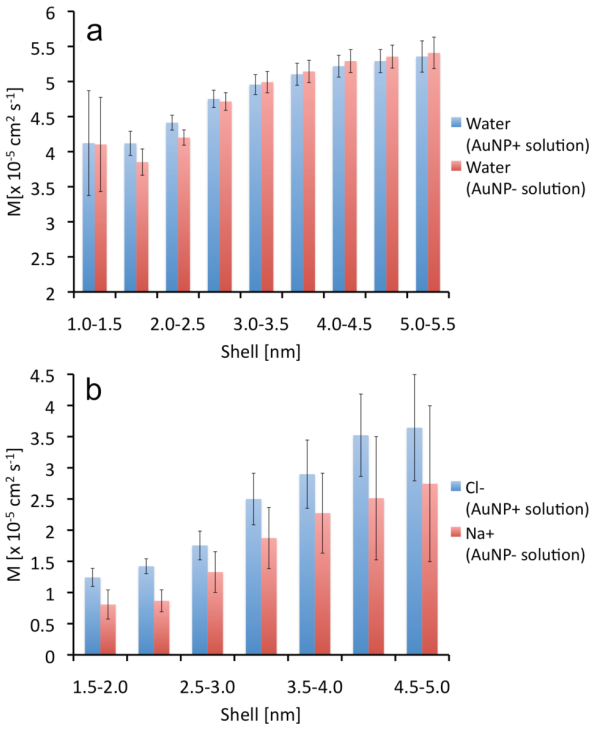

Figure 9. Solvent mobility around AuNPs in spherical shells. (a) Mobility of water and (b) counterions located at AuNP centered Δr = 0.5 nm shells for time windows of Δt = 200 ps (water) and Δt = 500 ps (counterions) averaged over the 0−200 ns simulation time. The $AuNP^+$ and $AuNP^-$ histograms are presented using blue and red colors, respectively. The error bars correspond to standard deviation.

counterions), and this makes the H_2O positions more restricted close to AuNP. For water, the rate of increase in short-time diffusion factors as a function of distance is lower than for the counterions. This can be explained by the type of bonds which water and ions form with AuNP: An H-bond between AuNP and an H_2O molecule is weaker and of shorter range than the electrostatic interaction between AuNP and a counterion.

The effect of AuNP in solvent diffusion extends at least to 5 nm from the AuNP center (3 nm from the surface, Figure 9), which indicates that the solvent transmits the interaction shell-by-shell by intermediating the orientation of water molecules. This phenomenon is evident in the solvent orientation data shown for the AuNP solutions in Figure 10. As for the short-time diffusion analysis, the water orientations also depend strongly on distance: The first shell surrounding the NH_3^+ terminal groups aligns water molecules in such a manner that oxygen is closer to $AuNP^+$ than the H atoms, and vice versa for $AuNP^-$. This effect arises from the electrostatic forces (of H-bonding) between the oppositely charged terminal groups of AuNPs and polarized water molecules, and it results in opposite trends for the two AuNPs.

CONCLUSIONS

Gold nanoparticles are being used extensively in biotechnology and nanosciences, and revealing the details of their interactions with biological fluids at an atomistic level is very relevant. We have performed a series of classical MD simulations for monolayer-protected AuNPs with functionalized (charged) alkanethiol side groups in aqueous solutions. It should be emphasized that the nanoparticle composition matches one of

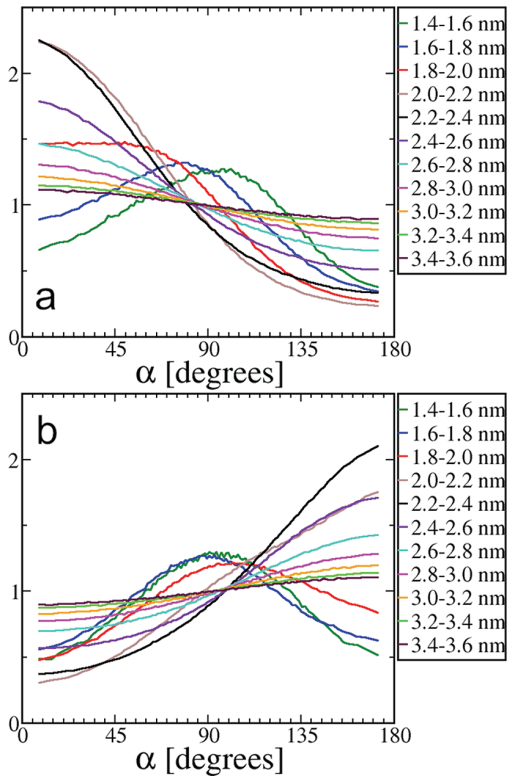

Figure 10. Distribution of water orientation for different distances from the AuNP center: (a) $AuNP^+$ and (b) $AuNP^-$. Orientation is characterized by the angle α, which is defined by a vector from the AuNP center to a water oxygen and a vector from this oxygen to a midpoint between two H atoms in the same H_2O molecule. If the two vectors are aligned pointing in the same direction, then the angle is $\alpha = 0$. Solvent orientation is calculated for AuNP centered spherical shells of thickness $\Delta r = 0.2$ nm over the simulation simulation time 0−200 ns. Note that the most likely location for the terminal groups is between 1.8 and 2.2 nm, (Figure 3).

the most ubiquitous synthesized AuNP sizes (29 kDa, ∼2 nm) and its mass-spectrometrical analysis ($Au_{144}(SR)_{60}$),[43−46] and the AuNP structure incorporates the structural details observed for several cluster sizes, where the Au core is a nearly spherical polyhedron and a part of the Au atoms participate (in oxidized form) in the Au−SR ligand shell.[3]

Cationic and anionic AuNPs were modeled with amine (NH_3^+) and carboxyl (COO^-) terminal groups and Na^+/Cl^- counterions. For the two systems, RDFs (Figure 3) were found to be rather similar: The side chains and terminal groups showed significant flexibility and the water/counterion profiles had the same characteristics. However, the distance distributions of terminal groups (Figure 4, Supporting Information) showed that the NH_3^+-terminated alkyl thiols displayed a wider range of distances (fluctuations with respect to each other), and the atomic configurations (water/counterions) were significantly different around the NH_3^+ and COO^- terminal groups. The orientation of water was observed to be distinct for both AuNPs in the first solvation shell, and the AuNPs clearly caused a long-range effect in the solvent structure. This effect was particularly strong for counterions, emphasizing the importance of long-range interactions (electrostatics) in the present system.

The radial electrostatic potential profiles (Figures 4 and 5) displayed a minimum for $AuNP^-$ at about 2.0 nm from the nanoparticle center, marking a preferable location for Na^+, while the electrostatic potential of $AuNP^+$ rised almost monotonically and attracted Cl^- (in principle) further inside. However, other factors (such as reduced water concentration and larger ionic radius) exhibited Cl^- from entering inside $AuNP^+$. Despite its larger atomic mass, the self-diffusion coefficient of Cl^- was about 20% larger than that of Na^+, which is related to the details in ionic bonding with the terminal carboxylate/amine groups (reduced lifetime for Cl^- contacts). The short-time diffusion analysis around AuNPs revealed that the solvent diffusion is slower near AuNP due to H-bonds and ionic contacts with the terminal groups, and that the effect extends over 3 nm from the AuNP surface because of several solvation shells that transmit the effect.

When our data for counterion distributions were fitted to the Debye−Hückel description, we found the agreement to be very good. The interface between NP-bound and loosely associated counterions was observed to be around 2.4 nm from the AuNP center of mass, and a fit to the ion density distributions at distances larger than this one resulted in values of 0.27 and 0.20 nm for the Debye length in $AuNP^+$ and $AuNP^-$, respectively. The Debye lengths are small, and about an order of magnitude smaller than the NP size, allowing us to use the Smoluchowski theory for zeta potential determination. Consideration in this spirit results in zeta potentials of about 26 mV for $AuNP^+$ and 59 mV for $AuNP^-$. The results therefore do not support the idea of coagulation for the NPs studied here.

Concluding, our results highlight the importance of electrostatics and the nanoparticle−solvent interface in determining the properties of AuNPs considered in this work. The results provide a great deal of insight into the properties of charged and functionalized NPs in aqueous surroundings. Considering that the model used in this work is particularly realistic and is in agreement with a wide range of experiments (see the Introduction), its predictions for AuNPs are expected to be highly useful in follow-up considerations of NP effects on biological systems.

Our data show that NPs of this type cannot be considered as distinct bodies, but on the contrary, due to long-range interactions, they form complexes together with the ions and solvent molecules surrounding them. This implies that in NP solutions there are interactions between the nanoparticles due to the ordering effects of water and ions around the NPs, which give rise to long-range solvent-mediated interactions that complement those due to hydrodynamics (conservation of momentum). The significance of these effects is stressed by the fact that nanomaterials in biological environments are rarely pristine neutral particles, as instead (synthetic) NPs under these conditions are usually charged or polar. The present results may therefore have generic interest especially in biological situations where synthetic nanomaterials interact with and aim to access cells. The main barrier that they need to overcome is the cell membrane characterized by a membrane potential coupled to a cloud of salt ions. Therefore, the central issue that is worth clarifying is the interaction between NP complexes and cell membranes. On the basis of our results, the characteristic length over which charged AuNPs may affect biological molecules or complexes (such as lipid membranes) in terms of water-mediated interactions is at least ∼10 nm. Depending on the NP charge and the molecular composition of the membrane, the reorganization of the lipid membrane system that results from this interplay is expected to vary. Work in this direction to clarify these issues is underway.

dx.doi.org/10.1021/jp301094m | J. Phys. Chem. C 2012, 116, 9805−9815

■ ASSOCIATED CONTENT

Supporting Information

Additional data for methodology, radius of gyration, moment of inertia vector autocorrelation function, rotational correlation function, detailed radial distribution functions of AuNP terminal groups, terminal group distance distributions, mean-squared displacements of the systems, diffusion coefficients of the canonical NVT ensemble, and visualizations of the alkyl chain ends close to the Au core with overall AuNP conformations.

This material is available free of charge via the Internet at http://pubs.acs.org.

■ AUTHOR INFORMATION

Corresponding Author

*E-mail: jaakko.akola@tut.fi.

Notes

The authors declare no competing financial interest.

■ ACKNOWLEDGMENTS

We thank Pu-Chun Ke for inspiring discussions. The computations were performed on the Juropa (Intel Xeon 5570) and Cray XT4/XT5 computers in the FZ Jülich (Germany) and CSC - IT Centre for Science Ltd (Espoo, Finland). Financial support from the Academy of Finland (E.H., H.M.-S., I.V., J.A.) and the Alexander von Humboldt Foundation (A.A.G.) is gratefully acknowledged.

■ REFERENCES

(1) Daniel, M.; Astruc, D. *Chem. Rev.* **2004**, *104*, 293−346.
(2) Murray, R. W. *Chem. Rev.* **2008**, *108*, 2688−2720.
(3) Walter, M.; Akola, J.; Lopez-Acevedo, O.; Jadzinsky, P.; Calero, G.; Ackerson, C.; Whetten, R.; Grönbeck, H.; Häkkinen, H. *Proc. Natl. Acad. Sci. U.S.A.* **2008**, *105*, 9157−9162.
(4) Lopez-Acevedo, O.; Kacprzak, A. K.; Akola, J.; Häkkinen, H. *Nat. Chem.* **2010**, *2*, 329−334.
(5) Shichibu, Y.; Negishi, Y.; Tsunoyama, H.; Kanehara, M.; Teranishi, T.; Tsukuda, T. *Small* **2007**, *3*, 835−839.
(6) Beek, W. J. E.; Wienk, M. M.; Janssen, R. A. J. *Adv. Mater.* **2004**, *16*, 1009−1013.
(7) Caldwell, M. A.; Raoux, S.; Wang, R. Y.; Wong, H. S. P.; Milliron, D. *J. Mater. Chem.* **2010**, *20*, 1285−1291.
(8) Kelly, K. L.; Coronado, E.; Zhao, L. L.; Schatz, G. C. *J. Phys. Chem. B* **2003**, *107*, 668−677.
(9) Peng, P.; Milliron, D. J.; Hughes, S. M.; Johnson, J. C.; Alivisatos, A. P.; Saykally, R. J. *Nano Lett.* **2005**, *5*, 1809−1813.
(10) Biswas, S.; Belfield, K. D.; Das, R. K.; Ghosh, S.; Hebard, A. F. *Chem. Mater.* **2009**, *21*, 5644−5653.
(11) Papaefthymiou, G. C. *Nano Today* **2009**, *4*, 438−447.
(12) Chung, T.-H.; Wu, S.-H.; Yao, M.; Lu, C.-W.; Lin, Y.-S.; Hung, Y.; Mou, C.-Y.; Chen, Y.; Huang, D.-M. *Biomaterials* **2007**, *28*, 2959−2966.
(13) AshaRani, P. V.; Mun, G. L. K.; Hande, M. P.; Valiyaveetti, S. *ACS Nano* **2009**, *3*, 279−290.
(14) Zhang, Y.; Yang, M.; Park, J.-H.; Singelyn, J.; Ma, H.; Sailor, M. J.; Ruoslahti, E.; Ozkan, M.; Ozkan, C. *Small* **2009**, *5*, 1990−1996.
(15) Lin, C.-A. J.; Yang, T.-Y.; Lee, C. H.; Huang, S. H.; Sperling, R. A.; Zanella, M.; Li, J. K.; Shen, J.-L.; Wang, H. H.; Yeh, H.-I.; Parak, W. J.; Chang, W. H. *ACS Nano* **2009**, *3*, 395−401.
(16) Ackerson, C. J.; Jadzinsky, P. D.; Sexton, J. Z.; Bushnell, D. A.; Kornberg, R. D. *Bioconjugate Chem.* **2010**, *21*, 214−218.
(17) Bowman, M. C.; Ballard, T. E.; Ackerson, C. J.; Feldheim, D. L.; Margolis, D. M.; Melander, C. *J. Am. Chem. Soc.* **2008**, *130*, 6896−6897.
(18) Chen, R.; Ratnikova, T. A.; Stone, M. B.; Lin, S.; Lard, M.; Huang, G.; Hudson, J. A. S.; Ke, P. C. *Small* **2010**, *6*, 612−617.
(19) Cho, E. C.; Xie, J.; Wurm, P. A.; Xia, Y. *Nano Lett.* **2009**, *9*, 1080−1084.
(20) Cho, E. C.; Au, L.; Zhang, Q.; Xia, Y. *Small* **2009**, *6*, 517−522.
(21) Kim, C.; Agasti, S. S.; Zhu, Z.; Isaacs, L.; Rotello, V. M. *Nat. Chem.* **2010**, *2*, 962−966.
(22) Bresee, J.; Maier, K. E.; Boncella, A. E.; Melander, C.; Feldheim, D. L. *Small* **2011**, *7*, 2027−2031.
(23) Verma, A.; Uzun, O.; Hu, Y.; Hu, Y.; Han, H.-S.; Watson, N.; Chen, S.; D.J., I.; Stellacci, F. *Nat. Mater.* **2008**, *7*, 588−595.
(24) Leroueil, P. R.; Berry, S. A.; Duthie, K.; Han, G.; Rotello, V. M.; McNerny, D. Q.; Baker, J. R., Jr.; Orr, B. G.; Banaszak Holl, M. M. *Nano Lett.* **2008**, *8*, 420−424.
(25) Verma, A.; Stellacci, F. *Small* **2010**, *6*, 12−21.
(26) Chithrani, B. D.; Ghazani, A. A.; Chan, W. C. W. *Nano Lett.* **2006**, *6*, 662−668.
(27) Roiter, Y.; Ornatska, M.; Rammohan, A. R.; Balakrishnan, J.; Heine, D. R.; Minko, S. *Nano Lett.* **2008**, *8*, 941−944.
(28) Lin, J.; Zhang, H.; Chen, Z.; Zheng, Y. *ACS Nano* **2010**, *4*, 5421−5429.
(29) Yang, A.-C.; Weng, C.-J. *J. Chem. Phys.* **2010**, *114*, 8697−8709.
(30) Zhang, S.; Lykotrafitis, G.; Bao, G.; Suresh, S. *Adv. Mater.* **2009**, *21*, 419−424.
(31) Lin, J.-Q.; Zheng, Y.-G.; Zhang, H.-W.; Chen, Z. *Langmuir* **2011**, *27*, 8323−8332.
(32) Gurtovenko, A. A.; Anwar, J.; Vattulainen, I. *Chem. Rev.* **2010**, *110*, 6077−6103.
(33) Gurtovenko, A. A.; Vattulainen, I. *J. Am. Chem. Soc.* **2007**, *129*, 5358−5359.
(34) Gurtovenko, A. A.; Vattulainen, I. *J. Phys. Chem. B* **2008**, *112*, 4629−4634.
(35) Vácha, R.; Berkowitz, M.; Jungwirth, P. *Biophys. J.* **2009**, *96*, 4493−4501.
(36) Gurtovenko, A. A. *J. Chem. Phys.* **2005**, *122*, 244902.
(37) Lee, S. J.; Song, Y.; Baker, N. A. *Biophys. J.* **2008**, *94*, 3565−3576.
(38) Gurtovenko, A. A.; Vattulainen, I. *J. Phys. Chem. B* **2009**, *113*, 7194−7198.
(39) Arvizo, R. R.; Miranda, O. R.; Thompson, M. A.; Pabelick, C. M.; Bhattacharya, R.; Robertson, J. D.; Rotello, V. M.; Prakash, Y. S.; Mukherjee, P. *Nano Lett.* **2010**, *10*, 2543−2548.
(40) Salonen, E.; Lin, S.; Reid, M. L.; Allegood, M. S.; Wang, X.; Rao, A. M.; Vattulainen, I.; Ke, P. C. *Small* **2008**, *4*, 1986−1992.
(41) Milano, G.; Santangelo, G.; Ragone, F.; Cavallo, L.; Di Matteo, A. *J. Phys. Chem. C* **2011**, *115*, 15154−15163.
(42) Monticelli, L.; Salonen, E.; Ke, P. C.; Vattulainen, I. *Soft Matter* **2009**, *5*, 4433−4445.
(43) Chaki, N.; Negishi, Y.; Tsunoyama, H.; Shichibu, Y.; Tsukuda, T. *J. Am. Chem. Soc.* **2008**, *130*, 8608−8610.
(44) Qian, H.; Jin, R. *Nano Lett.* **2009**, *9*, 4083−4087.
(45) Fields-Zinna, C. A.; Sardar, R.; Beasley, C. A.; Murray, R. W. *J. Am. Chem. Soc.* **2009**, *131*, 16266−16271.
(46) Qian, H.; Jin, R. *Chem. Mater.* **2011**, *23*, 2209−2217.
(47) Jadzinsky, P. D.; Calero, G.; Ackerson, C. J.; Bushnell, D. A.; Kornberg, R. D. *Science* **2007**, *318*, 430−433.
(48) Heaven, M. W.; Dass, A.; White, P. S.; Holt, K. M.; Murray, R. W. *J. Am. Chem. Soc.* **2008**, *130*, 3754−3755.
(49) Akola, J.; Walter, M.; Whetten, R.; Häkkinen, H.; Grönbeck, H. *J. Am. Chem. Soc.* **2008**, *130*, 3756−3757.
(50) Qian, H.; Eckenhoff, W.; Zhu, Y.; Pintauer, T.; Jin, R. *J. Am. Chem. Soc.* **2010**, *132*, 8280−8281.
(51) Lopez-Acevedo, O.; Akola, J.; Whetten, R.; Grönbeck, H.; Häkkinen, H. *J. Phys. Chem. C* **2009**, *113*, 5035−5038.
(52) Schaaff, T. G.; Shafigullin, M. N.; Khoury, J. T.; Vezmar, I.; Whetten, R. L. *J. Phys. Chem. B* **2001**, *105*, 8785−8796.
(53) Hicks, J. F.; Miles, D. T.; Murray, R. W. *J. Am. Chem. Soc.* **2002**, *124*, 13322−13328.

(54) Laaksonen, T.; Ruiz, V.; Liljeroth, P.; Quinn, B. M. *Chem. Soc. Rev.* **2008**, *37*, 1836−1846.
(55) Berendsen, H. J. C.; van der Spoel, D.; van Drunen, R. *Comput. Phys. Commun.* **1995**, *91*, 43−56.
(56) Tieleman, D. P.; Berendsen, H. J. C. *Biophys. J.* **1998**, *74*, 2786−2801.
(57) Mukhopadhyay, P.; Monticelli, L.; Tieleman, D. P. *Biophys. J.* **2004**, *86*, 1601−1609.
(58) Heinz, H.; Vaia, R. A.; Farmer, B. L.; Naik, R. R. *J. Phys. Chem. B* **2008**, *112*, 17281−17290.
(59) Berendsen, H. J. C.; Postma, J. P. M.; van Gunsteren, W. F.; Hermans, J. In *Intermolecular Forces*; Pullman, B., Ed.; Reidel: Dordrecht, The Netherlands, 1981; Chapter Interaction models for water in relation to protein hydration.
(60) Essmann, U. L.; Perera, L.; Berkowitz, M. L.; Darden, T.; Lee, H.; Pedersen, L. G. A. *J. Chem. Phys.* **1995**, *103*, 8577−8593.
(61) Van Der Spoel, D.; Lindahl, E.; Hess, B.; Groenhof, G.; Mark, A. E.; Berendsen, H. J. C. *J. Comput. Chem.* **2005**, *26*, 1701−1718.
(62) Berendsen, H. J. C.; Postma, J. P. M; Van Gunsteren, W. F.; Dinola, A.; Haak, J. R. *J. Chem. Phys.* **1984**, *81*, 3684−3690.
(63) Van der Spoel, D.; Van Maaren, P.; Larsson, P.; Timneanu, N. *J. Phys. Chem. B* **2006**, *110*, 4393−4398.
(64) Chaikin, P.; Lubensky, T. *Principles of Condensed Matter Physics*; Cambridge University Press: Cambridge, U.K., 1995.
(65) Gurtovenko, A. A.; Patra, M.; Karttunen, M.; Vattulainen, I. *Biophys. J.* **2004**, *86*, 3461−3472.
(66) Sammalkorpi, M.; Karttunen, M.; Haataja, M. *J. Phys. Chem. B* **2009**, *113*, 5863−5870.
(67) Mark, P.; Nilsson, L. *J. Phys. Chem. A* **2001**, *105*, 9954−9960.
(68) Gurtovenko, A. A.; Vattulainen, I. *J. Phys. Chem. B* **2008**, *112*, 1953−1962.

II

THE JOURNAL OF PHYSICAL CHEMISTRY C

Article

pubs.acs.org/JPCC

Cationic Au Nanoparticle Binding with Plasma Membrane-like Lipid Bilayers: Potential Mechanism for Spontaneous Permeation to Cells Revealed by Atomistic Simulations

Elena Heikkilä,[†,‡,▽] Hector Martinez-Seara,[†,▽] Andrey A. Gurtovenko,[§,∥] Matti Javanainen,[†] Hannu Häkkinen,[#] Ilpo Vattulainen,[†,&] and Jaakko Akola*[,†,‡,@]

[†]Department of Physics, Tampere University of Technology, P.O. Box 692, FI-33101 Tampere, Finland

[‡]COMP Centre of Excellence, Department of Applied Physics, Aalto University, FI-00076 Aalto, Finland

[§]Institute of Macromolecular Compounds, Russian Academy of Sciences, Bolshoi Prospect 31, V.O., St. Petersburg 199004, Russia

[∥]Department of Molecular Biophysics, Faculty of Physics, St. Petersburg State University, St. Petersburg 198504, Russia

[#]Departments of Physics and Chemistry, Nanoscience Center, University of Jyväskylä, FI-40014 Jyväskylä, Finland

[&]Center for Biomembrane Physics (MEMPHYS), University of Southern Denmark, Odense DK-5230 Denmark

[@]PGI-1, Forschungszentrum Jülich, D-52425 Jülich, Germany

Supporting Information

ABSTRACT: Despite being chemically inert as a bulk material, nanoscale gold can pose harmful side effects to living organisms. In particular, cationic Au nanoparticles ($AuNP^+$) of 2 nm diameter or less permeate readily through plasma membranes and induce cell death. We report atomistic simulations of cationic Au nanoparticles interacting with realistic membranes and explicit solvent using a model system that comprises two cellular compartments, extracellular and cytosolic, divided by two asymmetric lipid bilayers. The membrane−$AuNP^+$ binding and membrane reorganization processes are discovered to be governed by cooperative effects where $AuNP^+$, counterions, water, and the two membrane leaflets all contribute. On the extracellular side, we find that the nanoparticle has to cross a free energy barrier of about 5 k_BT prior forming a stable contact with the membrane. This results in a rearrangement of the zwitterionic lipids and nanoparticle side groups in the contact area, giving rise to the initial stage of pore formation on the membrane surface. Such behavior is not seen on the cytosolic side, where $AuNP^+$ is spontaneously captured by the negatively charged phosphatidylserine lipids that diffuse to enrich the membrane leaflet underneath $AuNP^+$, further pointing to $AuNP^+$ accumulation on the inner leaflet of a plasma membrane. The results suggest $AuNP^+$ permeation to take place through the formation of a pore together with partial nanoparticle neutralization/deprotonation, leading to membrane disruption at higher nanoparticle concentrations. The data also suggest a potential mechanism for cytotoxicity as $AuNP^+$ binding to the extracellular leaflet may trigger apoptosis through translocation of phosphatidylserine.

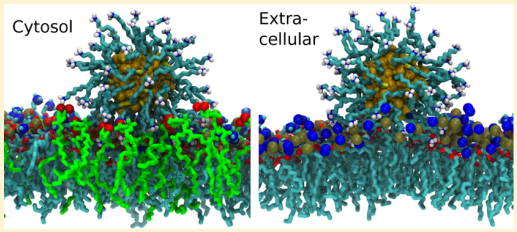

INTRODUCTION

Metal nanoparticles (NPs) provide new functionalities of matter at the nanoscale. Their properties can be tuned via chemical composition, size, binding strength between the core and ligand shell, overall charge, and stability in a given medium.[1] Quantum confinement effects arise as the NP size decreases down to a few nanometers, which is reflected, e.g., in optical properties and catalytic reactivity.[2−4] In this context, gold nanoparticles (AuNPs) are among the most studied systems as they have potential for applications in molecular electronics, molecular recognition, catalysis, biolabeling and sensing, and drug delivery.[1,5−7]

Medical applications of AuNPs cover practically all fields, including diagnostics, therapy, prophylaxis, and hygiene.[8] AuNPs can be used as intrinsic drug agents or drug delivery vehicles, and they can be applied as stabilizing agents for other drug delivery vehicles such as vesicles. AuNPs have demonstrated applicability in photothermal therapy due to their optical properties which enable local heating at cellular level. As composite materials AuNPs may function as triggers for drug release. For example, they enable an efficient treatment of diseased sites (tumors) with small side effects in the body as the local AuNP concentration is high only at the targeted site.[9] This approach is based on size-selective accumulation of AuNPs due to the disordered vascular characteristics of tumors, and the targeting effects can be further enhanced by covering nanoparticles by additional recognition units which are selective for specific tumor sites.[9]

Nanotoxicology is a special field of toxicology which considers potential harmful effects of NPs in living organisms.[10]

Received: March 10, 2014
Revised: April 30, 2014
Published: April 30, 2014

These effects differ from those of larger particles as NPs are able to translocate inside the body from the site of deposition (e.g., lungs) to different organs and tissues (such as blood–brain barrier) more effectively. The important factors for NP toxicity are particle size, composition, shape, surface modification, concentration, agglomeration, and solubility.[11] For example, the large surface-to-volume ratio of NPs is related to increasing chemical reactivities, leading to enhanced formation of reactive oxygen species which may cause damage to proteins, DNA, and cell membranes via oxidative stress.[10] Recently, AuNPs have also been found to enhance the formation of amyloid fibrils that is known as a fundamental step in Alzheimer's and Parkinson's diseases.[12,13]

Small cationic Au nanoparticles of diameters less than 2 nm are able to penetrate cell membranes, and they can be extremely toxic.[4,6,14−16] This has been demonstrated, e.g., for 1.4 nm AuNPs which were observed to cause necrosis and mitochodrial damage to various cell lines.[17] Experimental results indicate that the nanoparticle translocation occurs via self-penetration, where the charge and specific structure/composition of the ligand shell affect the process: Cationic AuNPs with an alternating pattern of aliphatic (hydrophobic) and functionalized side groups (striped AuNPs) show increased penetration activity in comparison to randomly distributed side groups.[18] Cationic nanoparticles have been reported to generate holes in both model and living cell membranes, where the phase of the lipid bilayer plays a role for the level of disruption.[14,19−21] Most recently, it was shown that striped anionic AuNPs (with amphiphilic surface) can pass non-disruptively through model membranes, and this activity depends closely on the AuNP diameter.[22]

Obviously, the spontaneous permeation of AuNPs and its effect on cell membranes call for urgent attention to assess the potential risks of AuNPs for future biomedical applications. As cells and cellular compartments are surrounded by membranes, it is highly relevant to investigate the interaction of AuNPs with lipid bilayer surfaces at the atomistic level. Our computer simulations focus on this issue in detail as we test the self-penetration theory and shed light on the source of the cytotoxicity of AuNPs.

Recent experiments by Tatur et al. for model membrane systems provide a valuable reference for simulations,[23] as they considered 2 nm diameter AuNPs floating between single-component bilayers composed of zwitterionic DSPC lipids (1,2-distearoyl-*sn*-glycero-3-phosphocholine). On the basis of neutron reflectometry measurements, they concluded that AuNPs with cationic head groups penetrate inside the hydrophobic interior of the lipid bilayers and disrupt the membranes at increased concentrations, while anionic AuNPs stay outside. The penetration of cationic AuNPs occurs after elevating the temperature up to 53 °C, which suggests that the process requires the crossing of a free energy barrier at physiological temperatures. These findings can be compared straightforwardly with simulations as there are no complications arising from other components that exist in real membranes, such as membrane proteins and the protruding glycocalyx network.

The primary objective of our work is to unlock the atomistic details of complexation between AuNPs and plasma membrane -like lipid membranes, determine how the complexation can possibly alter cell function, and evaluate how AuNPs can permeate spontaneously through plasma membranes. For this purpose, we have performed a series of atomistic molecular dynamics (MD) simulations of a monolayer-protected AuNP$^+$ [$Au_{144}(SR)_{60}$, where R = $-(CH_2)_{11}$-NH_3^+].[24−27] The simulations have been carried out in an aqueous solution in the presence of a model lipid bilayer mimicking the plasma membrane, where we differentiate between the extracellular (EC) and intracellular/cytosolic (IC) leaflets. To our knowledge, this is the first attempt to tackle this complex problem at the atomistic scale, and we pay particular attention to the role of counterions, water, and specific lipid molecules to gain a full understanding of electrostatics that is expected to be important in the binding and permeation events. Importantly, our work provides a great deal of added value to previous theoretical work on AuNPs interacting with lipid bilayers, as previous studies[28−33] have been based on coarse-grained (CG) models that lack the atomistic details for AuNP as well as the hydrodynamic degrees of freedom. Meanwhile, earlier atomistic studies of AuNPs have explored only the role of solvent,[34,35] including our recent work that is the basis of this study.[36]

COMPUTATIONAL MODELS AND METHODS

Cells use compartmentalization to create specific environments to perform their vital functions, and they achieve this objective by using membranes. In our context, the most important one is the plasma membrane, which separates cells from their surroundings. Cationic gold nanoparticles (AuNP$^+$) are known to be able to reach the interior of cells,[11,12,14,19,37,38] yet the mechanism how they do it is not known.

For studying the AuNP$^+$–plasma membrane interaction, we have designed two model systems described in Figure 1. Essentially, our models are double bilayer systems with periodic boundary conditions applied in all directions (Figure 1b). This setup effectively provides us with two independent compartments in each system.[33,39] We mimic the extracellular and intracellular/cytosolic environments by using asymmetric bilayers with lipid compositions resembling eukaryotic plasma membranes with different ion compositions in each compartment (EC, IC). The lipid composition in the outer EC leaflet is described by zwitterionic POPC [1-palmitoyl-2-oleoyl-*sn*-glycero-3-phosphocholine], while a mixture of POPC (81.25%) and negatively charged POPS [1-palmitoyl-2-oleoyl-*sn*-glycero-3-phosphoserine] (18.75%) is used to model the inner IC leaflet. The upper and lower membranes are inverted, and this results in an EC compartment only in contact with the pure POPC leaflets and an IC compartment in contact with the POPC/POPS mixture. Cholesterol, one of the abundant lipid types in plasma membranes of eukaryotic cells, was not included in the model since (for computational efficiency) we wanted to speed up the dynamics that is slowed down by cholesterol.

Further, a cationic gold nanoparticle with a 2 nm core diameter (144 Au atoms and 60 side groups with positively charged amine terminals) with Cl^- counterions is placed in either the EC or IC compartment (Figure 1c,d). We compensate for the negative charge of POPS by including additional K^+ ions in IC. Some simulations have been performed also with salt by placing 150 mM of NaCl and KCl in the EC and IC compartment, respectively, in order to mimic the physiological ion distribution in both cases.

All MD simulations were performed with the GROMACS simulation package (versions 4.0.5, 4.6.3).[40] Each asymmetric bilayer contains in total 252 lipids in the double bilayer setup (see Figure 1). The lipid compositions of each leaflet has been chosen to be representative of the outer leaflet (124 POPC)

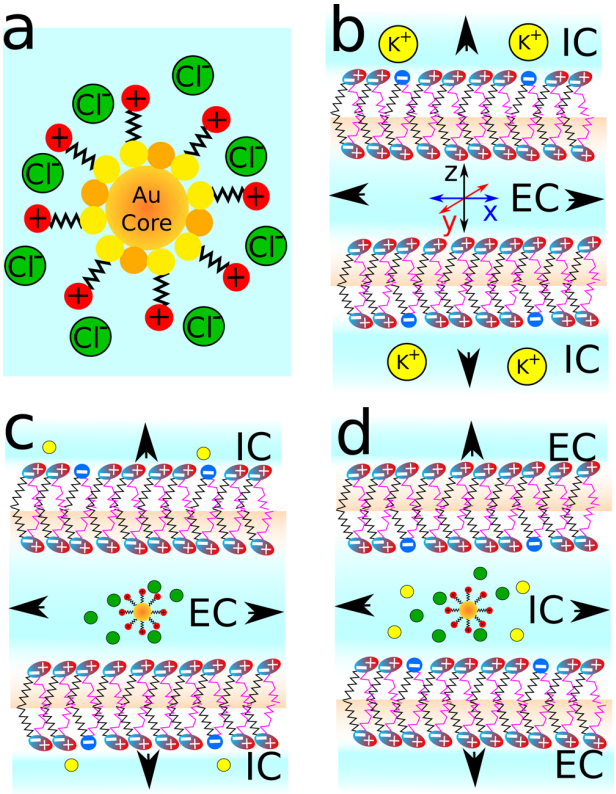

Figure 1. Schemes of the different models simulated: (a) $AuNP^+$ in aqueous solution; (b) double asymmetric bilayer; (c) $AuNP^+$ in EC compartment; and (d) $AuNP^+$ in IC compartment. Color code: $AuNP^+$ [Au (orange), S (yellow), alkyl chain (black), primary amine (red)]; lipids [chains: palmitoyl *sn*-1 chain (black), oleyol *sn*-2 chain (magenta); head groups: phosphatidylserine (blue), phosphatidylcholine (cyan/red)]; ions [Cl^- (green), K^+ (yellow)]. EC refers to the "extracellular" and IC to the "intracellular" compartment. The leaflet next to the EC regime corresponds to pure POPC while the other monolayer is a POPC/POPS mixture. Black arrows visualize the periodic boundary conditions used in this study.

and inner leaflet (104 POPC and 24 POPS) of an animal plasma membrane. The IC compartment hosts 48 (K^+) counterions to neutralize the negatively charged head groups of the 48 POPS lipids, 24 per leaflet. For both models, the simulation box was adjusted around 9.0 × 9.2 × 22.2 nm after density relaxation by *NPT* simulations at 1 bar. In order to maximize the efficiency of the simulations, i.e., reduce the number of atoms in the system, the compartments are not equally sized. Distance between the bilayers' centers of mass (COMs) across the compartment containing the $AuNP^+$ was significantly larger in both cases, ∼14.9 nm, while the other compartment was left with ∼7.3 nm. The overall number of particles in both systems was around 143 000.

All simulated systems use a united atom force field which is largely compatible with the Berger force field.[41] Essentially, the force field is a mixture of a tuned united OPLS (nonbonded interactions) and GROMOS (bonded interactions) force fields. The used POPC is implemented as originally developed by Berger et al.[41,42] with adjustments for the double bond extracted from Bachar et al.[43] The POPS force field model obeys the Mukhopadhyay et al. implementation.[44] Water molecules were represented using the SPC model.[45] The gold nanoparticle has been assembled as described in Heikkilä et al.,[36] and it is based on a realistic atomic model for $Au_{144}SR_{60}$, which is in agreement with experimental data.[26] $AuNP^+$ is associated with 60 Cl^- counterions in each compartment. In addition, 150 mM of salt has been added to the systems in two simulations. The counterions Na^+, Cl^-, and K^+ use their original GROMACS-87 parameters.[46]

Prior to the actual production runs, all prepared systems were energy minimized. The production simulations were performed over 200 ns for each setup (IC and EC systems with and without salt, each). Four extra replicas of the IC and EC systems (without salt) were also simulated for 100 ns with different initial velocities in order to gain statistics. In addition to the freely diffusing systems, we also applied constraints to bring $AuNP^+$ in contact with the EC leaflet, and the system was simulated for 300 ns after releasing the constraints. (The same procedure was also carried out for IC although it is not necessary for achieving the membrane attachment.) The time step was set to 2 fs, and the neighbor list (cutoff 1.0 nm) was updated for every 10th step (20 fs). Furthermore, in order to study particularly rapid processes related to water hydrogen bonds and counterion contacts between $AuNP^+$ and the surrounding solution, a set of ten 1 ns MD simulations starting at different frames of the original simulations were performed by storing data every 0.5 ps.

The simulations were performed in the canonical *NPT* ensemble by setting the temperature equal to 310 K using the Berendsen thermostat[47] with a time constant of 0.1 ps and with a pressure coupling using the Berendsen algorithm[47] with a compressibility of 4.5×10^{-5} bar^{-1}, time constant of 5 ps, and reference pressure of 1 bar. Long-range electrostatic interactions were calculated using the particle-mesh Ewald summation (PME) method.[48] A real space cutoff of 1.0 nm and a reciprocal grid of 77 × 78 × 189 cells with a fourth-order *B*-spline interpolation were employed. For van der Waals interactions, a cutoff distance of 1.0 nm was used.

The umbrella sampling method[49] was employed to calculate the free energy profile of the nanoparticle approaching the extracellular leaflet of one of the bilayers. The reaction coordinate was chosen to be the distance between the core gold atoms and the phosphorus atoms of the target leaflet in the direction normal to the bilayer (z). A harmonic biasing potential was employed, and a total of 23 windows were simulated with the minimum of this biasing potential located between 0.6 and 5.0 nm with a spacing of 0.2 nm. A force constant of 2000 kJ/(mol nm^2) was chosen as this resulted in sufficient sampling of the total reaction coordinate. The windows with the nanoparticle close to the membrane interface (0.6−3.6 nm) were simulated for 100 ns, whereas the rest of the windows (3.8−5.0 nm) were simulated for 50 ns. The data for the last 40 ns were employed in the analysis for all windows. Other simulation parameters follow those of the presented equilibrium simulations. The profiles and their statistical error estimates were obtained by the GROMACS tool g_wham.[50]

RESULTS

$AuNP^+$ Faces a Free Energy Barrier for Binding on the Extracellular Side but Binds Spontaneously to the Intracellular Leaflet. Four $AuNP^+$−double membrane setups were simulated for 200 ns at 310 K: EC, EC with salt, IC, and IC with salt (Figure 2). On the IC side, $AuNP^+$ always approaches the membrane within 10−20 ns, with and without added salt (Figure 2c,d), and it attaches rapidly to the membrane in a manner where the functional amine groups

dx.doi.org/10.1021/jp5024026 | J. Phys. Chem. C 2014, 118, 11131−11141

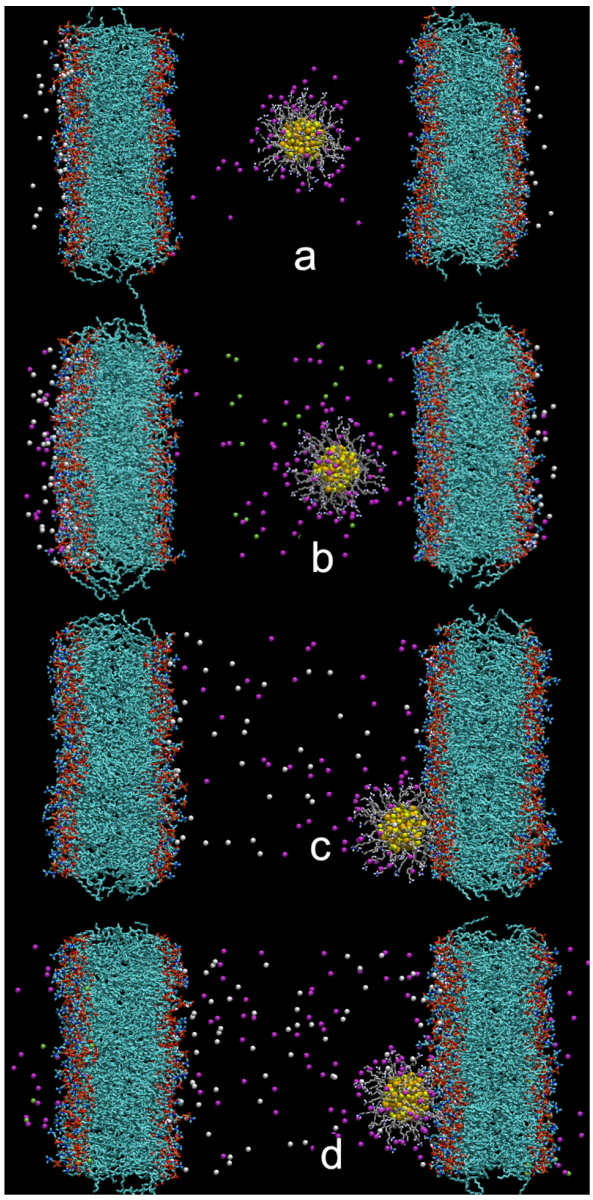

Figure 2. Visualization of $AuNP^+$ with membranes. $AuNP^+$ is placed between membranes in the extracellular (EC) and intracellular (IC) compartments. (a) EC; (b) EC with NaCl; (c) IC; (d) IC with KCl. Color code: $AuNP^+$ [Au (orange), S (yellow), alkyl chains (gray), primary amine (blue and white)]; lipids [C (cyan), O (red), P (brown), N (blue)]; ions [Na^+ (lime), Cl^- (magenta), K^+ (white)].

are in contact with the membrane surface (see Figure S1 in Supporting Information). Meanwhile, $AuNP^+$ largely fluctuates between the bilayers in the EC compartment, and it does not form direct contacts with the membrane during the time scale of the simulations (Figure 2a,b and Figure S1). Four shorter simulation replicas, 100 ns each, for systems without extra salt and with different initial conditions were performed to validate the results, providing the same outcome as above.

The fact that $AuNP^+$ does not bind spontaneously to the EC leaflet is intriguing. We considered this binding process more carefully through free energy (umbrella sampling) simulations. The results depicted in Figure 3 highlight that there is a free energy barrier of about 11.7 kJ/mol (4.7 k_BT) for the binding of

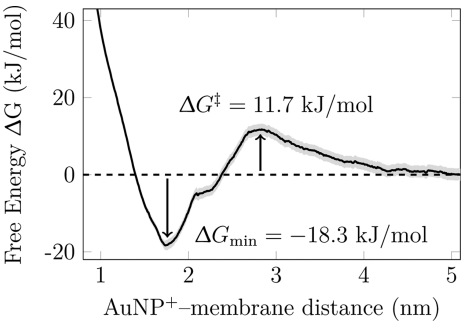

Figure 3. Free energy (umbrella sampling) profile of $AuNP^+$ adsorption to the membrane–water interface on the EC side. The simulation conditions refer to those without additional salt. The distance is measured between the $AuNP^+$ center and membrane surface plane (P atoms).

$AuNP^+$ to the EC leaflet. The free energy computations also revealed that once the barrier is crossed, the nanoparticle is stably bound to the EC leaflet at the membrane–water interface, about 1.7 nm from the membrane center, with a well depth of about 18.3 kJ/mol (7.4 k_BT). These data are in full agreement with experiments[23] as discussed in detail below.

Further, the finding that $AuNP^+$ binds to the IC leaflet is also intriguing (see Figure 2c,d), as this highlights that there is a strong force driving NP to the surface of the IC leaflet. However, the nanoparticle does not spontaneously penetrate through the membrane, neither in IC nor in EC simulations. As the discussion below shows, one of the reasons causing this is the considerable charge of the $AuNP^+$ explored here. We conclude that $AuNP^+$ binds spontaneously to the IC leaflet, but on the EC side there is a free energy barrier to cross prior to NP binding.

Cl^- Counterions Screen $AuNP^+$ but Do Not Inhibit Binding to the Intracellular Leaflet. The partial density profiles in the IC case show $AuNP^+$ in a stable contact with the membrane (see Figure 4a,b). Instead, the EC profiles in Figure 4c,d show a broader distribution for $AuNP^+$, consistent with its fluctuation around the compartment center. Each case shows a rather compact ionic cloud of Cl^- around $AuNP^+$, screening its

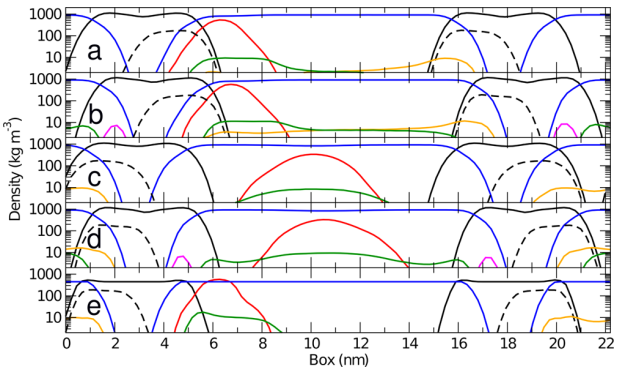

Figure 4. Partial density distributions of individual atoms/molecular groups of the $AuNP^+$ systems in (a) IC, (b) IC with salt, (c) EC, (d) EC with salt, and (e) EC constraint-released. The location $x = 0$ corresponds to the side of the simulation box. Color code: membrane (black, solid), NP (red, solid), water (blue, solid), POPS (black, dashed), K^+ (orange, solid), Cl^- (green, solid), and Na^+ (magenta, solid).

dx.doi.org/10.1021/jp5024026 | J. Phys. Chem. C 2014, 118, 11131–11141

positive charge. The halo pattern of Cl^- in the IC compartment is not as symmetric as in EC since the anion concentration has been reduced in the membrane contact zone. Furthermore, the K^+ ions have accumulated close to the opposite membrane surface with respect to $AuNP^+$ in the IC compartment, and the net negative charge of the cytosolic leaflet is more exposed to the nanoparticle. The source of this K^+ asymmetry is the overcharging effect caused by the high surface charge density of $AuNP^+$.

The halo pattern of counterions is highlighted in Figure 5, where the Cl^- concentration has been visualized for the EC and IC cases. For IC, the limited number of contacts of Cl^- with the membrane, and in particular with POPS lipids, becomes evident despite the fact that there are also K^+ ions around. There are no Cl^- counterions between the nanoparticle and the membrane as the negative charge of POPS causes repulsion. The tight space between the thiol chains of $AuNP^+$ together with a less hydrated environment makes it difficult for the relatively voluminous Cl^- to penetrate into the soft surface region of $AuNP^+$, allowing the nanoparticle surface to behave effectively as a charged wall. The terminal amino groups are distributed in equidistant positions which causes ripples in the Cl^- concentration. It is also clear that the surface charge density is not large enough to fully condense the counterions to the surface. This is expected as both Cl^- and NH_3^+ are monovalent and relatively small.[51] Under these conditions and in agreement with the Gouy−Chapman model, one expects the formation of a diffuse anionic cloud around $AuNP^+$, and this is indeed clearly seen in the anion density maps and more vaguely also in the Cl^- density profiles along the membrane normal direction (Figure 4).

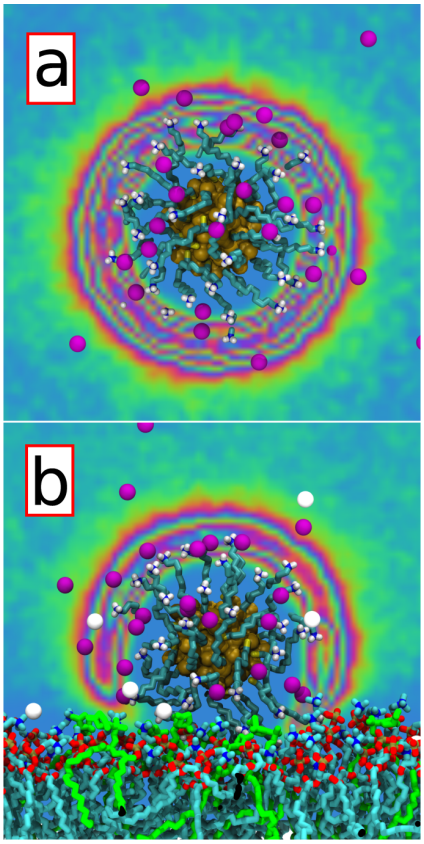

Figure 5. Visualization of Cl^- counterion density around $AuNP^+$ in (a) the EC compartment (free, as in bulk-like water) and (b) the IC compartment (membrane−water interface). The counterion concentrations have been averaged over 60 ns simulations. Suggestive transient positions for the ions are also shown as given by the color code: Cl^- (magenta) and K^+ (white), next to a membrane where POPS lipids (green) are shown separately. Color scale for the density from low to high: light-blue, green, yellow, orange, red, purple.

$AuNP^+$ Binds to the Extracellular Leaflet Once the Free Energy Barrier Has Been Overcome, and the Binding Is Stable and Suggestive of Pore Formation. The results discussed above do not seem to support the current experimental evidence that $AuNP^+$ originally outside a cell could spontaneously reach the cytoplasmic region[11,12,14,19,37,38] or how it could self-penetrate to a cell.[23] Instead, we observe in the EC compartment that the nanoparticle resists the formation of a contact with the membrane (Figure 3). This result is understandable considering the surface charges of the proximal leaflets. For $AuNP^+$ in IC, the surrounding membrane leaflet contains POPS which is negatively charged, and this clearly explains the observed attraction of the positively charged $AuNP^+$. For $AuNP^+$ in EC, the proximal leaflet is composed of pure POPC which, although being neutral as a whole, has a zwitterionic headgroup $(NH_3^+-(CH_2)_2-O-(PO_2)^--O-)$ with a positive amine group pointing toward the aqueous region. This effectively creates a positive charged layer to the membrane surface, inducing a repulsive interaction with $AuNP^+$ (Figure 3).

Recent experimental evidence on pure synthetic DSPC membranes suggests that there is a free energy barrier for approaching $AuNP^+$.[23] In these experiments, the temperature of the model system had to be risen up to 326 K in order to activate $AuNP^+$ to bind with the membrane. Experiments also showed that subsequent cooling down of the sample to a working temperature of 298 K did not terminate the binding. This suggests that once the free energy barrier has been crossed, there is a net attraction between $AuNP^+$ and the membrane. Similarly, our MD simulations highlight the presence of a free energy barrier when $AuNP^+$ approaches the EC leaflet composed of POPC lipids (see Figure 3).

Having confirmed the activated binding on the EC side, we gradually pulled $AuNP^+$ closer to the membrane using a harmonic potential. Once in contact, 0.9 nm from $AuNP^+$'s center of mass to the membrane surface, we released the constraint and simulated the system for 300 ns; this system is here referred to as "EC constraint-released". We observed $AuNP^+$ to remain attached to the membrane. The corresponding partial density profiles over the last 150 ns are shown in Figure 4e.

Once proven that $AuNP^+$ attaches to both IC (POPC/POPS) and EC (pure POPC) layers, the latter being an activated process, it is interesting to compare the contact area between $AuNP^+$ and each of the two layers (see Figure 6). In the IC leaflet, the average equilibrium distance between the $AuNP^+$ center of mass and the POPC/POPS leaflet (phosphorus atom in POPC) is 1.4 ± 0.2 nm. The contact layer shows slightly convex bending toward $AuNP^+$, allowing the system to maximize the number of POPS contacts. $AuNP^+$ then rides over the membrane surface (see Figure 6a), with occasional but clear interdigitation between the $AuNP^+$ side chains and lipid head groups. If a positive side chain of $AuNP^+$ manages to cross the positively charged POPC choline region with the help of the negatively charged phosphatidylserine

dx.doi.org/10.1021/jp5024026 | J. Phys. Chem. C 2014, 118, 11131−11141

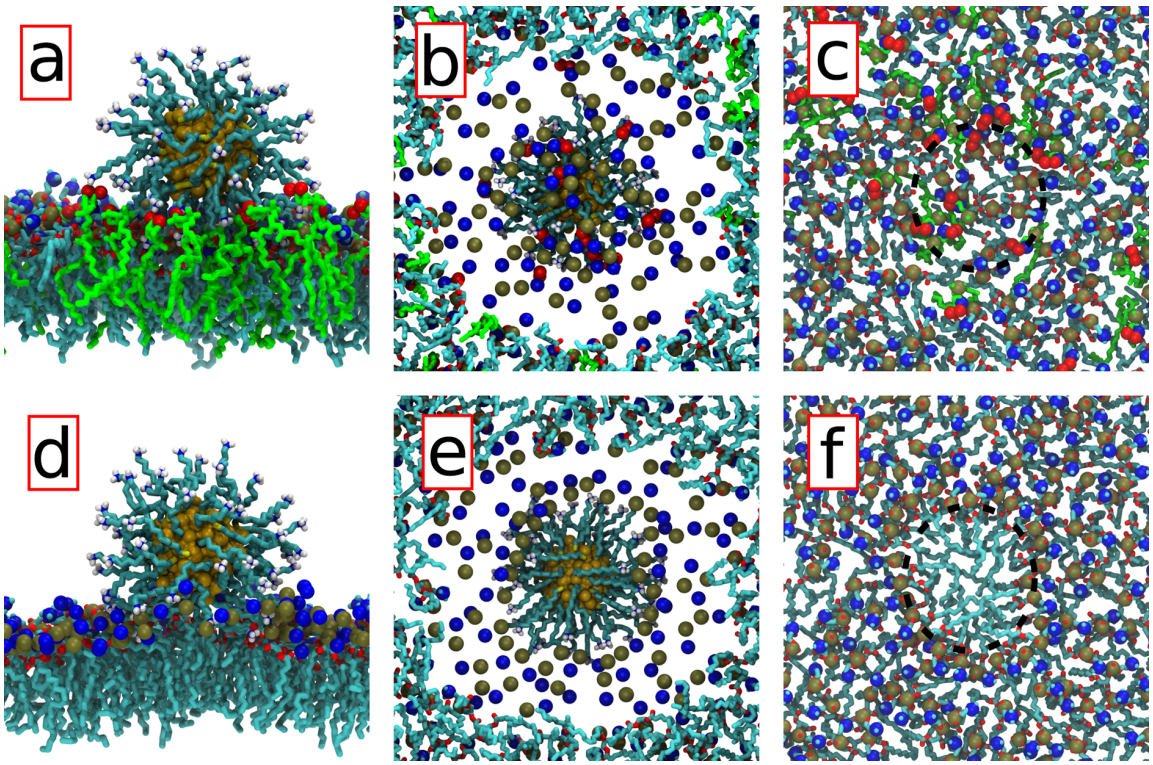

Figure 6. Morphology of the $AuNP^+$ attachment with IC (a, b, and c) and EC (d, e, and f) layers when the nanoparticle is in contact the membrane. In both cases, only the monolayer in contact with the nanoparticle is shown. Panels a and d correspond to the lateral view. Panels b and e depict the bottom view: here only the moieties in the head groups of POPC and POPS (not the glycerol or the hydrocarbon chains) below $AuNP^+$ are shown to monitor their effect on $AuNP^+$. Panels c and f illustrate the top view: here $AuNP^+$ has been removed to assess its effect on the membrane (nanoparticle position shown with a black circle). $AuNP^+$, POPS (green), and POPC are represented with rods. Head group phosphorus (khaki), amine nitrogen (blue), and serine carbonyl oxygen atoms (red) are highlighted as van der Waals spheres.

groups, it immediately becomes trapped deeper in the membrane due to the attraction of the underlying negatively charged region of the phosphate groups. Still, the most interesting feature is that $AuNP^+$ does not considerably perturb the underlying leaflet (Figure 6b,c) besides slowly recruiting POPS lipids beneath itself (Figure 6a). We discuss this in more detail below.

In the EC compartment, $AuNP^+$ positions itself partly embedded in the pure POPC layer at a distance of 1.6 ± 0.2 nm (phosphorus atom in POPC) (see Figure 6d). While having a larger separation distance than in IC, the nanoparticle appears to be embedded deeper in the induced concave curvature of the underlying layer. This slight membrane deformation allows the system to reduce the repulsion between the lipid head groups around $AuNP^+$, without exposing the hydrophobic acyl chains to the water solvent. In this case no side chain interdigitation is observed, and the lipid head groups are clearly pushed away underneath $AuNP^+$ (Figure 6f). Similarly, the facing $AuNP^+$ side chains bend toward the membrane plane, maximizing the number of contacts with the ring of the negatively charged phosphate groups (Figure 6e). This ring emerges because phosphatidylcholine groups strongly orient themselves, with the phosphates pointing toward $AuNP^+$. The nanoparticle penetration into the EC leaflet results in that the corresponding electrostatic potential (EP) maps show considerable variation in the contact area for both IC and EC (see Figure S2 in Supporting Information).

Potential Mechanism for $AuNP^+$ Translocation. In contrast to the IC system, not a single $AuNP^+$ side chain points toward the hydrophobic lipid core (along membrane normal direction), and we speculate that this could be a favorable initial stage for self-penetration. The fact that $AuNP^+$ manages to isolate its charged side groups from the hydrophobic (low dielectric constant) lipid tail groups allows it to move across the membrane without a large energy penalty. The lipids in contact with $AuNP^+$ can bend toward the membrane plane as $AuNP^+$ passes through the membrane, forming a pore. Recently reported coarse-grained simulations of $AuNP^+$ s in symmetric bilayers are in favor of this view, suggesting the formation of torus-like pores.[33] In the present case, in the absence of an artificially created electrostatic potential, the driving force pulling $AuNP^+$ into the membrane is the electrostatic attraction from the negatively charged POPS lipids on the IC side, and the described mechanism should evolve until $AuNP^+$ is fully embedded in the membrane. Importantly, prior to the translocation process, it is quite obvious that $AuNP^+$ has to neutralize/deprotonate, at least in part, since there are numerous studies showing that the translocation of drugs and other charged compounds across lipid membranes has a very high free energy barrier that is lowered substantially through neutralization.[52]

Overall, our observations are consistent with the formation of holes[53] observed in toxicity experiments.[11,12,14,19,37,38] However, our observations are not fully conclusive as no $AuNP^+$ penetration is observed during the simulations. This is due in

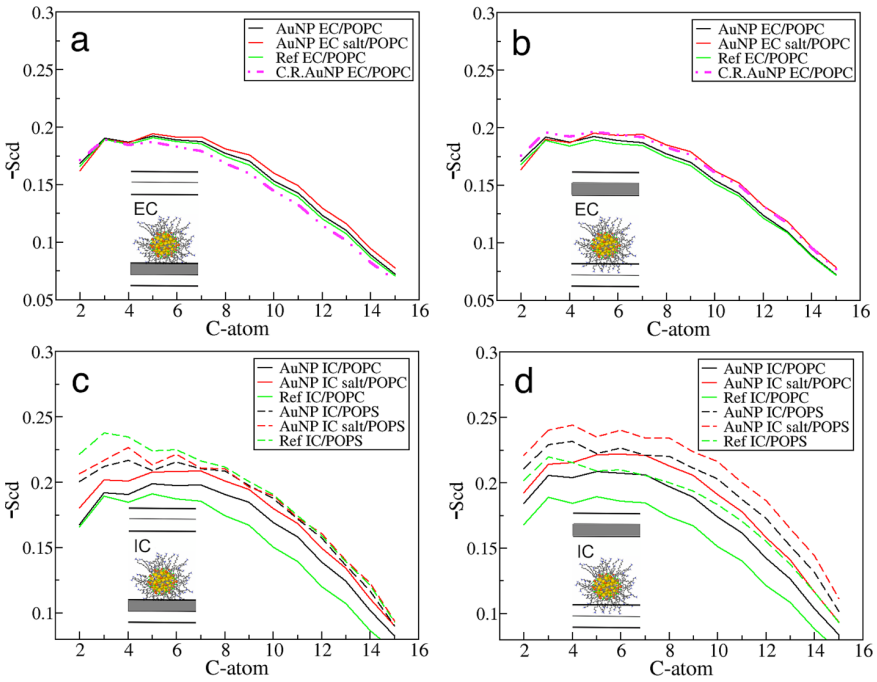

Figure 7. Order parameters ($-S_{CD}$) for the palmitoyl chains of lipids in the presence/absence of AuNP$^+$. (a) EC leaflet close to AuNP$^+$, data for POPC. (b) EC leaflet farther from AuNP$^+$, data for POPC. (c) IC leaflet closer to AuNP$^+$, data for POPC and POPS. (d) IC leaflet farther from AuNP$^+$, data for POPC and POPS. Data are given for $-S_{CD}$ in the AuNP$^+$ system without added salt (black), AuNP$^+$ system with added salt (red), and in the reference system without AuNP$^+$ or salt (green). Results for POPC (solid) and POPS (dashed) are shown separately. Data for the constraint-released (C.R.) simulation is depicted with a dashed magenta line. The results are based on sampling over 150 ns after skipping 50 ns for an equilibration phase. The results have been averaged over all the lipids in the leaflet in question.

part to the high charge concentration of the nanoparticle as well as the geometrical constraints inherent to the double bilayer setup used in the simulations. We discuss both of these features in the end of the article.

Structural Changes at the Extracellular and Intracellular Leaflets Are Consistent with the Proposed Mechanism. AuNP$^+$-induced perturbations in membrane structure were determined by considering changes in the lipid hydrocarbon chain order parameter (S_{CD}). The results are presented in Figure 7. The order parameters for the saturated palmitoyl tail (*sn*-1) of both POPC and POPS were calculated for both leaflets sharing the compartment with AuNP$^+$. The oleoyl (*sn*-2) tail provided qualitatively the same information (data not shown). Overall, all the S_{CD} profiles show that on the IC side AuNP$^+$ induces increasing order for POPC, and the increase is quite substantial. In addition, increasing the salt concentration to match the biological condition (~150 mM) increases the ordering further. Meanwhile, the results also show that AuNP$^+$ affects the POPC order very little on the EC side. Only for the constraint-released case where the nanoparticle is in direct contact with the leaflet, a slight effect can be observed (Figure 7a), but the change is marginal.

For the IC compartment, overall the ordering effects of AuNP$^+$ and salt are hence significantly amplified for both POPC and POPS, but the effect depends on the region considered. In the contact layer AuNP$^+$ induces clear ordering in POPC alkyl chains, but POPS actually becomes slightly disordered close to the head groups (Figure 7c). The underlying reason for this is the interdigitation of the AuNP$^+$ side chains in the contact layer, especially with POPS accumulated beneath the nanoparticle. In the opposite layer that is farther from the nanoparticle, we observe ordering to take place when AuNP$^+$ is present, and this effect is amplified with increasing salt (Figure 7d). The increased K$^+$ concentration close to the membrane causes this phenomenon[54,55] (see Figure 4a).

The results are in agreement with the self-penetration mechanism. When AuNP$^+$ approaches the EC leaflet, the high fluidity of the lipid layer remains unaffected, and this allows quick reordering of the lipids to form a hole around AuNP$^+$.[11,12,14,19,37,38] Instead, on the IC side the ordering increases in the contact layer, rendering this layer more impermeable. On the basis of this finding and the attractive electrostatic interaction (see Figures S1 and S2), one should expect AuNP$^+$ accumulation on the cytosolic layer.

Hydrogen Bonding Shows Binding at the Intracellular Leaflet To Be More Stable. For the overall view, it is important to discuss the stability of the nanoparticle contacts at the membrane interface. This is a topic largely related to hydrogen bonding (H-bonding) in atomic resolution and electrostatic interactions. To this end, we consider the interaction of AuNP$^+$ with water, lipids, and Cl$^-$ ions.

The average number and the lifetime of H-bonds and ion contacts between AuNP$^+$ and solvent (Table 1) show clear differences between the IC and EC solutions: The total number of H-bonds between water and AuNP$^+$ are 141.2 ± 3.7 and 169.7 ± 0.1, respectively, and also the number of ion contacts differs, 1.4 ± 0.8. and 4.9 ± 0.2. The number of water contacts is close to three per amine group in EC (60 groups), as expected, but the number of direct ion contacts is small despite the counterion cloud around the nanoparticle (see Figure 5). AuNP$^+$ attaches to the cytosolic leaflet in IC, and hence it has

dx.doi.org/10.1021/jp5024026 | J. Phys. Chem. C 2014, 118, 11131−11141

Table 1. Hydrogen Bonds and Ionic Contacts between $AuNP^+$ and Solvent/Lipids[a]

compartment	A	N_A	τ_A [ps]
IC	H_2O	141.2 ± 3.7	10.3 ± 0.8
	Cl^-	1.4 ± 0.8	11.3 ± 2.5
	lipid	78 ± 12	99.9 ± 19.7
IC (0.15 M KCl)	H_2O	137.3 ± 4.1	9.5 ± 1.3
	Cl^-	3.6 ± 0.8	6.4 ± 1.4
	lipid	96 ± 12	102.6 ± 15.0
EC	H_2O	169.7 ± 0.1	5.8 ± 0.2
	Cl^-	4.9 ± 0.2	5.5 ± 0.3
	lipid		
EC (0.15 M NaCl)	H_2O	169.7 ± 0.1	5.8 ± 0.1
	Cl^-	3.4 ± 0.2	5.0 ± 0.6
	lipid		
EC (C.R.)	H_2O	138.6 ± 1.7	11.9 ± 0.7
	Cl^-	7.3 ± 0.3	8.0 ± 1.0
	lipid	18 ± 6	224.3 ± 42.7

[a] N_A is the average number of hydrogen bonds and contacts, and τ_A is the average lifetime of the contacts, per solvent molecule/lipid. EC and IC are extracellular and intracellular compartments, respectively. C.R. refers to the EC constraint-released case.

fewer available terminal groups to make contacts with water and/or counterions. This is reflected not only in the number of H-bonds but also in contact lifetimes, which are considerably larger in IC. $AuNP^+$ moves freely in EC, whereas its movement is restricted in IC by the interactions with the membrane—the contacts are less interrupted and consequently last longer. For EC, the values of the number of contacts and lifetimes are similar to those in Heikkilä et al.[36] for the same $AuNP^+$ in aqueous solution without the presence of bilayers, 170.8 ± 0.2 and 6.5 ± 0.2 ps, respectively. Adding 150 mM of salt (KCl, NaCl) to the systems does not significantly affect the H-bonds between $AuNP^+$ and solvent. The AuNP–membrane contacts are numerous due to the NH_3^+ groups, and their lifetimes are of the order 100 ps, illustrating that AuNP moves relatively slowly along the membrane surface.

The situation changes in EC when $AuNP^+$ is pulled onto the POPC leaflet (constraint-released case). The interaction with water has decreased as the effective solvent interface of $AuNP^+$ is smaller, whereas the number of Cl^- contacts is larger, reflecting changes in the dielectric medium (water/membrane) and $AuNP^+$ screening charge. Comparing with the IC case, Cl^- contact values are significantly higher, corresponding to a tighter Cl^- cloud around $AuNP^+$ in the EC constraint-released system. Despite being attached to the membrane, there are not many H-bonds forming between $AuNP^+$ and the lipid head groups in accordance with Figure 6d–f.

Summarizing, the analysis based on H-bonding and contacts indicates that when $AuNP^+$ is bound to a membrane, it is more stable at the IC side compared to the EC leaflet.

Why We Have Not Observed Spontaneous Permeation in the Simulations? It is clear that this is, in part, due to the high charge of $AuNP^+$ studied here. Regardless of the environment, $AuNP^+$ is always equally charged (+60 e). A more realistic model to consider penetration would include deprotonation of the amine groups while $AuNP^+$ passes through the low dielectric lipid tail region (see discussion below). Based on earlier simulations, it is clear that deprotonation (neutralization of the nanoparticle) would strongly promote permeation across the membrane.[52] However, consideration of this topic is out of the scope of this work.

The substantial charge of the nanoparticle is a seemingly simple reason to explain why no translocation was observed in simulations. This view is supported by the fact that in experiments the coverage of positively charged alkyl chains rarely exceed 70% in contrast to 100% in our case. Also, the terminal choline groups are significantly more bulky than our small amine groups, and the positive charge is more delocalized. However, according to experimental results, also cationic Au nanoparticles with terminal groups which cannot deprotonate have proven to be capable of trespassing the membrane.[23] Therefore, deprotonation of the amine groups can explain the experimentally observed translocation rate only partially.

As for methodological matters related to simulations only, the use of the double bilayer setup hampers the penetration process as the lateral dimensions of the two membranes are coupled to each other via the simulation box and the periodic boundary conditions used (lateral strain). These imply that in the simulations we have done the bilayer through which the nanoparticle is translocating is not in a tensionless state, as it should be, and the tension arising from the use of the double bilayer setup will certainly increase the translocation free energy barrier. This issue could be minimized by using membrane systems much larger than the one employed in this work, but we consider it to be beyond the scope of this work. It should be noted that recent CG simulations using a double bilayer model (1032 lipids per membrane) achieved $AuNP^+$ translocation by using an external electric field of −1.5 eV, mimicking the transmembrane potential,[33] in favor of the views discussed above.

CONCLUSIONS

The nanoparticle–membrane interaction is very relevant for studying biomedical applications and potential toxic effects of nanomaterials. In this work, we have performed atomistic MD simulations of cationic gold nanoparticles ($AuNP^+$) in both extracellular (EC) and intracellular (IC) environments in order to test their tendency to penetrate through the cell membrane and shed light on the molecular mechanisms involved. For this purpose, we have applied a double asymmetric bilayer system, using animal plasma-like membranes, with two solvent compartments (EC and IC). Our theoretical approach is unique, and the double bilayer setup differs from most previous coarse-grained simulations. The atomistic description enables us to unlock the roles of the underlying interactions and chemical features in considerable detail.

All simulations show unequivocally that electrostatics drives $AuNP^+$ to move fast toward the negatively charged surface of the cytosolic leaflet, while it experiences a free energy barrier to bind with the extracellular leaflet, in agreement with experiments.[23] These results are understandable considering the opposite overall surface charge in the two leaflets. While the surface charge in the IC leaflet is dominated by the negative charge of the POPS headgroup (~20% of the lipids in the leaflet), in the case of the EC leaflet constituted by pure zwitterionic POPC, there is a local positive surface charge due to the positively charged choline groups facing water solvent. In other words, the distinct behavior, selectivity, arises from the specific lipid composition of each leaflet.

The results also highlight the active role of ions regulating the binding with a membrane. The counterions not only play a critical role by shielding the large charge of $AuNP^+$ during the

dx.doi.org/10.1021/jp5024026 | J. Phys. Chem. C 2014, 118, 11131–11141

transit to the membrane, but they also foster the process by migration to compensate for electrostatic potential imbalances. The role of counterions in this context was most evident on the IC side, and this process was further supported by POPS lipids that were observed to play an active role by slightly popping out of the membrane and capturing the nanoparticle, as the membrane reorganized through lateral diffusion of POPS to concentrate right underneath $AuNP^+$.

As mentioned above, $AuNP^+$ was found to experience a free energy barrier to bind with the EC leaflet, in agreement with experiments.[23] This may appear puzzling given that several *in vivo* experiments have shown $AuNP^+$ to interact with the EC layer spontaneously.[11,12,14,19,37,38] However, in real plasma membranes other membrane bound components, such as the negatively charged glycocalyx,[56] can play a similar role as POPS in the cytosolic compartment, thus facilitating the contact of $AuNP^+$ and the EC layer.

What would be a plausible mechanism for $AuNP^+$ permeation? $AuNP^+$ attaches to both the IC (POPC/POPS) and EC (POPC) layers in a stable manner, the latter taking place after the crossing of a free energy barrier. However, the nature of $AuNP^+$ membrane interaction differs significantly.

On the EC side, there are no lipid head groups beneath the nanoparticle as they migrate to the boundary of the $AuNP^+$ contact region and orient themselves with the phosphate groups pointing toward $AuNP^+$. The side chains of $AuNP^+$ also bend toward the membrane plane to be in contact with the surface phosphates. As a result, the $AuNP^+$ interacts with the EC membrane in a very singular way: Below the nanoparticle, hydrophobic interactions of the lipid tails and the mainly hydrophobic alkanethiol tails of $AuNP^+$ prevail, while in the borders of its projection there are ionic contacts between $AuNP^+$ amine terminal groups and oriented phosphate groups of POPC. This membrane reorganization gives room for the formation of a patch that is largely hydrophobic. Meanwhile, on the IC side, there is interdigitation between $AuNP^+$ side chains and lipid head groups and considerable enrichment of phosphatidylserines under $AuNP^+$.

We speculate that together these constitute the initial stage for pore formation, possibly having the torus shape[33,53] seen in experiments.[11,12,14,19,37,38] After $AuNP^+$ has adsorbed to the EC leaflet, at least partial deprotonation of the amine groups will occur before permeation takes place through formation of a pore. The proposed mechanism could be tested in experiments by decreasing the length of $AuNP^+$ side chains and monitoring the hole formation/toxicity. Presumably, shorter side chains will result in less holes/lower toxicity as the initial stages of the pore formation is hampered.

Combining these results, we propose that $AuNP^+$ is able to approach and attach to the plasma membrane aided by negatively charged membrane-bound components, e.g. glycocalyx. After this, $AuNP^+$ can form a large pore while moving toward the cytosolic layer, and we expect that the cytotoxicity of $AuNP^+$ arises here. The nanoparticle can simply destabilize the membrane as seen in experiments[23] or favor the diffusion of phosphatidylserine lipids from the cytoplasmic leaflet to the extracellular one through the pore boundaries, which can potentially initiate apoptosis. Finally, in case $AuNP^+$ manages to permeate all the way to the cytoplasm, it will strongly attach to the inner IC leaflet and accumulate. At this point, increasing nanoparticle concentration is expected to disturb many critical molecular functions due to the high $AuNP^+$ charge which can alter membrane protein conformations.

■ ASSOCIATED CONTENT

Supporting Information

Additional data for computational methods, nanoparticle distance from the membrane as a function of time for several MD simulations, and electrostatic potential profiles as contour plots of the 3D distributions. This material is available free of charge via the Internet at http://pubs.acs.org.

■ AUTHOR INFORMATION

Corresponding Author

*E-mail: jaakko.akola@tut.fi (J.A.).

Author Contributions

$^{\nabla}$E.H. and H.M.-S. contributed equally to the article.

Notes

The authors declare no competing financial interest.

■ ACKNOWLEDGMENTS

We thank Pu-Chun Ke for inspiring discussions. The computations were performed on the Juropa (Intel Xeon 5570) and Cray XT4/XT5 computers in the Forschungszentrum Jülich (Germany) and CSC - IT Centre for Science Ltd (Espoo, Finland). Financial support is provided from the Academy of Finland through its Centre of Excellence Programs (Project 251748, E. Heikkilä and J. Akola; Project 272130, H. Martinez-Seara, M. Javanainen and I. Vattulainen). H. Häkkinen is funded through the Academy of Finland project 128341, and I. Vattulainen acknowledges support from the European Research Council (Advanced Grant CROWDED-PRO-LIPIDS).

■ REFERENCES

(1) Leifert, A.; Pan-Bartnek, Y.; Simon, U.; Jahnen-Dechent, W. Molecularly Stabilised Ultrasmall Gold Nanoparticles: Synthesis, Characterization and Bioactivity. *Nanoscale* **2013**, *5*, 6224−6242.

(2) Shichibu, Y.; Negishi, Y.; Tsunoyama, H.; Kanehara, M.; Teranishi, T.; Tsukuda, T. Extremely High Stability of Glutathionate-Protected Au_{25} Clusters Against Core Etching. *Small* **2007**, *3*, 835−839.

(3) Lopez-Acevedo, O.; Kacprzak, K. A.; Akola, J.; Häkkinen, H. Quantum Size Effects in Ambient CO Oxidation Catalysed by Ligand-Protected Gold Clusters. *Nat. Chem.* **2010**, *2*, 329−334.

(4) Murphy, C. J.; Anand, M. G.; Stone, J. W.; Sisco, P. N.; Alkinaly, A. M.; Goldsmith, E. C.; Baxter, S. C. Gold Nanoparticles in Biology: Beyond Toxicity to Cellular Imaging. *Acc. Chem. Res.* **2008**, *41*, 1721−1730.

(5) Daniel, M.; Astruc, D. Gold Nanoparticles: Assembly, Supramolecular Chemistry, Quantum-Size-Related Properties, and Applications Toward Biology, Catalysis, and Nanotechnology. *Chem. Rev.* **2004**, *104*, 293−346.

(6) Sperling, R. A.; Gil, P. R.; Zhang, F.; Zanella, M.; Parak, W. J. Biological Applications of Gold Nanoparticles. *Chem. Soc. Rev.* **2008**, *37*, 1896−1908.

(7) Jin, R. Quantum Sized Thiolate-Protected Gold Nanoclusters. *Nanoscale* **2010**, *2*, 343−362.

(8) Dykman, L.; Khlebtsov, N. Gold Nanoparticles in Biomedical Applications: Recent Advances and Perspectives. *Chem. Soc. Rev.* **2012**, *41*, 2256−2282.

(9) Dreaden, E. C.; Alkilany, A. M.; Huang, X.; Murphy, C. J.; El-Sayed, M. A. The Golden Age: Gold Nanoparticles for Biomedicine. *Chem. Soc. Rev.* **2012**, *41*, 2740−2779.

(10) Nel, A.; Xia, T.; Mädler, L.; Ning, L. Toxic Potential of Materials at the Nanolevel. *Science* **2006**, 622−627.

(11) Khlebtsov, N.; Dykman, L. Biodistribution and Toxicity of Engineered Gold Nanoparticles: A Review of *in Vitro* and *in Vivo* Studies. *Chem. Soc. Rev.* **2011**, *40*, 1647−1671.

(12) Hirano, A.; Yoshikawa, H.; Matsushita, S.; Yamada, Y.; Shiraki, K. Adsorption and Disruption of Lipid Bilayers by Nanoscale Protein Aggregates. *Langmuir* **2012**, *28*, 3887−3895.
(13) Álvarez, Y. D.; Fauerbach, J. A.; Pellegrotti, J. V.; Jovin, T. M.; Jares-Erijman, E. A.; Stefani, F. D. Influence of Gold Nanoparticles on the Kinetics of a-Synuclein Aggregation. *Nano Lett.* **2013**, *13*, 6156−6163.
(14) Goodman, C. M.; McCusker, C. D.; Yilmaz, T.; Rotello, V. M. Toxicity of Gold Nanoparticles Functionalized with Cationic and Anionic Side Chains. *Bioconjugate Chem.* **2004**, *15*, 897−900.
(15) Lewinski, N.; Colvin, V.; Drezek, R. Cytotoxicity of Nanoparticles. *Small* **2008**, *4*, 26−49.
(16) Alkilany, A. M.; Nagaria, P. K.; Hexel, C. R.; Shaw, T. J.; Murphy, C. J.; Wyatt, M. D. Cellular Uptake and Cytotoxicity of Gold Nanorods: Molecular Origin of Cytotoxicity and Surface Effects. *Small* **2009**, *5*, 701−708.
(17) Pan, Y.; Leifert, A.; Ruau, D.; Neuss, S.; Bornemann, J.; Schmid, G.; Brandau, W.; Simon, U.; Jahnen-Dechent, W. Gold Nanoparticles of Diameter 1.4 nm Trigger Necrosis by Oxidative Stress and Mitochondrial Damage. *Small* **2009**, *5*, 2067−2076.
(18) Verma, A.; Uzun, O.; Hu, Y.; Hu, Y.; Han, H.-S.; Watson, N.; Chen, S.; D.J, I.; Stellacci, F. Surface-Structure-Regulated Cell-Membrane Penetration by Monolayer-Protected Nanoparticles. *Nat. Mater.* **2008**, *7*, 588−595.
(19) Mecke, A.; Lee, D.-K.; Ramamoorthy, A.; Orr, B. G.; Banaszak Holl, M. M. Synthetic and Natural Polycationic Polymer Nanoparticles Interact Selectively with Fluid-Phase Domains of DMPC Lipid Bilayers. *Langmuir* **2005**, *21*, 8588−8590.
(20) Leroueil, P. R.; Berry, S. A.; Duthie, K.; Han, G.; Rotello, V. M.; McNerny, D. Q.; Baker, J. R., Jr.; Orr, B. G.; Banaszak Holl, M. M. Wide Varieties of Cationic Nanoparticles Induce Defects in Supported Lipid Bilayers. *Nano Lett.* **2008**, *8*, 420−424.
(21) Chen, J.; Hessler, J. A.; Putchakayala, K.; Panama, B. K.; Khan, D. P.; Hong, S.; Mullen, D. G.; DiMaggio, S. C.; Som, A.; Tew, G. N.; Lopatin, A. N.; Baker, J. R.; Banaszak Holl, M. M.; Orr, B. G. Cationic Nanoparticles Induce Nanoscale Disruption in Living Cell Plasma Membranes. *J. Phys. Chem. B* **2009**, *113*, 11179−11185.
(22) Van Lehn, R.; Atukorale, P. U.; Carney, R. P.; Yang, Y.-S.; Stellacci, F.; Irvine, D. J.; Alexander-Katz, A. Effect of Particle Diameter and Surface Composition on the Spontaneous Fusion of Monolayer-Protected Gold Nanoparticles with Lipid Bilayers. *Nano Lett.* **2013**, *13*, 4060−4067.
(23) Tatur, S.; Maccarini, M.; Barker, R.; Nelson, A.; Fragneto, G. Effect of Functionalized Gold Nanoparticles on Floating Lipid Bilayers. *Langmuir* **2013**, *29*, 6606−6614.
(24) Fields-Zinna, C. A.; Sardar, R.; Beasley, C. A.; Murray, R. W. Electrospray Ionization Mass Spectrometry of Intrinsically Cationized Nanoparticles $[Au_{144/146}(SC_{11}H_{22}N(CH_2CH_3)_3^+)_x(S(CH_2)_5CH_3)_y]^{x+}$. *J. Am. Chem. Soc.* **2009**, *131*, 16266−16271.
(25) Qian, H.; Jin, R. Controlling Nanoparticles with Atomic Precision: The Case of $Au_{144}(SCH_2CH_2Ph)_{60}$. *Nano Lett.* **2009**, *9*, 4083−4087.
(26) Lopez-Acevedo, O.; Akola, J.; Whetten, R.; Grönbeck, H.; Häkkinen, H. Structure and Bonding in the Ubiquitous Icosahedral Metallic Gold Cluster $Au_{144}(SR)_{60}$. *J. Phys. Chem. C* **2009**, *113*, 5035−5038.
(27) Qian, H.; Jin, R. Ambient Synthesis of $Au_{144}(SR)_{60}$ Nanoclusters in Methanol. *Chem. Mater.* **2011**, *23*, 2209−2217.
(28) Li, Y.; Chen, X.; Gu, N. Computational Investigation of Interaction between Nanoparticles and Membranes: Hydrophobic/Hydrophilic Effect. *J. Phys. Chem. B* **2008**, *112*, 16647−16653.
(29) Li, Y.; Gu, N. Thermodynamics of Charged Nanoparticle Adsorption on Charge-Neutral Membranes: A Simulation Study. *J. Phys. Chem. B* **2010**, *114*, 2749−2754.
(30) Lin, J.; Zhang, H.; Chen, Z.; Zheng, Y. Penetration of Lipid Membranes by Gold Nanoparticles: Insights into Cellular Uptake, Cytotoxicity, and Their Relationship. *ACS Nano* **2010**, *4*, 5421−5429.
(31) Li, Y.; Li, X.; Li, Z.; Gao, H. Surface-Structure-Regulated Penetration of Nanoparticles across a Cell Membrane. *Nanoscale* **2012**, *4*, 3768−3775.
(32) Van Lehn, R. C.; Alexander-Katz, A. Free Energy Change for Insertion of Charged, Monolayer-Protected Nanoparticles into Lipid Bilayers. *Soft Matter* **2014**, *10*, 648−658.
(33) Lin, J.; Alexander-Katz, A. Cell Membranes Open "Doors" for Cationic Nanoparticles/Biomolecules: Insights into Uptake Kinetics. *ACS Nano* **2013**, *7*, 10799−10808.
(34) Li, Y.; Yang, Z.; Hu, N.; Zhou, R.; Chen, X. Insights into Hydrogen Bond Dynamics at the Interface of the Charged Monolayer-Protected Au Nanoparticle from Molecular Dynamics Simulation. *J. Chem. Phys.* **2013**, *138*, 184703−1−9.
(35) Van Lehn, R. C.; Alexander-Katz, A. Structure of Mixed-Monolayer-Protected Nanoparticles in Aqueous Salt Solution from Atomistic Molecular Dynamics Simulations. *J. Phys. Chem. C* **2013**, *117*, 20104−20115.
(36) Heikkilä, E.; Gurtovenko, A.; Martinez-Seara, H.; Vattulainen, I.; Häkkinen, H.; Akola, J. Atomistic Simulations of Functional $Au_{144}(SR)_{60}$ Gold Nanoparticles in Aqueous Environment. *J. Phys. Chem. C* **2012**, *116*, 9805−9815.
(37) Ruenraroengsak, P.; Novak, P.; Berhanu, D.; Thorley, A. J.; Valsami-Jones, E.; Gorelik, J.; Korchev, Y. E.; Tetley, T. D. Respiratory Epithelial Cytotoxicity and Membrane Damage (Holes) Caused by Amine-Modified Nanoparticles. *Nanotoxicology* **2012**, *6*, 94−108.
(38) Banaszak Holl, M. M. Nanotoxicology: A Personal Perspective. *WIREs Nanomed. Nanobiotechnol.* **2009**, *1*, 353−359.
(39) Gurtovenko, A. A. Asymmetry of Lipid Bilayers Induced by Monovalent Salt: Atomistic Molecular Dynamics Study. *J. Chem. Phys.* **2005**, *122*, 244902.
(40) Van Der Spoel, D.; Lindahl, E.; Hess, B.; Groenhof, G.; Mark, A. E.; Berendsen, H. J. C. GROMACS: Fast, Flexible and Free. *J. Comput. Chem.* **2005**, *26*, 1701−1718.
(41) Berger, O.; Edholm, O.; Jähnig, F. Molecular Dynamics Simulations of a Fluid Bilayer of Dipalmitoylphosphatidylcholine at Full Hydration, Constant Pressure, and Constant Temperature. *Biophys. J.* **1997**, *72*, 2002−2013.
(42) Tieleman, D. P.; Berendsen, H. J. C. A Molecular Dynamics Study of the Pores Formed by Escherichia Coli OmpF Porin in a Fully Hydrated Palmitoyloleoylphosphatidylcholine Bilayer. *Biophys. J.* **1998**, *74*, 2786−2801.
(43) Bachar, M.; Brunelle, P.; Tieleman, D. P.; Rauk, A. Molecular Dynamics Simulation of a Polyunsaturated Lipid Bilayer Susceptible to Lipid Peroxidation. *J. Phys. Chem. B* **2004**, *108*, 7170−7179.
(44) Mukhopadhyay, P.; Monticelli, L.; Tieleman, D. P. Molecular Dynamics Simulation of a Palmitoyl-Oleoyl Phosphatidylserine Bilayer with Na^+ Counterions and NaCl. *Biophys. J.* **2004**, *86*, 1601−1609.
(45) Berendsen, H. J. C.; Postma, J. P. M.; van Gunsteren, W. F.; Hermans, J. In *Intermolecular Forces*; Pullman, B., Ed.; Reidel: Dordrecht, 1981; Chapter Interaction models for water in relation to protein hydration.
(46) Tieleman, D. P.; Berendsen, H. J. C. Molecular Dynamics Simulations of a Fully Hydrated Dipalmitoylphosphatidylcholine Bilayer with Different Macroscopic Boundary Conditions and Parameters. *J. Chem. Phys.* **1996**, *105*, 4871−4880.
(47) Berendsen, H. J. C.; Postma, J. P. M.; Van Gunsteren, W. F.; Dinola, A.; Haak, J. R. Molecular Dynamics with Coupling to an External Bath. *J. Chem. Phys.* **1984**, *81*, 3684−3690.
(48) Essmann, U. L.; Perera, L.; Berkowitz, M. L.; Darden, T.; Lee, H.; Pedersen, L. G. A. Smooth Particle Mesh Ewald Method. *J. Chem. Phys.* **1995**, *103*, 8577−8593.
(49) Torrie, G. M.; Valleau, J. P. Nonphysical Sampling Distributions in Monte Carlo Free-Energy Estimation: Umbrella Sampling. *J. Comput. Phys.* **1977**, *23*, 187−199.
(50) Hub, J. S.; de Groot, B. L.; van der Spoel, D. g_wham - A Free Weighted Histogram Analysis Implementation Including Robust Error and Autocorrelation Estimates. *J. Chem. Theory Comput.* **2010**, *6*, 3713−3720.

(51) Lund, M.; Jagoda-Cwiklik, B.; Woodward, C. E.; Vácha, R.; Jungwirth, P. Dielectric Interpretation of Specificity of Ion Pairing in Water. *J. Phys. Chem. Lett.* **2010**, *1*, 300−303.
(52) Cramariuc, O.; Rog, T.; Javanainen, M.; Monticelli, L.; Polishchuk, A. V.; Vattulainen, I. Mechanism for Translocation of Fluoroquinolones across Lipid Membranes. *Biochim. Biophys. Acta* **2012**, *1818*, 2563−2571.
(53) Gurtovenko, A. A.; Anwar, J.; Vattulainen, I. Defect-Mediated Trafficking across Cell Membranes: Insights from In Silico Modelling. *Chem. Rev.* **2010**, *110*, 6077−6103.
(54) Gurtovenko, A. A.; Vattulainen, I. Effect of NaCl and KCl on Phosphatidylcholine and Phosphatidylethanolamine Lipid Membranes: Insight from Atomic-Scale Simulations for Understanding Salt-Induced Effects in the Plasma Membrane. *J. Phys. Chem. B* **2008**, *112*, 1953−1962.
(55) Magarkar, A.; Karakas, E.; Stepniewski, M.; Rog, T.; Bunker, A. Molecular Dynamics Simulation of PEGylated Bilayer Interacting with Salt Ions: A Model of the Liposome Surface in the Bloodstream. *J. Phys. Chem. B* **2012**, *116*, 4212−4219.
(56) Tarbell, J. M.; Pahakis, M. Y. Mechanotransduction and the Glycocalyx. *J. Int. Med.* **2006**, *259*, 339−350.

III

Atomistic simulations of anionic $Au_{144}(SR)_{60}$ nanoparticles interacting with asymmetric model lipid membranes

Elena Heikkilä,[†,‡] Hector Martinez-Seara,[†] Andrey A. Gurtovenko,[¶,§] Ilpo Vattulainen,[†,∥] and Jaakko Akola*[,†,‡,⊥]

Department of Physics, Tampere University of Technology, P.O. Box 692, FI-33101 Tampere, Finland, COMP Centre of Excellence, Department of Applied Physics, Aalto University, FI-00076 AALTO, Finland, Institute of Macromolecular Compounds, Russian Academy of Sciences, Bolshoi Prospect 31, V.O., St. Petersburg, 199004, Russia, Department of Molecular Biophysics, Faculty of Physics, St. Petersburg State University, St. Petersburg, 198504,Russia, Center for Biomembrane Physics (MEMPHYS), University of Southern Denmark, Odense, DK-5230 Denmark, and PGI-1, Forschungszentrum Jülich, D-52425 Jülich, Germany

E-mail: jaakko.akola@tut.fi

KEYWORDS: Gold nanoparticle, anionic nanoparticle, lipid bilayer, plasma membrane, molecular dynamics, atomistic simulations

*To whom correspondence should be addressed
[†]Tampere University of Technology
[‡]Aalto University
[¶]Russian Academy of Sciences
[§]St. Petersburg State University
[∥]University of Southern Denmark [⊥]Forschungszentrum Jülich

Abstract

Experimental observations indicate that the interaction between nanoparticles and lipid membranes varies according to the nanoparticle charge and the chemical nature of their protecting side groups. We report atomistic simulations of an anionic Au nanoparticle ($AuNP^{-}$) interacting with membranes whose lipid composition and transmembrane distribution are to a large extent consistent with real plasma membranes of eukaryotic cells. To this end, we use a model system which comprises two cellular compartments, extracellular and cytosolic, divided by two asymmetric lipid bilayers. The simulations clearly show that $AuNP^{-}$ attaches to the extracellular membrane surface within a few tens of nanoseconds, while it avoids contact with the membrane on the cytosolic side. This behavior stems from several factors. In essence, when the nanoparticle interacts with lipids in the extracellular compartment, it forms relatively weak contacts with the zwitterionic head groups (in particular choline) of the phosphatidylcholine lipids. Consequently, $AuNP^{-}$ does not immerse deeply in the leaflet, enabling, *e.g.*, lateral diffusion of the nanoparticle along the surface. On the cytosolic side, $AuNP^{-}$ remains in the water phase due to Coulomb repulsion that arises from negatively charged phosphatidylserine lipids interacting with $AuNP^{-}$. A number of structural and dynamical features resulting from these basic phenomena are discussed. We close the article with a brief discussion of potential implications.

1 Introduction

Gold nanoparticles (AuNPs) are useful in medical applications, such as in targeted drug delivery, drug release, and photo-thermal therapy.[1,2] However, nanoscale gold can also cause harmful side effects for living organisms that induce cell death.[3,4] In particular, cationic nanoparticles of 2 nm diameter or less have an enhanced cytotoxic activity,[5–9] as demonstrated for 1.4 nm AuNPs, which were observed to cause necrosis and

mitochodrial damage to various cell lines.[10] Experimental results suggest self-penetration as the potential membrane translocation mechanism. The process is affected by the AuNP charge and the composition of the protecting ligand shell. Cationic AuNPs with an alternating pattern of aliphatic (hydrophobic) and functionalized side groups, the so-called striped AuNPs, show increased penetration activity in comparison to randomly distributed functionalized side groups.[11] Therefore, it can be also concluded that the role of the gold core itself is less important for the translocation process due to the crowding of surrounding surfactants. The penetration activity of cationic AuNPs has been reported to generate holes in model and living membranes, where the level of disruption depends on the initial phase of the lipid bilayer.[5,12–14]

Anionic gold nanoparticles appear to have less effect on membranes. However, also anionic nanoparticles have been shown to interact with cells, and it is of importance to shed light on the details of these interactions on cellular level. Furthermore, understanding what makes anionic nanoparticles less active on cells can promote the development of safer and less toxic nanoparticle applications. Recently, it was demostrated that anionic striped AuNPs, which comprise an amphiphilic surface, can permeate non-disruptively through model membranes with size-dependent activity.[15] Furthermore, the nanoparticle-membrane interaction has been studied for 2 nm diameter AuNPs and model membranes by Tatur *et al*.[16] by following the activity of floating AuNPs between single-component bilayers comprised of zwitterionic DSPC lipids (1,2-distearoyl-*sn*-glycero-3-phosphocholine). The neutron reflectometry measurements indicated that AuNPs with cationic terminal groups penetrate inside the hydrophobic bilayer interior (after elevating the temperature up to 53°C) and result in membrane disruption at increased concentrations. There was no such effect observed for anionic AuNPs, which stayed outside the lipid bilayers. The results by Tatur *et al*. for model membranes provide a valuable reference for simulations

enabling a direct comparison between theory and experiments as there are no complicating factors arising from other components in real membranes (*e.g.*, membrane proteins and glycocalyx networks).

The effects of AuNPs on cell membranes and their nanotoxicity needs to be investigated in order to estimate potental risks in various biomedical and nanotechnological applications. Here, atomistic level simulations are able to provide new detailed information on the AuNP-membrane interaction. We have previously studied the interaction of a cationic AuNP with asymmetric lipid membranes, and our results showed that the cationic nanoparticle attaches to the bilayer surface on both the extracellular (EC) and intracellular (IC) sides.[17] However, the simulation results showed that the membrane leaflet binding to the cationic AuNP adjusts to the presence of the nanoparticle differently. On the EC side there is a rearrangement of zwitterionic lipids and nanoparticle side groups in the contact area, giving rise to the initial stage of pore formation on the membrane surface. This behavior is not observed on the IC side, where the cationic AuNP is spontaneously captured by the negatively charged phosphatidylserine lipids that diffuse underneath the nanoparticle.

In this work, we have performed a series of atomistic molecular dynamics (MD) simulations for an anionic monolayer-protected AuNP with functionalized (charged) alkanethiol side groups [$Au_{144}(SR)_{60}$ where R = $C_{11}H_{22}$ + carboxylic group] in aqueous solution in the presence of asymmetric lipid bilayers by using a double membrane setup[17] which divides the system in two compartments, EC and IC, depending on the leaflet next to the nanoparticle and the counterion composition. The lipid composition was chosen to be representative of an animal plasma membrane (the POPS fraction in membrane leaflets of mammalian cells is most commonly in the range of 10–20% [28-30]), and it comprises zwitterionic POPC [1-palmitoyl-2-oleoyl-*sn*-glycero-3-phosphocholine] in the outer EC leaflet, while a

mixture of POPC (81.25 mol%) and negatively charged POPS [1-palmitoyl-2-oleoyl-*sn*-glycero-3-phosphoserine] (18.75 mol%) is used for the inner IC leaflet.

The present study is a continuation of our previous work, where we considered, among other topics, anionic AuNPs in aqueous solution (in the absence of lipid membranes).[18] Here, $AuNP^-$ was simulated over an extensive period of 200 ns in double membrane systems, both in the EC and IC compartments, with and without salt. The purpose was to mimic the EC and IC fluids by adding a biologically relevant concentration of salt (150 mM) into the compartments. Simulations were performed both with counterions only and with counterions and salt to monitor the effects of the added salt on the systems. Furthermore, performing simulations/analysis of systems also without added salt made comparisons to our previous study of AuNPs in aqueous solution[18] more straightforward. As control set-ups, the corresponding reference configurations of the double membrane systems without the nanoparticle were also simulated. Our simulations complement previous theoretical work on AuNPs interacting with lipid bilayers[19–24] [coarse-grained models (CG)] and AuNPs with solvent-effects (atomistic simulations),[25,26] and provide new insights to $AuNP^-$-membrane interactions at the atomistic level.

Here, we observe that $AuNP^-$ attaches to the EC leaflet despite the fact that the overall charge of the membrane is negative. The nanoparticle-membrane interaction is mediated by the contact between terminal carboxylate ($AuNP^-$) and positively charged POPC choline groups, but it is rather weak and does not lead to nanoparticle immersion to the membrane. Consequently, $AuNP^-$ floats on top of the EC leaflet, allowing it to diffuse laterally along the membrane plane. The nanoparticle does not desorb spontaneously back to the water phase, indicating that there is quite a deep free energy barrier at the membrane-water interface region, and by residing therein, $AuNP^-$ alters some of the structural and dynamical properties of the membrane (see

Section 3). On the IC side, $AuNP^-$ does not bind to the membrane due to repulsive interaction with the negatively charged POPS lipids, thus also structural perturbations are limited. We close the article with a brief discussion of potential implications.

2 Materials and methods

The monolayer-protected gold nanoparticle (AuNP) of 144 Au atoms has been modeled with functionalized alkanethiol tail groups (undecanyl chain, R = $C_{11}H_{22}$, and a carboxylate terminal group), as described more in detail elsewhere.[18] The alkanethiol chains are modeled based on the united atom concept[27] that describes a CH_2 group as a single "united" bead. This approach includes explicit representation of polar hydrogen atoms, while nonpolar hydrogens are being excluded. The rigid 114-atom gold core possesses a nearly-spherical polyhedral geometry (rhombicosidodecahedron) based on the previous theoretical suggestion that fitted experimental x-ray data (structure factor) and was consistent with voltammetric measurements for different charge states of the metallic core.[28] The monolayer covering the Au core consists of 30 "oxidized" surface Au atoms and 60 alkylthiol ligands (SR^- with R = $C_{11}H_{22}$) with polar tail groups, and two ligands attached to each surface gold atom.[18] Each hydrocarbon chain is terminated by a terminal carboxylate group COO^- making the nanoparticle strongly charged, and the molecular formula of the particle can be represented as $Au_{144}(SRCOO^-)_{60}$.

Gold nanoparticles are charged, and one has to treat the electrostatics of the membrane as accurately as possible. Here, it is important to realize that in addition to zwitterionic lipids, the plasma membranes contain a certain amount of charged (anionic) lipids which are essential for the AuNP-membrane interactions.[17] Furthermore, the anionic lipids such as POPS are localized mostly within the inner leaflets of plasma membranes.

To address all these issues, we inserted anionic POPS lipids in one of the POPC leaflets. The leaflets were taken from the corresponding symmetric POPC bilayer, and special care was paid to build a tensionless membrane. The POPS fraction in membrane leaflets of mammalian cells varies rather widely depending on the cell type, but normally does not exceed 0.3, most commonly being in the range of 0.1–0.2.[29–31] Therefore, a valid fraction close to 0.2 was chosen for simulations. A symmetric POPC/POPS membrane was then built as follows: 24 head groups of PC lipids randomly chosen in each leaflet of the POPC membrane were converted to PS head groups. The resulting symmetric PC/PS lipid membrane was equilibrated for 20 ns. To match the areas of symmetric POPC and POPC/POPS membranes, 8 lipids were removed from the original POPC membrane, giving rise to a bilayer of 248 POPC lipids. The resulting asymmetric POPC/POPS lipid membrane was equilibrated for 10 ns before it was used to build up a double bilayer system. This procedure allows us to explicitly take into account the asymmetric transmembrane distribution of anionic lipids inherent for plasma membranes of eukaryotic cells, keeping the membrane model relatively simple. Further developments could involve including other essential lipid components into the membrane model, such as sphingomyelin, phosphatidyl-ethanolamine, and cholesterol, but those remain to be considered in future studies.

The simulation setup of $AuNP^{-}$ and two asymmetric lipid bilayers is visualized for three different cases in Figure 1. The simulation box dimensions were adjusted to 9 × 9 × 22 nm for the nanoparticle-membrane simulations with a double membrane setup. The asymmetric lipid bilayers were comprised of two different membrane leaflets, where the cytosolic (IC) leaflet consisted of a mixture of 104 POPC and 24 POPS lipids and the EC leaflet was comprised of 124 POPCs. Based on tests, this choice of lipid numbers was confirmed to result in flat lipid bilayers (with no spontaneous curvature). Two of such asymmetric lipid bilayers were inserted into the simulation box

such that the IC leaflets of the bilayers were face-to-face (membrane inversion). After placing $AuNP^-$ into the simulation box, it was filled with water, and 60 Na^+ (EC compartment) or 60 K^+ (IC compartment) counterions were added to the system, and additional 24 K^+ ions were put in to compensate for POPS charges on the IC side. In one case, we also added 150 mM of salt to the water phases (Na^+Cl^- to the EC compartment, K^+Cl^- to the IC compartment). The aim was to mimic cytosolic and extracellular fluids in mammalian cells by using K^+ and Na^+ ions, inside and outside the cell, respectively. The bilayer center of masses (COMs) were separated by a distance of (15.1 ± 0.2) nm across the compartment containing $AuNP^-$, which is

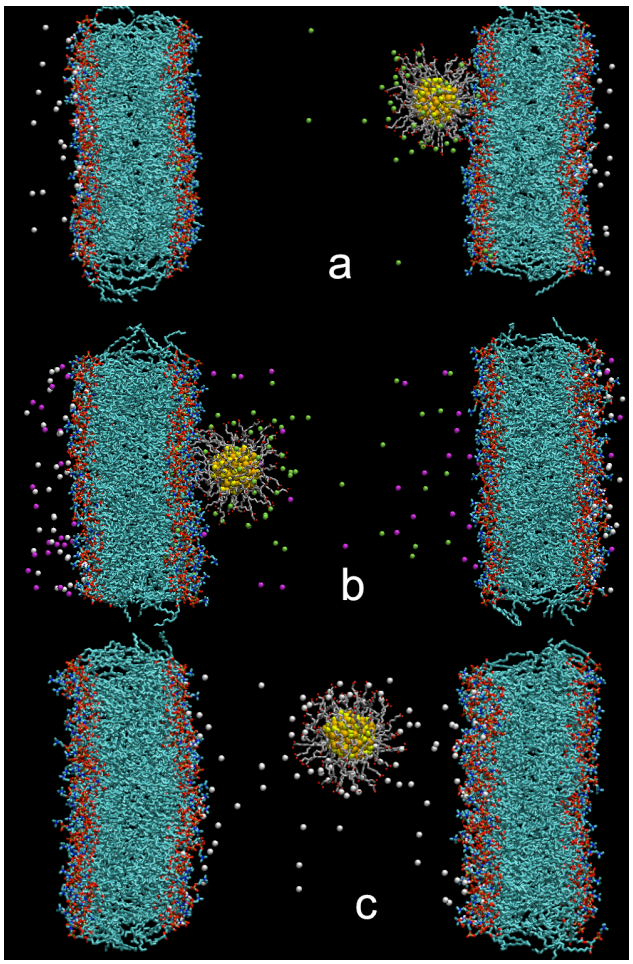

Figure 1: Visualization of $AuNP^-$ with membranes. $AuNP^-$ is placed between two lipid bilayers in extracellular (EC) and intracellular (IC) compartments. (a) EC, (b) EC with salt, and (c) IC. The snapshots were taken from the middle of the

200-ns trajectories; the position of $AuNP^-$ with respect to the membranes is spontaneous in all figures. After an initial equilibration, $AuNP^-$ fluctuates close to these positions during the rest of the simulations. Color code: Au (gold), S (yellow), C (united atom) (grey CPK), O (red), N (blue), P (maroon), Na^+ (lime), Cl^- (magenta), K^+ (white), and lipid bilayers carbons (cyan).

significantly larger than the bilayer thickness of (3.8 ± 0.1 nm, P-P distance across the leaflets) and the nanoparticle diameter of about 4.1 nm.[18] The chosen system sizes were confirmed to be consistent with the water density at the given temperature (T = 310 K) to set up a realistic simulation system with an appropriate amount of water. The overall number of atoms in the simulated $AuNP^-$ systems was around 143,000.

The simulations were carried out using a united atom force field which is largely compatible with the Berger force field,[32] and it is a mixture of a tuned united OPLS (non-bonded interactions) and GROMOS (bonded interactions) force fields. The POPC lipids are implemented as originally developed by Berger *et al*.[33,33] with adjustments for the double bond.[34] The POPS force field model follows the Mukhopadhyay *et al*. implementation.[35] The $AuNP^-$ composition and force field have been described in Heikkilä *et al*.,[18] and water molecules were represented using the SPC model.[36] The counterions Na^+, Cl^-, and K^+ use their original GROMACS-87 parameters.[37] The particle-mesh Ewald summation (PME) method[38] was used for electrostatic interactions with a real space cut-off of 1.0 nm and a reciprocal grid of 77 × 78 × 189 cells with a 4th order *B*-spline interpolation. For van der Waals interactions, we used a cut-off distance of 1.0 nm.

The MD simulations were performed by using the GROMACS program package[39] (versions 4.0.5 and 4.5.6) in the canonical *NPT* ensemble by setting the temperature to 310 K using the Berendsen thermostat[40] with a time constant of 0.1 ps. The

coupled barostat applied a semi-isotropic pressure coupling using the Berendsen algorithm[40] with compressibility of 4.5×10^{-5} bar^{-1}, time constant of 5 ps and reference pressure of 1 bar. The time step was set to 2 fs and the neighbor list (cut-off 1.0 nm) was updated for every 10th frame (20 fs). The SHAKE algorithm[41] was employed in the simulations. The prepared systems were energy minimized and each system was let to equilibrate for 50 ns at the target temperature before the actual productions simulation was started.

The dynamics of $AuNP^-$ was simulated in the EC and IC compartments of the double membrane system, and the details of these simulations are summarized in Table 1. First, $AuNP^-$ with counterions was simulated in the EC and IC sides for 200 ns (2×200 ns storing data every 10 ps). Additional simulations were carried out four times with the same parameters and coordinates but with different initial velocities, each for 100 ns ($2 \times 4 \times 100$ ns) in order to gain more statistics. In addition to $AuNP^-$/counterion simulations, 150 mM of salt was added in both compartments and MD simulations were performed for 200 ns. In order to study particularly rapid processes related to water hydrogen bonds (H-bonds) and counterion contacts between $AuNP^-$ and the surrounding solution, ten shorter simulations with a more frequent data storage rate $(0.5 \text{ ps})^{-1}$ were run (10×1 ns) starting from different snapshots of the longest 200 ns simulation trajectory for each system. Snapshots were taken from the time window between 100 and 200 ns, and they were separated by 10 ns. The purpose was to use uncorrelated starting structures for the 1-ns simulations.

As a reference, a 200-ns simulation without $AuNP^-$ was performed for the double bilayer systems, where the simulation box dimensions were adjusted to $9 \times 9 \times 13$ nm. Both compartments were filled with water and 48 K^+ ions to the IC side to compensate for the negative charge of POPS lipids. In the reference simulation the bilayers were (3.6 ± 0.1) nm thick and separated by a distance of (7.0 ± 0.2) nm, as determined

based on the average P-P distances of the corresponding leaflet pairs.

To visualize the ionic cloud around the nanoparticle in the presence of a membrane, 60-ns simulations were performed (both in EC and IC) constraining the distance between the center of masses of the Au core and POPC lipid P atoms of the closest leaflet to 2.84 nm by using a force constant of 10000 kJ mol^{-1} nm^{-1}. The visualization was carried out using VMD.[42]. The VolMap tool of the VMD plugin library was used for ion density calculation with a resolution of 0.5 Å and using an atom size parameter of 1.0, averaging over all frames of the 60-ns trajectory.

The structure of the membrane in the presence or absence of $AuNP^-$ was studied by calculating order parameters for POPC lipid hydrocarbon chains. The order parameters were computed using the angle θ between the bilayer surface normal and a vector between two lipid carbon palmitoyl tail atoms, C_{n-1} and C_{n+1}:[43,44]

$$S_{CD} = \frac{3}{2}\langle \cos^2 \theta \rangle - \frac{1}{2}. \quad (1)$$

In cases where the $AuNP^-$ approached the bilayer (EC), the order parameter was also calculated separately for lipids that were right in the vicinity of $AuNP^-$: To this end, we considered only those lipids whose nitrogen atom (choline) in the lipid head group was closer than a cut-off distance (3 nm) from the nanoparticle COM. The error of the order parameter was estimated to be no more than ± 0.001 due to extensive sampling.

Table 1: Simulations of $AuNP^-$-membrane systems. Charges compensating counterions were used in the solvent for each system with $AuNP^-$, and all systems contained counterions for POPS lipids. In one case, salt (150 mM) was added into both compartments. The "constr." cases refer to simulations with constrained nanoparticle-membrane distance of 2.8 nm. The reference system is a double membrane system without

AuNP⁻. The columns for the EC and IC compartments show the constituents, in addition to water.

Setup	EC compartment	IC compartment	Simulations
$AuNP^-$@EC	$AuNP^-$, Na^+	K^+	1×200 ns, 4×100 ns, 10×1 ns
$AuNP^-$@EC+salt	$AuNP^-$, Na^+, Na^+Cl^-	K^+, K^+Cl^-	1×200 ns, 10×1 ns
$AuNP^-$@EC constr.	$AuNP^-$, Na^+	K^+	1×60 ns
$AuNP^-$@IC	–	$AuNP^-$, K^+	1×200 ns, 4×100 ns, 10×1 ns
$AuNP^-$@IC constr.	–	$AuNP^-$, K^+	1×60 ns
Reference	–	K^+	1×200 ns, 10×1 ns

The analysis of H-bonds and ionic contacts was carried out by averaging over the time windows with a more frequent data storage rate of (Δt = 0.5 ps). Contacts between the $AuNP^-$ terminal groups, water molecules, and membrane head groups were considered within a cut-off distance of 0.35 nm for non-hydrogen atoms and an H-bond angle of 30°. Similarly, a cut-off distance of 0.35 nm was used for ionic bonds/contacts.

To characterize the diffusive motion of water and ions around $AuNP^-$, we computed their short-time diffusion factor M inside slices of thickness Δr = 0.5 nm (water) and 1.0 nm (counterions) between the two membranes along the membrane surface normal. For every time step n ($t = n\Delta t$) during the simulation, we determined the water molecules and ions that were at a given distance within the compartment, after which we determined the mean-square displacement $\mathrm{MSD}_A(t)$ of particles of type A (ions, water, *etc*.) as follows:

$$\mathrm{MSD}_A(t) = \langle |\mathrm{r}_i(t) - \mathrm{r}_i(0)|^2 \rangle_{i \in A}, \qquad (2)$$

and this was carried out over a short period of time; the width of the time window was τ = 20 ps and 50 ps for water and counterions, respectively. The data for MSD(t) for every time slice (representing a fixed location along the box z-axis) was averaged separately for water molecules and ions over the total

simulation time of 150 ns. Finally, we computed the short-time diffusion factor M by following the Einstein relation for the self-diffusion coefficient[45] and using a linear fitting of $MSD_A(t)$. The factor M is computed largely in a similar manner as the hydrodynamic diffusion coefficient, but now without the long-time limit. For the same reason, since M is not defined in the hydrodynamic long-time limit, we call it as a diffusion factor instead of the true diffusion coefficient.

3 Results

Three different simulation setups were prepared for $AuNP^-$: EC, EC with salt, and IC (Figure 1 and Table 1). The distance between $AuNP^-$ and the COM of the closest membrane along the z-axis of the box (bilayer surface normal) is shown in Figure 2. For comparison, the distance between the membrane COMs in the double bilayer system is approximately 15 nm (~11 nm with respect to the phosphate groups in the leaflets facing each other across the water phase). The radius of $AuNP^-$ is approximately 2 nm. The $AuNP^-$-membrane distance of ~5.5 nm corresponds to the situation where the nanoparticle is at the center of the simulation box between the membranes.

On the EC side, $AuNP^-$ approaches the extracellular leaflet within a few tens of nanoseconds in all five simulations regardless of the initial conditions (for atomic velocities) and with and without added salt, whereas in IC it stays in the middle of the compartment and does not approach the membranes during the time scale of the five separate simulations. Hence, it can be concluded that the nanoparticle attaches to the EC leaflet and thereby the functional groups of $AuNP^-$ and the zwitterionic surface groups of the EC leaflet are in close contact. Meanwhile, there is no contact between $AuNP^-$ and the IC leaflet during the course of the simulation.

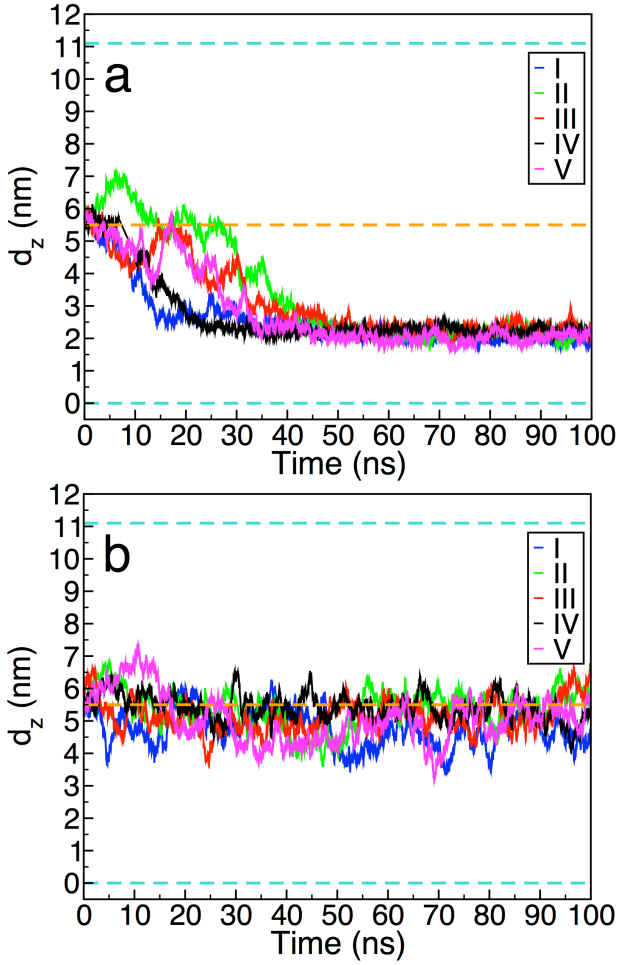

Figure 2: Distance between $AuNP^-$ and membrane for five independent simulations. The distance is defined between $AuNP^-$ (metallic core COM) and the closest membrane surface, where the surface position is defined by its phosphate group COMs along the *z*-axis of the simulation box (bilayer surface normal). Data is given for both systems: $AuNP^-$ in (a) EC and (b) IC. The radius of $AuNP^-$ is approximately 2 nm, thus the AuNP-membrane surface distance of 2 nm corresponds to a situation where $AuNP^-$ has adsorbed to the bilayer surface. The turquoise and orange dashed lines present the approximative positions of the membrane surfaces and the simulation box center, respectively.

Partial densities for groups of atoms were calculated after equilibration for a time window of 50–200 ns, using the trajectories of long simulations. Results are given along the vertical simulation box axis in Figure 3. They show that here the

nanoparticle binding in EC occurs on the opposite surfaces in systems with and without salt (Figures 3a,b), which is not surprising considering the identical composition of the two membranes. The partial density overlap between $AuNP^-$ and the membranes demonstrates that when the nanoparticle is in the EC compartment, it is in a stable contact with the membrane, interacting with the choline head groups. Instead, when $AuNP^-$ resides in the IC compartment, the density profile shows a broader distribution for $AuNP^-$ around the compartment center (Figure 3c), reflecting fluctuations of the nanoparticle position in bulk water phase. Clearly, there is no tendency for $AuNP^-$ to bind with the IC leaflet.

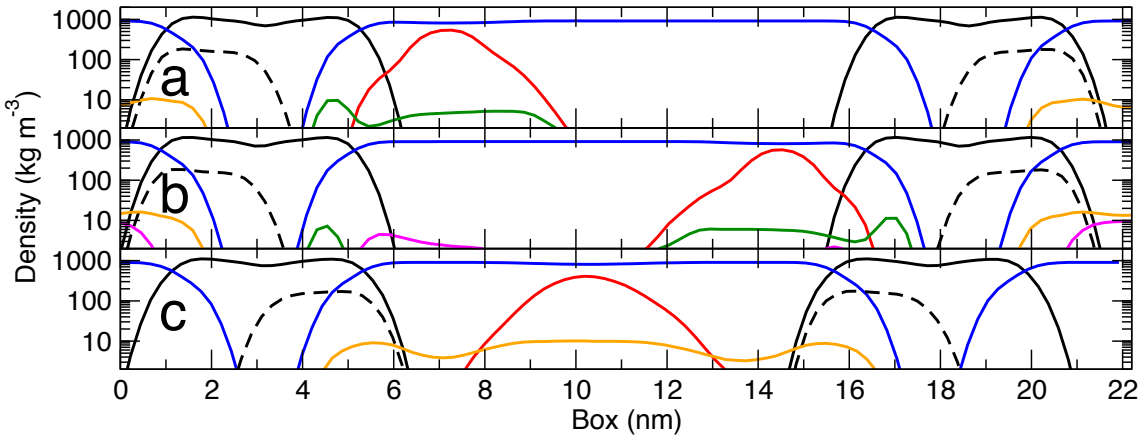

Figure 3: Partial densities of $AuNP^-$ systems in (a) EC, (b) EC with salt, and (c) IC. Color code: membrane (black full line), NP (red full line), water (blue full line), POPS (black dashed), K^+ (orange full line), Cl^- (magenta full line), and Na^+ (green full line). In EC (a,b), the nanoparticle can attach to both membranes with equal probability.

In EC, the ionic cloud of Na^+ around $AuNP^-$ is rather compact, but strongly biased towards the neighboring leaflet. The counterions have small maxima overlapping with the membrane due to contacts with (negative) phosphates. Interestingly, the EC system with salt (Figure 3b) shows that Na^+ and Cl^- counterions have accumulated on the opposite membrane surface with respect to the nanoparticle; this is coupled to the attraction

between POPC lipids and Na^+ and the high surface charge density of $AuNP^-$ repels Cl^-. The electrostatic interactions are mediated through the whole compartment (and beyond it), and the nanoparticle attachment is a co-operative process which involves all components in the solvent. Furthermore, the K^+ content on the IC side is already rather substantial without additional salt as the $AuNP^-$ and POPS counterions add up in a continuous distribution across the whole compartment, which screens the electrostatic interaction experienced by both the nanoparticle and the membrane surface (see Figure 3c).

In order to get more insight on the role of counterions in the binding of the nanoparticle with a membrane, in Figure 4 we consider the distribution of Na^+ (K^+) around $AuNP^-$ in the EC (IC) compartment, averaged over 60 ns simulations. Here, the nanoparticle COM has been constrained to a distance of 2.8 nm from the membrane, which is close to the average binding distance in the EC case. In the IC case, one has to bear in mind that the situation is only suggestive, since in our non-biased simulations we did not observe $AuNP^-$ to spontaneously attach to the IC leaflet (see Figure 2), and when $AuNP^-$ was taken to the IC surface and released, it moved quite rapidly (within tens of nanoseconds) back to the water phase (data not shown). Nonetheless, in both cases the counterions form a halo-pattern around $AuNP^-$, and the ripples close to the terminal COO^- groups demonstrate equidistant positions for the terminal groups and the organized solvent structure (ionic contacts and hydrogen bonds of water). Both cases also highlight the strength of electrostatic interaction, resulting in considerable aggregation of cationic counterions with $AuNP^-$, and showing how the entropic contribution to drive counterions to the water phase is here quite weak.

On the IC side, the larger number of K^+ compared to the EC case is evident (Figure 4), as there is a larger concentration of counterions between or close to $AuNP^-$ and the membrane. The system responds in this way to an energetically unfavorable

situation where the positive counterion charge is balancing the negative charge of the nanoparticle and the negatively charged membrane surface. Unlike for the cationic Au nanoparticle and Cl^-,[17,18] the cations are able to enter between the nanoparticle side chains, but the slightly positive effective charge of the metallic core hinders cations from penetrating deeper. One should also note that the POPS lipids are more exposed to the solvent (IC) due to the electrostatic interactions with K^+ ions.

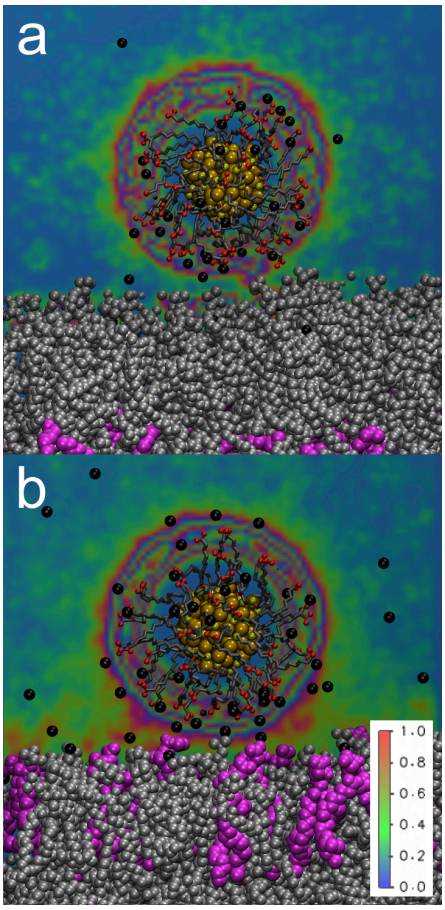

Figure 4: Visualization of $AuNP^-$ with (a) Na^+ counterions in EC, and (b) K^+ counterions in IC (cut-plane presentation, color code from high (max 1.0) to low (min 0.0) concentration: purple, red, green, and blue. Elevated concentration of counterions (green color) around the nanoparticle is obvious. The distance between the nanoparticle center and the POPC head groups of the nearest leaflet has been fixed to 2.8 nm in both cases. The counterion concentrations are averaged over 60 ns

simulations. Color code, molecules: Na^+/K^+ (black), and POPS lipids (magenta).

The average number and the lifetime of H-bonds and ion contacts between $AuNP^-$ and solvent (Table 2) show small differences between the EC and IC solutions: The total number of H-bonds between $AuNP^-$ terminal carboxylate groups and water is reduced from 397.7 ± 1.6 to 371.1 ± 1.1 by a change from EC to IC (note that there are 60 side chains and two H-bond acceptor atoms per terminal carboxylate group), and the corresponding lifetimes decrease similarly from 4.7 ± 0.3 ps to 3.3 ± 0.1 ps. This difference in water coordination is coupled with the number of counterion contacts (see below, Na^+ in EC and K^+ in IC). The longer H-bond lifetime values for water in EC can be explained by the $AuNP^-$-membrane interactions: The movement of $AuNP^-$ is restricted in EC due to the membrane attachment, and this causes its water solvation shell to be less interrupted and consequently the H-bonds live longer. Furthermore, the water mobility itself is reduced close to the membrane surface (see below).

Table 2: Hydrogen bonds and contacts between $AuNP^-$ and solvent/ions/lipids. N_A is the average number of hydrogen bonds or contacts between $AuNP^-$ and a solvent molecule/lipid, A. τ_A is the average lifetime of the contacts.

Compartment	A	N_A	τ_A [ps]
EC	H_2O	397.7 ± 1.6	4.7 ± 0.3
	Na^+	3.0 ± 0.3	9.8 ± 0.5
	lipid	5.0 ± 2.5	15.3 ± 2.2
EC with salt	H_2O	399.4 ± 0.7	4.2 ± 0.2
	Na^+	3.6 ± 0.4	10.3 ± 1.9
	lipid	4.6 ± 0.5	15.3 ± 1.4
IC	H_2O	371.1 ± 1.1	3.3 ± 0.1
	K^+	42.7 ± 1.2	20.9 ± 0.2
	lipid	—	—

The number of ion contacts differs by an order of magnitude between EC and IC: 3.0 ± 0.3 for Na^+ in EC and 42.7 ± 1.2 for K^+ in IC. The difference is partially explained by the fact that there are K^+ counterions present for both POPS lipids and $AuNP^-$ in the IC compartment. The ion contact lifetimes in IC are twice the lifetimes in EC, which is presumably related to the number of counterions in the solution and the repulsive ion-ion interactions in the $AuNP^-$ surroundings.

The counterions concentration affects the H-bonds as well, and the number of H-bonds with water is smaller in IC than in EC as the numerous contacts with ions diminish the number of H-bonds between the $AuNP^-$ terminal groups and water. For EC, the number of Na^+ ion contacts and lifetimes are similar to those observed earlier [18] for the same $AuNP^-$ in an aqueous solution without the presence of bilayers, 4.4 ± 0.4 and 10.1 ± 1.1 ps. The same applies to H-bonds where the corresponding values were 404.4 ± 0.5 and 3.5 ± 0.1 ps in an aqueous environment. Adding salt to the EC system does not significantly affect the numbers of contacts or lifetimes between $AuNP^-$ and the solvent.

Table 2 also lists values for the contacts between $AuNP^-$ and membranes, and the results show similar trends for the EC compartment with and without salt. The nanoparticle-membrane contact lifetimes are ~15 ps, which is rather short and indicates that $AuNP^-$ readily diffuses along the membrane surface. Small values for the membrane contacts indicate that $AuNP^-$ remains close to the surface of the EC leaflet, not penetrating deeply inside the membrane since it experiences the electrostatic repulsive force caused by the negatively charged lipid phosphate groups and the POPS lipids in the cytosolic leaflet. Concerning the number of water-membrane contacts, there are more of those in the IC compartment where $AuNP^-$ is not attached, as this leaves more lipid surface groups exposed to the water solvent (data not shown).

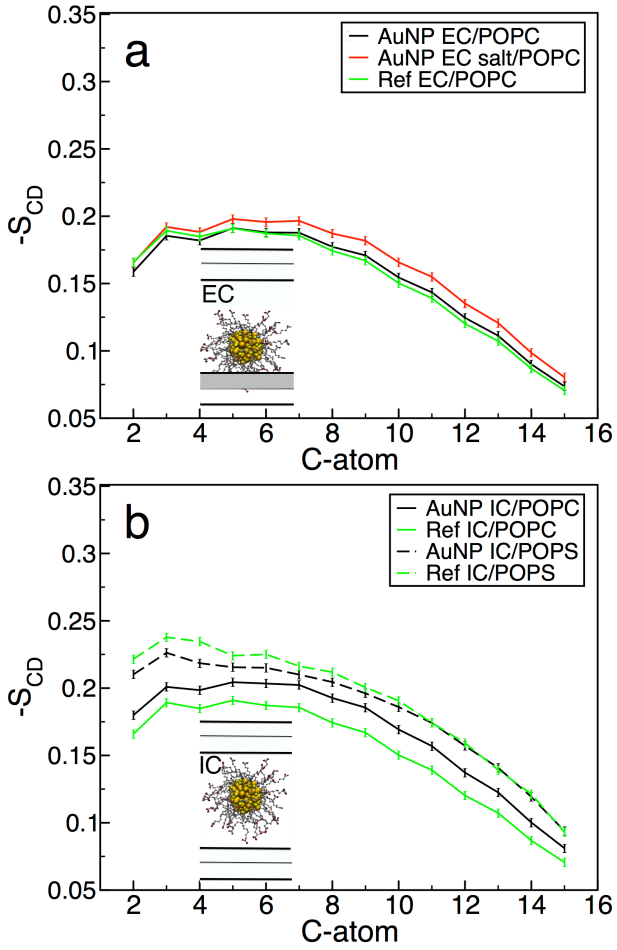

Figure 5: Order parameter results for POPC lipids in the EC and IC leaflets, in the presence/absence of $AuNP^{-}$. (a) EC compartment, data in the leaflet that is the closest to $AuNP^{-}$. (b) IC compartment, where $AuNP^{-}$ is largely in the middle of the water phase, the results shown here are an average of the two IC leaflets. Color coding in both panels corresponds to the $AuNP^{-}$ system without added salt (black), the $AuNP^{-}$ system with added salt (red), and the reference system without $AuNP^{-}$ and without additional salt (green). The results were computer over a period of 150 ns, each, and for saturated carbon chains only. The error bars are ± 0.001 based on the largest observed value.

The nanoparticle-membrane interactions described above are to some extent reflected in the order parameters of lipids, too, shown in Figure 5. In the EC compartment without added salt (Figure 5a), the POPC order parameters of are largely the same

regardless of the present of $AuNP^-$. When salt is added, the order parameter increases about 5–10 % compared to the reference system, but this is likely due to monovalent salt that is known to decrease the area per lipid in the membrane, thereby increasing membrane order, and stems from salt ion-induced lipid clustering.[46–48]

Additional analysis of the nearby lipids within 3 nm from the $AuNP^-$ COM and without salt shows a slight reduction of the outermost carbon atom order parameters (increased disorder) due to the interaction with the terminal COO^- groups, but the effect is subtle. In the IC compartment without additional salt, the results shown in Figure 5b indicate the ordering of POPCs to increase and the ordering of POPS lipids to decrease due to the presence of $AuNP^-$. It should be noted that $AuNP^-$ brings along 60 K^+ counterions which add up with the initial counterions balancing the POPS charge. It seems likely that the repulsive interactions between $AuNP^-$ and POPS give rise to lateral lipid reorganization where POPSs are displaced underneath $AuNP^-$, making room for a POPC-rich lipid region right under the nanoparticle. We consider that this phenomenon is possibly an artificial finite-size effect since $AuNP^-$ would drift farther from the IC surface in a larger simulation compartment.

The short-time diffusion factors of water molecules and counterions are shown in Figure 6 (water) and Figure 7 (counterions). They have been determined inside 0.5 nm and 1.0 nm thick lateral slices, respectively, along the membrane(s) surface normal in the $AuNP^-$ host compartment. In general, the water/counterion diffusion factors are reduced close to membrane surfaces. We remind that $AuNP^-$ attaches to the membrane surface in EC, but it stays at the middle of the compartment in IC. This behavior is evident in the distribution shapes as the water diffusion is reduced near $AuNP^-$, and the same effect is visible for the Na^+/K^+ counterions, too. Water forms an H-bond network around the terminal groups of $AuNP^-$ (and counterions), and this makes the H_2O positions more

restricted close to the nanoparticle. For water, the change in diffusion as a function of distance is smaller than for counterions. This can be explained by the type of bonds/contacts that water and ions form with $AuNP^{-}$: H-bonds between the terminal COO^{-} groups and water are weaker and of shorter range than the electrostatic interactions with counterions. Finally, the nanoparticle attachment (EC) results in an increase in solvent mobility at the opposite membrane surface, highlighting the fact that the $AuNP^{-}$ movement is reflected throughout the whole compartment, also in terms of dynamics.

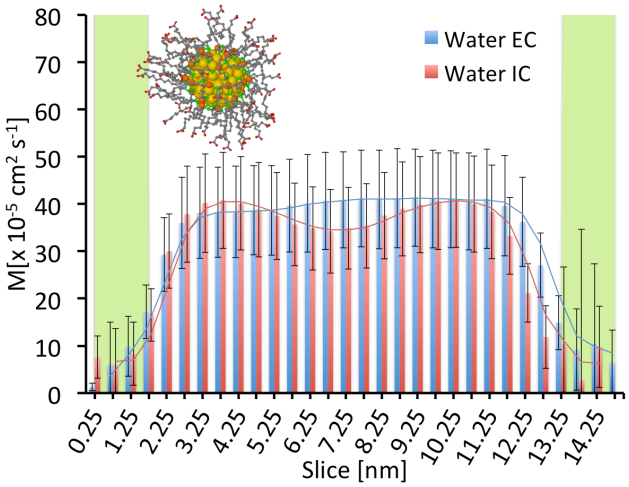

Figure 6: Mobility of water between membranes. The short-time diffusion factor has been calculated for water molecules (with respect to oxygen) inside Δr = 0.5 nm thick slices along the *z*-axis of the simulation box (along the membrane surface normal) between the two membranes averaged over the 50–200 ns simulation time. The histograms in EC and IC are presented using blue and red color, respectively. The error bars correspond to standard deviations. The zero-level has been defined with respect to the membrane center plane, and the green bars stand for the membrane surface planes.

As noted in previous work for cationic and anionic AuNPs in aqueous environment,[18] the choice of terminal groups (amine/carboxylate) affects the surrounding H-bond network, as evidenced for the H_2O orientations as a function of distance

from the nanoparticle center. Similar plots are presented for $AuNP^-$ in the EC and IC compartments in Supplementary Figure 1. As shown in Figure 6, the effect of $AuNP^-$ on the diffusion of solvent extends rather far (several nanometers), implying that the solvent transmits the interaction shell-by-shell by intermediating the orientation of water molecules. This phenomenon is evident in the data for water orientations, which depend strongly on the distance: The first shell surrounding the COO^- terminal groups aligns water molecules in such a manner that hydrogens are pointing towards $AuNP^-$ (carboxylates). This effect arises from the electrostatic forces between the COO^- groups and polarized water molecules. The differences between the two compartments, EC and IC, are very small despite the fact that $AuNP^-$ is in contact with the membrane surface in EC.

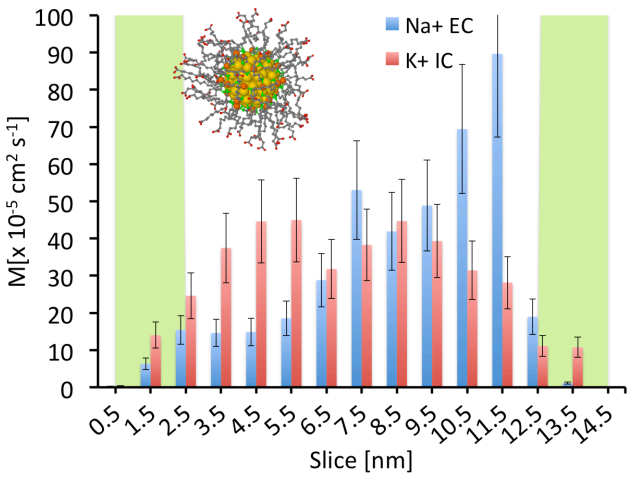

Figure 7: Short-time diffusion factor (*M*) of counterions shown as a function of distance from one of the membrane leaflets facing the given compartment (EC or IC), and extending across the water phase to the surface of the other leaflet in the same compartment. The results have been averaged over a period of 50–200 ns after the 50 ns equilibration period. Results in the EC (IC) compartments are shown in blue (red) color. The error bars correspond to standard deviation. The zero-level has been defined with respect to the membrane center plane, and the green bars stand for the membrane surface planes.

5 Discussion and Conclusions

Gold nanoparticles are being used extensively in biomedicine and nanotechnology, and assessing their potential health hazards is extremely timely. Here, revealing the atomistic details of their interactions with biomolecules and cell membranes is very relevant. To clarify the underlying molecular processes in such system, we have performed a series of MD simulations at atomistic scale for a monolayer-protected $AuNP^{-}$ with functionalized (negatively charged) alkanethiol side groups interacting with a realistic model lipid membrane system. The nanoparticle composition matches with one of the most ubiquitous synthesized AuNP sizes (29 kDa, 2 nm) and its mass-spectrometrical analysis ($Au_{144}(SR)_{60}$). Furthermore, the nanoparticle structure incorporates the recently found structural motifs of ligand-protected AuNPs where the metallic Au core is a nearly-spherical polyhedron, and part of Au atoms participate (in oxidized form) in the Au-SR ligand-shell.

Our model for the membrane is based on a double membrane setup able to describe the extracellular (EC) and intracellular (IC, cytosolic) compartments with different salt and counterion distributions, and the asymmetricity of lipid bilayers, thus mimicking the real animal plasma membranes. Given that our model systems also include an explicit solvent, it is fair to conclude that the present approach includes several very detailed features that have not been included in previous (simulation) studies,[19-24] except for a recent work on cationic AuNPs.[17] However, it is impossible (as well as out of the scope of this work) to model the complexity of a real mammalian cell and the diversity of all of its components. Further developments of the model could include, *e.g.*, integral membrane proteins and essential lipid components (such as cholesterol and sphingomyelin).

Experimental results suggest that the nanoparticle-membrane interaction depends on the AuNP charge as well as the nature

and arrangement of the protecting side groups. That is to say, it is not the Au core that determines the interaction with the membrane but the surfactant layer on the top of it. While cationic nanoparticles are known to penetrate through the cell membrane, less activity has been observed for anionic AuNPs.[16] The anionic AuNPs used in the experiments of Tatur *et al*.[16] had mercaptoundecanoic acid ($–S(CH_2)_{10}COOH$) surface groups, which are similar to the ones used in this study (with a difference of one CH_2 unit). Another study on anionic AuNP permeation by Van Lehn *et al*.[15] used 11-mercaptoundecane sulfonate ($–S(CH_2)_{11}SO_3^-$) and octanethiol ($–S(CH_2)_7CH_3$) ligands with varying morphologies. These surface groups differ from the ones presented here.

We observed for $AuNP^-$ that it attached spontaneously to the EC membrane surface within a few tens of nanoseconds. It seems evident that the binding of $AuNP^-$ with the membrane takes place through relatively weak contacts with the zwitterionic POPC head groups, since $AuNP^-$ did not immerse deeply in the membrane but floated on top of the bilayer surface, enabling lateral diffusion of the nanoparticle along the membrane. In the IC compartment, we found that $AuNP^-$ stayed in the middle of the compartment, with no adsorption to the membrane. Apparently there is no attractive interaction with the cytosolic leaflet due to the Coulomb repulsion between $AuNP^-$ and the negatively charged POPS lipids.

Based on the results, it seems that $AuNP^-$ has no tendency to cross the membrane or bind to its surface, either in EC or IC. However, if it would, it is not clear whether it would pass or remain in the middle of the membrane. After all, one possible scenario is that the charged side groups of $AuNP^-$ would be stabilized by the charged regions of the membrane lipids, while the core of the nanoparticle (with $(CH_2)_{11}$ chains) would reside in the hydrophobic membrane interior. This kind of NP-embedding and involved lipid rearrangement has been observed, *e.g.*, for charged dendrimers.[49]

One of the grand questions in the field concerns the influence of nanoparticles on the function of membrane-associated proteins.[50-52] While we cannot unlock this question through our work, let us consider the key background factor related to this theme: the binding of nanoparticles to membranes. In a previous work,[17] it was shown that while cationic $AuNP^+$ avoided adsorption to the EC leaflet due to electrostatics, the binding of $AuNP^+$ to the EC leaflet yet took place through the crossing of a free energy barrier (about 12 kJ/mol) that is quite comparable to thermal energy, suggesting that the rate of spontaneous $AuNP^+$ binding to the EC side would be quite reasonable. On the IC side, $AuNP^+$ was observed to adsorb to the membrane in no time due to strong electrostatic attraction with anionic POPS.[17] Here in this work, $AuNP^-$ was observed to bind to the membrane on the EC side, and this binding was driven by electrostatics. On the IC side, the anionic nanoparticle avoided contact with the membrane due to anionic POPS lipids. Moreover, $AuNP^-$ was observed to maximize its distance from the IC leaflet, suggesting that in the cytosol $AuNP^-$ would not favor being in any close proximity to the intracellular leaflet of the plasma membrane, assuming that there are no additional charged entities (fluctuations in lipid concentration, biomolecules).

Summarizing, these observations, comparisons, and earlier studies[5,15,17,23,53] highlight the importance of electrostatic interactions in the binding of nanoparticles with membrane surfaces. The research results suggest that once nanoparticles have attached to a membrane surface, they prefer to interact with membrane proteins whose juxtamembrane domains are appropriately charged or polar, or with proteins whose ectodomains (in the extracellular space) or cytosolic domains favor interactions with the given nanoparticle. Both situations are problematic considering protein function as they can potentially change protein conformation. As a single example, one of the key processes in cell membranes is communication driven by membrane receptors binding with their extracellular ligands. If the conformation of the receptor was altered by a

strong interaction with a nanoparticle that is attached to the membrane, its visibility could be impaired, thus slowing down the signaling process, and this can be expected to influence cellular function. Detailed simulation studies testing this potential scenario would be welcome. In the meantime, this scenario is supported by the observation that $AuNP^+$ binds to plasma membrane-like lipid bilayers more efficiently than $AuNP^-$, in agreement with experiments that have shown cationic gold nanoparticles to be more harmful to model membranes than anionic ones.[16]

Even though there exists a large body of literature published on the research of nanomaterials, the field still lacks systematic mapping of all the factors that are (or potentially might be) involved in the interactions between various kinds of studied nanoparticles and cells. Hence, it is of importance to perform detailed studies of specific model systems to clarify the effects of individual variables. For achieving a conclusive perspective, it is necessary to complement the computational results by experiments, and *vice versa*. The *in silico* predictions presented here could quite straightforwardly be verified experimentally using simplified POPC/POPS model membranes with corresponding $AuNP^-$, *i.e.*, in similar manner as in the recent study of Tatur *et al*.[16]

Concluding, the results presented in this study bring more weight to the idea that electrostatic interactions are particularly important in the nanoparticle-membrane binding, and that these may have consequences for cellular function.

Acknowledgement

The computations were performed on the Juropa (Intel Xeon 5570) and Cray XT4/XT5 computers in the Forschungszentrum Jülich (Germany) and CSC – IT Centre for Science Ltd (Espoo, Finland). Financial support has been provided by the Academy of Finland through its Centre of Excellence Programs (Project

251748 EH, JA; Project 272130 HMS, IV). IV also acknowledges support from the European Research Council (Advanced Grant CROWDED-PRO-LIPIDS).

Supporting Information

Supporting Information contains additional data for the orientation of water molecules around $AuNP^{-}$, the radial distribution functions centered at $AuNP^{-}$, and the radius of gyration and the moment of inertia vector autocorrelation function of $AuNP^{-}$ in the EC and IC compartments.

References

(1) Dreaden, E. C.; Alkilany, A. M.; Huang, X.; Murphy, C. J.; El-Sayed, M. A. The Golden Age: Gold Nanoparticles for Biomedicine. *Chem. Soc. Rev.* 2012, *41*, 2740–2779.

(2) Dykman, L.; Khlebtsov, N. Gold Nanoparticles in Biomedical Applications: Recent Advances and Perspectives. *Chem. Soc. Rev.* 2012, *41*, 2256–2282.

(3) Nel, A.; Xia, T.; Mädler, L.; Ning, L. Toxic Potential of Materials at the Nanolevel. *Science* 2006, 622–627.

(4) Khlebtsov, N.; Dykman, L. Biodistribution and Toxicity of Engineered Gold Nanoparticles: A Review of *In Vitro* and *In Vivo* Studies. *Chem. Soc. Rev.* 2011, *40*, 1647–1671.

(5) Goodman, C. M.; McCusker, C. D.; Yilmaz, T.; Rotello, V. M. Toxicity of Gold Nanoparticles Functionalized with Cationic and Anionic Side Chains. *Bioconjugate Chem.* 2004, *15*, 897– 900.

(6) Sperling, R. A.; Gil, P. R.; Zhang, F.; Zanella, M.; Parak, W. J. Biological Applications of Gold Nanoparticles.

Chem. Soc. Rev. 2008, *37*, 1896–1908.

(7) Lewinski, N.; Colvin, V.; Drezek, R. Cytotoxicity of Nanoparticles. *Small* 2008, *4*, 26–49.

(8) Alkilany, A. M.; Nagaria, P. K.; Hexel, C. R.; Shaw, T. J.; Murphy, C. J.; Wyatt, M. D. Cellular Uptake and Cytotoxicity of Gold Nanorods: Molecular Origin of Cytotoxicity and Surface Effects. *Small* 2009, *5*, 701–708.

(9) Murphy, C. J.; Anand, M. G.; Stone, J. W.; Sisco, P. N.; Alkinaly, A. M.; Goldsmith, E. C.; Baxter, S. C. Gold Nanoparticles in Biology: Beyond Toxicity to Cellular Imaging. *Acc. Chem. Res.* 2008, *41*, 1721–1730.

(10) Pan,Y.; Leifert, A.; Ruau, D.; Neuss, S.; Bornemann, J.; Schmid, G.; Brandau,W.; Simon, U.; Jahnen-Dechent, W. Gold Nanoparticles of Diameter 1.4 nm Trigger Necrosis by Oxidative Stress and Mitochondrial Damage. *Small* 2009, *5*, 2067–2076.

(11) Verma, A.; Uzun, O.; Hu, Y.; Hu, Y.; Han, H.-S.; Watson, N.; Chen, S.; D. J., I.; Stellacci, F. Surface-Structure-Regulated Cell-Membrane Penetration by Monolayer-Protected Nanoparticles. *Nat. Mat.* 2008, *7*, 588–595.

(12) Mecke, A.; Lee, D.-K.; Ramamoorthy, A.; Orr, B. G.; Banaszak Holl, M. M. Synthetic and Natural Polycationic Polymer Nanoparticles Interact Selectively with Fluid-Phase Domains of DMPC Lipid Bilayers. *Langmuir* 2005, *21*, 8588–8590.

(13) Leroueil, P. R.; Berry, S. A.; Duthie, K.; Han, G.; Rotello, V. M.; McNerny, D. Q.; Baker Jr., J. R.; Orr, B. G.; Banaszak Holl, M. M. Wide Varieties of Cationic Nanoparticles Induce Defects in Supported Lipid Bilayers. *Nano Lett.* 2008, *8*, 420–424.

(14) Chen, J.; Hessler, J. A.; Putchakayala, K.; Panama, B. K.;

Khan, D. P.; Hong, S.; Mullen, D. G.; DiMaggio, S. C.; Som, A.; Tew, G. N.; Lopatin, A. N.; Baker, J. R.; Banaszak Holl, M. M.; Orr, B. G. Cationic Nanoparticles Induce Nanoscale Disruption in Living Cell Plasma Membranes. *J. Phys. Chem. B* 2009, *113*, 11179–11185.

(15) Van Lehn, R.; Atukorale, P. U.; Carney, R. P.; Yang, Y.-S.; Stellacci, F.; Irvine, D. J.; Alexander-Katz, A. Effect of Particle Diameter and Surface Composition on the Spontaneous Fusion of Monolayer-Protected Gold Nanoparticles with Lipid Bilayers. *Nano Lett.* 2013, *13*, 4060–4067.

(16) Tatur, S.; Maccarini, M.; Barker, R.; Nelson, A.; Fragneto, G. Effect of Functionalized Gold Nanoparticles on Floating Lipid Bilayers. *Langmuir* 2013, *29*, 6606–6614.

(17) Heikkilä, E.; Martinez-Seara, H.; Gurtovenko, A.; I., V.; Häkkinen, H.; Akola, J. Cationic Au Nanoparticle Binding with Plasma Membrane-like Lipid Bilayers: Potential Mechanism for Spontaneous Permeation to Cells Revealed by Atomistic Simulations. *J. Phys. Chem. C* 2014, Just Accepted Manuscript; doi:10.1021/jp5024026.

(18) Heikkilä, E.; Gurtovenko, A.; Martinez-Seara, H.; Vattulainen, I.; Häkkinen, H.; Akola, J. Atomistic Simulations of Functional $Au_{144}(SR)_{60}$ Gold Nanoparticles in Aqueous Environment. *J. Phys. Chem. C* 2012, *116*, 9805–9815.

(19) Li, Y.; Chen, X.; Gu, N. Computational Investigation of Interaction between Nanoparticles and Membranes: Hydrophobic/Hydrophilic Effect. *J. Phys. Chem. B* 2008, *112*, 16647– 16653.

(20) Li, Y.; Gu, N. Thermodynamics of Charged Nanoparticle Adsorption on Charge-Neutral Membranes: A Simulation Study. *J. Phys. Chem. B* 2010, *114*, 2749–2754.

(21) Lin, J.; Zhang, H.; Chen, Z.; Zheng, Y. Penetration of Lipid Membranes by Gold Nanoparticles: Insights into Cellular Uptake, Cytotoxicity, and Their Relationship. *ACS Nano* 2010, *4*, 5421–5429.

(22) Li, Y.; Li, X.; Li, Z.; Gao, H. Surface-Structure-Regulated Penetration of Nanoparticles across a Cell Membrane. *Nanoscale* 2012, *4*, 3768–3775.

(23) Van Lehn, R. C.; Alexander-Katz, A. Free Energy Change for insertion of Charged, Monolayer-Protected Nanoparticles into Lipid Bilayers. *Soft Matter* 2014, *10*, 648–658.

(24) Lin, J.; Alexander-Katz, A. Cell Membranes Open "Doors" for Cationic Nanoparticles/Biomolecules: Insights into Uptake Kinetics. *ACS Nano* 2013, *7*, 10799–10808.

(25) Li, Y.; Yang, Z.; Hu, N.; Zhou, R.; Chen, X. Insights into Hydrogen Bond Dynamics at the Interface of the Charged Monolayer-Protected Au Nanoparticle from Molecular Dynamics Simulation. *J. Chem. Phys.* 2013, *138*, 184703–1–9.

(26) Van Lehn, R. C.; Alexander-Katz, A. Structure of Mixed-Monolayer-Protected Nanoparticles in Aqueous Salt Solution from Atomistic Molecular Dynamics Simulations. *J. Phys. Chem. C* 2013, *117*, 20104–20115.

(27) Berendsen, H. J. C.; van der Spoel, D.; van Drunen, R. GROMACS: A Message-Passing Parallel Molecular Dynamics Implementation. *Comp. Phys. Comm. 1995*, *91*(1–3):43–56.

(28) Lopez-Acevedo, O.; Akola, J.; Whetten, R.; Grönbeck, H.; Häkkinen, H. Structure and Bonding in the Ubiquitous Icosahedral Metallic Gold Cluster $Au_{144}(SR)_{60}$. *J. Phys. Chem. C*. 2009, *113*, 5035–5038.

(29) Van Deenen, L. L. M.; den Kamp, J. A. F. O.; Roelofsen,

B.; Wirtz, K. W. A. On Membrane Phospholipids and Protein-Lipid Association. *Pure Appl. Chem.* 1982, *54*, 2443–2454.

(30) Spector, A. A.; Yorek, M. A. Membrane Lipid Composition and Cellular Function. *J. Lipid. Res.* 1985, *26*, 1015–103.

(31) Gurtovenko, A. A.; Vattulainen, I. Membrane Potential and Electrostatics of Phospholipid Bilayers with Asymmetric Transmembrane Distribution of Anionic Lipids. *J. Phys. Chem. B* 2008, *112*, 4629–4634.

(32) Berger, O.; Edholm, O.; Jähnig, F. Molecular Dynamics Simulations of a Fluid Bilayer of Dipalmitoylphosphatidylcholine at Full Hydration, Constant Pressure, and Constant Temperature. *Biophys. J.* 1997, *72*, 2002–2013.

(33) Tieleman, D. P.; Berendsen, H. J. C. A Molecular Dynamics Study of the Pores Formed by Escherichia Coli OmpF Porin in a Fully Hydrated Palmitoyloleoylphosphatidylcholine Bilayer. *Biophys. J.* 1998, *74*, 2786–2801.

(34) Bachar, M.; Brunelle, P.; Tieleman, D. P.; Rauk, A. Molecular Dynamics Simulation of a Polyunsaturated Lipid Bilayer Susceptible to Lipid Peroxidation. *J. Phys. Chem. B* 2004, *108*, 7170–7179.

(35) Mukhopadhyay, P.; Monticelli, L.; Tieleman, D. P. Molecular Dynamics Simulation of a Palmitoyl-Oleoyl Phosphatidylserine Bilayer with Na^+ Counterions and NaCl. *Biophys. J.* 2004, *86*, 1601–1609.

(36) Berendsen, H. J. C.; Postma, J. P. M.; van Gunsteren, W. F.; Hermans, J. In *Intermolecular Forces*; Pullman, B., Ed.; Reidel: Dordrecht, 1981; Chapter Interaction models for Water in Relation to Protein Hydration.

(37) Tieleman, D. P.; Berendsen, H. J. C. Molecular Dynamics Simulations of a Fully Hydrated Dipalmitoylphosphatidylcholine Bilayer with Different Macroscopic Boundary Conditions and Parameters. *J. Chem. Phys*. 1996, *105*, 4871–4880.

(38) Essmann, U.L.; Perera, L.; Berkowitz, M.L.; Darden, T.; Lee, H.; Pedersen, L.G.A. Smooth Particle Mesh Ewald Method. *J. Chem. Phys*. 1995, *103*, 8577–8593.

(39) Van Der Spoel, D.; Lindahl, E.; Hess, B.; Groenhof, G.; Mark, A. E.; Berendsen, H. J. C. GROMACS: Fast, Flexible and Free. *J. Comput. Chem*. 2005, *26*, 1701–1718.

(40) Berendsen, H. J. C.; Postma, J. P. M.; Van Gunsteren, W. F.; Dinola, A.; Haak, J. R. Molecular Dynamics with Coupling to an External Bath. *J. Chem. Phys*. 1984, *81*, 3684–3690.

(41) Ryckaert, J.-P.; Ciccotti, G.; Berendsen, H. J. C. Numerical Integration of the Cartesian Equations of Motion of a System with Constraints: Molecular Dynamics of *n*-Alkanes. *J. Comp. Phys*. 1977, *23*(3):327–341.

(42) Humphrey, W.; Dalke, A.; Schulten, K. VMD – Visual Molecular Dynamics. *Molec. Graphics* 1996, *14.1*:33–38.

(43) GROMACS User manual version 4.0. 2010.

(44) Chau, P.; Hardwick, A. J. A New Order Parameter for Tetrahedral Configurations. *Mol. Phys*. 1998, *93*, 511–518.

(45) Chaikin, P.; Lubensky, T. *Principles of Condensed Matter Physics*; Cambridge University Press: Cambridge, 1995.

(46) Böckmann, R. A.; Hac, A.; Heimburg, T.; Grubmüller, H. Effect of Sodium Chloride on a Lipid Bilayer. *Biophys. J.*

2003, *85*, 1647–1655.

(47) Gurtovenko, A. A.; Vattulainen, I. Effect of NaCl and KCl on Phosphatidylcholine and Phosphatidylethanolamine Lipid Membranes: Insight from Atomic-Scale Simulations for Understanding Salt-Induced Effects in the Plasma Membrane. *J. Phys. Chem. B* 2008, *112*, 1953– 1962.

(48) Cordomi, A.; Edholm, O.; Perez, J. J. Effect of Force Field Parameters on Sodium and Potassium Ion Binding to Dipalmitoyl Phosphatidylcholine Bilayers. *J. Chem. Theory Comput*. 2009, *5*, 2125–2134.

(49) Gurtovenko, A. A.; Anwar, J.;. Vattulainen, I. Defect-Mediated Trafficking across Cell Membranes: Insights from *In Silico* Modelling. *Chem. Rev*. 2010, *110*, 6077–6103.

(50) Deng, Z. J.; Liang, M.; Monteiro, M.; Toth, I.; Minchin, R. F. Nanoparticle-Induced Unfolding of Fibrinogen Promotes Mac-1 Receptor Activation and Inflammation. *Nat. Nanotechnol*. 2011, *6*, 39–44.

(51) Karlsson, H. L.; Cronholm, P.; Hedberg, Y.; Tornberg, M.; De Battice, L.; Svedhem, S.; Wallinder, I. O. Cell Membrane Damage and Protein Interaction Induced by Copper Containing Nanoparticles – Importance of the Metal Release Process. *Nanotoxicology,* 2013, *313*(1):59–69.

(52) Rahman, M.; Laurent, S.; Tawil, N.; Yahia, L. ; Mahmoudi, M. *Protein-Nanoparticle Interactions: The Bio-Nano Interface*; Springer-Verlag: Berlin Heidelberg, 2013.

(53) Dykman, L.; Khlebtsov, N. Uptake of Engineered Gold Nanoparticles into Mammalian Cells. *Chem. Rev*. 2014, *114*, 1258–1288.

Tampereen teknillinen yliopisto
PL 527
33101 Tampere

Tampere University of Technology
P.O.B. 527
FI-33101 Tampere, Finland

ISBN 978-952-15-3337-2
ISSN 1459-2045